TECHNISCHE UNIVERSITÄT MÜNCHEN

TUM School of Natural Sciences

Active Layer Morphology in Non-Fullerene Organic Solar Cells

Xinyu Jiang

Vollständiger Abdruck der von der TUM School of Natural Sciences der Technischen Universität München zur Erlangung des akademischen Grades einer

Doktorin der Naturwissenschaften (Dr. rer. nat.)

genehmigten Dissertation.

Vorsitz:	Prof. Dr. Martin Zacharias
Prüfer der Dissertation:	1. Prof. Dr. Peter Müller-Buschbaum
	2. apl. Prof. Dr. Hristo Iglev

Die Dissertation wurde am 31.05.2023 bei der Technischen Universität München eingereicht und durch die TUM School of Natural Sciences am 17.07.2023 angenommen.

Abstract

Organic photovoltaics have entered a new era of rapid development as a consequence of the spring-up of novel non-fullerene acceptors, making it a promising alternative to address today's energy issues. Despite the material innovation, the morphology of the active layer with the donor and acceptor domains on the nanoscale is the key to the performance of the organic solar cells, since it determines the exciton diffusion and dissociation, carrier transport and recombination. In this thesis, active layer morphology for the non- fullerene acceptor-based photovoltaics is investigated with advanced grazing-incidence X-ray scattering techniques. The active layer morphology was tuned using a solvent additive, and the relationship between active layer morphology, charge carrier dynamics, and device performance is elaborated. Furthermore, important insights into the morphology evolution during the active layer formation processes with different solvents were studied in situ. Besides, the illumination light-induced active layer morphology degradation with different non-fullerene acceptors is studied in an organic solar cell via in-operando measurements. Thus this thesis provides fundamental information on the active layer morphology in non-fullerene organic solar cells.

Zusammenfassung

Die organische Photovoltaik ist als Folge des Aufkommens neuartiger Fulleren-freier Akzeptormoleküle in eine neue Ära rasanter Entwicklung eingetreten, was sie zu einer vielversprechenden Alternative zur Lösung der heutigen Energieprobleme macht. Trotz der Materialinnovation ist die Morphologie der aktiven Schicht mit den Donor- und Akzeptordomänen auf der Nanoskala der Schlüssel zur Leistung der organischen Solarzellen, da sie die Exzitonen- diffusion und -dissoziation, den Ladungsträgertransport und die Rekombination bestimmt. In dieser Dissertation wird die Morphologie aktiver Schichten für die auf Fullerenfreien Akzeptormolekülen basierte Photovoltaik mit fortschrittlichen Röntgenstreutechniken unter streifendem Einfall untersucht. Die Morphologie der aktiven Schicht wird unter Verwendung eines Lösungsmitteladditivs abgestimmt, und die Beziehung zwischen der Morphologie der aktiven Schicht, der Ladungsträgerdynamik und der Geräteleistung ausgearbeitet. Darüber hinaus werden wichtige Einblicke in die Morphologieentwicklung während der Prozesse zur Bildung aktiver Schichten mit verschiedenen Lösungsmitteln in situ untersucht. Außerdem wird die durch Beleuchtungslicht induzierte Morphologiedegradation der aktiven Schicht mit verschiedenen Fulleren-freien Akzeptormolekülen in einer organischen Solarzelle durch in operando Messungen untersucht. Somit liefert diese Arbeit grundlegende Informationen zur Morphologie der aktiven Schicht in organischen

Solarzellen, die auf Fulleren-freien Akzeptormolekülen basieren.

Contents

Abstract ii

List of Abbreviations ix

1 Introduction 1

2 Theoretical Background 7
- 2.1 Polymer . . . 7
  - 2.1.1 Definition . . . 7
  - 2.1.2 Conductivity in a Polymer . . . 8
- 2.2 Organic Photovoltaics . . . 9
  - 2.2.1 Working Principle . . . 9
  - 2.2.2 Architecture of Organic Solar Cells . . . 11
  - 2.2.3 Degradation Mechanisms of Organic Solar Cells . . . 13
- 2.3 X-ray Scattering . . . 14
  - 2.3.1 Basic Principles . . . 14
  - 2.3.2 Scattering Geometry . . . 15
  - 2.3.3 Grazing-Incidence Small-Angle X-ray Scattering . . . 17
  - 2.3.4 Grazing-Incidence Wide-Angle X-ray Scattering . . . 19
  - 2.3.5 Data Treatment . . . 21

3 Characterization Methods 25
- 3.1 Spectroscopic and Electronic Characterization . . . 25
  - 3.1.1 UV-Vis Spectroscopy . . . 25
  - 3.1.2 Photoluminescence . . . 27
  - 3.1.3 Time-Resolved Photoluminescence . . . 29
  - 3.1.4 X-ray Photoelectron Spectroscopy . . . 30
  - 3.1.5 Transient Absorption . . . 31
- 3.2 Real-Space Structural Characterization . . . 32
  - 3.2.1 Atomic Force Microscopy . . . 32
- 3.3 Reciprocal-Space Structural Characterization . . . 33
  - 3.3.1 X-Ray Reflectivity . . . 33

3.3.2 Grazing Incidence Small-Angle X-Ray Scattering . . . 34
3.3.3 Grazing Incidence Wide-Angle X-Ray Scattering . . . 36
3.4 Device Characterization . . . 37
3.4.1 Current-Voltage Characterization . . . 37
3.4.2 External Quantum Efficiency . . . 38
3.4.3 Space-charge-limited Current . . . 39
3.5 In-Situ and Operando Characterization . . . 40
3.5.1 In-Situ Characterization of Active Layer . . . 40
3.5.2 Operando Characterization of Organic Solar Cells . . . 41

4 Fabrication Processes 43
4.1 Materials . . . 43
4.1.1 Donor Polymers and Acceptor Molecules . . . 43
4.1.2 Blocking Layer and Electrode Materials . . . 48
4.1.3 Solvents and Additives . . . 49
4.1.4 Substrates . . . 50
4.2 Cleaning Process . . . 51
4.2.1 Acid Bath Cleaning . . . 51
4.2.2 Ultrasonic Cleaning . . . 52
4.2.3 Oxygen Plasma Treatment . . . 52
4.3 Fabrication Process . . . 53
4.3.1 Solution Preparation . . . 53
4.3.2 Thin Film Deposition and Treatment . . . 54
4.4 Assembly of Solar Cells . . . 57
4.4.1 Invert Structure of Organic Solar Cells . . . 57
4.4.2 Hole-Only Device . . . 58
4.4.3 Electron-Only Device . . . 61

5 Solvent Additive in the Active Layer 63
5.1 Optical, Electronic Properties and Device Performance . . . 65
5.1.1 Absorption . . . 65
5.1.2 Photoluminescence . . . 67
5.1.3 Charge Carrier Dynamics . . . 68
5.1.4 Device Performance . . . 70
5.2 Morphology and Crystallinity of the Active Layer . . . 71
5.2.1 Surface Morphology . . . 71
5.2.2 Inner Morphology . . . 73
5.2.3 Crystallinity . . . 75

5.3 Vertical Distribution of the Donor and Acceptor in the Active Layer 80
5.3.1 Surface Composition 80
5.3.2 Vertical Distribution 81
5.4 Conclusion 83

6 Active Layer Processing via Scaling-Up Fabrication Method 85
6.1 Optical, Electronic Properties and Device Performance 87
6.1.1 Absorption and Photoluminescence 87
6.1.2 Charge Carrier Dynamics 89
6.1.3 Device Performance 91
6.2 Film Morphology 92
6.2.1 Surface Morphology 92
6.2.2 Inner Morphology 93
6.2.3 Crystalline Structure 96
6.3 Active Layer Formation Kinetics 102
6.3.1 Aggregation and Conformation Kinetics 102
6.3.2 Crystallinity Formation Kinetics 105
6.4 Conclusion 111

7 Formation Kinetics of the Active Layer Printed Out of A Non-Halogen Solvent 113
7.1 Active Layer Formation Kinetics 114
7.1.1 Morphology Formation Kinetics 114
7.1.2 Aggregation and Conformation Kinetics 117
7.2 Crystalline Structure 121
7.3 Conclusion 123

8 Active Layer Degradation in Organic Solar Cells 125
8.1 Optical, Electronic Properties and Device Performance 127
8.1.1 Absorption 127
8.1.2 Transient Absorption 129
8.1.3 Device Performance 134
8.2 Film Morphology 136
8.2.1 Surface Morphology 136
8.2.2 Crystalline Structure 137
8.3 Active Layer Degradation in Device 140
8.3.1 J-V Evolution 141
8.3.2 Inner Morphology Evolution 143
8.4 Conclusion 148

9 Conclusion and Outlook **151**

Bibliography **155**

List of Publications **174**

Aknowledgements **183**

List of Abbreviations

AFM	atomic force microscopy
Ag	silver
Al	aluminum
BHJ	bulk-heterojunction
BTP-4F (Y6)	(2, 20 - ((2Z, 20Z) - ((12, 13 - bis (2ethyl hexyl) - 3, 9 - diundecyl - 12, 13 - dihydro - [1,2,5] thiadiazolo [3, 4 - e] thieno [2,''30':4',50] thieno [20,30:4,5] pyrrolo [3,2-g] thieno [20,30:4,5] thieno [3,2-b]indole-2,10-diyl) bis (methanylylidene)) bis (5, 6 - difluoro - 3 - oxo- 2,3 - dihydro - 1 H - indene - 2, 1 - diylidene)) dimalononitrile)
CB	chlorobenzene
CF	chloroform
DI water	deionized water
DIO	1,8-diiodooctane
DWBA	distorted wave Born approximation
EBL	electron blocking layer
EH-IDTBR	(Z) - 5 - [5 - (15 - 5 - [(Z) - (3 - ethyl - 4 - oxo - 2 - thioxo - 1, 3 - thiazolidin - 5 - ylidene) methyl] - 8 - this - 7.9 diazabicyclo [4.3.0] nona - 1 (9), 2, 4, 6- tetraen -2 - yl -9, 9, 18, 18 - tetrakis (2- Ethylhexyl) - 5.14 dithiapentacyclo [10. 6. 0.03, 10.04, 8.013, 17] octadeca - 1 (12), 2, 4(8), 6, 10, 13 (17), 15 - heptaen -6 - yl)- 8 - thia-7.9 - diazabicyclo [4.3.0] nona- 1(9), 2, 4, 6- tetraen -2- yl] methylidene - 3- ethyl -2 - thioxo -1, 3- thiazolidin -4- one
EQE	external quantum efficiency

ETA	monoethanolamine
FF	fill factor
FWHM	full width at half maximum
GISAXS	grazing incidence small angle X-ray scattering
GIWAXS	grazing incidence wide angle X-ray scattering
GSB	ground state bleach
H_2O_2	hydrogen peroxide
H_2SO_4	sulfuric acid
HBL	hole blocking layer
HOMO	highest occupied molecular orbital
ICT	intramolecular charge transfer
IT-4CL	3,9-bis (2- methylene-((3-(1,1- dicyanomethylene) -6,7- dichloro)-indanone)) -5,5,11,11- tetrakis (4- hexylphenyl)- dithieno [2,3-d:2′,3′-d′]-s- indaceno [1,2-b:5,6-b′] dithiophene
IT-4F	3,9- bis (2-methylene- ((3- (1,1- dicyanomethylene) -6,7 -difluoro) -indanone))-5, 5, 11, 11-tetrakis (4-hexylphenyl) -dithieno [2,3-d : 2′,3′-d′]-s-indaceno [1,2-b:5,6-b′] dithiophene
IT-M	3,9-bis (2-methylene -((3-(1,1- dicyanomethylene)-6/7- methyl)-indanone))-5,5,11,11- tetrakis (4-hexylphenyl)- dithieno [2,3-d:2′,3′-d′]-s- indaceno [1,2-b:5,6-b′] dithiophene
ITO	indium doped tin oxide
Jsc	shortcircuit current density
JV	current-voltage characteristics
LED	light emitting diode
LMA	local monodisperse approximation
LUMO	lowest unoccupied molecular orbital
MoO_3	molybdenum oxide

MPP	maximum power point
NFA	non-fullerenen acceptor
OSC	organic solar cell
PBDB-T-2F (PM6)	poly [(2,6-(4,8- bis (5-(2- ethylhexyl -3- fluoro) thiophene-2-yl) benzo [1,2-b:4,5-b']dithiophene))-alt-(5,5-(1',3'-di-2-thienyl-5',7' bis (2-ethylhexyl) benzo [1',2'-c:4',5'-c'] dithiophene -4,8- dione)]
$PC_{71}BM$	[6,6]-phenyl-C_{71} butyric acid methyl ester
PCE/η	power conversion efficiency
PDI	polydispersity index
PDTBT2T-FTBDT (D18)	poly [(2,6-(4,8-bis(5- (2- ethylhexyl-3-fluoro) thiophen-2-yl)-benzo [1,2 - b: 4, 5-b'] dithiophene)) -alt -5, 5'- (5, 8-bis(4- (2-butyloctyl) thiophen - 2 - yl) dithieno [3',2': 3,4; 2'',3'': 5,6] benzo [1,2 - c][1, 2, 5] thiadiazole)]
PEDOT:PSS	poly (3,4-ethylenedioxythiophene):poly(styrenesulfonate)
PffBT4T-2OD	poly [(5,6-difluoro-2,1,3-benzothiadiazol-4,7-diyl) -alt- (3, 3'''-di(2-octyldodecyl)- 2, 2'; 5', 2'';5'',2-quaterthiophen-5,5'''-diy)]
PIA	photoinduced absorption
PL	photoluminescence
PTFE	polytetrafluoroethylene
PV	photovoltaic
SCLC	space-charge-limited current
SDD	sample-detector distance
SLD	scattering length density
TAS	transient absorption spectroscopy
TMB	1,2,4-trimethylbenzene
TRPL	time-resolved photoluminescence
UV-Vis	uv-vis spectroscopy

Voc ..... open-circuit voltage

XPS ..... X-ray photoelectron spectroscopy

XRR ..... X-ray reflectivity

ZAD ..... zinc acetate dihydrate

ZnO ..... zinc oxide

1 Introduction

Nowadays, the sustainable and stable industrialization development of human society is based on energy. The current energy sources are mainly coal, oil, natural gas and other fossil fuels, which are non-renewable. [1],[2],[3] In addition, fossil fuels cause serious pollution to the environment during combustion. Thus, for a sustainable future, we must look for clean and renewable alternative energy sources. [4],[5] Solar energy is one of the most abundant sustainable energy sources. [6] It is reported that the energy generated by radiating to the earth within one hour could fulfill the energy demands of human activities for a whole year. [7] Solar cells directly convert solar energy into electricity based on the photoelectric effect [8], are one of the most promising candidates to solve today's energy issue. According to the different light absorption layers, solar cells are mainly divided into silicon-based, [9],[10] perovskite, [11],[12] quantum dots, [13],[14] organic and other solar cells. [15],[16] Silicon-based solar cells are currently the longest-developed and best-commercialized cells. Today, the power conversion efficiency (PCE) of commercial crystalline silicon (c-Si) photovoltaic (PV) modules is over 16%. However, due to their rigid and opaque appearance, silicon-based solar cells are mostly installed either on the roofs of buildings or in large-scale solar power plants which limits the space utilization of solar energy conversion. [17] In order to open additional fields of application to photovoltaics, solution-based perovskite, [18],[19] quantum dots and organic solar cells have been decently developed in recent decades. [20] Compared to silicon-based solar cells, these devices allow for an easy fabrication process, cost-efficient processability, optical tuneability, and mechanical flexibility. Although perovskite solar cells receive more and more interest with the breaking through efficiency over 25%, [21] lead in materials is doomed to its environmental hazards. [22],[23],[24] Different from perovskite photovoltaics, organic solar cells (OSCs) are considered potentially environmentally friendly candidates for next-generation PV technologies. In addition, the semi-transparent appearance with tunable colour properties extends the application of organic photovoltaic (OPV) in architectural aesthetics. [25]

As reported, organic solar cells use organic material as an absorbing layer to realize solar energy conversion, which contains an electron donor (D) and an electron acceptor (A) component. However, excitons diffusion lengths in organic materials are only on the order of 10 nm and thus most of the generated excitons are recombined before reaching the interface

of the next layer. Consequently, the efficiency is very low in a traditional D-A bilayer system. In 1995, A. J. Heeger et al. proposed a bulk heterojunction (BHJ) layer concept where the donor and acceptor are intermixed in one layer, allowing for the generated excitons to reach the interface in a very short time scale. [26] This BHJ geometry of the active layer is beneficial for the performance of the OSCs and ever-growing records of efficiencies bring OPV into a new era. [27] However, historically organic solar cells use fullerene derivative acceptor [6,6]-phenyl-C-butyric acid methyl ester (PCBM) as the acceptor, which exhibits weak absorption in the visible and near-infrared (NIR) regions, restricting the opportunities for absorbing variation wavelengths and resulting in the OSCs' efficiencies of only about 10 % to 12 %, much lower than that of silicon cells. [28],[29],[30] The demand for replacing fullerenes has driven a rapid development of non-fullerene acceptors (NFAs) in the OPV field. Owing to the advantages of non-fullerene acceptors with easily tunable optical/electronic properties and easy solubility in various solvents, the efficiency bottleneck of organic solar cells has been successfully overcome. The PCE reaches over 19 % in single-junction and over 20 % in tandem architectures. OSCs are expected to move forward in the global PV market. [31],[32] Since the light is absorbed and the excitons are generated in the active layer, the OSCs' performance in terms of the NFAs-based devices is highly dependent on the morphology of the active layer. Multiply studies reveal that with better miscibility between the donor and acceptor in the active layer, a better charge-transport pathway is confirmed. [33],[34],[35] In addition, the active layer morphology is very easily influenced by additives, host solvents, atmospheres, etc., especially for NFAs-based materials. A deep understanding of the mechanism of how the additive, host solvent as well as the atmosphere induced the active layer morphology is an inevitable prerequisite for their development. Thus, the target of this thesis is to track the underneath correlation between the active layer inner morphology and the device performance in the field of non-fullerene organic solar cells. The mechanism of the active layer morphology in different states is revealed by a combination of grazing incidence small/wide angle X-ray scattering (GISAXS/GIWAXS) and several auxiliary techniques. Several studies have already proved that GISAXS/GIWAXS is a promising technique to reveal the inner morphology of the active layer in the range of one to hundreds of nanometers with a statistical approach. [36],[37],[38],[39] Moreover, high-brilliance X-rays from large-scale synchrotron radiation facilities allow us to obtain information about the kinetic morphology evolution on the active layer of the OSCs. [40],[41] The thesis is organized as the following: After a brief introduction, an overview of the theoretical background on organic conjugated polymers, OSCs, as well as the scattering techniques related to this thesis are discussed in Chapter 2. Then the used characterization methods and the corresponding experimental settings are introduced in Chapter 3. The characteristics of all materials used in this thesis and the sample fabrication processes are listed in Chapter 4. The main discussions

in this thesis related to the active layer morphology in non-fullerene organic solar cells are schematically illustrated in Figure 1.1 and sequentially discussed in Chapters 5-8.

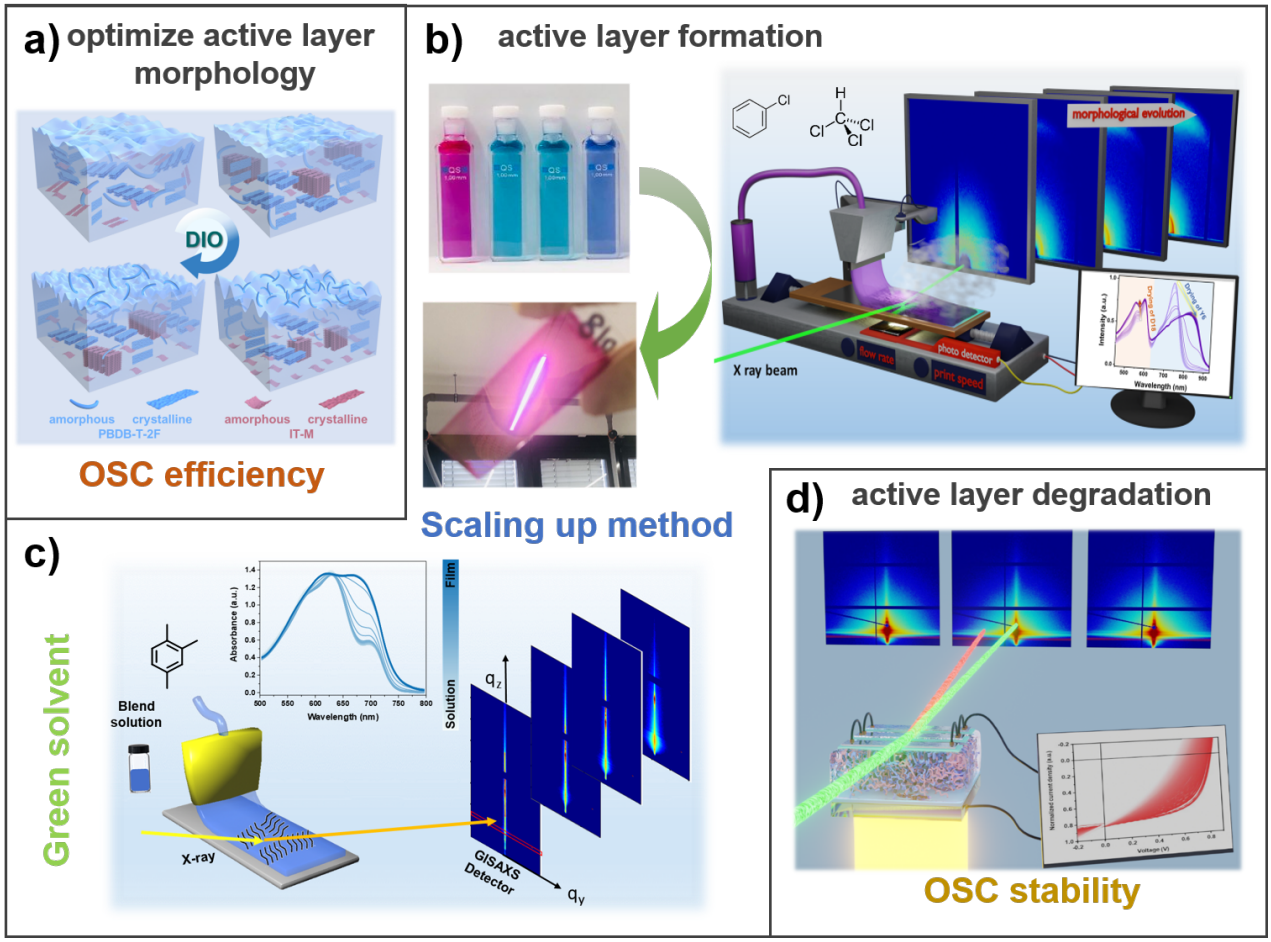

Figure 1.1: Schematic overview of the research topics addressed in the present thesis. a) Optimizing the active layer morphology by the solvent additive to improve the OSC performance. b) and c) Observing the active layer formation kinetics in a combination of in-situ measurements and slot-die coating method. d) Studying the active layer morphology evolution of the organic solar cell based on different non-fullerene acceptors via operando measurements .

The first study of this work is the investigation of the mechanisms of active layers with different morphologies for non-fullerene OSCs. As in many reports, the active layer morphology with fullerene acceptors could be easily adjusted by adding functional additives to achieve decent efficiencies. This strategy has also been applied to the morphological regulation of NFA OSCs. However, the underlying mechanisms by which the active layer morphology is tuned by additives remain unclear. Based on the above considerations, an experiment focused on the variation of the additive amount is required in Chapter 5. The wide bandgap polymer donor PBDB-T-2F and a non-fullerene small acceptor IT-M as p- and n-type components of the active layer are selected. The functional solvent additive

1,8-diiodooctane (DIO) is used to tailor the nanoscale morphology of the active layer. The mechanisms of additives on the active layer inner morphology of NFA OSCs are revealed and the device dynamics of charge carriers caused by the morphology are discussed.
In order to realize the commercialization of organic solar cells, finding a large-scale fabrication method being cost-effective is the way to go. Meniscus-guided slot die coating is currently the most promising alternative to traditional laboratory spin coating. For its scaling-up, fast, low solution consumption, and reproducible properties are beneficial when producing the thin film. [42] However, the thin film drying kinetics are different compare to spin-coating. The spin coating method utilizes the centrifugal force generated by high-speed rotation so that the solution on the substrate moves outward from the center to form a uniform film, and the solvent volatilization process is extremely rapid. However, for the slot-die coatings fabrication method, solvent evaporation mainly depends on its own saturated vapor pressure and the solvent evaporation rate is slow compared to spin-coating. As a result, the material has sufficient time to equilibrate, especially with respect to the interaction between donor and acceptor. Thus, the final active layer morphology processed by the slot-die coating method highly depends on the host solvent evaporation. For slot-die coating, it is very important to understand the morphology growth kinetics of the active layer for optimizing device efficiency. Therefore, the second part of this thesis is focused on the active layer morphology formation kinetics of NFA OSCs during the host solution drying process. The novel high-efficiency polymer donor, PDTBT2T-FTBDT, and the small molecule acceptor, BTP-4F, have been selected as the active layer and printed with slot-die coating method. The host solvents chloroform (CF) and chlorobenzene (CB) are selected to tune the morphology of the neat PDTBT2T-FTBDT and BTP-4F films and the PDTBT2T-FTBDT:BTP-4F blend films. By the in situ UV-Vis and in situ GIWAXS techniques, the active layer formation kinetics as well as the donor-acceptor interaction during the thin film drying are observed. The evolution of morphology, aggregation, and crystallite structure, as well as crystallite orientation, is discussed in Chapter 6. Moreover, towards an industrial large-scale of printed OSCs in an environment-friendly way, the utilization of a non-halogen-based host solvent coupled with the slot-die coating method and in-depth analysis of film formation kinetics are of great importance. [43],[44] In Chapter 7, the active layer containing the low band gap donor polymer PffBT4T-2OD and the non-fullerene acceptor EH-IDTBR is printed out of the environment-friendly halogen-free solvent 1,2,4-trimethylbenzene (TMB) at 60 °C with the slot-die coating method. The film formation kinetics of the active layer PffBT4T-2OD: EH-IDTBR is probed in terms of the temporal evolution in the morphology as well as molecular conformation and aggregation as revealed by in situ GISAXS and UV-Vis spectroscopy during the film printing process.
To bring organic solar cells into the field of application, the stability of the device is another

important factor that cannot be ignored. Previous studies have revealed that the chemical reactions in the interface between the blocking layers and the active layer exacerbates the device's performance loss in water and oxygen atmosphere. [45],[46],[47] The performance loss caused by chemical degradation could be ameliorated by simply replacing or modifying the reactive group of the blocking layer and isolating the water and oxygen by encapsulation. However, the loss of device performance due to the material itself is difficult to improve by adjusting external conditions. Though the performance of the OSCs is reaching 20 % through the innovation of new active layer materials, the poor operational stability of these OSCs remains a significant bottleneck, limiting their practical application and necessitating immediate attention. Thus it is crucial to understand the intrinsic degradation mechanisms induced by the material itself during device operation. The third part of the thesis discusses the evolution of active layer morphology based on different non-fullerene acceptors during long-term illumination in Chapter 8. A combination of GISAXS measurement and current-voltage tracking system on operating solar cells under vacuum is used to provide the active layer inner morphology and the photovoltaic characteristics simultaneously. With the aid of advanced techniques, an in-depth analysis of the complicated degradation stability relationship between device performance and active layer morphological evolution based on different high-efficiency acceptors is revealed.
Finally, Chaptper 9 summarizes the major findings of the present thesis. In addition, an outlook discusses the potential developments in the field of OSCs.

2 Theoretical Background

In this chapter, the theoretical aspects of polymers, organic solar cells and the methods of X-ray scattering related to this thesis are briefly introduced. The basic concepts of polymers are discussed in the section 2.1. Following the working principles and the architecture of organic solar cells as well as the degradation mechanisms in section 2.2. A detailed introduction of the X-ray scattering techniques, including the grazing incidence small/wide angle X-ray scattering, is presented in section 2.3.

2.1 Polymer

2.1.1 Definition

Polymer refers to a macromolecule with a very large molecular weight (M) made of a repeating chemical sub-units structure by covalent bonds. In the case of a polymer, the M is larger than 10 kg/mol. The molecule is called an oligomer if M is smaller than 10 kg/mol. [48] The repeating chemical units are called monomers. The process of combining monomers is called polymerization, and the number of monomers in the polymer is defined as the degree of polymerization. The average molecular weight (M_W) of a polymer could be given by

$$M_W = \frac{\sum_i n_i M_i^2}{\sum_i n_i M_i} \tag{2.1}$$

where the n_i refers to the molecular number of the repeating unit i and M_i is the number molar mass of the sub-unit. The number average molar mass (M_n) of a polymer is defined as

$$M_n = \frac{\sum_i n_i M_i}{\sum_i n_i} \tag{2.2}$$

The polydispersity index (PDI) in a polymer could obtain from the quotient of M_W and M_n

$$PDI = \frac{M_W}{M_N} = 1 + U \tag{2.3}$$

where U refers to the inconsistency coefficient, which could describe the distribution width. In the case of U $\geq$ 0, from the Equation 2.3, PDI $\geq$ 1, revealing the polydispersity of a

monodisperse polymer, while higher values indicate larger distribution widths.

2.1.2 Conductivity in a Polymer

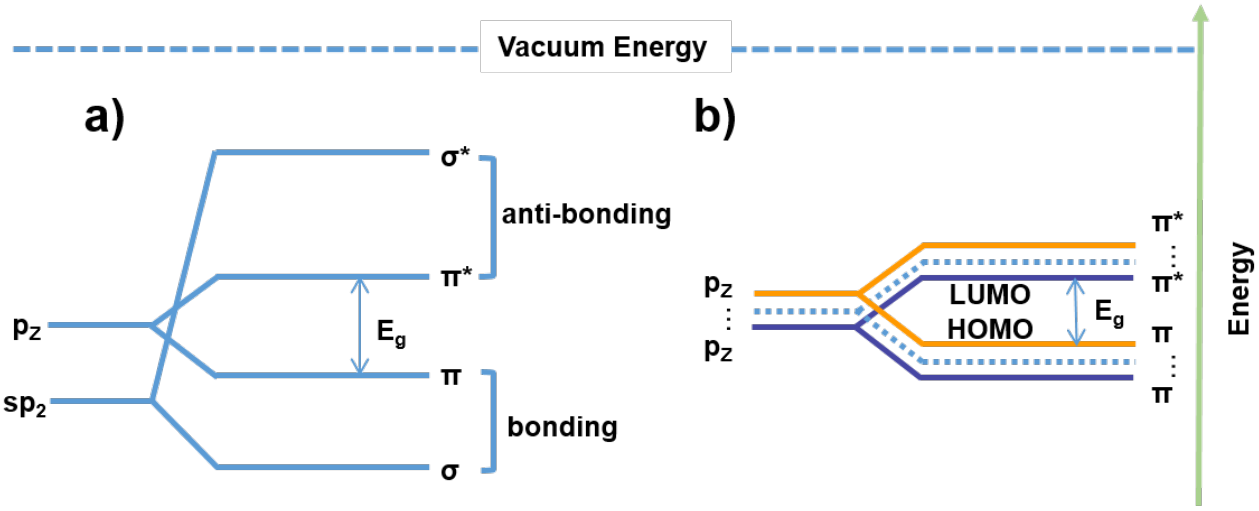

Figure 2.1: a) The energy diagram of the sp^2 hybridization, which formed bonding and anti bonding. b) For infinity coupled carbon units, the HOMO (in π orange) and the LUMO (in π^* purple) levels are separated by a band gap (E_g).

Polymers are considered insulation materials of inferior conductivity. However, the conductivity could be significantly improved by the introduction of alternating single and double bonds into the polymer backbone. This type of conductive polymer is called a conjugated polymer. In a conjugated system, the carbon atoms in the backbone exhibit sp^2 hybridization, where the sp^2 orbitals overlap thereafter providing strong localized σ bonds. In addition, the remaining p_z orbitals overlap in the out-of-plane direction eventually forming very weak so-called "π bonds". Thus, the energy splitting between bonding and anti-bonding states is higher in the strong σ bonds than in the weak π bond, resulting in an energy gap sketched in Figure 2.1a. However, the further polymerization with increasing chain length, the conjugated carbon atoms are increased, and the number of bonding π and the anti-bonding π^* close to infinity form two closed packing π and π^* bands, which are separated by the energy gap of the material. [49] As shown in Figure 2.1b, when the π bonding state is occupied with the highest energy, denoted the highest occupied molecular orbital (HOMO), similar to the valence band for inorganic semiconductors. When the anti-bonding π^* state is empty, it refers to the lowest unoccupied molecular orbital (LUMO), corresponding to the conduction band for the inorganic semiconductors. The band gap (E_g) for the conjugated polymer refers to the difference in energy level between the LUMO and HOMO. The band gap could reveal the electron-donating or withdrawing ability of the

polymer, which could be tuned by the introduction of electron-rich or -deficient domains in the polymer chains, such as nitrogen and sulfur elements. [50],[51],[52] In principle, organic conjugated semiconductors have bandgaps ranging from 1.5 to 3.5 eV [53],[54],[55], higher than silicon (1.1 eV) [56] or GaAs (1.4 eV) [57] those common inorganic semiconductors.

2.2 Organic Photovoltaics

Organic photovoltaics (OPVs) take organic materials as a functional layer to realize solar energy conversion via the photovoltaic effect. [58] Compared with silicon-based devices, OPVs have strong advantages like flexibility, transparency, low cost, and lightweight. [59],[60],[61] For the bulk heterojunction (BHJ) structure solar cells, the electron donor and acceptor materials are mixed together to generate the charger carriers and realize fast charge transfer to the corresponding anodes/cathodes efficiently. [62] The BHJ active layer in this thesis is fabricated from a mixture of a donor polymer and a small molecule acceptor with a certain weight ratio. The working principles of the organic solar cells are explained in section 2.2.1, and the geometry of the organic solar cells are introduced in section 2.2.2. The degradation mechanisms of the organic solar cells are discussed in section 2.2.3.

2.2.1 Working Principle

In organic solar cells, the conversion from light to electricity can be divided into five steps: 1) light absorption and exciton formation in the active layer, 2) exciton diffusion to the interface, 3) exciton dissociation to different phase regions, 4) charge carriers transport and extract in the corresponding blocking layers and finally (5) collecting free charge carriers into the electrodes. [63] Figure 2.2 briefly illustrates the working principle of an organic solar cell.

Light Absorption and Exciton Generation

A photon with the energy E= $\hbar\nu$ arrives on the active layer. If the photon energy (E) is larger than the optical bandgap of the active layer material, the photon could be absorbed. Then the electron-hole pair will be generated in the active layer, as shown in process (1) in Figure 2.2. The generated electron and hole could not separate due to the Coulomb binding energy.

Exciton Diffusion

Instead of the recombination of the electron-hole pairs, a certain amount of electron-hole pairs will diffuse into the interface of the donor and acceptor as shown in Figure 2.2 process

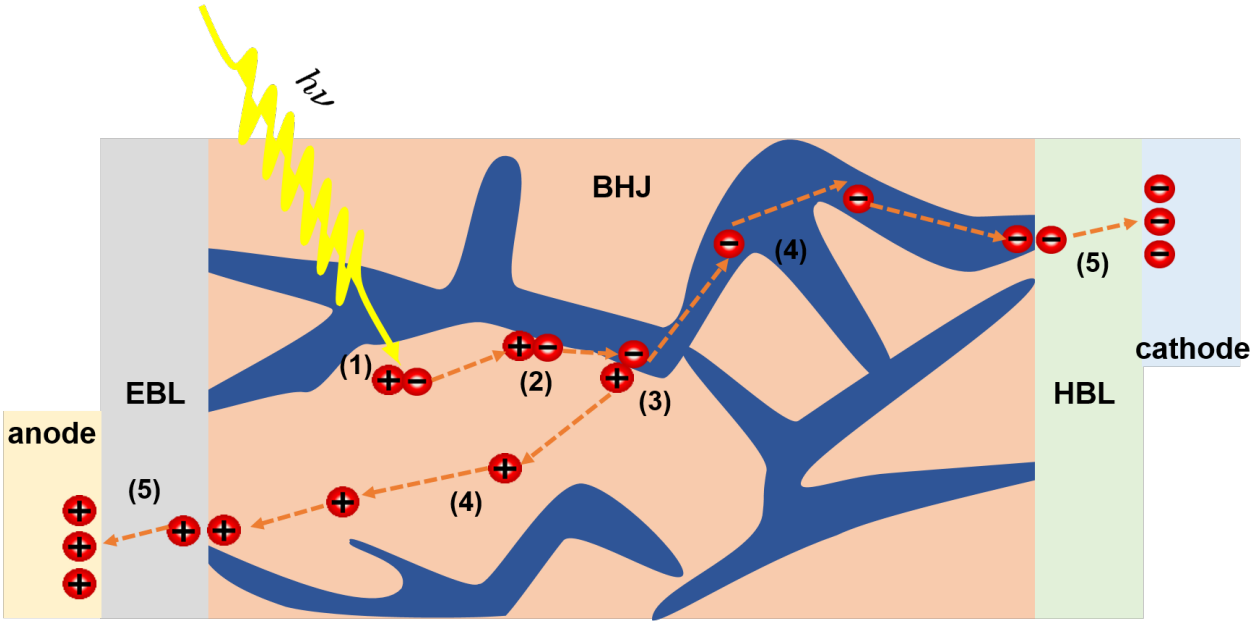

Figure 2.2: Schematic illustration of the working principle in an organic solar cell. The shallow yellow and blue bulk refer to the anode and cathode, respectively. The electron blocking layer (EBL)/ hole blocking layer (HBL) is the interlayer, which only permits the hole/electron of the charge carriers to go through to the corresponding electrodes. The blue and orange regions in the BHJ layer are the donor and the acceptor phases, respectively. The yellow arrow refers to a single photon with the energy of $\hbar\nu$.

(2). The diffusion length (L_D) can describe the distance of the electron-hole pair that could diffuse in the active layer before recombination. It is described as

$$L_D = \sqrt{(D_c \tau)} \tag{2.4}$$

Where D_c refers to the diffusion coefficient of the electron-hole pairs, τ refers to the electron-hole pair lifetime. Typically, for conjugated polymers, the diffusion lifetime is much shorter than in inorganic materials, in the range of ps-ns. Therefore, the electron-hole pair diffusion length in the active layer is less than 20 nm. [64]

Exciton Dissociation

Once the electron-hole pair reaches its interface between the donor and acceptor materials, it will get dissociated immediately, as shown in process (3) in Figure 2.2. The reason for that is due to the donor and the acceptor have an offset in the highest occupied molecular orbital (HOMO) and lowest unoccupied molecular orbital (LUMO) levels, there is a strong electric field in the interface of the donor and the acceptor. Once the energy level difference between the donor polymer HOMO and the small molecule acceptor LUMO is large enough

to get rid of the constraint of Coulomb binding energy, exciton dissociation happens. The amounts of the dissociation of polaron pairs (P(A)) could be calculated from Braun-Onsager model, [65],[66]

$$P(A) = \frac{k_d(A)}{k_d(A) + kr} \tag{2.5}$$

where the $k_d(A)$ refers to the coefficient of polaron dissociation, k_r refers to the recombination rate in the polaron pairs.

Charge Carrier Transport and Extraction

Once the electron-hole pairs are successfully separated in the active layer, the charge carriers start to transport to the corresponding interlayer as shown in Process (4) in Figure 2.2. Since the donor normally has a higher HOMO level than the acceptor, the hole prefers to migrate to the donor-dominated region. While the electron tends to diffuse in the acceptor-dominated region due to a lower LUMO level in the acceptor material. When the charge carriers arrive at the boundary of the active layers, the electrons diffuse into the hole-blocking layer (HBL) while the holes are blocked. And the holes diffuse into the electron-blocking layer (EBL) while the electrons are blocked.

Charge Carrier Collection

After the selection of the holes and electrons by the blocking layers, the free charge carriers will be collected at the neighboring metal or transparent electrode layer, respectively. The photo-current could be generated from the collected free-charge carriers.

2.2.2 Architecture of Organic Solar Cells

When light illuminates an organic solar cell, it will pass through a highly conducting electrode and an electron/hole-blocking layer. These two layers require excellent transmittance in the visible light range. According to the Lambert-Beer law, most of the light is absorbed by the active layer, and the rest of the light penetrates the second electron/hole-blocking layer. Finally, it is reflected by the metal electrode and reabsorbed by the active layer. Typically, the transparent electrodes are fabricated from indium-doped tin oxide (ITO) materials and the metal electrode is evaporated from Ag or Al material. Blocking layers are widely used to select the charge carrier type by tuning the energy level arrangement at the electrode/bulk active layer interface. [67] According to the work function of the material, CPE-K [68] and PEDOT:PSS [69] are typically applied as electron blocking layers, while LiF [70], ZnO [71], PFN [72], PFN-Br [73], PDINO [74] and PDINN [75] are used as hole blocking layers.
By placing different types of blocking layers into the active layer/electrode interface, two

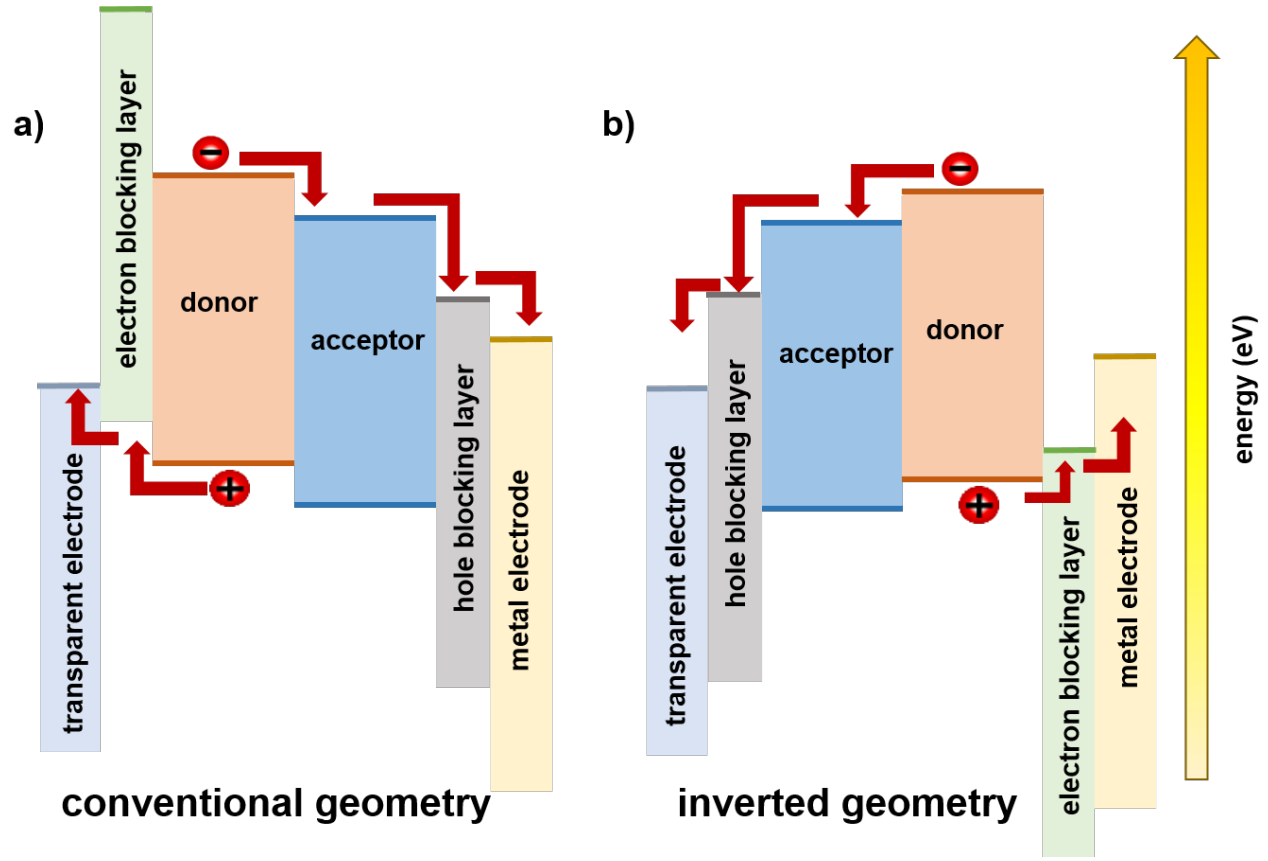

Figure 2.3: Energy level diagram of two types of widely established OSC geometry: a) conventional and b) inverted device geometry, respectively.

different geometries of the organic solar cells are defined as shown in Figure 2.3. According to the pathway of incident light in Figure 2.3a, the arrangement of the functional layers of the solar cell is as follows: transparent cathode (ITO)/the electron blocking layer/BHJ active layer/hole blocking layer/ metal anode, denoted as conventional device geometry. With this geometry, only holes are selected and transported to the ITO cathode, corresponding to the electrons selected and collected to the metal anode. If the incidence light pathway follows the geometry of transparent cathode (ITO)/hole blocking layer/BHJ active layer/the electron blocking layer/ metal anode shown in Figure 2.3b, in which only electrons selected and transport to the ITO anode while holes are selected and collect to the metal cathode. It is called inverted device geometry.

In the case of the LUMO level between the hole-blocking layer much higher than the acceptor in the conventional geometry, the electrons encounter the depletion region. Based on the quantum mechanism equation, [76] the penetration probability of the electron (E_p) is related to

$$E_p \propto \varepsilon \, exp\left[-\frac{\pi^2}{\hbar}\left(\frac{E_g}{e\varepsilon}\right)\sqrt{2mE_g}\right] \tag{2.6}$$

where the E_g refers to the bandgap of the blocking layer, ε refers to the permittivity, $\hbar$ is the Planck constant.

2.2.3 Degradation Mechanisms of Organic Solar Cells

In addition to the performance of the organic solar cell, the stability of the organic solar cells is another major aspect, which has to be considered for the step of commercialization. Factors that could cause the performance decrease of organic solar cells under illumination, could be briefly categorized into physical degradation and chemical degradation, respectively. [77],[45] In the case of chemical degradation, which suggests chemical redox reactions occur in the organic solar cell during illumination. Water and oxygen are attributed to the common external causes leading to chemical degradation in the organic solar cell. Oxygen in the atmosphere could penetrate the active layer and reacts especially with the small molecule acceptors and damage the conjugated backbone through the photo-oxidation reaction. [78] The photo-oxidation of the active layer is induced by superoxide ions (O_2^-), which are associated with the LUMO level of acceptors. [79] Water in the atmosphere, could damage the interface of the device in terms of the blocking layer and the active layer under illumination. Water and oxygen are easily absorbed into the ZnO blocking layer and generate hydroxyl radicals(-OH) which react with the non-fullerene acceptors. Thereafter, the original structure of the active layer is provoked, resulting in a reduced electron collection ability from the active layer to the electrodes. [80],[46]
Concerning the physical degradation process, which is closely related to the intrinsic causes of the organic solar cells, in terms of the morphology deterioration of the active layer under light-soaking. The aggregation and reorganization of active layer blends exacerbate morphological changes when the thermodynamic equilibrium state of the active layer domain composition is disrupted by illumination. This results in an electron/hole mobility imbalance, which in turn leads to severe charge trapping and recombination losses. [81] The polymer domains both in the fullerene and non-fullerene-based active layer, tend to become coarse during long-term light exposure, leading to a continuous decrease in the short-circuit current. [82],[83] The coarsening of polymer domains leading to unfavorable phase separation of the active layer is not the only degradation route in organic solar cells. Moreover, a shrinkage of polymer domains in the active layer which is caused by the evaporation of the high-boiling point solvent additive during the illumination. [84]

2.3 X-ray Scattering

Structural investigation of the active layer in reciprocal space is performed by using advanced scattering techniques. In contrast to real space imaging techniques, X-ray scattering techniques provide statistical information with a certain penetration depth in the range of 10 to 100 nanometers. [85] In the present thesis, only the information from elastic scattering is measured, where the energy of the incident beam equals the final outcome beam.

2.3.1 Basic Principles

X-rays are electromagnetic waves produced by oscillating magnetic and electric fields, with photon energies ranging from 100 eV to 100 KeV. When it travels through a medium material, the full complex refractive index n is determined by the equation [86]

$$n = 1 - \delta + i\beta \tag{2.7}$$

where δ refers to the dispersed deviation from unity, i refers to the imaginary number that manifests the wavelength-dependent absorption of X-rays by a single atom, and β refers to the absorption component. In the hard X-ray regime, $\beta \approx 10^{-7}...10^{-9}$, thus the refractive index is approximately real and smaller than 1. The critical angle α_c with respect to the sample surface of organic material in the active layer is of great importance for the small angle scattering experiment and could be approximated and simplified by the Snell's law [87]

$$\alpha_c = 90^\circ - Re(arcsin(n)) \tag{2.8}$$

When the sample was illuminated with X-rays under a grazing incidence small angle, an anomalous surface scattering from thin films where an intensity peak appears under the critical angle. This anomalous scattering leads to enhanced scattering intensity at the critical angle when interdigitated structures of different materials exist in the investigated thin film samples as observed by Yoneda. [88] In order to extract the desired signal, however, the critical angle of the material under study must be known. For most materials, there are no explicit values for the refractive index at different X-ray energies listed in the literature. Henke et al. used atomic scattering form factors to approximate the refractive indices. And the atomic form factor f_k of an element k can be described by [89]

$$f_i = f_k^{(0)} + f_k'(\lambda) + if_k''(\lambda) = f_k^{(1)} + if_k^{(2)}(\lambda) \tag{2.9}$$

The scattering length density (SLD) can be described by

$$SLD = \gamma_0 \rho_e \frac{\sum_{k=1}^{N} c_k f_k}{\sum_{k=1}^{N} Z_k} \tag{2.10}$$

ρ_e refers to the average electron density of a material, c_k is the stoichiometric fraction of the atomic species k, and Z_k is the total number of electrons per species k and unit volume. And the γ_0 refers to the classical Thomson scattering radius described by:

$$\gamma_0 = \frac{e^2}{4\pi\varepsilon_0 m_e c^2} \tag{2.11}$$

Since the electron density is often unknown, the SLD also can be approximated by the equation:

$$SLD = \gamma_0 \rho N_A \frac{\sum_{k=1}^{N} c_k f_k}{\sum_{k=1}^{N} M_k} \tag{2.12}$$

The ρ refers to the mass density, and M_k refers to the specific molar mass of each item k. N_A refers to Avogadro's constant. In terms of the grazing-incidence X-ray scattering (GIXS) experiments, the momentum transfer $\vec{q} = \vec{k}_f - \vec{k}_i$ is small.Thus, the atomic scattering factors can be approximated by $f_k^{(0)} \approx Z_k$ and $f_k' \ll f_k^{(0)}$, the refractive index can also approximated via:

$$n = 1 - \frac{\lambda^2}{2\pi}\gamma_e \rho_e + i\frac{\lambda}{4\pi}\mu \tag{2.13}$$

with the linear absorption coefficient $\mu(\lambda)$ for X-rays:

$$\mu(\lambda) = \frac{4\pi\beta(\lambda)}{\lambda} \tag{2.14}$$

And the characteristic absorption length $\wedge_{abs}(\lambda)$ as

$$\wedge_{abs}(\lambda) = \frac{1}{\mu} = \frac{\lambda}{4\pi\beta(\lambda)} \tag{2.15}$$

For hard X-rays, the dispersive and absorbing part of the refractive index is typically in the order of $\delta \approx 10^{-6}$, $\beta \approx 10^{-7}...10^{-9}$. [90],[91] Therefore, the scattering contrast for X-ray experiments relies on electron density fluctuations in a sample.

2.3.2 Scattering Geometry

When a plane electromagnetic wave impinges on a single object with a specific shape, the wave is scattered. The scattering vector $\vec{q}$ expresses the momentum transfer from a sample

to the scattered beam and can be described as:

$$\vec{q} = \vec{k}_f - \vec{k}_i \tag{2.16}$$

where $\vec{k}_f$ refers to the final outcome beam and $\vec{k}_i$ refers to the incident beam.

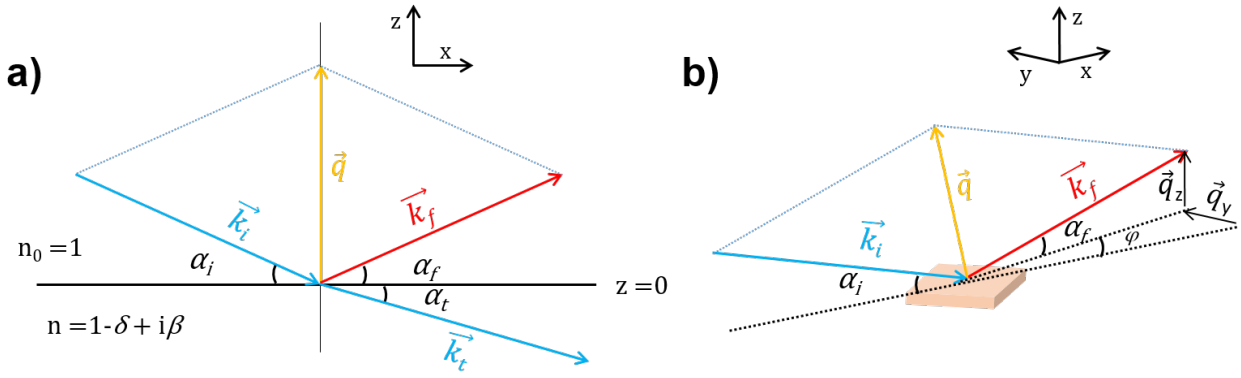

Figure 2.4: Different geometries and definitions for grazing incident X-ray scattering. a) For the specular scattering, where the reflected angle with respect to the sample surface is equal to the incidence wave ($\alpha_f = \alpha_i$). b) For the diffuse scattering, the final angle of the reflected wave with a different momentum wave angle ($\alpha_f \neq \alpha_i$) in xz-plane and an additional scattering angle φ in the y-direction is detected.

Figure 2.4 illustrates a schematic diagram of two different scattering geometries with the basic definitions of the angles. The incident beam with the wave vector $\vec{q}$ impinges the sample under the incident angle α_i with respect to the sample surface. For specular reflection geometry in Figure 2.4a, such as X-ray reflectivity (XRR), the final angle α_f is equal to the incident angle α_i along the xz-plane. The modulus of the wave vector k= $\frac{2\pi}{\lambda}$ is constant with the incident vector while varies in the direction, assuming only the elastic scattering is considered. For the diffuse scattering in Figure 2.4b, the final angle varies from the incident angle ($\alpha_f \neq \alpha_i$) in the xz-plane, and an additional scattering angle φ in xy-plane is observed. [92] Based on Snell's law, partly beam $\vec{k}_t$ is transmitted through the sample with an exit angle α_t. The scattered exiting beam is expressed as $\vec{k}_f$ with an angle of α_f. The transmitted beam angle depends on the incident angle and the reflection index (n) of the material. Based on Shell's law

$$n_0 cos(\alpha_i) = n cos(\alpha_t) \tag{2.17}$$

Considering the incident beam impinges the investigated sample at an air interface where the reflection index is 1, total external reflection happens below a certain incident angle (α_t = 0). With the small angle approximation according to the Taylor series (cos(α_c) = 1-$\frac{\alpha_c^2}{2}$), the

critical angle of the sample can be expressed as

$$n = cos(\alpha_c) \approx 1 - \frac{\alpha_c^2}{2} \Rightarrow \alpha_c = \sqrt{2-2n} = \sqrt{2\delta} = \lambda\sqrt{\frac{\rho}{\pi}} \tag{2.18}$$

2.3.3 Grazing-Incidence Small-Angle X-ray Scattering

In this thesis, small-angle X-ray scattering experiments are performed in grazing incidence geometry to investigate the inner morphology in the active layer of organic solar cells. A small grazing incident angle which above the material critical angle is used to detect the thin film information (α_c<α_i<1°). According to the Figure 2.4b, the scattering vector based on Equation 2.16 can be described as [93]

$$\vec{q} = \begin{pmatrix} q_x \\ q_y \\ q_z \end{pmatrix} = \frac{2\pi}{\lambda} \begin{pmatrix} cos(\alpha_f)cos(\psi_f) - cos(\alpha_i)cos(\psi_i) \\ cos(\alpha_f)sin(\psi_f) - cos(\alpha_i)sin(\psi_i) \\ sin(\alpha_f) - sin(\alpha_i) \end{pmatrix} \tag{2.19}$$

In the case of ψ_i = 0 in the xy-plane, the scattering vector can be simplified as

$$\vec{q} = \frac{2\pi}{\lambda} \begin{pmatrix} cos(\alpha_f)cos(\psi_f) - cos(\alpha_i) \\ cos(\alpha_f)sin(\psi_f) \\ sin(\alpha_f) - sin(\alpha_i) \end{pmatrix} \tag{2.20}$$

Since only elastic scattering is considered in this thesis, the modulus of the final wave vector is equal to the incident wave vector, therefore the $\vec{k}_f$=$\vec{k}_i$. [94] In grazing incidence small angle scattering, additional reflection or refraction phenomena may happen at the sample-to-substrate interface, since a small incident angle is applied. Distorted-wave Born approximation (DWBA) is utilized to account for these additional events. [95],[96] A simplified graphical representation including four types of scattering events inside the frame of DWBA is depicted in Figure 2.5. The incident beam with the momentum transfer $\vec{k}_i$ could be scattered on the structure directly with the final beam with the momentum transfer $\vec{k}_f$ (Figure 2.5a), or reflected on the substrate firstly, then scattered on the structure (Figure 2.5b). In another case, the incident beam can also be scattered on the structure, then reflected on the subtracted (Figure 2.5c). In the most complicated case, the incident beam is reflected on the substrate, followed by scattering on the object, and then reflected on the substrate (Figure 2.5d).

When the sample is irradiated with X-rays at shallow angles, abnormal surface scattering results in enhanced scattering intensity in the critical angle range, presented as Yoneda Peak. In this scope, the material structure information is revealed. In order to extract lateral structural information from the Yoneda peak, the horizontal line cuts are made at the peak

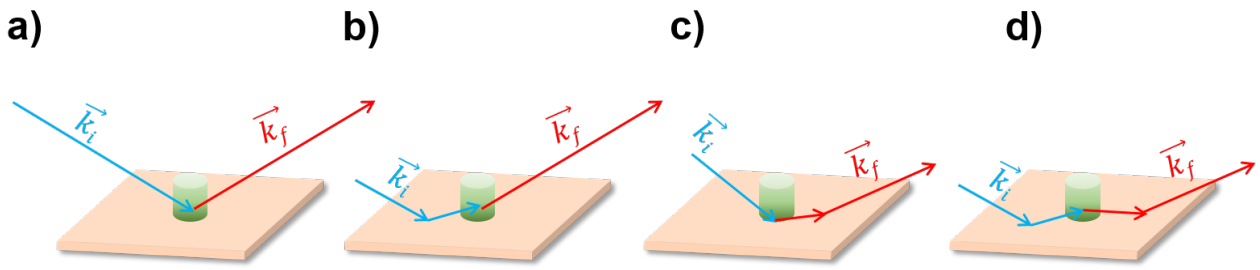

Figure 2.5: Schematic description of scattering and reflection contributions in the DWBA. a) Directly scattered beam; b) scattered and reflected beam; c) reflected and scattered beam; d) reflected-scattered-reflected beam, respectively.

positions. Therefore, the analysis is performed for fixed q_z values, in which only lateral correlations in the thin film are considered. A further simplification can be obtained by the effective interface approximation (EIA), where the height correlation function of the sample is described by an efficient interface. [97] Perturbations are highly dependent on the film roughness and lateral structure, therefore the interfaces between the material to the substrate should be perfectly smooth. Differential cross-sectional diffuse scattering on a sample can be calculated by

$$\frac{\mathrm{d}\delta}{\mathrm{d}\Omega} = \frac{A\pi^2}{\lambda^4}(1-n^2)^2 \mid T_i \mid^2 \mid T_f \mid^2 P_{diff}(\vec{q}) \propto P_{diff}(\vec{q}) \tag{2.21}$$

where A is the illuminated area, $P_{diff}(\vec{q})$ is the diffuse scattering. T_i and T_f are the Fresnel transmission coefficients of the incident and scattered beam respectively. At a small angle regime where identical objects are in a geometrical arrangement, assuming the form factor $F(\vec{q})$ of mesoscopic objects with approximately homogeneous refractive index, the overall scattering factor $P_{diff}(\vec{q})$ is related to [98]

$$P_{diff}(\vec{q}) \propto N \mid F(\vec{q}) \mid^2 S(\vec{q}) \tag{2.22}$$

where N refers to the number of scattering objects, $S(\vec{q})$ is the structure factor.
Despite the DWBA and EIA, further simplification and approximation named the local monodisperse approximation (LMA) is used to analyze the GISAXS scattering data in this thesis. [99] In the LMA model, the scattering weight of each object is replaced by its mean value over the size distribution. Therefore, crossing coupling between different objects structures (j) is assumed by the superimposition of each form factors type

$$P_{diff}(\vec{q}) \propto N_j \mid F_j(\vec{q}) \mid^2 S_j(\vec{q}) \tag{2.23}$$

A further assumption in this thesis for GISAXS modeling, is the scattering objects are approximated in their arrangement by a one-dimensional paracrystalline lattice (1DDL). [100] In addition, a cylinder or sphere is used to model the scattering object, where with a Gaussian distribution of the size and of the mean inter-domain distance. [82]

2.3.4 Grazing-Incidence Wide-Angle X-ray Scattering

In the regime of grazing-incidence wide-angle X-ray scattering, a small length scale in the sub-manometers with respect to the crystalline lattice spacing is detected based on the change of the wave vector momentum in reciprocal space. For X-rays, the scattering signal is related to the periodic electron density cloud of a lattice of single atoms, which could be approximated by the atomic scattering factor in Equation 2.9. Thus, wide-angle scattering measurements can reveal the crystallinity of the thin films.

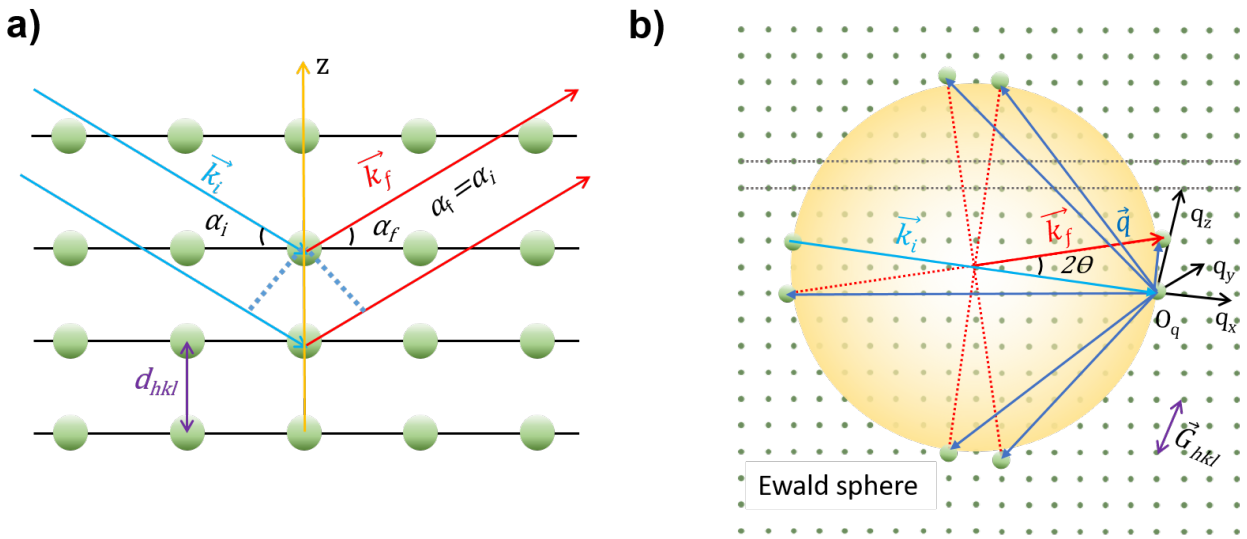

Figure 2.6: a) Illustration of X-ray diffraction with respect to Bragg's law: the incoming beam (blue) scatters on a hkl-plane. The reflected waves (red) leave the sample with an angle of α_f, which is equal to the angle of the incoming beam (α_i). b) Graphical representation of Ewald sphere (yellow sphere) in reciprocal space, assuming the Laue condition $\vec{G}_{hkl} \equiv \vec{q}$ (green dots), constructive interference occurs and the consequent diffraction vector of X-ray beam ($\vec{k}_f$) under the angle of 2θ, and the scattering vector $\vec{q} = \vec{k}_f$ - $\vec{k}_i$, where the $\vec{k}_i$ is the incident beam.

X-rays go through a crystalline structure of a sample with an incident angle of α_i, subsequently, a reflected scattering with the periodic lattice plane {hkl} is revealed as shown in Figure 2.6a. The exit angle of α_f is equal to α_i, since the elastic scattering. For simplicity, θ is defined as the incident/final angle. Therefore, the lattice plane distance (d_{hkl}) can be

calculated via Bragg's equation

$$d_{hkl} = \frac{n\lambda}{2sin(\alpha_i)} = \frac{n\lambda}{2sin(\theta)} \tag{2.24}$$

where the λ refers to the wavelength of the X-ray and n refers to the refractive index. If the scattering vector ($\vec{q}$) only depends on the z-component, the lattice plane distance (d_{hkl}) could approximate as

$$d_{hkl} = n\frac{2\pi}{q} \tag{2.25}$$

The crystal lattice in real space is normally transformed into a reciprocal space through Fourier transformation to investigate the complete set of wave vectors that contribute to scattering. Considering Huygens' principle each scatters is based on an elementary wave. Therefore, if the momentum transfer matches a reciprocal lattice vector ($\vec{G}_{hkl}$) under the Laue condition, constructive interference occurs. The reciprocal lattice vector ($\vec{G}_{hkl}$) can be expressed as:

$$\vec{q} \equiv \vec{Q}_{hkl} = h\vec{a} + k\vec{b} + l\vec{c} \tag{2.26}$$

Where the $\vec{a}$, $\vec{b}$ and $\vec{c}$ refer to the reciprocal lattice vectors. h, k, l are the Miller Indices.
As shown in Figure 2.6b, a diffuse scattering (small green dots) with an incident beam ($\vec{k}_i$) in real space, the scattered beam ($\vec{k}_f$) is deflected by an angle of 2θ versus the incoming beam, describes a sphere in reciprocal space, defined as the Ewald sphere. The Ewald sphere acts as a "bridge" connecting the real space and reciprocal space, thus the coordinate system from (x,y,z) in real space could be transformed to lattice vectors ($\vec{a}$,$\vec{b}$,$\vec{c}$) in reciprocal space. To get the momentum transfer translated from the reciprocal space to the real-space coordinate system, two conditions have to be fulfilled: 1) satisfying the Laue condition $\vec{G}_{hkl} \equiv \vec{q}$, which means the momentum is transferred to the final wavevector $\vec{k}_f$, and the momentum transfer is described to $\vec{q}$. 2) the incident lattice and scattering lattice points must be on the surface of Ewald's sphere. In real space, similar to the GISAXS scattering geometry (Figure 2.4b), the scattering angle can be described by an azimuthal contribution φ, and an out-of-plane contribution α_f. Since the wavevector transfer also contributes in the $\vec{q}_x$ direction, a non-negligible contribution in q_{xy} and q_{xz} planes on a two dimensional (2D) GIWAXS detector has to be considered. [101] As the q_z and q_y component cannot be decoupled from the q_x from the detected 2D scattering pattern, it results in a missing wedge for the non-accessible q ranges as shown in Figure 2.7.

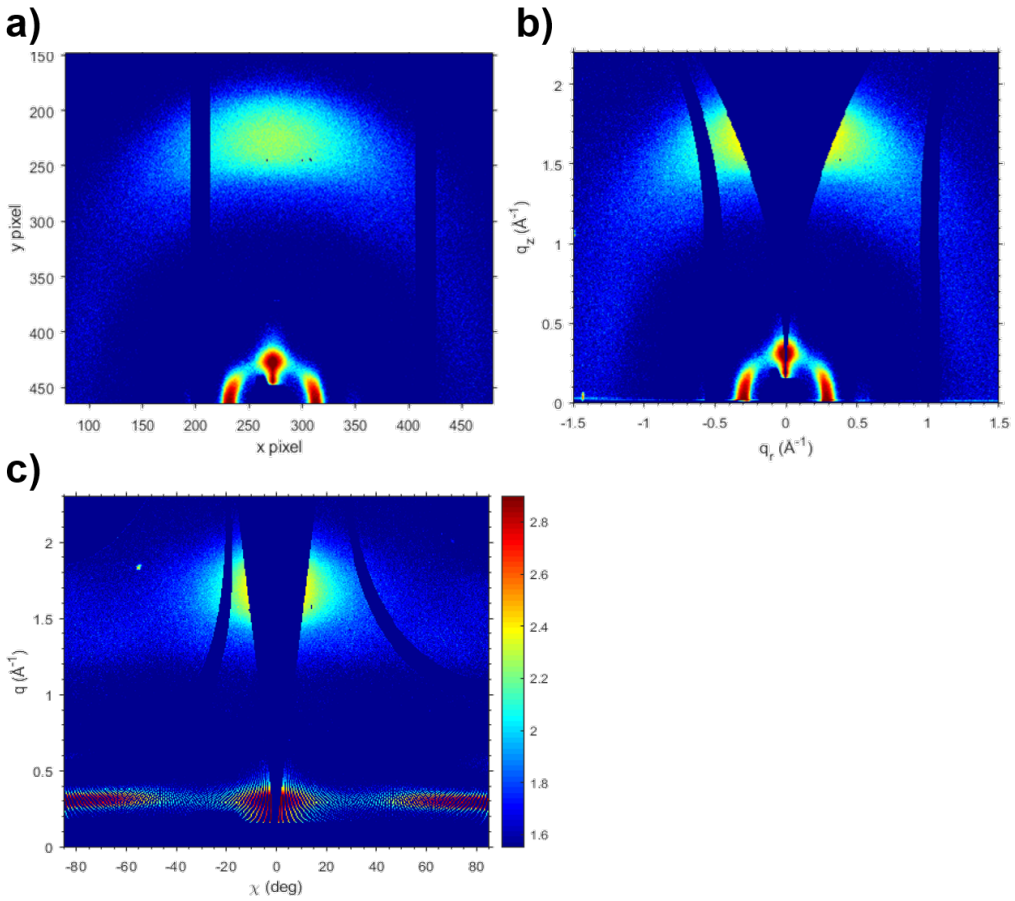

Figure 2.7: a) Raw detector image with in-plane and the out-of-plane angle in pixel values, (b) q transformation resulting in a missing wedge as lattice points with $q_r = 0$ are not accessible, (c) total q transformation versus χ values.

2.3.5 Data Treatment

The GIWAXS technique can determine the crystal size and orientation of a thin film. The thin film, which contains conjugated D-A polymer or monomer structure, readily packed into crystalline or ordered structures with different orientations. Assuming a single conjugated polymer chain as a lamella, three typical geometry of the crystalline structure in the field of organic solar cells and the corresponding GIWAXS patterns are demonstrated in Figure 2.8. In the case of a crystalline thin film with an orientation of all crystal planes parallel to the substrate, called "face-on" orientation, two distinguished symmetrical (100) peaks located at low q range along the q_{xy} direction and a well pronounced broad (010) peak located at large q range along the q_z direction appear on a GIWAXS detector (Figure 2.8a). In the case of the crystal planes perpendicular to the substrate, called "edge-on" orientation, a (100) peak in the low q range with two symmetric (010) peaks in the high q range are detected in the q_z direction and q_{xy} direction, respectively (Figure 2.8b). In the case of crystal film with

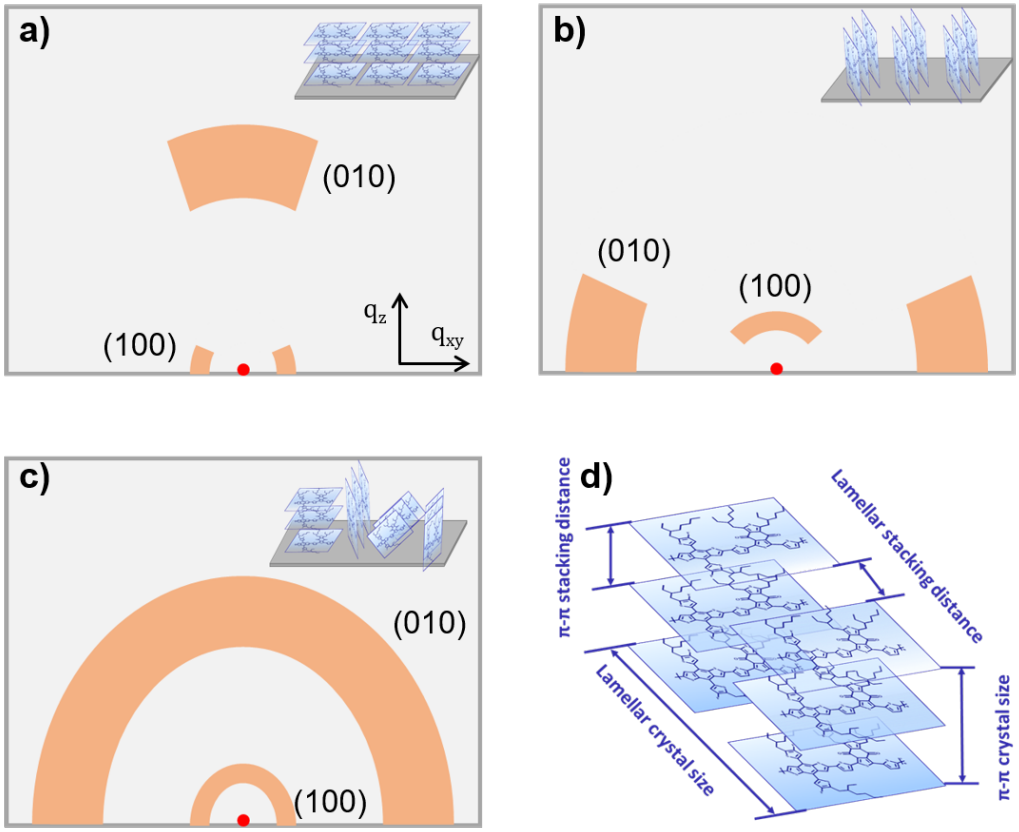

Figure 2.8: Illustration of different crystal orientations (a) face-on, b) edge-on, c) isotropic) in an organic thin film and the corresponding 2D GIWAXS scattering signal. d) Schematic diagram of lamellar and π-π stacking in a single polymer crystal. The red dot represents the direct beam position, and the orange pattern suggests the scattering intensity on the GIWAXS detector.

random orientations, the typical (100) and (010) Bragg peaks switch into Debye-Scherrer rings, as Figure 2.8c, called "isotropic" orientation.
The lamellar or π-π the stacking distance of a crystal in Figure 2.8d could be estimated by the Bragg equation

$$d = \frac{n\lambda}{2sin(\theta)} = \frac{n2\pi}{q} \tag{2.27}$$

where q is the peak position. The crystal size of the investigated material in this thesis is estimated by the Scherrer equation [102]

$$D = \frac{K\lambda}{FWHMcos(\theta)} \tag{2.28}$$

where D is the crystal size to the peak's full width at half maximum (FWHM), K is the shape factor of the crystal, and normally K= 0.9 is used for the organic materials. The FWHM is

obtained by modeling the respective Bragg peaks in the azimuthal q integral of the GIWAXS data with Gaussian functions. Before the line cuts process, the following corrections need to be applied to the measured data.

Flat Field Correction (C_{FF}), Dark Field Correction (C_{DF})

Flat field correction (C_{FF}) and dark field correction (C_{DF}) take the role to dismiss the different sensitivities for the individual pixels from the detector. The C_{FF} can be directly performed on the 2D raw image by a calibration file from the manufacturer. The C_{DF} can be performed by extracting the not functional pixel out via a mask file, which only includes a neat detector image.
All pixels of a 2D detector have equal size, since the measurement geometry of GIWAXS, every pixel with the area ($A_0 = L_x\ L_y$) covers a different solid angle distribution. The solid angle correction is used to dismiss the geometrical effect.

$$C_\Omega = \frac{\triangle\Omega_0}{\triangle\Omega_{2\theta}} \tag{2.29}$$

where the $\triangle\Omega_0$ refers to the solid angle to the pixel at the direct beam position on the detector (x_0, y_0), r_0 refers to the sample to detector distance (SDD) and $\triangle\Omega_{2\theta}$ can be obtained from

$$\triangle\Omega_0 = \frac{A_0}{r_0^2}, \triangle\Omega_{2\theta} = \frac{A_{2\theta}}{r_{2\theta}^2} \tag{2.30}$$

The scattering angle (2θ) with respect to the pixel position (x_k, y_k) can be obtained from the equation:

$$2\theta = arctan\sqrt{\frac{L_x^2(x_k - x_0)^2 + L_y^2(y_k - y_0)^2}{SDD}} \tag{2.31}$$

With this correction, the scattering intensity is normalized from the direct beam position.

Polarization Correction

Synchrotron sources, such as DESY PETRA III, distinct in their radiation generation method, produce horizontally linearly polarized radiation, achieving a polarization efficiency of about 98%. [101] In the probed material, dipole oscillations directed towards this polarization result in a reduction in the scattered intensity at small angles between the plane of polarization and the scattered beam. As a consequence, the scattering intensity at such small angles is underrepresented and requires an adjustment via the so-called polarization correction. [103] The calculation of the polarization correction (C_p) could describe as:

$$C_P = A \mid sin\phi \mid^2 + (1 - A)cos^2\alpha_f = A(1 - cos^2\alpha_f sin^2\phi) + (1 - A)cos^2\alpha_f \tag{2.32}$$

Where the ϕ is the angle between the polarization direction and the scattering wavevector $\vec{q}_f$. A is the X-ray horizontal polarization fraction, $0 \leq A \leq 1$

Efficiency Correction

When the scattered X-rays travel to the detector through a medium such as air, or the photons scattered at different oblique scattering angles, the beam intensity is attenuated. Therefore, these influences need to be taken into account through efficiency correction.

Lorentz Correction

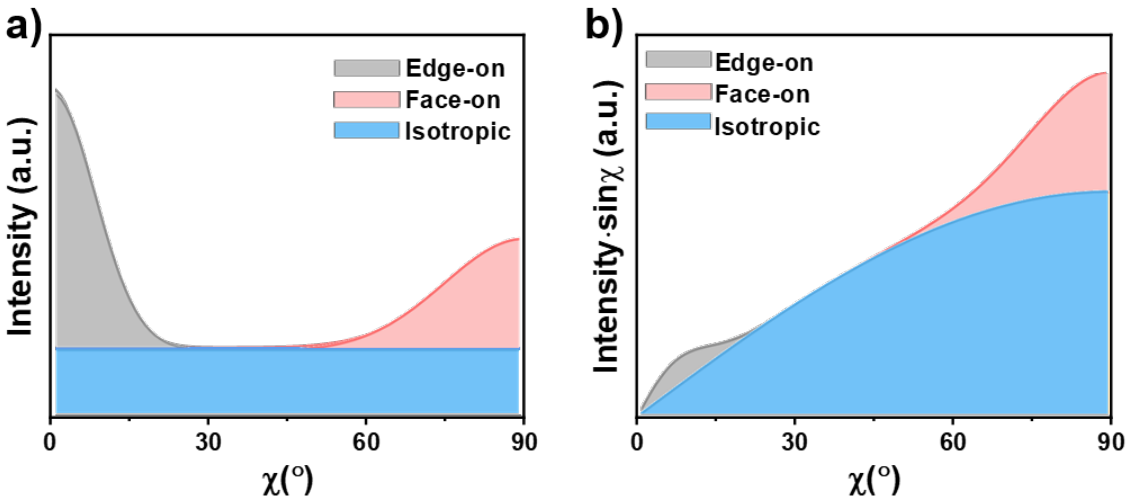

Figure 2.9: Schematic diagram of the edge-on (grey), face-on (red) and isotropic (blue) crystallite distribution a) before and b) after the Lorentz correction of the 2D GIWAXS tube cut data. [104] Reproduced with permission from Wiley, Copyright 2022.

Since the Ewald sphere only probes a single slice and not the full scattering intensity through the 3D reciprocal space, a conversion is needed. Therefore, to quantity the orientation distribution for the organic thin film materials from tube cut data, a Lorenz correction is needed. [105],[106] The corrected intensity I_{corr} shown in Figure 2.9 could obtained by

$$I_{corr} = I_0 \sin(\chi) \tag{2.33}$$

where I_0 is the background-subtracted intensity along the angle, and χ is the integration angle.

3 Characterization Methods

In this chapter, various techniques are carried out to characterize the BHJ active layer thin films and the respective non-fullerene organic solar cells. The instrument specifications, working principles and data analysis details are discussed. In Section 3.1, spectroscopic and electronic characterizations to probe the active layer thin films are discussed. The characterization methods in real space and reciprocal space used to investigate the surface and inner morphology of the active layer are given in Section 3.2 and 3.3, respectively. Section 3.4 listed the characterizations for the non-fullerene organic solar cells. Moreover, the detail of in situ and operando measurements are discussed in Section 3.5

3.1 Spectroscopic and Electronic Characterization

3.1.1 UV-Vis Spectroscopy

Ultraviolet-Visible (UV-vis) spectroscopy is used to probe the absorption of light of organic materials in the ultraviolet-visible spectral region, providing information about the energetic levels of materials. In this thesis, all the measurements are performed in transmission geometry to probe the absorbance of the active layer materials in solid films or diluted solutions. For all static samples in this thesis, the measurements are carried out on a Lambda 35 spectrometer by PerkinElmer. The spectrometer is equipped with a deuterium lamp and a tungsten halogen lamp, which generate UV light in a wavelength range of 190 nm - 326 nm and light in the visible and near-infrared spectrum (326 nm - 1100 nm), respectively. The lamps are automatically switched at the wavelength of 326 nm. Figure 3.1, represents the schematic setup of a UV-vis spectrophotometer. The generated light is monochromatized by an optical grating. Subsequently, the monochromatic beam is equally split into two beams of which one probes the sample and the other one detects a reference sample. Typically, the scan speed is set to 1 nm/s with a spectrum slit width of 1 nm. Usually, a transparent substrate e.g. glass, ITO is used as the reference sample. A cuvette (Hellma 110-1-PK-40) made of suprasil quartz material with a 1 mm optical path length is used for the solution samples, to avoid the solution evaporation during the measurement, a PTFE closure cap is used to seal the opening. The host solvent is used as the reference

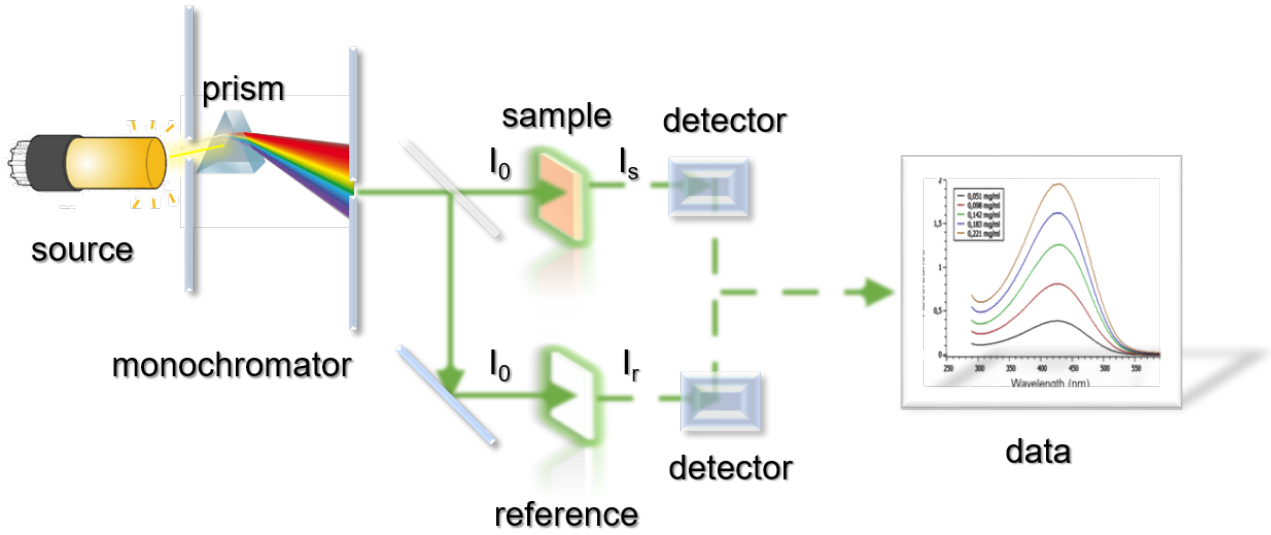

Figure 3.1: Schematic setup of a UV-vis spectrophotometer

sample for the solution measurement. At last, the transmission intensity of both beams is recorded by two photodiodes. The absorbance A(λ) from transmission spectrum T(λ) is obtained via the Lambert-Beer law: [107]

$$A(\lambda) = \lg \frac{I_t(\lambda)}{I_0(\lambda)} = -lg(T(\lambda)) \tag{3.1}$$

where $I_0(\lambda)$ and $I_1(\lambda)$ represent the transmitted intensity of the incident beam that goes through the reference and the sample, respectively. Due to the absorption process, light intensity decays exponentially on its way through the medium and is given by

$$I(\lambda) = I_0(\lambda) exp(\alpha L) \tag{3.2}$$

with α being the material-specific linear absorption coefficient and L being the optical path length through the medium (thickness of the thin film or cuvette). Therefore the material-specific absorption coefficient can be calculated by

$$\alpha = ln(10) \frac{A(\lambda)}{L} \tag{3.3}$$

For reflective samples, e.g. thin films, intensity losses due to total or partial reflection of light from interfaces with different refractive indices become significant and therefore, reflection processes have to be taken into account. Thus, the absorbance A(λ) can be expressed by [108]

$$A(\lambda) = -lg \frac{T(\lambda)}{I(\lambda) - R(\lambda)} \tag{3.4}$$

with $R(\lambda)$ being the intensity of reflected light.
In addition, the extinction coefficient (ϵ_{ex}) can be obtained from the absorption coefficient (α) and the corresponding wavelength (λ) via the equation:

$$\epsilon_{ex} = \alpha \frac{\lambda}{4\pi} \tag{3.5}$$

Tauc plot can be used to determine the optical bandgap (E_g) of the active layer material by the relationship:

$$\alpha\hbar\nu = A \times (\hbar\nu - E_g)^n \tag{3.6}$$

in which A is a constant, $\hbar\nu$ is the photon energy. In terms of a direct bandgap semiconductor, n equals 1/2, and n equals 2 in terms of indirect bandgap semiconductors. For the organic polymer donors and small molecule acceptors utilized in this thesis, which exhibit direct band gap properties, therefore n= 1/2 is applied to estimate the optical band gap.

3.1.2 Photoluminescence

Photoluminescence (PL) spectroscopy is a form of light emission spectroscopy in which light emission comes after the photo-excitation (absorption) process. [109] As the light is directed onto a sample, the electrons within the material move into excited states. This process is called excitation. When the electrons come down from the excited states to their equilibrium states, the energy can be released in the form of light, called relaxation or emission. The photo-excitation and relaxation processes can be illustrated by a Jablonski diagram in Figure 3.2. [110] Based on the diagram, two mechanisms of radiative photoluminescence processes and three non-radiative transition processes during the emission process is distinguished. The emission of the photons in the same spin multiplicity from S_1 to S_0 state radiative transition is known as fluorescence with a timescale of 10^{-10} to 10^{-7} s (blue solid arrows). Another radiative photoluminescence process called phosphorescence (purple solid arrows) refers to the photo emissions in different spin multiplity from T_1 to S_0 state. Phosphorescence is in principle a forbidden transition, therefore the lifetime being in the 10^{-6} to 10 s range is longer than fluorescence.
Among all non-radiative transitions, the energy loss through a transition to a lower vibrational level within the same electronic state is called vibrational relaxation. It exhibits the fastest timescale in the 10^{-12} to 10^{-10} s range (blue dash arrows). When the transition happens between two electronic states of the same spin multiplicity (orange dash line), e.g. $S_3 \rightarrow S_2$, $S_2 \rightarrow S_1$, called internal conversion. Internal conversion is immediately followed by vibrational relaxation to the lowest vibrational level of the electronic state rapidly on a timescale of 10^{-11} to 10^{-9} s. Intersystem crossing refers to the transition to fluorescence and

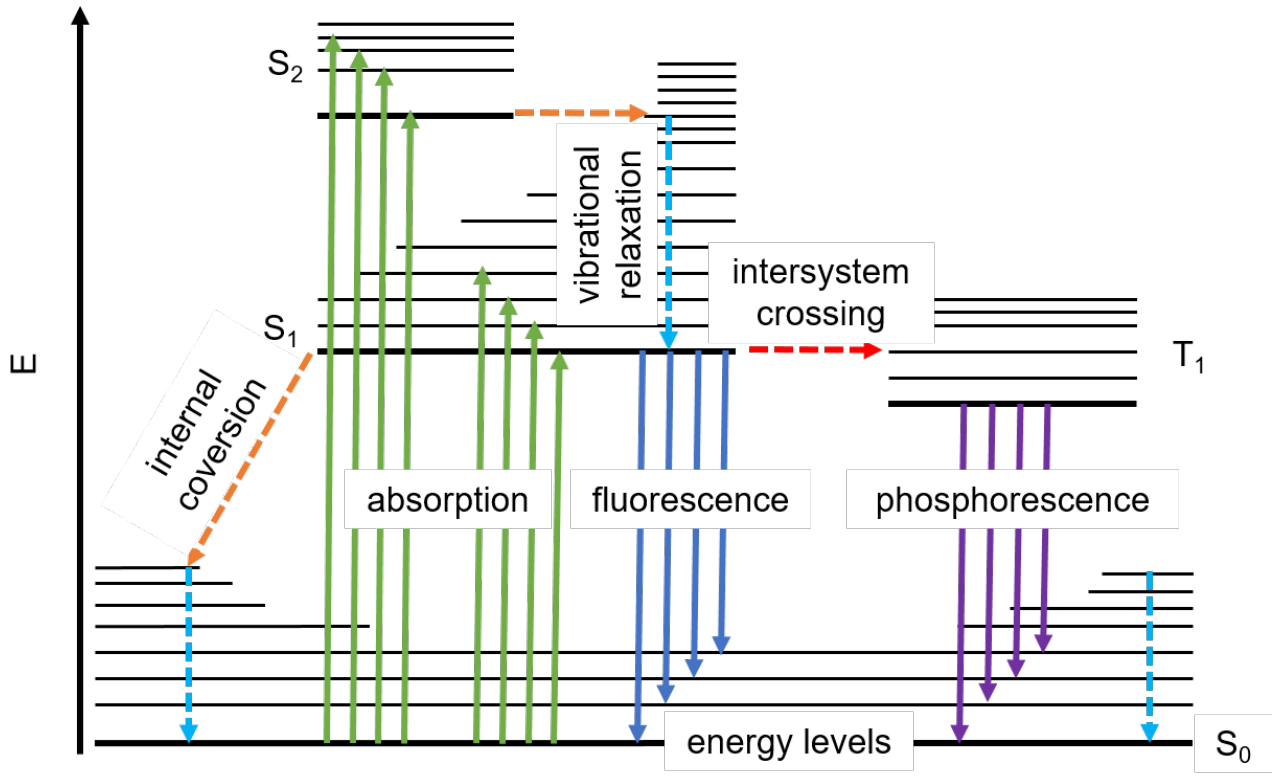

Figure 3.2: Simplified Jablonski diagram illustrating processes occurring upon absorption and subsequent emission of photons. S_0 is the singlet ground state of the molecule; S_1 is the first excited singlet state and S_2 is the second excited singlet state. T_1 is the first excited triplet state. The solid arrows represent radiative energy transitions and the dashed arrows represent non-radiative energy transitions between two molecular states. The bold lines represent the lowest vibrational level of each electronic state, with the higher vibrational levels represented by thinner lines. The vibrational levels become more closely spaced as energy increases and eventually form a continuum; for clarity, only a subset of these vibrational levels are represented on the diagram.

internal conversion is intersystem crossing from the S_1 to the T_1 state (red dash arrow), with a time scale of the 10^{-10} to 10^{-6} s. After intersystem crossing, the molecule will immediately undergo vibrational relaxation to the ground vibrational level of T_1. PL spectroscopy is useful in determining the electronic structure and properties of organic materials as it gives the peak light intensity that materials are able to emit for a certain wavelength. Both absorption and emission spectrum are likely to have mirror image relation if the spacing of vibrational levels is approximately equivalent and if the probability of transition is alike. In addition, the emission spectrum is usually red-shifted compared to the absorbance as shown in Figure 3.3. This shift towards lower energies is well-known as the Stokes-shift. [111]
PL spectroscopy measurements are carried out on a home-built measurement setup, comprising of a 405 nm diode laser (iBeam, Toptica Photonics) for excitation and liquid nitrogen

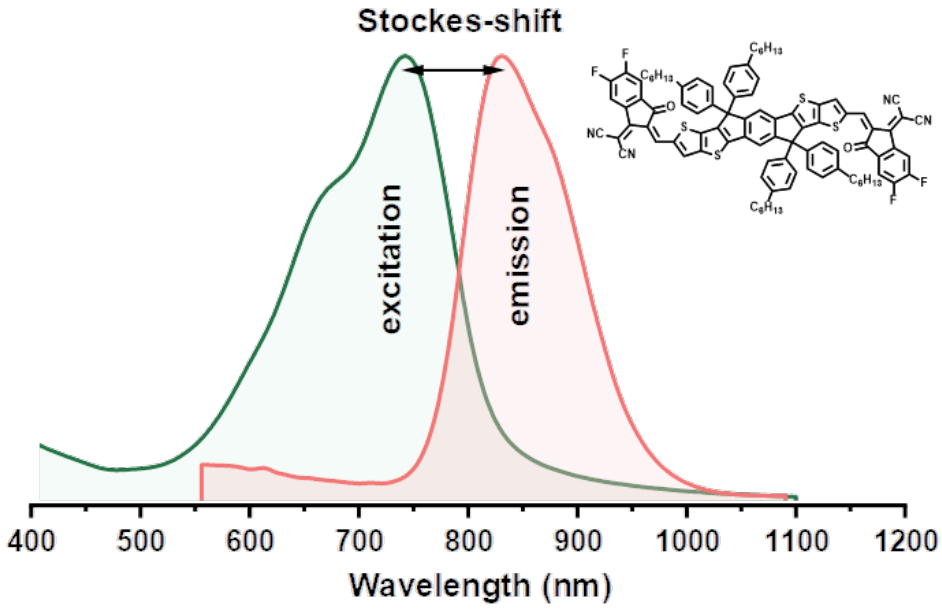

Figure 3.3: Excitation (green) as well as emission (red) spectra of ITIC-4F small molecule thin film obtained from the absorption and emission spectra

cooled CCD (Symphony II, Horiba) mounted to a spectrometer (iHR550, Horiba) for detection. The excitation and detection light are routed through the same microscopy objective (UMPlanFL 50x, NA: 0.8, Olympus) in a geometry similar to fluorescence microscopy.

3.1.3 Time-Resolved Photoluminescence

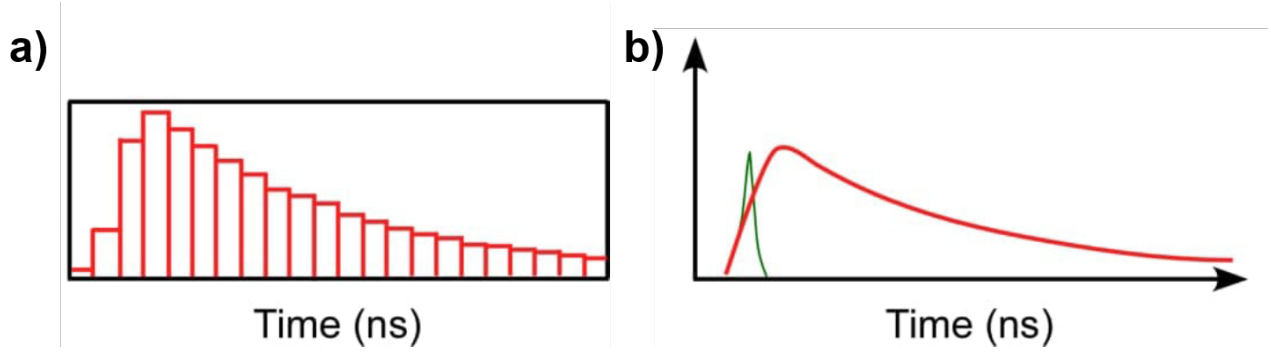

Figure 3.4: a) Histogram of the number of photons detected for the time difference by the TCSPC method, b) the measured waveform. Image is cited from Nian Li's PhD thesis. [112]

Time-Resolved Photoluminescence (TRPL) is measured by exciting luminescence from a sample with a pulsed light source, and then measuring the subsequent decay in photoluminescence (PL) as a function of time. [113],[114] The essential components of a spectrometer include: a pulsed laser source, and detect the PL with a photodiode, streak camera, or

photomultiplier tube (PMT) set up for upconversion or single-photon counting. It is used to characterize and understand the recombination mechanisms especially in calculating the lifetime of the active layer for organic solar cells in this thesis. A time-correlated single photon counting (TCSPC) method is carried out to detect active layer fluorescence decays in a time domain with a high resolution of 20 ps. In principle, single photons of the organic material are excited from a certain leaser pulse (405 nm in this thesis) with a high repetition rate. Then the excited photons are detected with a high-gain photomultiplier and the time related to the excitation pulse is recorded. By counting many events a histogram of the photon distribution over time is built up as Figure 3.4a. The photon distribution represents the waveform of the decay signal with respect to the lifetime in Figure 3.4b. To calculate the average decay time τ_{aver} of the sample, multi-exponential decay functions are used as follows:

$$\tau_{aver} = \frac{\sum_i A_i \tau_i^2}{\sum_i A_i \tau_i} \tag{3.7}$$

where τ_i is the decay time for different components and A_i is the amplitude fraction with respect to the lifetime component.

TRPL spectroscopy is performed using a TCSPC system integrated with the aforementioned photoluminescence setup at the WSI department of TU Munich. The samples are excited with a 405 nm pulsed diode laser (LDH-P-C-405B, PicoQuant) at a repetition rate of 10 MHz. The signal is detected using an avalanche photodiode (PDM PD-100-CTE, Micro Photon Devices) mounted to the secondary exit of the previously mentioned spectrometer. This allowed for TCSPC measurements at specific wavelengths with a spectral bandwidth of around 10 nm. The decay lifetimes are fitted by deconvolution using the software EasyTau 2 (Picoquant). The instrument response function necessary for this fitting procedure is recorded at a wavelength of 700 nm using a dilute solution of Allura Red AC.

3.1.4 X-ray Photoelectron Spectroscopy

X-ray photoelectron spectroscopy (XPS) in the thesis is used to quantify the donor/acceptor ratio on the surface of the thin film through the detected elemental composition (Chapter 5). XPS is a surface-sensitive quantitative technique based on the absorption of light and the resulting photoelectric effect. It could identify the elements of the organic or inorganic material, their chemical state as well as the density of the electronic states on the surface. This technique requires the X-ray with a photo energy $\hbar\omega$ generated with AlKα or Mg Kα radiation as the emitting source which could be absorbed by electrons inside the measured material. [115] XPS measurements are usually performed under ultra-high vacuum to reduce the scattering of the emitted photo-electron caused by air. To make the electron be able to escape the surface of the thin film, the electrons need higher transferred energy than

the sum of binding energy E_B and the working function Ω_ω of the investigated element. All additional energy is used to excite the electron to states of higher kinetic energy E_{kin} (movement). By measuring the kinetic energy of the emitted photon-electrons, the relation can be described as

$$E_{kin} = hw - E_B - \Omega_\omega \tag{3.8}$$

The measurements are conducted in the chair of Surface and Interface Physics (E20) at Physics department of TU Munich with a laboratory-based XPS. A twin-anode X-ray source (PSP Vacuum Technology) is used to deliver non-monochromatized Mg Kα radiation (photon energy: 1253.6 eV) under ultrahigh vacuum (10^{-7} Pa). A hemispherical electron energy analyzer (ES200 spectrometer, AEI Scientific Apparatus Ltd) with high energy resolution and spatial selection is utilized to detect the emitted electrons. The thin film is coated on the p-typed silicon substrate to improve the conductivity, therefore reducing the surface charge. The electron detection angle is fixed at 45° to reflex the maximum emitted electron intensity. The binding energy scale is calibrated using the Au4f 72 core-level line at 84.0 eV from a gold strip mounted on the sample holder. The core-level spectra is collected at the souse power energy of 10 keV and fitted with a Gaussian distribution function by Origin Software.

3.1.5 Transient Absorption

Transient absorption (TA) is used to determine the charge transfer process between the donor and acceptor in the active layer. For the transient absorption measurements, a Yb amplifier (PHAROS, Light Conversion), operating at 38 kHz and generating 200 fs pulses centred at 1030 nm with an output of 14.5 W is used. The 200 fs pump pulse is provided by an optical parametric amplifier (Light Conversion ORPHEUS). The probe is provided by a white light supercontinuum generated in a YAG crystal from a small amount of the 1030 nm fundamental. After passing through the sample, the probe is imaged using a Si photodiode array (Stresing S11490). The probe beam is split into two identical beams by a 50/50 beamsplitter which allows the use of a second reference beam to pass through the sample but does not interact with the pump. The reference measurement is used to correct any shot fluctuations in the probe to reduce the structured noise in the experiments. Thus, the TA signals could be obtained from $\Delta T/T = 1 \times 10^{-5}$. All TA measurements were conducted at the Cavendish Laboratory, Department of Physics, University of Cambridge.

3.2 Real-Space Structural Characterization

3.2.1 Atomic Force Microscopy

Atomic force microscopy (AFM) is one of the scanning probe microscopy methods to obtain the polymer surface information with a resolution on the order of fractions of a nanometer. Typically for an AFM device, four components are included: the AFM probe, leaser and photo-detector, sample stage, as well as feedback system. Figure 3.5 illustrates a typical AFM setup. The AFM probe normally consists of a spring-like cantilever with a super sharp tip. At the backside of the cantilever, a reflective material is coated to reflect the emitting laser. A laser is directed to the back of the cantilever and the reflected light is then collected by a photo-detector, which is very sensitive to the positions of the laser beam. The sample is mounted on a sample stage combined with a piezoelectric scanner. When using the AFM to scan across the active layer of the organic solar cells, the cantilever is used as a force sensor, the tip acts like an elastic based on Hooke's Law. [116] Depending on the amount of force between the tip and the thin film, the cantilever compresses and stretches. The photo-detector records the changes to the reflected laser beam position proportional to the movement of the cantilever. An electronic feedback system is employed to keep the probe-sample force constant during scanning by controlling the distance along the z-axis between the AFM probe and the sample stage system. Thereafter, detailed topographical or phase information can be captured by scanning across the surface of the thin film.
In general, two primary groups of operating modes are widely described as static (contact) and dynamic (non-contact, tapping) modes where the cantilever is vibrated or oscillated at a fixed frequency. In contact mode, the tip is dragged across the active layer surface, and the profile of the surface is measured either directly using the deflection of the cantilever or using the feedback signal required to keep the cantilever at a fixed height. In non-contact mode, the tip of the cantilever does not touch the surface of the sample. Instead, the cantilever oscillates at or just above its resonant frequency (frequency modulation) or just above (amplitude modulation), where the oscillation amplitude is typically a few nanometers (<10 nm) to several picometers. In tapping mode, the cantilever is driven to oscillate up and down at or around its resonant frequency. Such oscillations are typically achieved by small piezoelectric elements in cantilever mounts, but other possibilities include alternating magnetic fields (with magnetic cantilevers), piezoelectric cantilevers, or periodic heating using modulated laser beams. The amplitude of this oscillation typically varies from a few nanometers to 200 nanometers. In the tapping mode, the frequency and amplitude of the drive signal are kept constant, causing the cantilever to oscillate with a constant amplitude as long as there is no drift or interaction with the surface. Today, tapping mode is the most frequently used when operating AFM under ambient conditions.

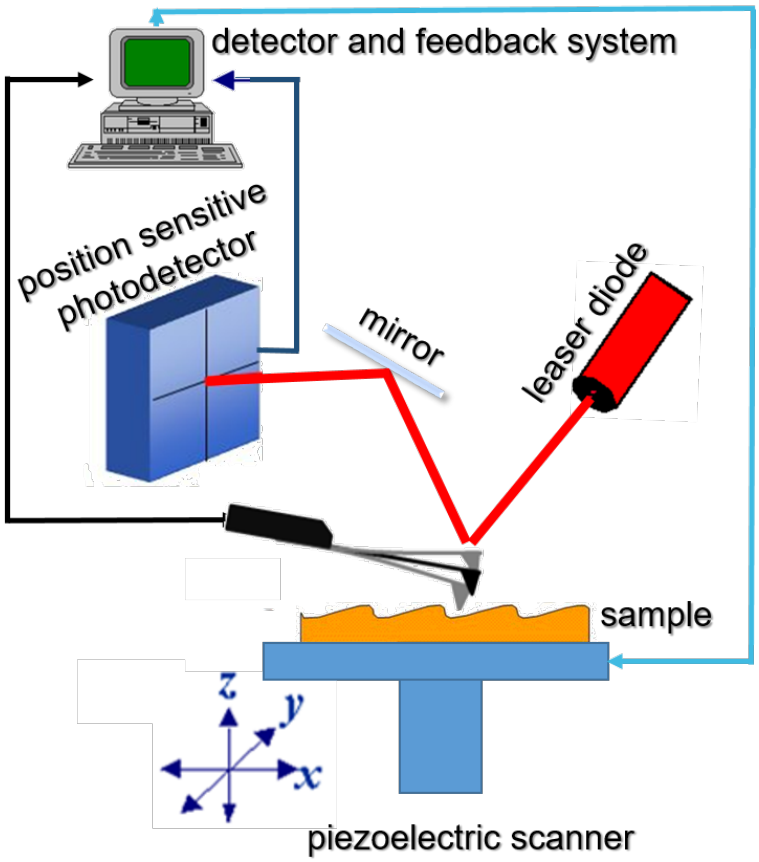

Figure 3.5: Schematic setup of a AFM

In this thesis, the top morphology and the phase separation information of the thin film is detected by an AFM instrument (MFP-3D, Asylum Research) in tapping mode using conical-shaped tips with a radius of 7 nm in ambient. The collected data are analyzed using the open-source software Gwyddion. [117]

3.3 Reciprocal-Space Structural Characterization

3.3.1 X-Ray Reflectivity

X-ray reflectivity (XRR) is used to obtain the neat thin film scattering length density (SLD) and analysis the vertical composition of the active layer for the organic solar cells. For x-rays, the scattering length density arises from the electron density and is related to the material density of a material. Therefore, it enables the identification of different materials with different SLD inside a blended thin film. Within this thesis, the SLD variation of the donor and acceptor is investigated via the XRR measurement, therefore to determine the vertical layer composition in the non-fullerene active layer. A typical XRR setup contains

three major parts, the X-ray source, the sample stage, and the detector. The generated X-rays are monochromatized and then imprinted on the sample surface with an incident angle α_i. The reflected beam intensity is recorded with a 1D detector as a function of α_i. Since it is an elastic scattering, the momentum transfer ($\vec{q}$) only depends on the redirection of the photons. Therefore, the momentum transfer could express as

$$\vec{q} = \frac{4\pi}{\lambda} sin\alpha_i \tag{3.9}$$

In the case of an incident angle (α_i) smaller than the material critical angle (α_c), total reflection occurs. When the incident angle equals the critical angle of the measured material, the beam begins to penetrate the thin film, showing a drop in the reflection intensity, called a critical edge. [118] For the incident angle larger than the critical angle of the measured material, the beam is split into a reflected and the transmitted part at each interface. Multiple reflections and refractions at different vertical positions inside the film occur. The superposition of the reflected beams results in the characteristic Kiessig fringes of the reflectivity pattern. The thin film thickness could be approximately equal to

$$d \approx \frac{2\pi}{\triangle q_z} \tag{3.10}$$

where the $\triangle q_z$ refers to the distance between adjacent Kiessig fringes and is expressed as:

$$\triangle q_z = \mid q_{z,2} - q_{z,1} \mid \tag{3.11}$$

XRR measurements in this thesis are performed by an X-ray diffractometer (D8 Advance Diffractometer, Bruker) with a CuKα X-ray generator. The beam with a wavelength of 1.54 Å collimated with 0.2 mm size slits before imprints on the sample. In order to improve the accuracy of the reflectivity, the exciting beam is collimated with a second set of slits with sizes 0.1 mm and 0.05 mm, too. The sample is scanned from 0.2 ° to 2 °. with a step of 0.005 °/min. The obtained reflectivity data are modeled with the Motofit plugin installed in the IGOR PRO (version 6.37) software. [119]

3.3.2 Grazing Incidence Small-Angle X-Ray Scattering

Grazing Incidence Small-Angle X-Ray Scattering (GISAXS) is a non-destructive measurement technique, which gives the lateral structure of the thin film in the range of 1 nm - 1 μm by adjusting the set-up working distance and the X-ray energy. Since a very shallow incident angle (< 1 °), X-ray has a large footprint on the sample, normally over 1 cm, which could provide high statistical significance. Compare to the real space imaging technique such as

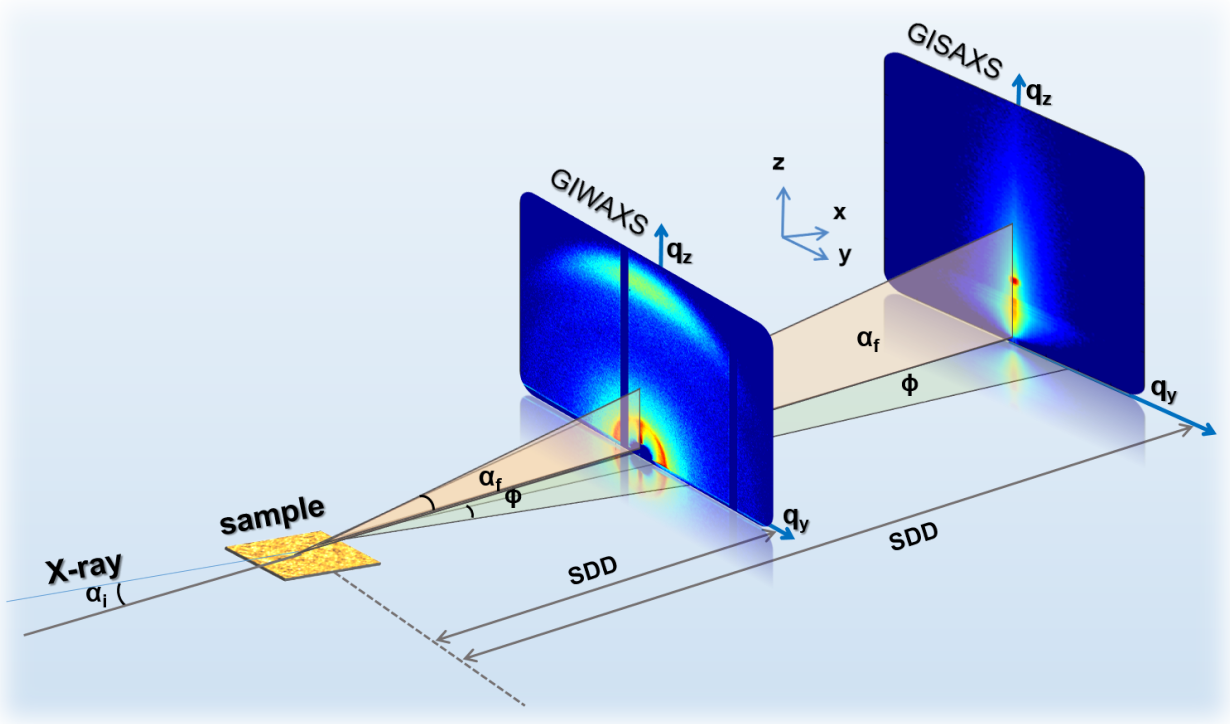

Figure 3.6: Schematic geometry of grazing incidence X-ray scattering setups. The X-ray beam impinges on the sample with the incident angle α_i and is scattered under an angle α_f. The wide and small angle scattering signals are recorded by setting the detector at short and long sample-detector distances, respectively.

AFM or SEM, which only provides a small surface area information, GISAXS/GIWAXS offers the inner film structure with a thickness of tens to hundreds of nanometers depending on the material penetration depth. In Figure 3.6 a schematic setup of a typical GISAXS/GIWAXS technique is depicted. The incident angle (α_i) is set to be above the material critical angle in the probe thin film, normally around 0.3 - 0.5 $^{\circ}$ for the organic materials. The out-coming elastically scattering photons are distributed in the lateral angle range (φ) with respect to the specular plane (xz-plane). The GISAXS measurement with a long sample to detector distance (SDD) is used to obtain structural information in a large size range.
The GISAXS results in different chapters discussed in this thesis are carried out in the MiNaXS beamline P03 of the PETRA III storage ring at DESY (Hamburg, Germany) [120], the Ganesha SAXSLAB instrument at TU Munich and the AUSTRIAN SAXS beamline of the Elettra Sincrotrone (Trieste, Italy), respectively.
For the GISAXS measurements performed in the DESY P03 beamline, the X-ray energy is set at 11.65 keV with the beam wavelength of 1.06 Å. A Pilatus 1M detector (981 × 1043 pixels with pixel size: 172 μm × 172 μm) is used to collect the data. The sample-detector distance

(SDD) is 5262 mm and the incident angle is 0.40 °, to separate the Yoneda peak of the donor and acceptor. Due to the long SDD, a vacuum flight tube is installed in the X-ray pathway, in order to minimize air scattering. The direct beam and specular beam are shielded by beamstops, to protect the detector from oversaturation.
For the in-house Ganesha SAXSLAB instrument, the X-ray energy is fixed at 8.05 keV, which corresponds to an X-ray wavelength of 1.54 Å. The sample-detector distance (SDD) is set at 1045 mm with an incident angle of 0.40 °. The scattering signal is collected with a Pilatus 300 K detector (Dectris Ltd) with dimensions 487 × 619 pixels (pixel size 172 μm × 172 μm) in a vacuum.
For the operando GISAXS measurement performed at AUSTRIAN SAXS beamline at the Elettra Sincrotrone, the X-ray energy is set to 8.05 keV, corresponding to a wavelength of 1.54 Å. The SDD is set to 2.0 m with an incident angle of 0.40 °. A vacuum fly tub is mounted along the path of the scattered X-ray routine to minimize air scattering. The scattering signals are collected by a Pilatus 1M Detector (Dectris Ltd) with dimensions 981 × 1043 pixels (pixel size 172 μm × 172 μm).
The evaluation of the GISAXS data is done by performing the vertical and the horizontal line cuts through the DPDAK software. [121] The Yoneda peak position of the measured material is confirmed by the vertical line cuts in q_z direction, then horizontal line cuts are conducted at the Yoneda peak position. The horizontal line cuts reveal lateral structure information of the probed thin film. To model the lateral structures, cylindrical and spherical objects with different radii are used in the framework of the distorted wave Born approximation (DWBA) assuming the effective interface approximation (EIA), which is discussed in Section 2.3.3 Furthermore, the mean distances between the scattering objects are represented by the structure factor.

3.3.3 Grazing Incidence Wide-Angle X-Ray Scattering

Grazing Incidence Wide-Angle X-Ray Scattering reveals information on the crystalline structure of thin films. The setup is mostly identical to GISAXS whereby a shorter sample detector distance (SDD) is used, normally around 5-30 cm. The lattice constants, crystal sizes and crystal orientations of the active layer are extracted from the GIWAXS measurements. More theoretical detail with respect to the working principle is described in Chapter 2.3.4. In this thesis, partly of the GIWAXS measurement are performed with the in-house Ganesha SAXSLAB instrument at TU Munich. The rest of the experiments are done in DESY P03 beamline. In-house GIWAXS measurements are carried out with a Ganesha SAXSLAB laboratory beamline using a CuKα X-ray source (8.05 keV, 1.54 Å) and a Pilatus 300K detector. The samples for GIWAXS measurements are fabricated on silicon substrates. The incident angle is 0.2° with a sample-to-detector distance (SDD) of 95 mm for the measurement. For

the static samples measured at DESY, using an X-ray beam wavelength of 1.06 Å (energy of 11.65 keV), the SDD is 155 mm and the incident angle is 0.15°. The solid angle correction, efficiency correction and polarization correction are performed with GIXSGUI plug in the MATLAB software. [122] For analyzing the crystallinity of the organic polymer, the vertical and/or horizontal-sector integrals are taken from the corrected reciprocal space patterns, as shown in Figure 5.9g. The corresponding data fits are done with Gaussian functions in the Origin software.

3.4 Device Characterization

3.4.1 Current-Voltage Characterization

To evaluate the photovoltaic performance of organic solar cells, current-voltage (J-V) analysis methods are carried out. Figure 3.7 represents a typical J-V curve of an organic solar cell

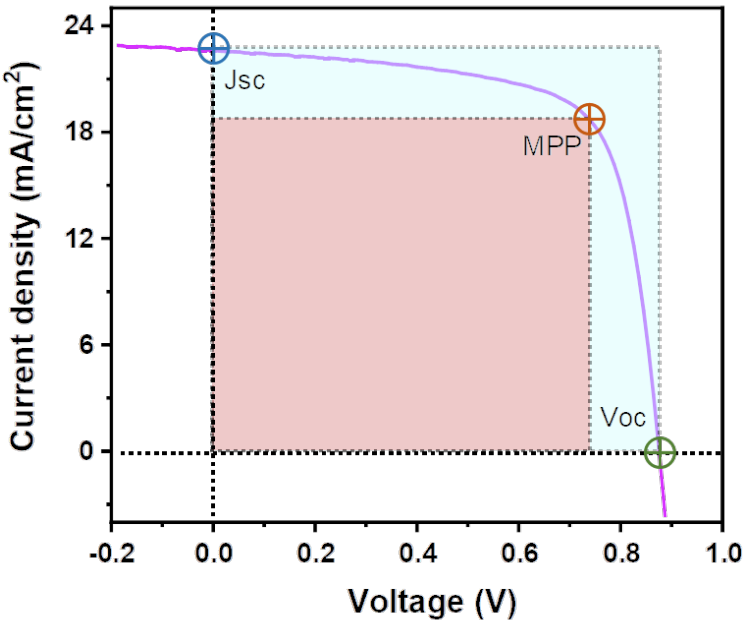

Figure 3.7: Illustration of exemplary J-V curves of an organic solar cell under AM 1.5 G sunlight illumination. Voc, Jsc and maximal power point (MPP) are indicated.

under AM 1.5 G sunlight illumination. The applied voltage (V) of every single solar cell is swept from -0.2 V to 1.2 V and the corresponding generated current (I) is recorded during measurement. The current density of the solar cell is calculated by

$$J = I / A_{area} \tag{3.12}$$

where the A_{area} refers to the effective illumination area of the device. From the J-V curve measured under illumination, the related photovoltaic parameters such as open-circuit voltage (Voc), shortcircuit current density (Jsc), maximum power point (MPP), power conversion efficiency (PCE or η) and fill factor (FF), are extracted. The Voc is the voltage at which no current flows through the external circuit. It is the maximum voltage that a solar cell can deliver. Voc depends on the photo-generated current density (J_{ph}) and assuming that the net current is zero, it can be calculated from

$$Voc = \frac{k_B T}{q} ln(\frac{J_{ph}}{J_0} + 1) \approx \frac{k_B T}{q} ln(\frac{J_{ph}}{J_0}) \tag{3.13}$$

J_0 refers to the saturation current density, k_B is the Boltzmann constant, T is the temperature and q is the electronic charge. The short-circuit current Jsc is the current density that flows through the external circuit when the electrodes of the solar cell are short-circuited, which can result in strong depending on the optical properties of the solar cell, such as absorption in the active layer and reflection. The fill factor is the ratio between the maximum power point (MPP) generated by a solar cell and the product of Voc with Jsc:

$$FF = \frac{J_{mpp}\, V_{mpp}}{Jsc\, Voc} \tag{3.14}$$

The PCE is calculated as the ratio between the maximum power point (MPP) and the incident power P_{in}:

$$PCE = \frac{J_{mpp}\, V_{mpp}}{P_{in}} = \frac{Jsc\, Voc\, FF}{P_{in}} \tag{3.15}$$

In the present work, the J-V measurements are obtained by using the Keithley 2611B Source Meter under different light conditions. For the J-V measurement under light conditions, a simulated AM 1.5 G sunlight at 100 mV cm^{-2} irradiance is generated by a solar simulator (LOT-Quantum Design GmbH). The light is calibrated to the standard intensity with a KG-5 filter Si reference cell. Each device is performed in sequence with one dark and several light measurements to sort out the best device performance. To calculate the current density of the solar cells, the effective illumination area of each solar cell is fixed by an opaque mask.

3.4.2 External Quantum Efficiency

For an ideal organic solar cell, each photon would produce an electron–hole pair. Consequently, all these charge carriers will go toward the depletion region and then be separated and collected. [123] External quantum efficiency (EQE) measurements could assess the spectral sensitivity and determine the generated photocurrent densities that are measured under

the specified range of wavelength for organic solar cells. The EQE can be determined by [124]

$$EQE(\lambda) = \frac{1}{P(\lambda)} \frac{Jsc(\lambda)}{q} \frac{\hbar c_0}{\lambda} \tag{3.16}$$

where P(λ) is the photon flux density of the applied light, e being the electron quantity, Jsc(λ) is the measured short-circuit current density at a certain wavelength, $\hbar$ being the Planck constant and c_0 being the speed of light in vacuum and λ refers to the wavelength of incident photons.

The EQE measurement can be used to calculate the short-circuit current (JSC) of the cell under illumination.

$$Jsc = \int qEQE(\lambda)P(\lambda)d(\lambda) \tag{3.17}$$

In this thesis, EQE spectra are obtained on a commercial EQE measurement system (Taiwan, Enlitech, QE-R3011). The light intensity at each wavelength is calibrated by a standard single-crystal Si photovoltaic cell. The measurement range is from 300-1000 nm with a step of 10 nm/s.

3.4.3 Space-charge-limited Current

Space-charge-limited current (SCLC) measurements have been widely used to study the charge carrier mobility and trap density in organic solar cells. The idea to obtain the SCLC in an organic solar cell device consists of applying a potential difference between two parallel plate contacts at both sides of the active layer. In order to have monopolar SCLC, the devices are prepared such that the injecting contact is Ohmic, i.e. the current flow is not limited by injection from the contact but by the space charge formed within the active layer. To extract only the hole or electron from the active layer, so different geometry of the devices are fabricated and discussed in Chapter 4. Figure 3.8 shows a typical current-voltage characteristic of a hole/electron-only organic solar cell device, where there are two regions, one is the ohmic region and the other is the space charge region and both regions can be differentiated with the order of slope. [125] The transition of both ohmic and space charge regions is taken place at a specific voltage termed as threshold voltage V_T. At low voltage, the polymer diode offers ohmic behavior (J-V) with a slope at order 1, while at higher voltage, the polymer exhibits space charge–limited current (J-V^2) with a slope of order 2. The hole and electron mobilities could be determined by fitting the dark current to the model of a single carrier in the SCLC region, which is shown by the Mott-Gurney equation:

$$J = \frac{9}{8}\varepsilon_0\varepsilon_r\mu\frac{V^2}{d^3} \tag{3.18}$$

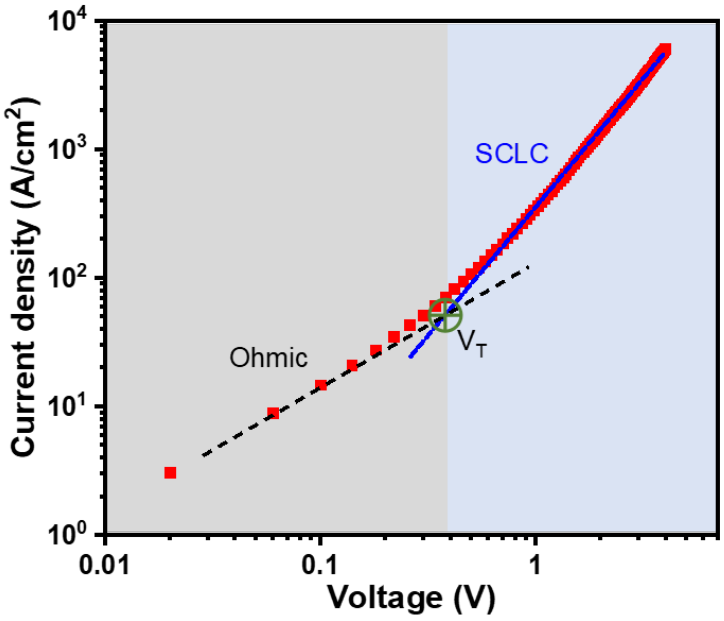

Figure 3.8: Space charge-limited current behavior for an organic solar cell with only ohmic and trap-free space charge-limited current regions.

where J is the current density, μ is the mobility of holes (μ_h) or electrons (μ_e), ε_0 the permittivity of the vacuum, (ε_r) the relative permittivity of the material and d the thickness of the active layer.
And, V denotes the voltage

$$V = V_{appl} - V_{bi} \tag{3.19}$$

where V_{appl} is the applied voltage, and V_{bi} the built-in potential determined by electrode work function difference. In this case, V_{bi} = 0 V both for hole-only and electron-only devices. The mobility is calculated from the slope of the J-V plots.
In this thesis, the SCLC measurements are performed with a computerized Keithley 2611B SourceMeter in the dark. The applied Voltage range from -4.0 to 4.0 V with the step of 0.02 V.

3.5 In-Situ and Operando Characterization

3.5.1 In-Situ Characterization of Active Layer

In situ UV-vis spectroscopy is performed using a CAS 140 CT Instrument Systems Compact Array spectrometer and an MBB1D1 broadband light-emitting diode (THORLABS), which

is installed below the sample holder inside the slot-die coater. A photodetector (Instrument Systems GmbH, CAS 140 CT, Germany) is used to detect the transmittance signal simultaneously in a broad variety of wavelengths from 250 nm to 1000 nm with high time resolution (200 ms/spectrum). The in situ GIWAXS measurements are carried out at the P03 beamline, PETRA III, DESY in Hamburg (Germany), using an X-ray beam wavelength of 0.99 Å (energy of 12.57 keV).
For the in situ GIWAXS measurements, the SDD is 180 mm and the incident angle is 0.11°. For the in situ GISAXS measurements, the incident angle is set to 0.4° and the SDD is 3174 mm to obtain the active layer morphology evolution over time.

3.5.2 Operando Characterization of Organic Solar Cells

Operando experiment is performed at the Austrian SAXS beamline of the Elettra Sincrotrone Trieste. A custom-made chamber is built and designed to perform GISAXS and current-voltage measurements simultaneously, which is built by M. Ruderer, J. Schlipf and B. Kalis. [82],[84] Two Kapton windows allow the X-ray beam to enter and exit the chamber. A quartz glass window at the bottom enabled the simultaneous illumination of the sample. On the left side of the chamber, a PerkinElmer PX5 150 W xenon arc lamp is mounted to simulate the sun's radiation spectrum. The solar simulator is used to provide the illumination (100 mW/cm^2). The solar cell is installed into an evacuated chamber with a pressure of $5x10^{-2}$ mbar. The inner chamber is stabilized at 15 °C by a Julabo cooling system to prevent the influence of temperature. Before the operando measurements, the organic solar is aligned so that the beam is positioned on the active layer close to the Ag top electrodes. The current-voltage (J-V) curves as a function of time are recorded by source meter Keithley (2400) with an acquisition frequency of one scanning per 10 s. The whole measurement is performed for 180 min. For the GISAXS measurement, the data acquiesce every 5 min for the first 10 min, then the GISAXS measurements are recorded every 10 min till the end. Each measurement time is 5 s to get a better signal-to-noise contrast.

4 Fabrication Processes

The present chapter provides a detailed explanation of the various preparation steps for the samples investigated in the frame of this thesis, including the materials, cleaning method, solution preparation, thin film deposition techniques, etc. In Section 4.1, all the materials characteristics, substrates type as well as supplier information are summarized. In addition, the chemical structures of donor polymers and small molecule acceptors are drawn to identify their system. Section 4.2 explains the particular cleaning method for different substrate types. Section 4.3 lists the fabrication methods required for the related solutions, the active layer thin films as well as for the organic solar cell (OSC) devices. Then, the fabrication process of different types of organic solar cells is given in Section 4.4.

4.1 Materials

In the following, the characteristics of the materials used in this thesis are elaborated. This section is divided into four parts, beginning with the polymer and acceptor materials for the active layers, the rest of the functional materials for the organic solar cell, followed by the used solvents for the particular materials, and the used substrates materials information. In addition to PEDOT: PSS solution, all materials are used as received without any further purification.

4.1.1 Donor Polymers and Acceptor Molecules

For a systematic and in-depth study of the effect of active layer morphology on organic solar cells, three high-efficiency donors and five non-fullerene small molecule acceptors with different structures were selected as the active layer components. The fullerene acceptor is also used as a comparison. In this section, the active layer material structure and the related optical and electron characteristic are details listed. In addition to the ITIC-4F acceptor obtained from Solarmer Inc.(China), other materials are purchased from 1 Material Inc. (Canada).

PBDBT-2F

The conjugated low bandgap polymer named poly [(2,6-(4,8- bis (5-(2- ethylhexyl -3- fluoro) thiophene-2-yl) benzo [1,2-b:4,5-b']dithiophene))-alt-(5,5-(1',3'-di-2-thienyl-5',7' bis (2-ethylhexyl) benzo [1',2'-c:4',5'-c'] dithiophene -4,8- dione)] (denoted PBDBT-2F or PM6) (Mn = 30282 g mol^{-1}, PDI = 2.9) is selected as the donor. [126] The chemical structure is shown in Figure 4.1. The backbone contains a 4,8-bis(5-(2- ethylhexyl)-4- fluorothiophen -2-yl) benzo [1,2-b:4,5-b'] dithiophene (BDT-F) unit, enhancing the electron-donating effect of the polymer increases the hole mobility and contributes to a planar molecular structure. And the unit of 1,3-bis (thiophene-2-yl) -5,7-bis (2-ethylhexyl) benzo- [1,2-c:4,5-c '] dithiophene -4,8- dione (BDD) has an electron-withdrawing effect and facilitates excitation of the polymer. The thiophene units take the role of enlarging the conjugated π-system and the alkyl side chains are grafted to improve the solubility of the polymer in common organic solvents. Moreover, the fluorination-modified thiophene units could further down-shift the energy level. The ingeniously designed structure makes PBDB-T-2F exhibit a large optical bandgap of $\sim$ 1.8 eV and a deep highest occupied molecular orbital (HOMO) level of -5.45 eV, which is beneficial for a high Voc in the organic solar cells. [127],[128]

PDTBT2T-FTBDT

The narrow bandgap polymer named poly[(2, 6 - (4, 8 - bis (5- (2 - ethylhexyl - 3 -fluoro) thiophen - 2 - yl)-benzo [1,2-b:4,5-b'] dithiophene)) - alt - 5,5'- (5,8-bis(4- (2 - butyloctyl) thiophen-2-yl) dithieno [3', 2': 3, 4;2'', 3'':5, 6] benzo [1,2-c] [1,2,5] thiadiazole)] (referred PDTBT2T-FTBDT or D18) (Mn = 31378 g mol^{-1}, PDI = 2.38) is provided to investigate the in-situ formation of the active layer thin film in Chapter 6. [129] It is with an alternating backbone electron donating benzodithiophene (BDT) and electron-accepting fused-ring dithienobenzothiadiazole (DTBT) units, exhibits a larger molecular plane structure with a higher degree of conjugation from DTBT, the chemical structure is shown in Figure 4.1. [130] Same with the PBDBT-2F, the end-capped alkyl side chains are utilized to improve the solubility of the polymer in common organic solvents. PDTBT2T-FTBDT displays an excellent hole mobility of 1.59×10^{-3} cm^2 V^{-1} s^{-1}, realized the record efficiency of over 19 % in single-junction organic solar cells. [127],[31]

PffBT4T-2OD

Another typical conjugated polymer name poly[(5,6-difluoro-2,1,3-benzothiadiazol-4,7-diyl) -alt- (3, 3'''-di(2-octyldodecyl)- 2, 2'; 5', 2'';5'',2-quaterthiophen-5,5'''-diy)](PffBT4T-2OD) (Mn = 55674 g mol^{-1}, PDI = 2.02) is used as a donor. According to the chemical structure, the 2-octyldodecyl (2OD) alkyl chains on quaterthiophene provide the PffBT4T-2OD with a

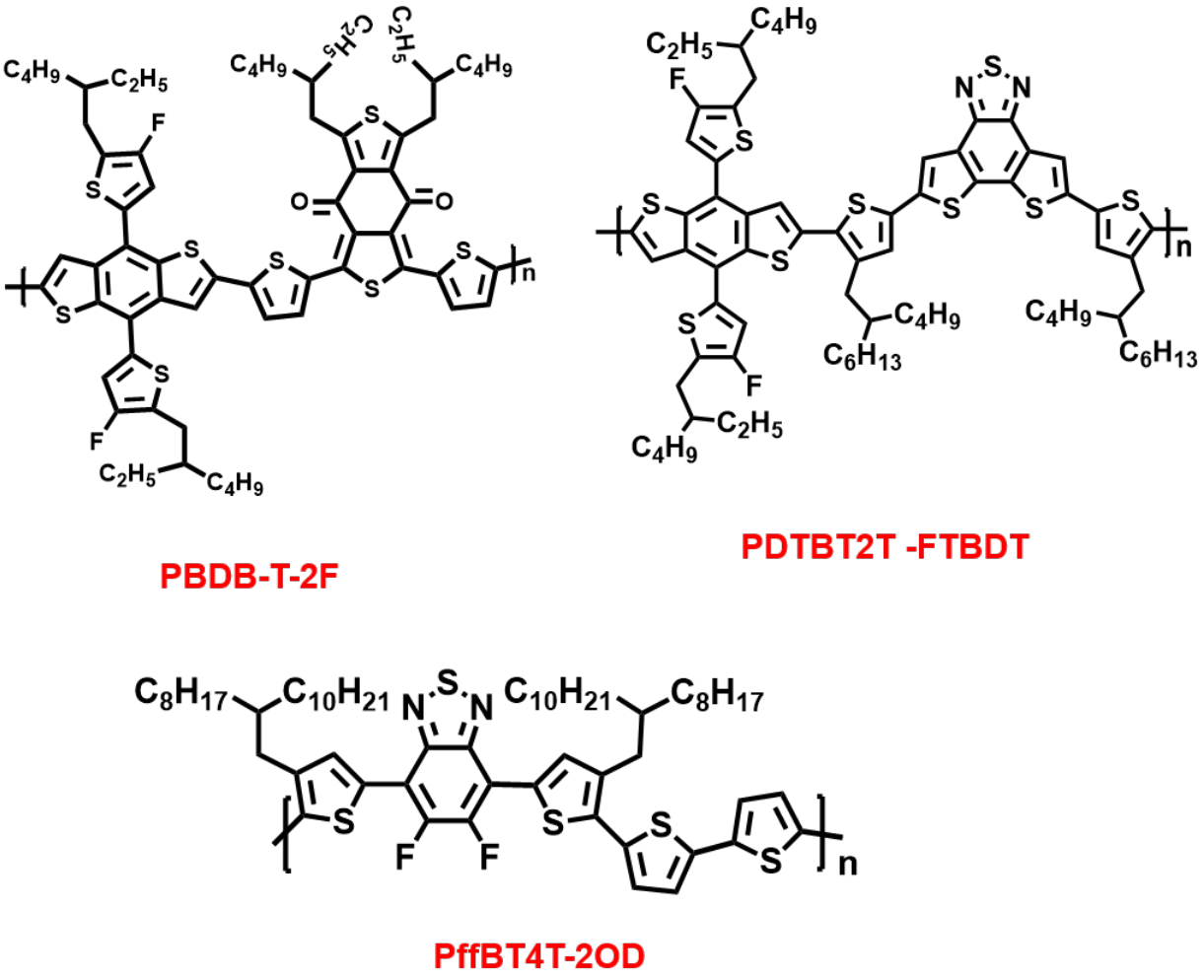

Figure 4.1: Chemical structure of donor polymers

temperature-dependent aggregation characteristic. It has a high degree of crystallinity and absorbs light from 400 to 700 nm. The thin film exhibits excellent hole mobility on the order of 10^{-2} cm2V^{-1} s^{-1}, which has yielded PCEs approaching 11 %. [131]

BTP-4F

The n-typed non-fullerene electron acceptor named (2,20-((2Z,20Z)-((12,13-bis (2ethyl hexyl)-3,9-diundecyl-12,13-dihydro-[1,2,5]thiadiazolo [3,4-e] thieno [2,"30':4',50] thieno [20,30:4,5] pyrrolo [3,2-g] thieno [20,30:4,5] thieno [3,2-b]indole-2,10-diyl) bis (methanylylidene)) bis (5,6-difluoro-3-oxo-2,3-dihydro-1H-indene-2,1-diylidene)) dimalononitrile) based on fused-unit dithie-nothiophen [3.2-b]-pyrrolobenzothiadiazole (TPBT) is shown in Figure 4.2. [132] The fused TPBT central unit preserves conjugation along the length of the molecule, which allows tuning of the electron affinity. The 2-(5,6-Difluoro-3-oxo-2,3-dihydro-1H-inden-1-ylidene) malononitrile (2FIC) end units were used as flanking groups to promote intermolecular

interactions and improve optical absorption, hence, facilitate the charge transport. [133] BTP-4F exhibits a HOMO level of -5.65 eV and the lowest unoccupied molecular orbital (LUMO) level of -4.10 eV.

IT-4F

The non-fullerene small molecule acceptor named 3,9- bis (2-methylene- ((3- (1,1- dicyanomethylene) - 6,7 -difluoro) -indanone))-5, 5, 11, 11-tetrakis (4-hexylphenyl) -dithieno [2,3-d : 2',3'-d']-s-indaceno [1,2-b:5,6-b'] dithiophene, (denoted ITIC-4F or IT-4F) is a derivative from ITIC molecule. [134] ITIC is based on a bulky seven-ring fused core (indacenodithieno [3,2-b]thiophene, IT), end-capped with 2- (3-oxo-2, 3- dihydroinden -1- ylidene) malononitrile (INCN) groups, and with four 4-hexylphenyl groups substituted on it. The chemical structure is shown in Figure 4.2. By introducing two fluorines (F) into each INCN group, IT-4F exhibits a better absorption coefficient and a more red-shifted absorption. This could be can be ascribed to enhanced intramolecular charge transfer. The HOMO level of -5.66 eV and the LUMO level of -4.14 eV of IT-4F is obtained from the CV measurement.

IT-4CL

Another ITIC derivative non-fullerene acceptor named 3,9-bis (2- methylene-((3-(1,1- dicyanomethylene) -6,7- dichloro)- indanone)) -5,5,11,11- tetrakis (4- hexylphenyl)- dithieno [2,3-d:2',3'-d']-s- indaceno [1,2-b:5,6-b'] dithiophene, (denoted ITIC-DCL or IT-4CL) in Figure 4.2. [135] By replacing the F with Cl, IT-4CL has a larger dipole moment, resulting to lower HOMO (-5.75 eV) and LUMO (-4.09 eV) levels. Its absorption spectra shifts towards a higher wavelength compared with IT-4F small molecule.

IT-M

The non-fullerene acceptor named 3,9-bis (2-methylene -((3-(1,1- dicyanomethylene)-6/7-methyl)- indanone))-5,5,11,11- tetrakis (4-hexylphenyl)- dithieno [2,3-d:2',3'-d']-s- indaceno [1,2-b:5,6-b'] dithiophene, shown in Figure 4.2.By adding a methyl group on the phenyl ring from the INCN groups of ITIC, IT-M shows increased solubility of the structure, benefiting its miscibility with polymer donor. [136] In addition, IT-M has slightly more electron-rich components than ITIC, resulting in a higher energy level with an elevated LUMO (-3.98 eV) level.

EH-IDTBR

The non-fullerene small molecule named (Z)- 5- [5-(15-5-[(Z)- (3-ethyl -4- oxo -2- thioxo -1,3 -thiazolidin -5 -ylidene) methyl]-8- this -7.9 diazabicyclo [4.3.0]nona-1(9),2,4,6-tetraen-2-yl-

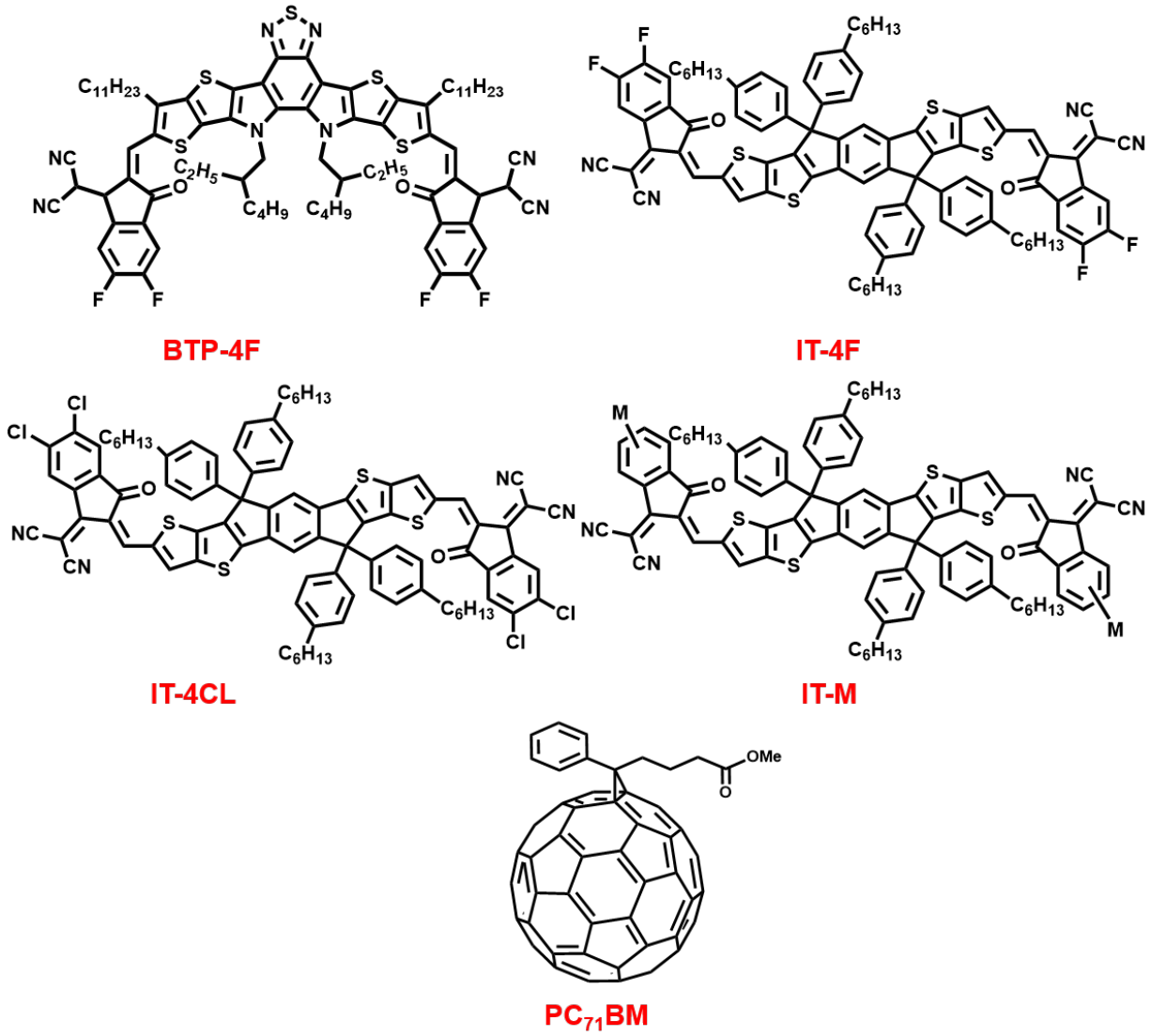

Figure 4.2: Chemical structure of acceptors

9,9,18,18-tetrakis (2-ethylhexyl)-5.14 dithiapentacyclo [10.6.0.03, 10.04, 8.013, 17] octadeca -1(12), 2, 4(8), 6, 10, 13(17), 15- heptaen -6- yl) -8-thia-7.9-diazabicyclo [4.3.0] nona-1(9), 2, 4, 6-tetraen- 2 -yl] methylidene -3-ethyl -2-thioxo-1,3- thiazolidin-4-one (EH-IDTBR) is used as an acceptor. With an absorption range of 400–700 nm, it displays a HOMO level of -5.58 eV and a LUMO level of –3.9 eV. [137]

$PC_{71}BM$

The fullerene electron acceptor named [6,6]- phenyl-C71- butyric acid methyl ester, (denoted $PC_{71}BM$) is selected for comparison with other non-fullerene acceptors. [138] The chemcial structure is shown in Figure 4.2. The non-symmetrical C_{70} cage of $PC_{71}BM$ enables energetic transitions that are forbidden in C60, improving the absorption characteristics over $PC_{60}BM$

for the visible range. The HOMO level is -5.9 eV and the LUMO level is -3.9 eV.

4.1.2 Blocking Layer and Electrode Materials

The original materials used for the electron-blocking, hole-blocking layers and the metal contact layer material responsible for a solar cell device are presented as follows.

Molybdenum Oxide (MoO_3)

Molybdenum oxide (MoO_3, 99.98%) powder was purchased from Carl Roth GmbH + Co. KG (Germany). Since the well matches the energy level with the anode, it acts as an electron-blocking layer for the organic solar cells. MoO_3 has a density of 4.69 g/cm^3, a melting point of 805 °C and a molar mass of 143.94 g/mol.

PEDOT:PSS

The polymer mixture poly(3,4-ethylene dioxythiophene): poly (styrene sulfonate), (denoted PEDOT: PSS) is used as the electron blocking layer for the hole transport only organic solar cell. Poly(3,4-ethylene dioxythiophene) (PEDOT) is a conjugated polymer that exhibits high conductivity with hydrophobic characteristics and carries a positive charge based on polythiophene. While the sodium polystyrene sulfonate (PSS) counterpart is hydrophilic electrically insulating and carries negative charges. PEDOT: PSS typically comes as a water-based emulsion which is created via the polymerization of PEDOT monomers in a polystyrene sulfonic acid solution. Since the properties of PEDOT: PSS vary from the PEODT to PSS dispersion ratio, the type of AI 4083 is purchased from Ossila BV. (Netherlands) to fabricate the hole-transport layer upon the ITO glass. Since PEDOT: PSS dispersions easily form aggregates at room temperature, normally it needs to be stored in the fridge between 5 °C and 10 °C. Prior to using the PEDOT: PSS, a 450 um hydrophilic filter is utilized to remove the big aggregates.

Zinc Acetate Dihydrate (ZAD)

Zinc acetate dihydrate, abbreviated as ZAD, is an inorganic precursor material for the zinc oxide (ZnO) electron-blocking layer of organic solar cells. The white salt powder has a density of 1.74 g/cm3, a melting point of 237 °C and a molar mass of 183.48 g/mol.

Silver Pellets (Ag)

Silber pellets (99.99%) were provided by Carl Roth GmbH + Co. KG (Germany). The metal has a density of 10.5 g/cm^3 and a melting point of 960 °C. It shows excellent electrical

conductivity (1.59 $\mu\Omega$/cm, 20 °C), ductility and reflectivity and is used as cathode material for organic solar cells.

Aluminum Pellets (Al)

Aluminium pellets (99.99%) were purchased from ChemPUR and used as cathode material for inverted organic solar cells. The metal has a density of 2.70 g/cm^3, a melting point of 660 °C and a molar mass of 26.98 g/mol.

4.1.3 Solvents and Additives

The following solvents and additives used for the organic solar cells are purchased from Merck (Germany) with the grade of anhydrous (99%).

Chlorobenzene (CB)

Chlorobenzene (CB) is a colorless, flammable, aromatic organic compound liquid with the formula C_6H_5Cl. CB has a density of 1.11 g/cm^3 and a boiling point of 132 °C and is a common solvent for organic polymer and novel non-fullerene acceptors.

Chloroform (CF)

Chloroform or trichloromethane (CF) is a colorless, volatile chlorinated organic solvent with the formula $CHCI_3$. With the low boiling point (61 °C) property and excellent solubility for organic materials, CF is used to dissolve the donor and acceptors in this thesis, too. Since its light sensitivity, CF easily degrades with time. In order to alleviate this problem, 0.5-1.0 % ethanol is added as a stabilizer.

1,2,4-trimethylbenzene (TMB)

1,2,4-trimethylbenzene (TMB) or pseudocumene is a colorless liquid with the chemical formula $C_6H_3(CH_3)_3$. TMB has a density of 0.87 g/cm^3 and a boiling point of 171 °C. It is a non-halogen solvent for organic polymer and novel non-fullerene acceptors.

1,8-diiodooctane (DIO)

1,8-diiodooctane (DIO) has been employed as a processing additive to improve the device performance of organic solar cells by tuning the active layer morphology. The solvent additive with formula $C_8H_16I_2$ has a density of 1.84 g/cm^3 and a boiling point of 167–169 °C. In order to suppress the degradation, a copper chip is added as a stabilizer.

2-methoxyethanol

2-methoxyethanol ormethyl cellosolve is a clear, colorless, organic compound liquid with formula $C_3H_8O_2$. It exhibits a notable ability to dissolve a variety of different types of chemical compounds and miscibility with other solvents. In this thesis, it is used for the preparation of the ZnO precursor solvent. The ether-like odor liquid has a density of 0.97 g/cm^3 and a boiling point of 124 °C.

Monoethanolamine (ETA)

Monoethanolamine, 2-aminoethanol or monoethanolamine (ETA or MEA), is a bifunctional organic chemical compound with the formula C_2H_7NO, containing both a primary amine and a primary alcohol. The colorless, viscous liquid has a density of 1.01 g/cm^3 and a boiling point of 170 °C. ETA is majorly used in pharmaceutical formulations in buffer systems, and emulsion preparations. In this work, the main responsibility is the stabilizer for the ZnO precursor solvent.

4.1.4 Substrates

In this thesis, various substrates are used to reach the requirements of the demand measurements technique. For the single active layer thin films, typically, glass substrates are used for the UV-Vis, PL, TRPL, as well as other Spectroscopic measurements. Silicon substrates are normally used for the GISAXS, GIWAXS, XRR and AFM measurements since the silicon show less scattering signal at a low incident angle with a super smooth surface, which could distinguish the substrate from the polymer peak. P-type silicon substrate shows promising conductivity, therefore it is ideally used for the XPS measurement. For the organic solar cell device such as IV, EQE, SCLC, and TA measurements, a leaser pattern indium-doped tin oxide (ITO) substrates are applied as the transparent electrodes.

Glass Substrates

Due to its optical transparency in the visible range of light and its electrical insulating properties, glass is well suited for the purpose of electrical and optical characterization of thin films. For this purpose, standard microscope glass slides with dimensions of 76 x 26 mm^2 and 1 mm thickness, provided by Carl Roth GmbH + Co. KG, are used. The glass slides are cut with the aid of a diamond cutter to the desired substrate size of typically 25 x 26 mm^2.

Silicon Substrates

The p-doped silicon wafers with a resistivity of 10 Ω cm – 20 Ω cm were provided by Silicon Materials (Kaufering, Germany). The round-shaped wafers have a size of 100 mm in diameter with a polished side, which coincides with the <100> crystal direction. Thus, the surface roughness of the polished side of Rq < 0.5nm is achieved for the 0.5mm thick wafers. The wafers are cut along a crystal direction with a diamond cutter to the desired substrate size of typically 1.5 x 1.5 cm^2 for the spin-coated samples or 2.5x 7.5 cm^2 for printed samples.

Indium-doped Tin Oxide (ITO) Substrates

Leaser-patterned Indium-doped tin oxide (ITO) covered glass substrates are purchased from Advanced Election Technology CO, Ltd. (Liaoning, China). The substrate's size of typically 2. 5x 2.5cm^2 with a thickness of roughly 1mm for the fabrication of organic solar cells. A high transmittance over 80% in the visible range with a sheet resistance of 15 Ωcm^{-2} could be achieved on the substrate, benefiting the current generation of the device.

4.2 Cleaning Process

Before thin film deposition, the substrate with the desired size needs to be cleaned in order to remove surface chemical contamination. In this thesis, the silicon and glass substrates are cleaned by the acid bath method to remove any impurities or organic traces. Since ITO reacts with acid solvents, an ultrasonic cleaning process uses several organic solvents in order to clean the ITO substrate. After the chemical cleaning process, all types of substrates are subjected to an oxygen plasma treatment to improve the wettability of the polar solvents or the working function of ITO.

4.2.1 Acid Bath Cleaning

Acid bath cleaning is that a method of thoroughly removing substrate impurities at a specific high temperature with a solvent made up of a certain ratio of acid, hydrogen peroxide and water. The details of the acid bath are processed as follows: 54 mL deionized water (H_2O), 84 mL hydrogen peroxide (H_2O_2, 30%), and 198 mL concentrated sulfuric acid (H_2SO_4, 95% – 98%) are subsequently put into a glass beaker. Then the beaker with acid is nested into a larger beaker filled with water. The two beakers are put on a hot plate (IKA Werke GmbH, G-MAG HP4, Germany) to have constant stirring during the heating process. When the water in the outer beaker is heated at 80 °C, substrates are immersed in the acid solution for 20 min with the aid of acid-resistant polytetrafluoroethylene (PTFE) holder. In the whole

acid bath, the water level needs to be slightly higher than the acid solvents level. Afterwards, substrates together with the holder are immediately transferred and subsequently rinsed in three beakers, filled with deionized water to dilute the acid residuals. To fully remove any acid residuals and dry the substrate, each individual substrate is continuously washed with deionized water for at least 30 s, followed by drying with nitrogen flow.
As a strong oxidant, the acid bath solution can promote the generation of SiO_X on the substrate surface, especially for the silicon substrate, therefore this process increases the hydrophilicity of the substrate.

4.2.2 Ultrasonic Cleaning

For the ITO glass substrates, the ultrasonic cleaning method with organic solvents is used to prevent the transparent alkaline electrode. ITO substrates are placed on a designed PTEE sample holder to avoid their movement during cleaning. The ITO substrates were cleaned sequentially through a diluted Hellmanex III (2:98 volume ratio in the deionized water), deionized water, ethanol, acetone and isopropanol for 15 min under an ultrasonic bath. After each step, the substrates together with the sample holder are rinsed with the solvent of the subsequent step. In the end, the substrates are removed one by one from the IPA solvent and are dried under a continuous nitrogen flow.

4.2.3 Oxygen Plasma Treatment

Prior to the thin film deposition, all types of substrates are subjected to oxygen plasma treatment in order to improve the wettability as well as remove all traces of organic matter. Oxygen plasma refers to the plasma treatment performed while introducing oxygen to the plasma chamber. The substrates are placed in the vacuum chamber under a 0.4 mbar oxygen atmosphere. When a power of 250 W with a frequency of 40 kHz is applied to the chamber, oxygen atoms are excited to higher energy states and ionized. During the relaxation, it releases photons and plasma-activated species. Most organic bonds of surface contaminants are disrupted and reacted to form H_2O, CO, CO_2, or other lower molecular weight hydrocarbons, which are expelled from the chamber during the treatment. The resulting substrate surface is super clean. In this thesis, the plasma treatment is carried out with a Nano Plasma Cleaner (Diener Electronic).

4.3 Fabrication Process

4.3.1 Solution Preparation

Synthesis of ZnO Precursor

ZnO nanoparticles solution was synthesized by the sol–gel method using zinc acetate dihydrate as precursors. In detail, 250 mg of zinc acetate dihydrate was added into 2.5 ml of 2-methoxyethanol solvent, and then 71 μl monoethanolamine stabilizer was added into the mixture solution. Then the solution was under stirring for at least 8 h for hydrolysis reaction and aging as previous report. [139]

PBDBT-2F:IT-M Solutions with Additive

PBDB-T-2F: IT-M blend solution with different amounts of DIO additive was prepared in a nitrogen glovebox by fixing the polymer blend concentration as well as weight ratio while varying the volume ratio of CB/DIO. In detail, PBDB-T-2F and IT-M were dissolved in CB with a total concentration of 20 mg/mL and stirred at 40 ºC overnight, respectively. Then the donor and the acceptor were mixed with a ratio of 1:1 in weight and the mixture was kept stirring for at least 8 h. After that, the different volumes of DIO were added to the mixture solution and stirred for at least 2 h before spin coating. Here, four different CB/DIO volume ratios (100/0, 99.5/0.5 99/1, and 98/2) were studied. [140]

PDTBT2T-FTBDT:BTP-4F Solution

PDTBT2T-FTBDT: BTP-4F mixture based on different solvents were fabricated as follows: PDTBT2T-FTBDT and BTP-4F were dissolved in CF or CB with a total concentration of 8 mg/mL (11 mg/mL for the spin-coated samples) and stirred at 38 °C for at least 4 h. Then the donor and the acceptor were mixed with a ratio of 1:1.6 in weight and the mixture was kept stirring for at least 4 h under 38 °C. [104]

PffBT4T-2OD:EH-IDTBR Solution

The donor and acceptor were mixed in a 1:1 weight ratio and added into the TMB solution with a total concentration of 15 mg/ml. The neat solutions of PffBT4T-2OD and EH-IDTBR were fabricated with a concentration of 8 mg/ml for the in situ UV-Vis measurements, respectively. All the solutions were kept stirred for at least 8 h under 80 °C. [141]

PBDBT-2F:Acceptor Solution without Additive

PBDBT-2F: different acceptors blend solutions were fabrication as follows: For the non-fullerene blend solutions, PBDBT-2F and the non-acceptors were dissolved in CF with a concentration of 14.6 mg/ml and 17.4 mg/ml, respectively. For the fullerene blend solutions, the PBDBT-2F and $PC_{71}BM$ were dissolved in CB with a concentration of 14.6 mg/ml and 17.4 mg/ml, respectively. After the neat solutions were stirring 4h at room temperature, the donor and the acceptor were mixed with a weight ratio of 1:1.2 and the mixture was kept stirring for at least 4 h at room temperature. All the steps were done inside a nitrogen-filled glove box (Braun, Germany).

4.3.2 Thin Film Deposition and Treatment

In the following sections, various deposition methods for the thin films used in the thesis will be described.

Spin Coating

Spin coating is one of the laboratory methods to make uniform thin films on solid surfaces using centrifugal force, viscous force and surface tension. Its main advantages are controllable and uniform film thickness, low operating cost, and rapidity. The thickness of the final dried film (d_{final}) could be determined mainly by the spinning speed, surface tension, and viscosity of the solution, thus can be simply described by Schubert's Equation:

$$d_{final} = C_{int} c_0 \omega^{-1/2} M_W^{1/4} \tag{4.1}$$

where C_{int} refers to the experiment paremeter from each sample system,c_0 is the initial concentration of the solution, ω refers to the angular velocity. M_W being the molecular weight of the solute. [142]

For the fabrication of PEDOT: PSS and ZnO blocking layers, the spin-coater (Süss MicroTec Lithography GmbH, Delta 6 RC TT, Germany) are utilized. The setup consists of a rotating plate with well defined acceleration and rotation speed. The device consists of a rotating plate with well-defined acceleration and rotational speed. The sample was mounted on the rotating stage with double-sided tape. In this experiment, a static spin-coating method was used, that is, the spin-coating process started immediately after the entire substrate surface was completely covered with a 120μl of solution on the substrate size of 2.5x2.5 cm^2. To obtain a dry film of 30 nm thickness, spin coating parameters were set to 5 s to accelerate to 3500 rpm and then spin for 60 s To maintain a reproducible sample environment in ambient, the lid was kept closed during deposition and the top of the spin-coater was kept closed.

For the active layers, the spin-coater (Novocontrol Tech. GmbH, SCI-10, Germany) was put into a nitrogen glovebox and used to get the dry film. Since the viscosity of the polymer varies in different solvents, the spin-coating speed was set to 1800 rpm for the CB-based solutions and the speed was changed to 4000 rpm for the CF-based solutions and kept for the 60s. The final thickness of the active layers is around 100 nm, which is desired for the organic solar cell.
Due to the increased velocity on the outer parts of the sample, a thickness gradient from the rotation centre to the sample edges cannot be avoided and limits the size of the substrate. Therefore, the spin-coating method severely limits the large-scale fabrication of organic solar cells.

Slot-die Coating

Slot die coating is a thin-film deposition technique in which a solution is delivered to a substrate through narrow grooves close to the surface. This technique scales up the manufacturing process with minimal waste of material compared to spin-coating methods. Thus, slot-die coating is considered one of the most promising fabrication methods for printing large-scale organic solar cells.

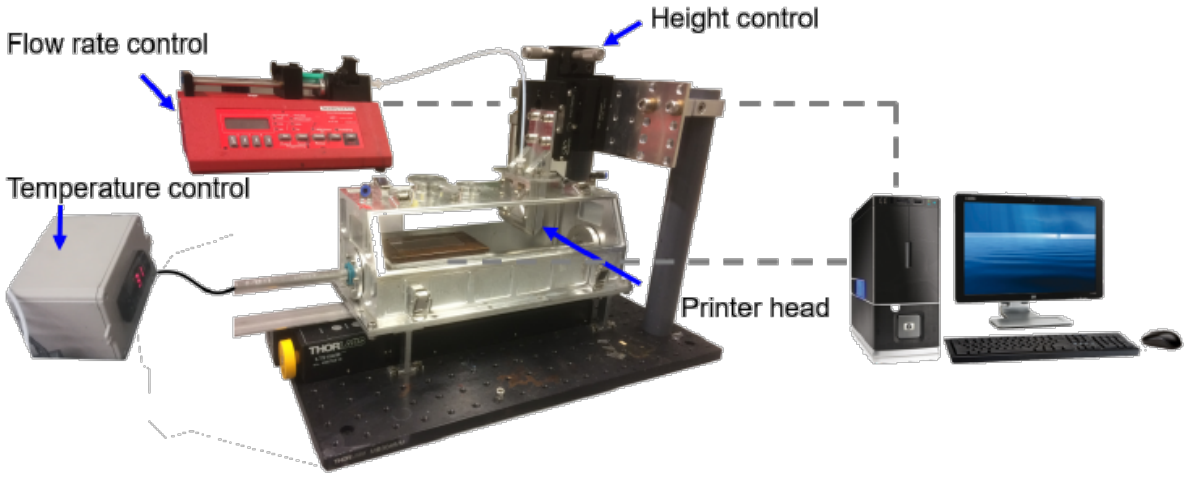

Figure 4.3: Graphic overview of the custom-made slot-die printing set-up used in this thesis, which was designed and built by Sebastian Grott and Rodrigo Delgado Andres from the group. Image is cited from Nian Li's PhD thesis. [112]

In this thesis, the active layer which is printed with a custom-made meniscus-guided slot-die coater shown in Figure 4.3. It contains five parts: A pump system for storing and delivering active layer solution at a constant flow rate; A slot-die head which is used for distributing coating solution over desired coating width prior to printing on the substrate; Substrate

drive system that loads the substrate and moves the slot die and the substrate at relative speeds during coating; Height control system to set the desired hight distance between the meniscus and the substrate; And a computer control system that can set the parameters. The final dried thin film thickness (d_{final}) in room temperature could be described as :

$$d_{final} = \frac{c_0 \Omega}{\rho V W} \tag{4.2}$$

where the c_0 refers to the concentration of the solution, Ω is the volumetric pump rate, ρ is the density of the volumetric density of the coated material, V is the printing speed, and W is the printing width. [143] The printing speed is 5 mm/s with a volumetric pump rate of 100 ml/min to achieve the requisite dried thin film thickness of around 90 nm for the active layer. The head-to-substrate distance for the PDTBT2T-FTBDT:BTP-4F active layer is adjusted to 150 um for the CF solvents and 300 um for the CB solution, respectively. Using the initial solutions, the neat PDTBT2T-FTBDT and BTP-4F thin films were prepared in the same conditions. The distance from the head to the substrate for printing the PffBT4T-2OD:EH-IDTBR active layer in TMB solvent is set to 200 um. For the neat PffBT4T-2OD, EH-IDTBR, and PffBT4T-2OD:EH-IDTBR films, the substrates were additionally heated to 60 °C during the printing at ambient conditions.

Thermal Deposition

Thermal evaporation (also called vacuum deposition) is an established method of coating thin layers, especially for insoluble solids with lowing boiling points. [144] The source material is evaporated in a vacuum due to high-temperature heating, and the vapour particles move to the substrate and become a solid thin film. In this method, charge-holding boats or resist coils are used in the form of powder or solid rods. [145] Figure 4.4 shows a schematic of a thermal evaporation system.
In this work, the 8 nm of MoO_3 electron blocking layer and the 100 nm of silver as the back electrode for organic solar cells are fabricated by this method. To get a homogeneous thin film with desired thickness and avoid damaging the underneath layer, the evaporation rate was controlled at 0.02 nm/s for the MoO_3. For the Ag electrode, a slow evaporation rate of 0.02 nm/s is used for the first 10 nm, then continuously increased to 0.2 nm/s for the rest of the thin film.

Thermal Annealing

Thermal annealing refers to a heat treatment process in which a material is exposed to high temperatures for an extended period of time and then cooled slowly. The annealing process

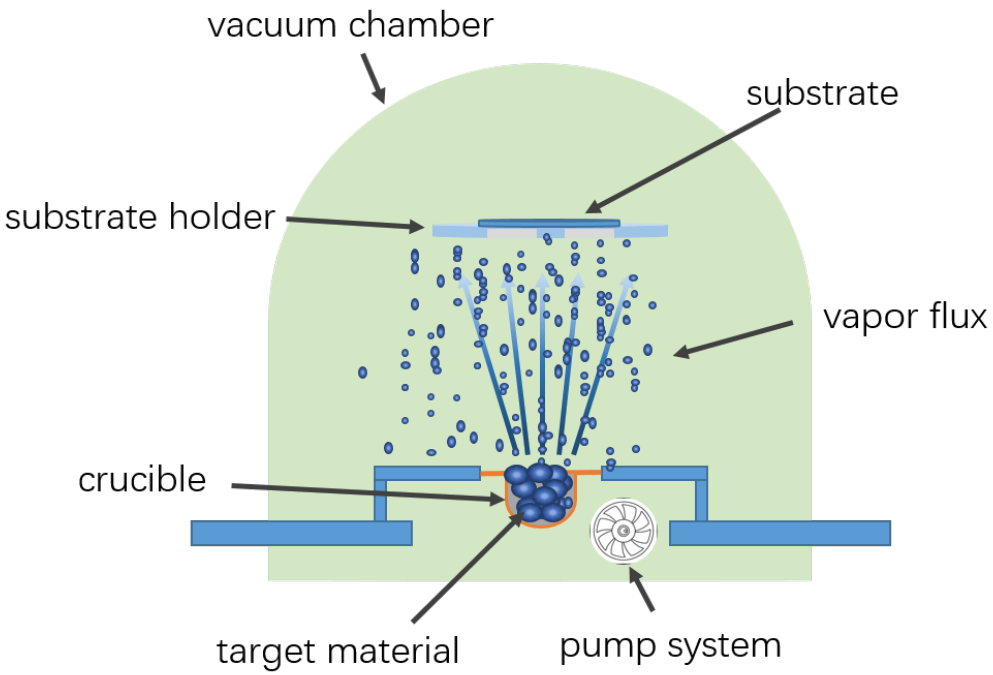

Figure 4.4: The phenomenon of thermal evaporation in a schematic.

is carried out for several purposes. One is that the residual solvent evaporates, and thus the film is dried. Furthermore, by keeping the sample at a certain temperature, the relaxation of the material chains can be promoted. This has a great effect on the morphology and crystallinity of nanoscale films.
In this thesis, the thermal annealing process is implemented immediately after the spin-coating process. The PEDOT: PSS thin film was annealed at 140 °C for 10 min with a hot plate (IKA Werke GmbH, G-MAG HP4, Germany) and ZnO thin film was annealed at 200 °C for 20 - 40 min and in ambient. For the active layer spin-coated with CB-based solution, the temperature was set to 100 °C for 10 min in the Nitrogen glove box.

4.4 Assembly of Solar Cells

4.4.1 Invert Structure of Organic Solar Cells

Device for PBDBT-2F:IT-M Solutions with Additive

Solar cells based on PBDB-T-2F: IT-M were fabricated with an inverted device architecture as glass/ITO/ZnO/PBDB-T-2F: IT-M/MoO_3/Al as shown in 4.5. The ZnO layer with a thickness of around 30 nm was achieved by spin-coating the precursor on a clean ITO substrate with a speed of 4500 rpm for 40 s with a post-annealing treatment at 200 °C for

1 h in air. Then, the substrate was transferred to the nitrogen glovebox. The PBDB-T-2F: IT-M active layer was spin-coated on the ZnO layer with a speed of 1200 rpm for 1 min and treated by thermal annealing at 100 °C. Afterwards, 10 nm of MoO_3 and 100 nm of Al electrode were deposited on the active layer in sequence by thermal evaporation.

Device for PDTBT2T-FTBDT: BTP-4F Solution

Solar cells based on PDTBT2T-FTBDT: BTP-4F were fabricated with an inverted device architecture as glass/ITO/ZnO/ PDTBT2T-FTBDT: BTP-4F /MoO_3 /Ag, as shown in Figure 4.6). 30 nm ZnO layer was spin-coated on a clean ITO substrate with a post-annealing treatment for 40 min in the air as in previous work. Then the solution of the active layer was printed on the top of the ZnO layer by a slot-die coater at ambient conditions. The film thickness of the active layer was controlled at around 80–90 nm by adjusting the print parameters. The active layer was dried in ambient conditions without any post-treatment process (thermal annealing, solvent vapor annealing, etc.). Afterwards, the samples were transferred into a nitrogen-filled glove box and 8 nm of MoO_3 and 100 nm of Ag electrode were deposited on the active layer in sequence by thermal evaporation. For the N_2 atmosphere printed devices, the active layers were fabricated with the slot-die coater and dried inside an N_2 filled chamber with an N_2 flow rate of 30 sccm during printing. For the spin-coated devices, the active layer was spin-coated and dried inside an N_2 glovebox, with the thickness being around 90 nm.

Device for PBDBT-2F:Acceptor Solution without Additive

Solar cells based on the PBDBT-2F with the different acceptors were fabricated with an inverted device architecture as glass/ITO/ZnO/active layer/MoO_3/Ag. The ITO glass was cleaned sequentially under sonication with a diluted Hellmanex III (2:98 volume ratio in the deionized (DI) water), deionized water, ethanol, acetone and isopropanol, and then dried with nitrogen gas. After UV-ozone treatment for 20min, a 30 nm ZnO ink was spin-coated on ITO substrate with a post-annealing treatment for 40 min in air. Then the samples were transferred into a nitrogen glovebox and the prepared active layer solution was spin-coated on the top of the ZnO layer with a speed of 3000rpm 40s. Afterwards, 10 nm of MoO_3 and 100 nm of Ag electrode were deposited on the active layer in sequence by thermal evaporation.

4.4.2 Hole-Only Device

The structure for the hole-only device is ITO/PEDOT: PSS/ PBDB-T-2F: IT-M/MoO_3/Al. The 30 nm PEDOT: PSS was spin-coated on a cleaned ITO substrate. The PEDOT: PSS thin

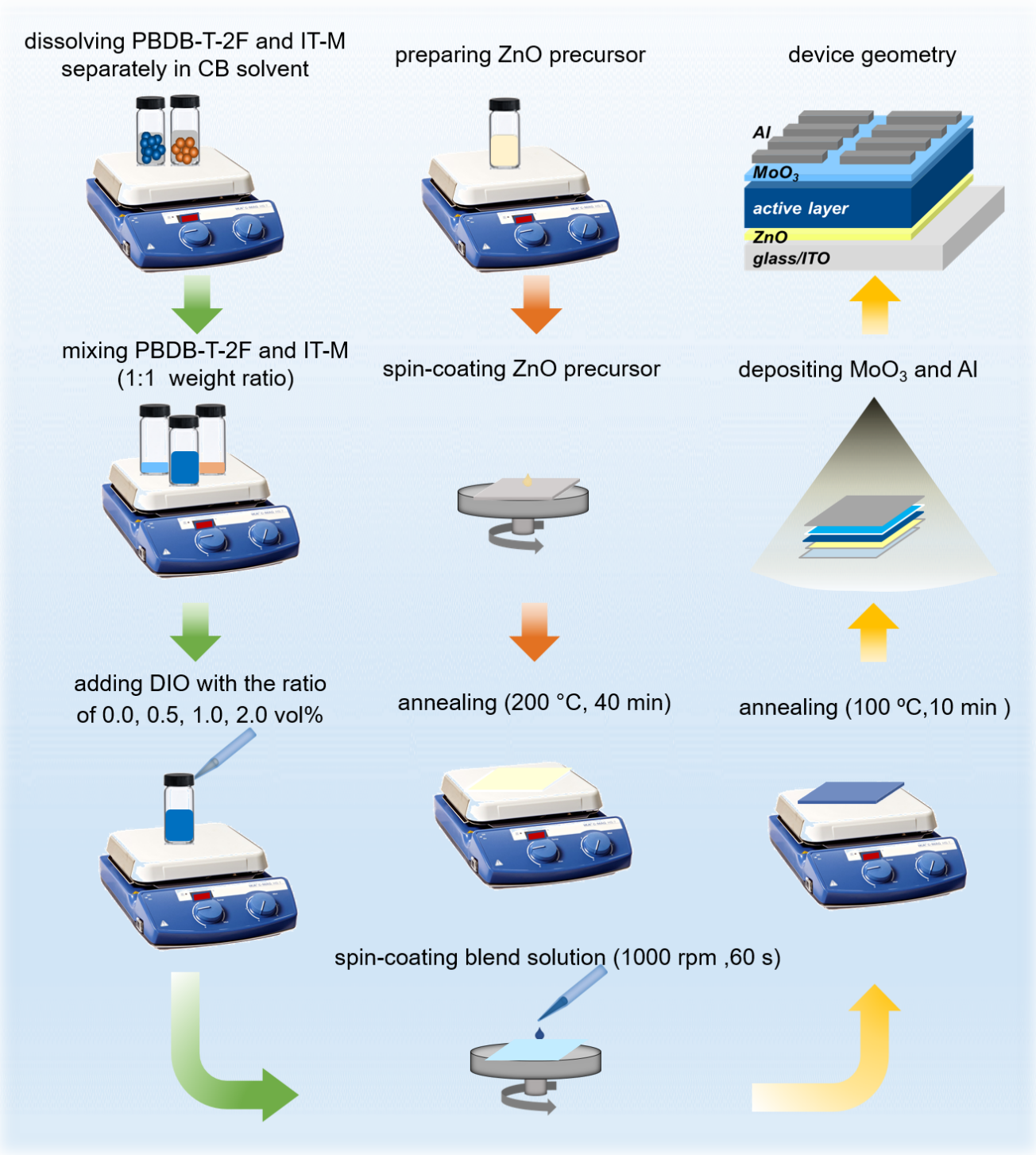

Figure 4.5: Details of the fabrication process of the PBDB-T-2F:IT-M based wide-bandgap non-fullerene OSC with different amounts of DIO addition. Reproduced with permission from the Royal Society of Chemistry, Copyright 2020. [140]

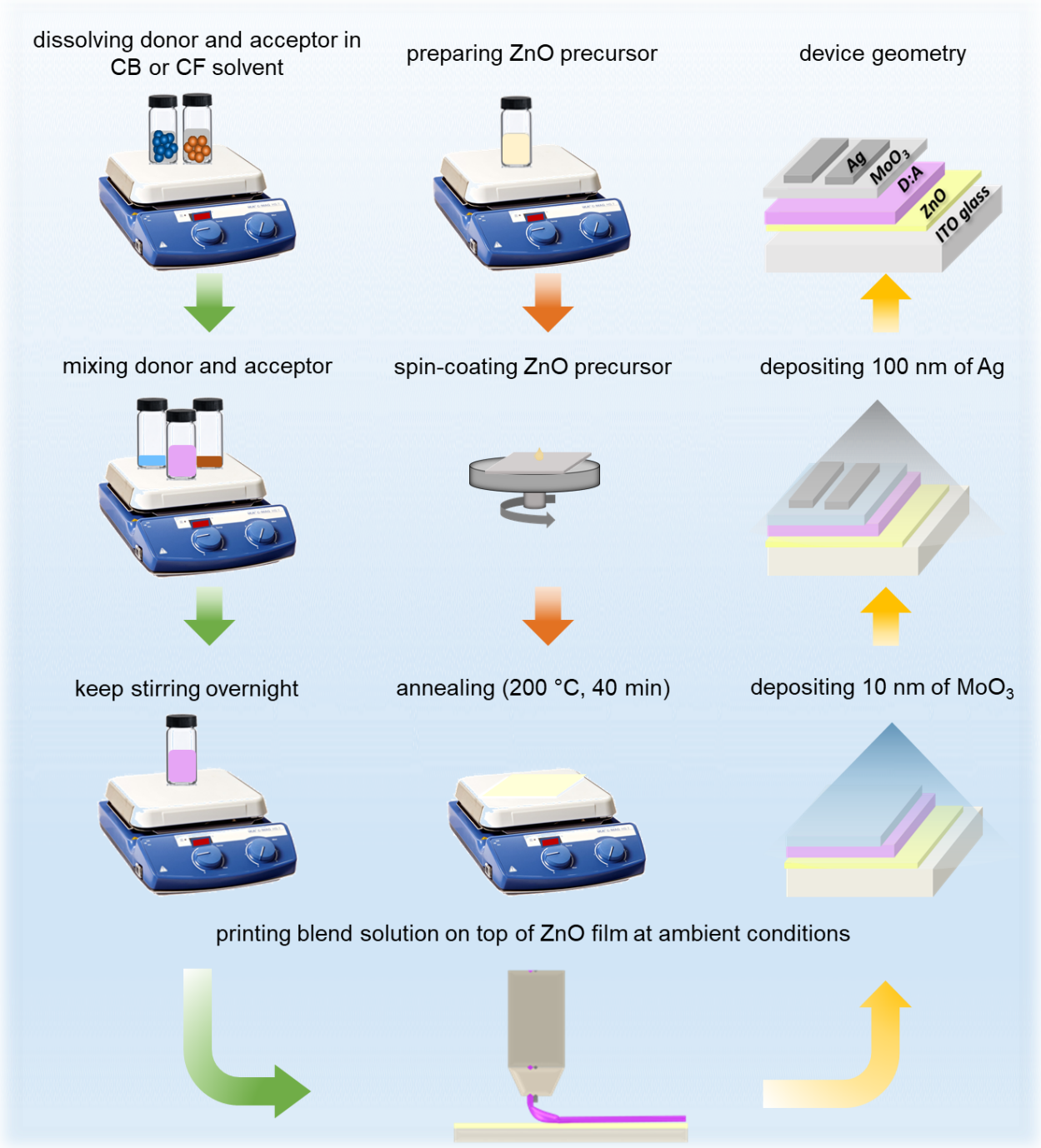

Figure 4.6: Details of the device fabrication process of printed PDTBT2T-FTBDT:BTP-4F active layer-based OSCs using different solvents in ambient conditions. Reproduced with permission from Wiley, Copyright 2022. [104]

film was annealed at 150°C for 10 min in air. The substrate was then transferred to the nitrogen glovebox. The PBDB-T-2F: IT-M active layer was spin-coated on the ZnO layer with a speed of 1200 rpm for 1 min and treated by thermal annealing at 100 °C. Afterwards, 10 nm of MoO_3 and 100 nm of Ag electrode were deposited on the active layer sequentially by thermal evaporation.

4.4.3 Electron-Only Device

The structure for electron-only devices is ITO/ZnO/ PBDB-T-2F: IT-M/Al. [146] The ZnO layer with a thickness of around 30 nm was achieved by spin-coating on a clean ITO substrate with a post-annealing treatment at 200 °C for 1 h in air. Then, the substrate was transferred to the nitrogen glovebox. The PBDB-T-2F: IT-M active layer was spin-coated on the ZnO layer with a speed of 1200 rpm for 1 min and treated by thermal annealing at 100 °C. Afterwards, 100 nm of Ag electrode was deposited on the active layer in sequence by thermal evaporation. [140]

5 Solvent Additive in the Active Layer

The following chapter is mainly based on the publication "Internal Nanoscale Architecture and Charge Carrier Dynamics of Wide Bandgap Non-Fullerene Bulk Heterojunction Active Layers in Organic Solar Cells" *(Xinyu et al., Journal of Materials Chemistry A, 2020, DOI:10.1039/D0TA09671G)* . [140] Reproduced with permission from the Royal Society of Chemistry, Copyright 2020.

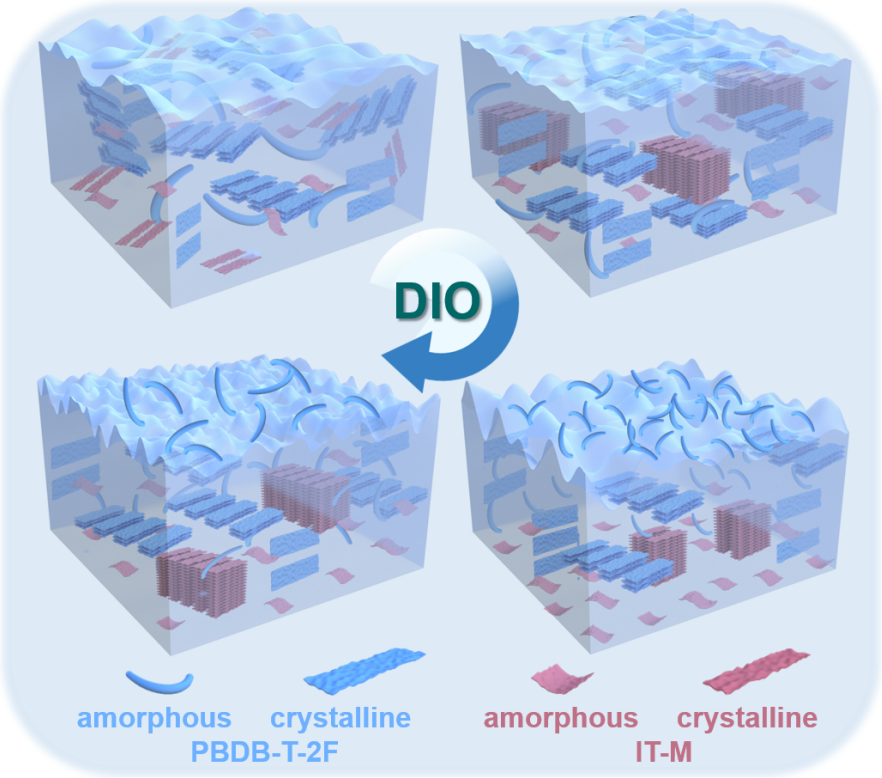

Recently, organic solar cells (OSCs) have achieved significant progress due to the development of new non-fullerene small molecule acceptor materials with the advantages of high flexibility, tunable light absorption spectra, and easy synthesis processes. [147],[148],[149],[150],[151] Encouragingly, bulk heterojunction (BHJ) single-junction OSCs using non-fullerene acceptors have made breakthroughs with champion devices demonstrating efficiencies over 18% due to the material innovation as well as inner structure optimization of the active layer on the nanoscale. [129],[152] Despite the recent notable improvements in efficiency, there are two

main challenges in the field of non-fullerene OSCs which need to be addressed. [147],[148],[149] Firstly, compared with perovskite solar cells and silicon solar cells, OSCs suffer from more severe energy loss (E_{loss}), resulting in a poor open-circuit voltage (Voc), which generally lowers the device performance. [153],[154] Secondly, the internal nanoscale structure and charge carrier dynamics in the non-fullerene active layer is still inadequate and deficient, thus restricting the further development of OSCs. [155],[156] To address the E_{loss} issue in OSCs, new donor materials received increasing attention, especially novel wide bandgap donors were developed. [154],[157],[158] Since wide bandgap polymer donors typically exhibited a deeper highest occupied molecular orbital (HOMO) level, a high Voc in OSCs was enabled based on small molecule acceptors with low-lying lowest unoccupied molecular orbital (LUMO) level. [136],[159],[160],[161],[162],[163] For example, Zhang et al. firstly synthesized a wide-bandgap polymer named poly[(2,6-(4,8-bis(5-(2-ethylhexyl-3-fluoro)thiophen-2-yl)-benzo[1,2-b:4,5-b']dithiophene))-alt-(5,5-(1',3'-di-2-thienyl-5',7'-bis(2 ethylhexyl) benzo [1',2'-c:4',5'-c']dithiophene-4,8-dione)] (PBDB-T-2F). As one of the PBDB-T congeners, PBDB-T-2F exhibited an excellent optical bandgap of 1.80 eV and a deep HOMO level at -5.45 eV, favoring a high Voc in OSCs. [164] Further, Yuan et al. synthesized a new non-fullerene acceptor composed of a fused thienothienopyrrolo-thienothienoindole core base and 2-(5,6-difluoro-3-oxo-2,3-dihydro-1H-inden-1-ylidene)malononitrile end units named Y6 (or BTP-4F), which has an electron-deficient-core-based central fused ring to match with PBDB-T-2F, and thus enabled a single junction OSC with over 15% efficiency. [132] Using the non-fullerene acceptor 3,9-bis(2-methylene-(3-(1,1-dicyanomethylene)-indanone))-5,5,11,11-tetrakis (4-hexylphenyl) -dithieno [2,3 - d:2',3'-d']-s- indaceno [1,2-b:5,6-b'] dithiophene (ITIC). Wang et al. developed PBDB-T-2F:ITIC based solar cells that showed a high Voc of 1.04 V. The E_{loss} reduced to 0.51 eV for PBDB-T:ITIC based OSCs. [165] Thus, PBDB-T-2F is a promising polymer donor material to reduce the energy losses in next-generation single junction non-fullerene OSCs. The internal nanoscale structure as well as the charge carrier dynamics of the active layer have great importance to the performance of OSCs. Both could be easily tuned by several approaches, such as introducing additives, third components and post-treatments. [165],[166],[167] Among these methods, introducing additives is a pervasive and effective way. Solvent additives enable polymers to have a higher degree of molecular order, which is beneficial for the device's performance. [168],[169],[170],[171] For example, Wienhold et al. showed that the addition of 0.25 vol% 1,8-diiodooctane (DIO) additive in printed OSCs of PBDB-T-SF blended with the non-fullerene acceptor IT-4F resulted in the best device performance due to an optimized morphology. [172] Wang et al. also used DIO to optimize the nanoscale morphology of OSC based on the non-fullerene acceptor ITIC, thereby improving the exciton dissociation and charge extraction of PBDB-T-2F:ITIC active layers. [165] Li et al. reported that 3.0 vol% toluene addition improved the ITIC stacking in wide-bandgap donor materials,

which optimized the heterojunction morphologies. [173] Despite the successful use of additives, a more fundamental understanding of how additives influence the inner morphology of the active layer of OSCs with respect to the spatial distribution of donor and acceptor components on the nanoscale and the charge carrier dynamics will be beneficial to further improve wide bandgap donor non-fullerene acceptor based OSCs.
In this chapter, the wide bandgap polymer donor PBDB-T-2F and a non-fullerene small acceptor IT-M are selected as p-type and n-type components of the active layer. The deep HOMO level of PBDB-T-2F (-5.56 eV) matches well with the LUMO level of IT-M (-3.98 eV). [132],[174] The small Δ_E HOMO in PBDB-T-2F: IT-M reduces the Voc loss and allows for a high Voc in OSCs. [175],[176] An investigation based on the influence of the amount of the solvent additive DIO to tailor the nanoscale morphology of the active layer. A combination of several measurement techniques, the effect of different DIO concentrations on the morphology and optical and electrical properties of the active layer is studied. In more detail, the inner architecture of additive doped PBDB-T-2F: IT-M active layers by using grazing-incidence small-angle X-ray scattering (GISAXS), grazing incidence wide-angle X-ray scattering (GIWAXS), X-ray reflectivity (XRR) as well as X-ray photoelectron spectroscopy (XPS) is systemically investigated. Based on these methods, the characteristic lateral domain sizes and domain distances on the nanoscale, the crystalline part, the orientation of crystallites and the enrichment layer at the surface is compared. [177],[178] To correlate the morphology with the charge carrier behavior, time-resolved photoluminescence (TRPL) is used to estimate the lifetime of the photon-generated charge carriers. Best-performing OSCs are achieved with 0.5 vol% DIO. These devices show a Voc of 1.0 V and a Jsc of 16.12 mA/cm^{-2} due to having the best active layer morphology. In addition, the space charge limited current measurements also show improved hole and electron mobilities in the case of 0.5 vol% DIO addition.

5.1 Optical, Electronic Properties and Device Performance

5.1.1 Absorption

The absorption of PBDB-T-2F mainly lies in the range of 450-700 nm as shown in Figure 5.1a. The absorption of IT-M is mainly located in the range of 500-800 nm, which is complementary to that of PBDB-T-2F. From the solution to the dry thin films, the absorption range becomes broaden in both materials. A significant red shift in the IT-M suggests serious J-aggregate formed after sample has dried. DIO as a solvent additive could tune the solubility of the donor and the acceptor to adjust the morphology of the active layer. In Figure 5.1b, PBDB-T-2F rarely dissolves in the DIO solution. On the contrary, IT-M

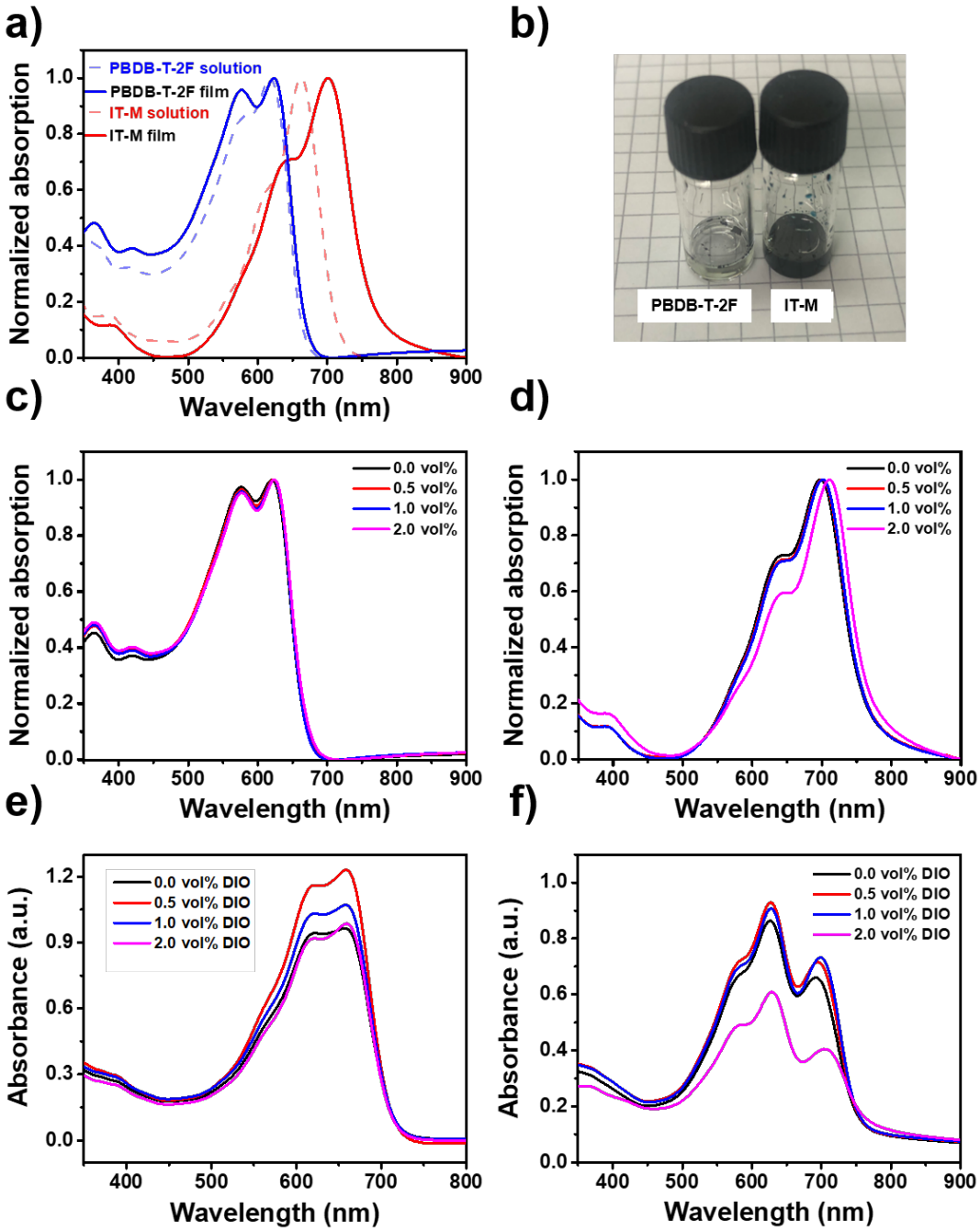

Figure 5.1: a) Normalized UV-vis absorption of PBDB-T-2F and IT-M in solution and in a dried thin film. b) 10mg/ml of PBDBT-2F and IT-M in DIO solution. Normalized UV-vis absorption of c) PBDB-T-2F and d) IT-M neat films with different DIO addition UV-vis absorbance of PBDB-T-2F:IT-M blend e) solutions and f) thin films with different DIO addition. Reproduced with permission from the Royal Society of Chemistry, Copyright 2020. [140]

shows superior solubility in the DIO solution. The difference in solubility of the donor and acceptor in DIO could vary the optical properties of the thin film with various DIO

addition in the host solvent. As shown in 5.1c and 5.1d, the main peak of neat PBDB-T-2F thin film linearly shifts from 621 to 624 nm with increased DIO addition. However, the main peak of IT-M thin film shifts from 698 to 701 nm with the addition of small volume DIO. When 2.0 vol% DIO is added into IT-M, the peak shifts to 711 nm. This suggests that rather the IT-M than the PBDB-T-2Fthin film is easier affected by the large volume addition of DIO. The UV-vis spectra of the blend processed with different amounts of DIO in the solution state are shown in Figure 5.1e. As a function of the added amount of DIO, the absorbance of the PBDB-T-2F: IT-M solution varies, suggesting an influence of DIO on the structure via self-assembly. The highest absorbance is observed in solution with 0.5 vol% DIO addition. Thus, already a small amount of DIO addition can increase the absorption ability of both, PBDBT-2F and IT-M. UV-vis absorption spectroscopy measurements are shown in Figure 5.1f for the PBDB-T-2F: IT-M films. All blend thin films show a broad light absorption in the range of 450-760 nm, which corresponds to an optical band gap of 1.69 eV. [179] Samples prepared with addition of (0.5 vol% and 1.0 vol%) DIO show higher absorbance in the entire wavelength range, which enhances the light-harvesting ability of the active layers and can provide an increased Jsc of the respective device. [180] As compared with 0.5 vol% DIO addition, the sample with 1.0 vol% DIO addition shows a slightly lower absorbance in the donor regime and a higher absorbance in the acceptor region. Moreover, we see an apparent red shift of the peak position from the acceptor and no shift of the donor with increasing DIO addition. This suggests that IT-M is more easily influenced by DIO during the drying process. It should be noted, that the red shifted IT-M peak position also reveals the enhanced intramolecular charge transfer (ICT) effects of the acceptors, which are beneficial for the device light absorption capability while sacrificing the Voc. In contrast, the sample with 2.0 vol% DIO addition shows a weak absorbance in the entire wavelength range. Moreover, a lower optical band gap of 1.66 eV, suggests a pronounced Voc loss. The significantly reduced absorbance is caused by a decreased light absorption ability and the pronounced red shift of the IT-M peak, if 2.0 vol% DIO are added (Figure 5.1f).

5.1.2 Photoluminescence

To investigate the influence of DIO on exciton dissociation and charge transfer in the active layers, photoluminescence (PL) measurements are performed and the relevant spectra are presented in Figure 5.2. The PL emission peaks of pure PBDB-T-2F and IT-M are located at 688 nm and 750 nm in Figure 5.2a, respectively. At the used excitation wavelength of 500 nm, the PL spectra of the active layers are located in the range of 650 to 800 nm in Figure 5.2b. Without DIO addition, in the blend film the emission peak of PBDB-T-2F is mostly quenched and the peak of IT-M is shifted to 745 nm, indicating a high charge transfer efficiency from the donor and a lower charge transfer efficiency from the acceptor. [181]

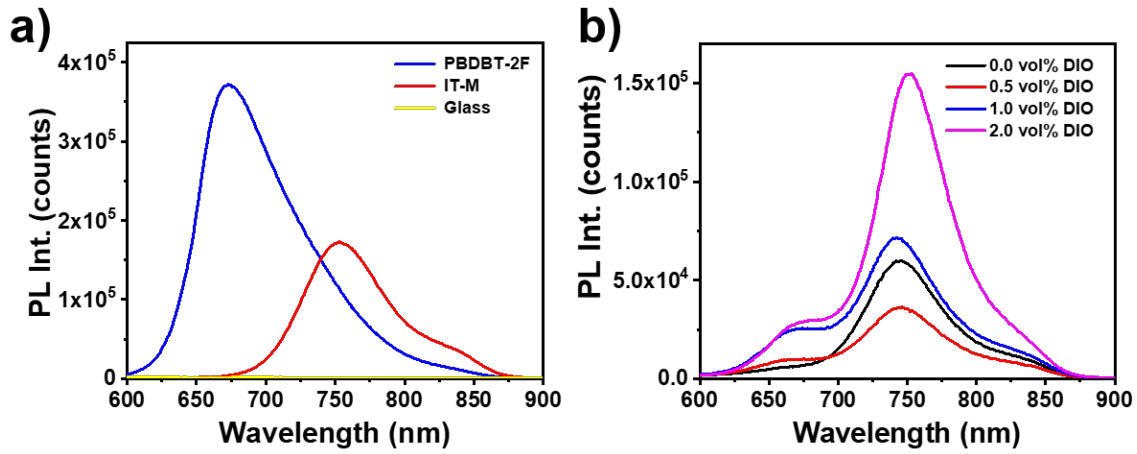

Figure 5.2: a) PL spectroscopy data of PBDB-T-2F, IT-M neat films, a glass substrate, respectively. b) PL spectroscopy data of PBDB-T-2F:IT-M active layers with different DIO addition at 750 nm. Reproduced with permission from the Royal Society of Chemistry, Copyright 2020. [140]

Table 5.1: TRPL parameters of fit with a two-phase exponential decay function

DIO (vol%)	A_1	τ_1 (ps)	A_2	τ_2 (ps)
0.0	1.20	148 ± 2	0.03	1710 ± 290
0.5	1.18	136 ± 2	0.03	1650 ± 260
1.0	1.19	150 ± 2	0.04	1590 ± 260
2.0	1.28	196 ± 2	0.03	1980 ± 450

When 0.5 vol% DIO is introduced to the blend, the overall PL signal decreases, which reveals that the exciton dissociation and charge transfer are enhanced. The slight increase of the signal at 670 nm shows the onset of a reduced efficiency of the donor component. With 1.0 vol% DIO addition, the overall PL emission increases. In particular, the peak at 670 nm becomes more pronounced, which shows that the exciton transport is inhibited from PBDB-T-2F to IT-M, which is not beneficial for the photovoltaic performance. Increasing the amount of DIO to 2.0 vol% causes a further strong PL increase. Moreover, the primary emission peak red shifts to 753 nm. It reveals severe IT-M aggregation, which provokes a frustrated exciton transport and poor charge transfer between donor and acceptor.

5.1.3 Charge Carrier Dynamics

Two-dimensional time-resolved photoluminescence (TRPL) data sets detected for the PBDB-T-2F: IT-M active layer with different DIO addition are provided in Figure 5.3a. All the samples show a very short decay lifetime within 1 ns among all the detection ranges, suggesting the fast charge carrier recombination in the active layers. The intensity of the charge carrier in the whole range decrease with the increased volume of DIO addition.

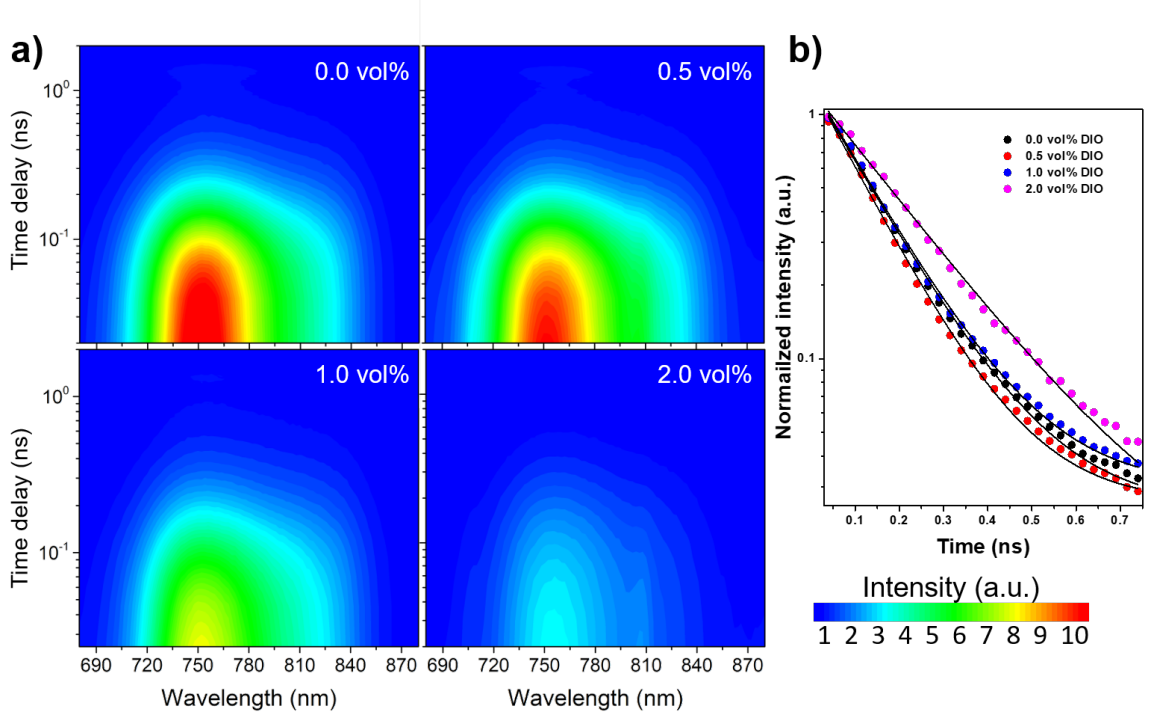

Figure 5.3: a) 2D mapping of the TRPL lifetime curves of the of PBDB-T-2F:IT-M active layer with different DIO addition. b) TRPL lifetime curves at 750 nm active layers. Reproduced with permission from the Royal Society of Chemistry, Copyright 2020. [140]

Normalized TRPL lifetime data taken at the maximum peak position of the 2D data are presented in Figure 5.3b. To quantify the charge carrier lifetime in the active layers, a double-component exponential decay model is used to fit the TRPL curves, in which lifetime τ denotes the fast decay process originating from energy transport or non-radiative recombination. A shorter τ_1 can be contributed by higher charge carrier mobility. Lifetime τ_2 belongs to the slow decay process revealing the radiative recombination or trap-assisted recombination. The detailed extracted parameters are shown in Table 5.1. Without DIO addition, the fast decay lifetime is 148 ps, which changes to 136 ps, 150 ps and 196 ps for 0.5 vol%, 1.0 vol% and 2.0 vol% DIO addition, respectively. Thus, at 0.5 vol% DIO, we find the fastest decay process which is possibly attributed to the fast injection from the donor component and also a faster energy transport configuration inside of the blend for the non-radiative recombination. The slow decay lifetimes suggest that a small amount of additives can increase the trap states, thereby decreasing the lifetimes. However, this tendency reverses at high DIO addition. Overall, at 0.5 vol% DIO addition, the radiative recombination is restrained which can induce a fast charge transport increasing the short circuit current. [182]

5.1.4 Device Performance

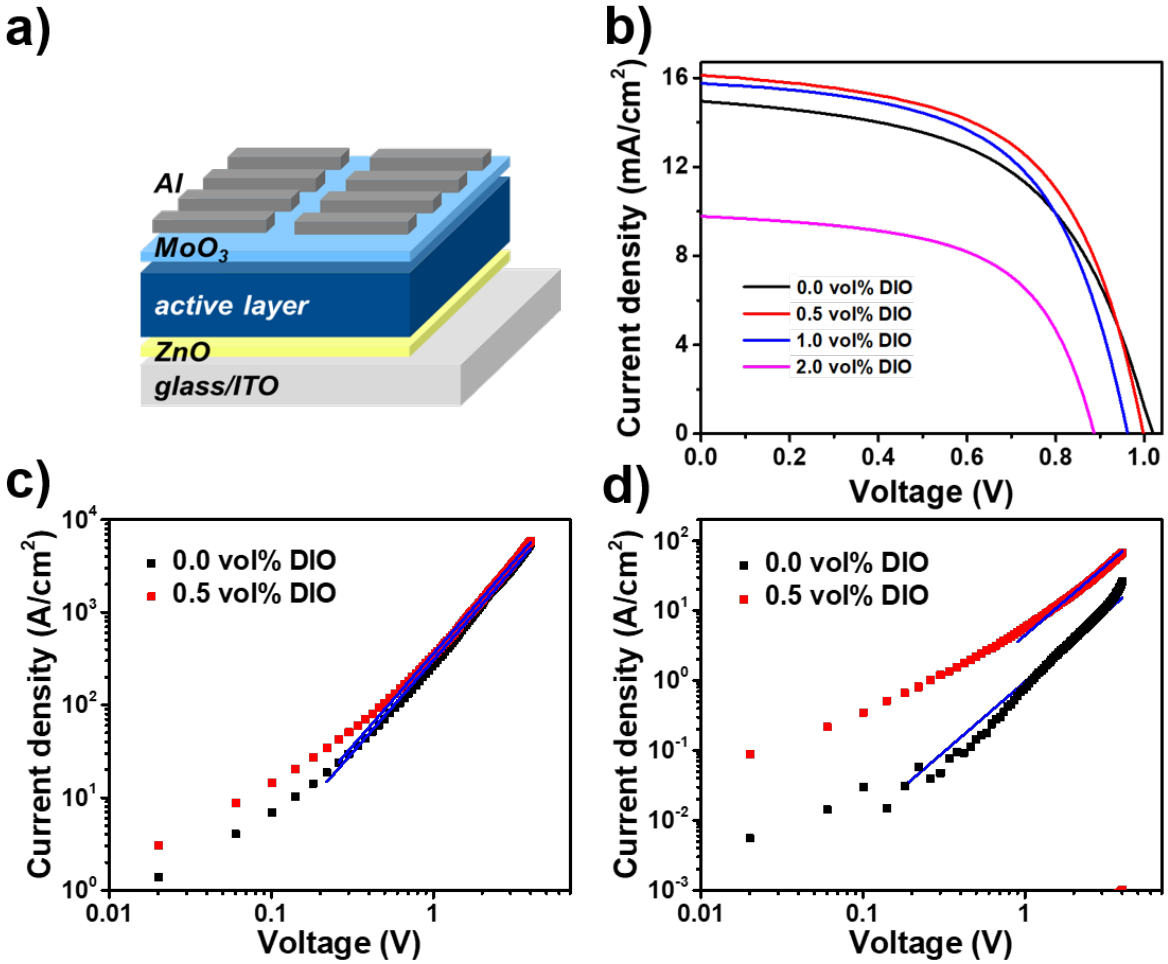

Figure 5.4: a) Fabricated inverted OSC geometry in this chapter b) TRPL lifetime curves at 750 nm active layers. b) J-V curves of the best-performing devices based on the PBDB-T-2F:IT-M blend thin films with varying DIO content. J-V curves as well as and the corresponding fits (blue line) for the c) hole-only device and d) electron-only device, without DIO addition (black) and with 0.5 vol% DIO addition (red), respectively. Reproduced with permission from the Royal Society of Chemistry, Copyright 2020. [140]

To investigate the DIO effect on the device performance, OSCs are fabricated in an inverted geometry using a functional stack as ITO/ZnO/PBDB-T-2F:IT-M blend/MoO_3/Al, in which ZnO and MoO_3 serve as the hole and the electron blocking layers, is provided in Figure 5.4a. The current density-voltage (J-V) curves of best-performing devices are shown in Figure 5.4b. The detailed photovoltaic parameters are listed in Table 5.2. Without DIO addition, a PCE of 8.26 % is achieved due to a Jsc of 14.95 mA cm^{-2} and a rather poor fill factor (FF) of 0.54. Notably, the devices with 0.5 vol% DIO addition yield the highest PCE of 9.17

Table 5.2: Photovoltaic parameters of PBDB-T-2F:IT-M OSCs with different DIO addition

DIO (vol%)	Jsc (mA cm^{-2})	Voc (V)	FF	PCE (%)
0.0	14.64 ± 0.30 [14.95]	1.01 ± 0.01 [1.02]	0.54	8.05 ± 0.21 [8.26]
0.5	15.81 ± 0.31 [16.12]	0.99 ± 0.01 [1.00]	0.57	9.00 ± 0.17 [9.17]
1.0	15.19 ± 0.51 [15.70]	0.95 ± 0.01 [0.96]	0.57	8.51± 0.14 [8.65]
2.0	9.05 ± 0.73 [9.78]	0.86 ± 0.03 [0.89]	0.58	4.68 ±0.34 [5.02]

[ ] Champion values are given in brackets

Table 5.3: Electron and hole mobilities obtained by SCLC method

DIO (vol%)	μ_h (cm^2 V^{-1} s^{-1})	μ_e (cm^2 V^{-1} s^{-1})	μ_h / μ_e
0.0	1.14 x 10^{-4}	3.59 x 10^{-7}	317.5
0.5	1.35 x 10^{-4}	1.67 x 10^{-6}	80.8

% with a Voc of 1.00 V, a JSC of 16.12 mA cm^{-2} and a FF of 0.57, which suggest a highly efficient interface configuration in the active layer of the device. Increasing the amount of DIO to 1.0 vol% reduces the performance. The Jsc decreases to 15.70 mA cm^{-2} and also Voc decreases to 0.96 V, resulting in a reduced PCE of 8.65 %. A further severe decrease in the device performance is observed, when a further increased amount of DIO additive is introduced in PBDB-T-2F: IT-M active layer fabrication. At 2.0 vol% DIO, the lowest PCE of 5.02 % originates from the significantly decreased Jsc of 9.78 mA cm^{-2} and Voc of 0.89 V. To compare the mobility of the carriers of the device with and without DIO addition, J-V measurements of the hole-only device and electron-only device are conducted in Figure 5.4c and 5.4d, respectively. The hole and electron mobility are obtained by a space charge limited current (SCLC) method from previous reports. [146] The hole mobility μ_h increases from 1.14 x 10^{-4} cm^{-2} V^{-1} s^{-1} to 1.35 x 10^{-4} cm^{-2} V^{-1} s^{-1}, the electron mobility μ_e from 3.59 x 10^{-7} cm^{-2} V^{-1} s^{-1} to 1.67 x 10^{-6} cm^{-2} V^{-1} s^{-1} after 0.5% DIO addition, as shown in Table 5.3. The ratio of μ_h /μ_e reduces from 317.5 to 80.8, suggesting a better-balanced hole and electron mobility with 0.5 vol% DIO addition.

5.2 Morphology and Crystallinity of the Active Layer

5.2.1 Surface Morphology

Figure 5.5, Figure 5.6 and Figure 5.7 present the height (a-d) and phase (e-h) information of PBDB-T-2F, IT-M, as well as their blend films with increasing DIO volume addition as

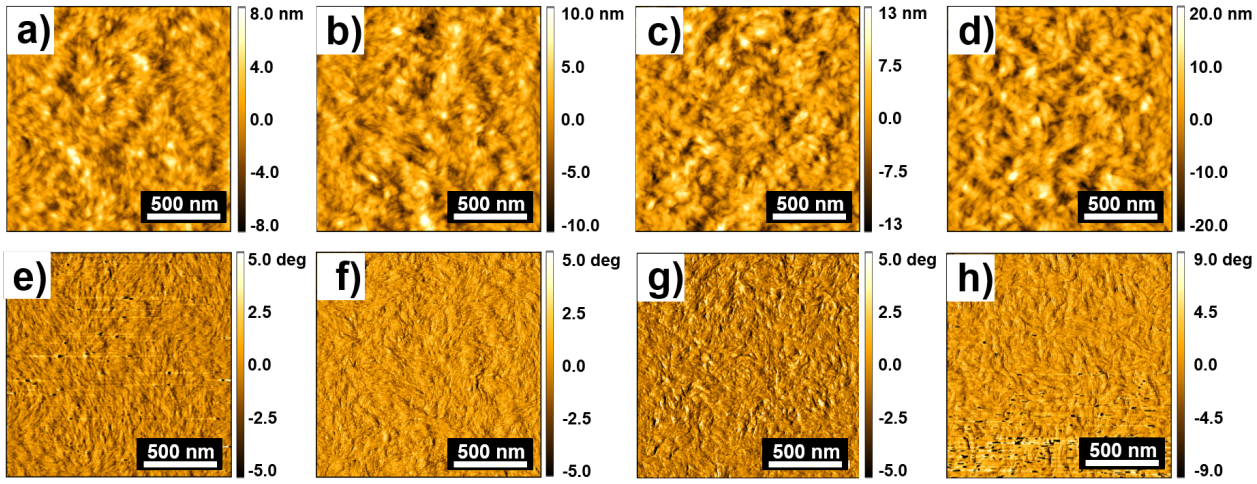

Figure 5.5: AFM height (a-d) and phase (e-h) images of PBDBT-2F films prepared with different amounts of DIO addition.Reproduced with permission from the Royal Society of Chemistry, Copyright 2020. [140]

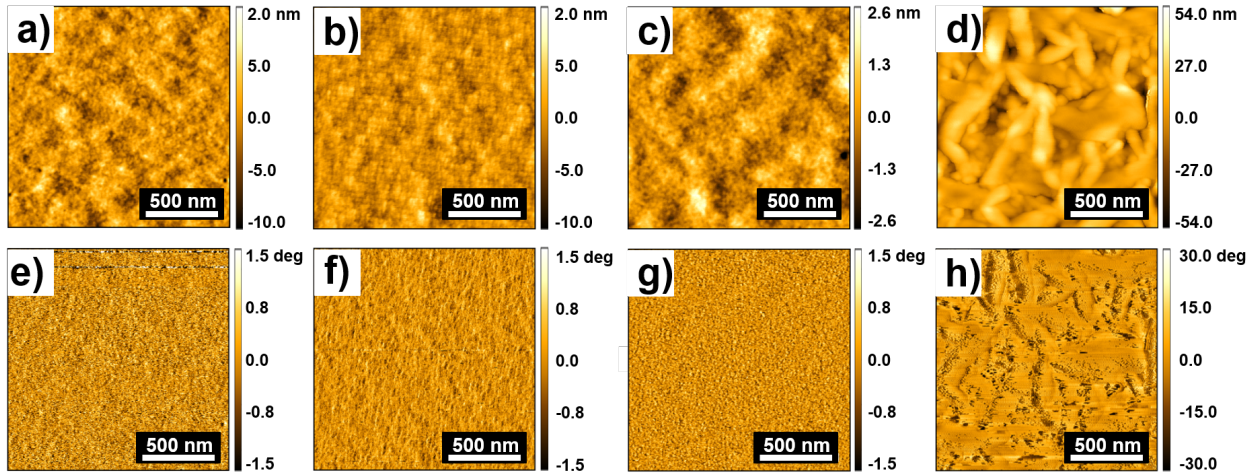

Figure 5.6: AFM height (a-d) and phase (e-h) images of IT-M films prepared with different amounts of DIO addition.

probed with atomic force microscopy (AFM). The corresponding root-mean-square (RMS) roughness of each thin film is listed in Table 5.4. For the neat PBDBT-2F thin films, the roughness and the phase separation are slightly increased when an increased volume of DIO is added. For the IT-M small molecule, there is no obvious difference both in phase and roughness when 0.5 vol% DIO is added. Moreover, the RMS increased from 0.3 to 0.5 nm with 1.0 vol% DIO addition. In particular, at 2.0 vol% DIO, the RMS of IT-M is 9.9 nm, suggesting large IT-M crystallites form at the surface. For the blended thin films surface, with increasing DIO concentration, the topography changes from a round "cotton-like" structure (Figure 5.7a, 5.7e) into an elongated "rope-like" structure, resulting in the

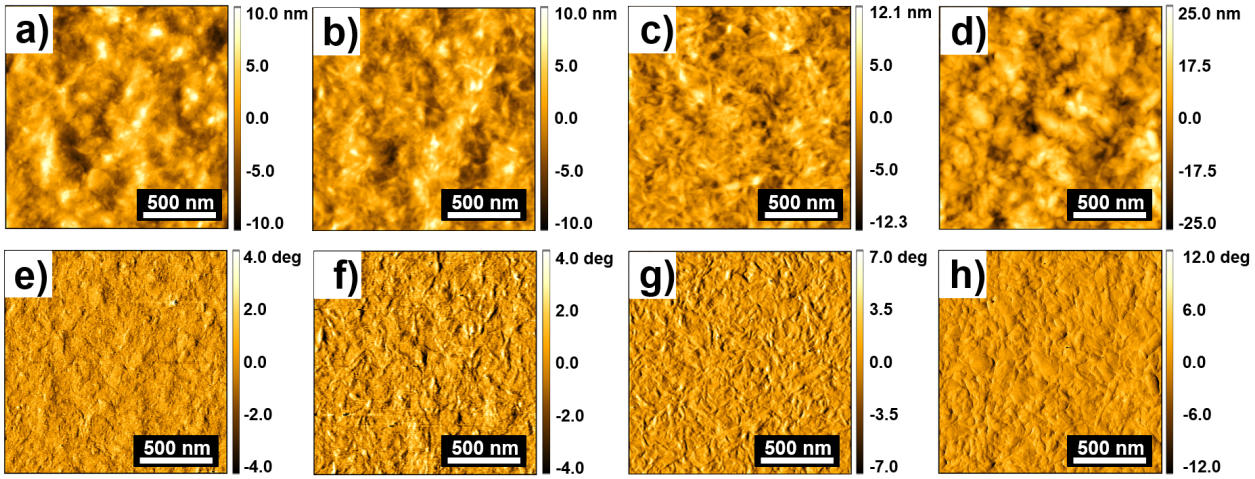

Figure 5.7: AFM height (a-d) and phase (e-h) images of PBDBT-2F:IT-M films prepared with different amounts of DIO addition. Reproduced with permission from the Royal Society of Chemistry, Copyright 2020. [140]

Table 5.4: Roughness (nm) of the thin films prepared with different amounts of DIO addition

DIO (vol%)	PBDBT-2F	IT-M	PBDBT-2F:IT-M
0.0	1.4	0.3	2.0
0.5	1.9	0.3	1.9
1.0	2.7	0.5	2.1
2.0	4.0	9.9	5.3

formation of an interpenetrating network for charge carrier transport. At 2.0 vol% DIO, apparently, aggregations appear (Figure 5.7d, Figure 5.7h), in which the interpenetrating network collapses. In more detail, the RMS of the film surface is (2.0 ± 0.1) nm at 0.0 vol%, (1.9± 0.1) nm at 0.5 vol%, (2.1 ± 0.1) nm at 1.0 vol% and increases to (5.3 ± 0.5) nm by adding 2.0 vol% DIO. A smoother active layer surface can be envisioned to have better contact with the top blocking layer and top electrode, both being beneficial for the charge collection in OSC. The observed changes in the surface topography are assigned to the significantly different solubilities of PBDB-T-2F and IT-M in DIO as discussed in Section 5.1.1. Obviously, DIO addition causes stronger changes in IT-M surface morphology compared to PBDB-T-2F, confirmed by the neat thin films.

5.2.2 Inner Morphology

The inner nanoscale morphology of PBDB-T-2F: IT-M thin films with different amounts of DIO addition is investigated with GISAXS measurements, which probe the nanoscale structure over macroscopic areas. [39] The 2D GISAXS data of PBDB-T-2F: IT-M blend films

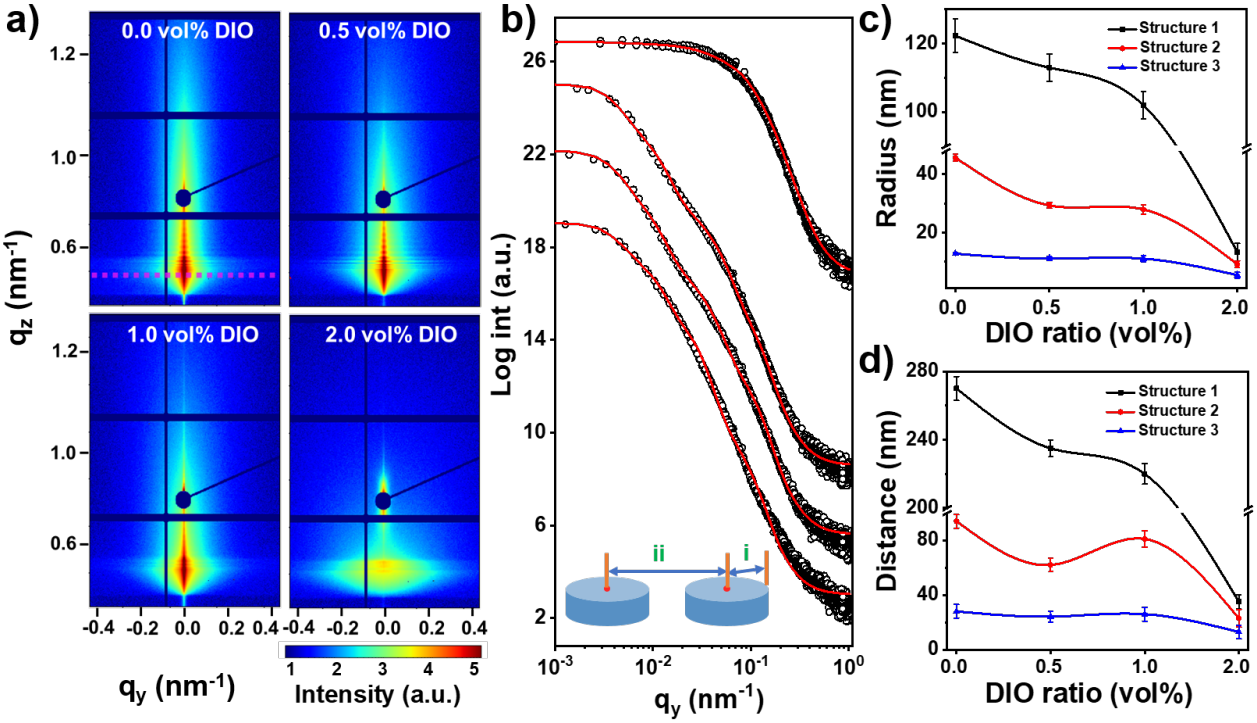

Figure 5.8: a) 2D GISAXS data of the active layers with the addition of different DIO volumes as indicated. The red dotted line represents the Yoneda peak position of PBDB-T-2F. b) Horizontal line cuts of 2D GISAXS data (black circles) for PBDB-T-2F: IT-M thin films prepared with the addition of different DIO volumes (from bottom to top: 0.0, 0.5, 1.0, 2.0 vol%). The red lines represent the model fits. All curves are shifted along the y-axis for clarity of the presentation. Extracted modeling parameters: c) Polymer domain radii and d) domain centre-to-centre distances. Reproduced with permission from the Royal Society of Chemistry, Copyright 2020. [140]

with different DIO volume fractions are displayed in Figure 5.8a. Without DIO, the 2D intensity shows a narrow intensity distribution along the scattering plane, while the intensity becomes broader and extends toward higher q_y values with increasing the DIO concentration. Moreover, fringes in intensity are seen along the q_z direction, which is caused by the X-ray waveguide effect, suggesting a conformal roughness between the substrate and the active layer surfaces. [183] Notably, the ripple structure becomes most pronounced when 0.5 vol% DIO is added, while it smears out gradually as the DIO concentration increases. The critical angle of PBDBT-2F is 0.12°, as determined from the scattering length density (SLD) obtained from the XRR measurements. It is higher than the IT-M critical angle of 0.11° and both can be well separated due to the user settings. For further analysis, horizontal line cuts of the 2D GISAXS data are performed at the Yoneda peak position of PBDB-T-2F to investigate the characteristic PBDB-T-2F structures. To model the lateral polymer structures in the active layer, three cylindrical objects with different radii and inter-distances are used in

the framework of the distorted wave Born approximation assuming the effective interface approximation as discussed in Section 2.3.3. The modelling results are shown in Figure 5.8b (red lines). The corresponding characteristic values of the PBDB-T-2F domain radii and centre-to-centre distances from the modelling are displayed in Figure 5.8c and 5.8d. All PBDB-T-2F domain radii decrease with increasing the concentration of DIO. In more detail, in the film without DIO additive, the average large, medium, and small-sized domain radii are (122 ± 5) nm, (46 ± 2) nm, and (13 ± 1) nm, respectively. Adding 0.5 vol% DIO, they decrease to (113 ± 4) nm, (29 ± 2) nm, and (11 ± 1) nm, for 1.0 vol% DIO to (103 ± 4) nm, (28 ± 2) nm, and (11 ± 1) nm and for 2.0 vol% DIO to (13 ± 3) nm, (9 ± 1) nm, and (5 ± 1) nm. The large-radii domains (structure 1) and medium-radii domains (structure 2) are not relevant for the charge carrier generation as they a significantly larger than typical exciton diffusion lengths. According to previous studies, the small-radii domains (structure 3) on the order of tens of nanometers demonstrate a suitable structure size for the extraction of charge carriers. [172] Therefore, they can be considered as most relevant for the OSCs, except for 2.0 vol% DIO where the large-radii and medium-radii domains take over this role. The PBDB-T-2F domain distances on average also decrease gradually, although not monotonically, with increasing DIO concentration in the active layer. Specifically, in the case of 0.5 vol% DIO, the domain distance of the medium-radii domains (structure 2) is smaller than at 1.0 vol%. It decreases from (94 ± 5) nm (no DIO) to (62 ± 5) nm at 0.5 vol%, then shows a slight increase to (81 ± 6) nm at 1.0 vol% and finally decreases again to (23 ± 7) nm at 2.0 vol%. When the donor and acceptor are well blended, smaller distances between neighboring donor domains appear to be beneficial for the OSCs to facilitate the inner charge carrier transport. Thus, from a morphology perspective, the addition of 0.5 vol% DIO will cause the best-suited inner film morphology on the nanoscale by balancing domain distance and sizes to match exciton diffusion lengths.

5.2.3 Crystallinity

The information about the crystalline phase of the thin films is determined with grazing-incidence wide-angle X-ray scattering (GIWAXS). Reshaped and corrected 2D GIWAXS data are displayed in Figure 5.9. In the out-of-plane (OOP) direction shown in Figure 5.9g, the neat PBDB-T-2F film exhibits (100), (200), and (010) Bragg reflection peaks with positions at 0.29 $Å^{-1}$, 0.61 $Å^{-1}$ and 1.68 $Å^{-1}$, respectively. In the in-plane (IP) direction, the neat PBDB-T-2F film shows a (100) Bragg peak at 0.27 $Å^{-1}$ and a (010) Bragg peak at 1.60 $Å^{-1}$, suggesting both a face-on and an edge-on orientation. The IT-M thin film shows a pronounced (100) Bragg reflection peak at 0.33 $Å^{-1}$ together with a (010) Bragg peak from the π -π stacking at the position of 1.8 $Å^{-1}$ in the OOP direction, corresponding to a face-on orientation with respect to the substrate surface. Both findings agree well with

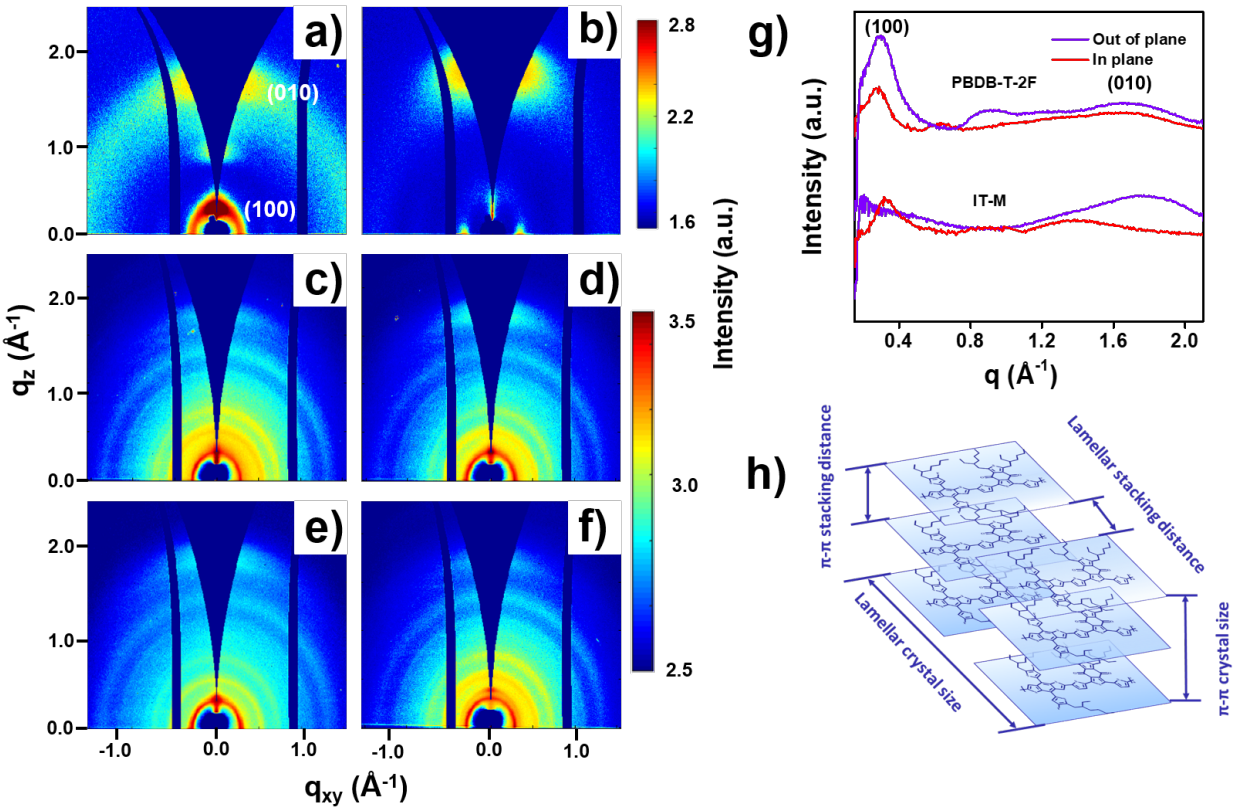

Figure 5.9: 2D GIWAXS data of a) PBDB-T-2F and b) IT-M films and PBDB-T-2F: IT-M active layers with c) 0.0, d) 0.5, e) 1.0 and f) 2.0 vol% DIO addition. g) Cake cuts of 2D GIWAXS data in out-of-plane (purple line) and in-plane (red line) direction of PBDB-T-2F (top) and IT-M (bottom) films. h) Schematic diagram of lamellar and π -π stacking of PBDB-T-2F crystal. The corresponding (100) and (010) peak positions are marked. Reproduced with permission from the Royal Society of Chemistry, Copyright 2020. [140]

earlier literature reports. [134],[170] For the PBDB-T-2F:IT-M active layers both, face-on and edge-on orientations are observed (Figure 5.9c-5.9f).

To give more insights into the effect of DIO on the crystallinity of the individual components from the active layers, Bragg peaks in the cake cuts from the 2D GIWAXS data are analyzed with a Gaussian model (Figure 5.10). The detailed fit parameters are shown in Table 5.5 (PBDB-T-2F) and Table 5.6 (IT-M) and the resulting crystal structure information is comprised in Tables 5.7 and 5.8. In the PBDB-T-2F: IT-M blend without DIO, the face-on and edge-on oriented IT-M crystallites vanished or dramatically decreased in number as seen from the vanishing OOP (010) IT-M Bragg peak and the significantly weaker IP (100) IT-M Bragg peak. Thus, blending IT-M with PBDB-T-2F hinders IT-M crystallization. Moreover, the PBDB-T-2F: IT-M film prepared with 0.5 vol% DIO shows the strongest diffraction intensities

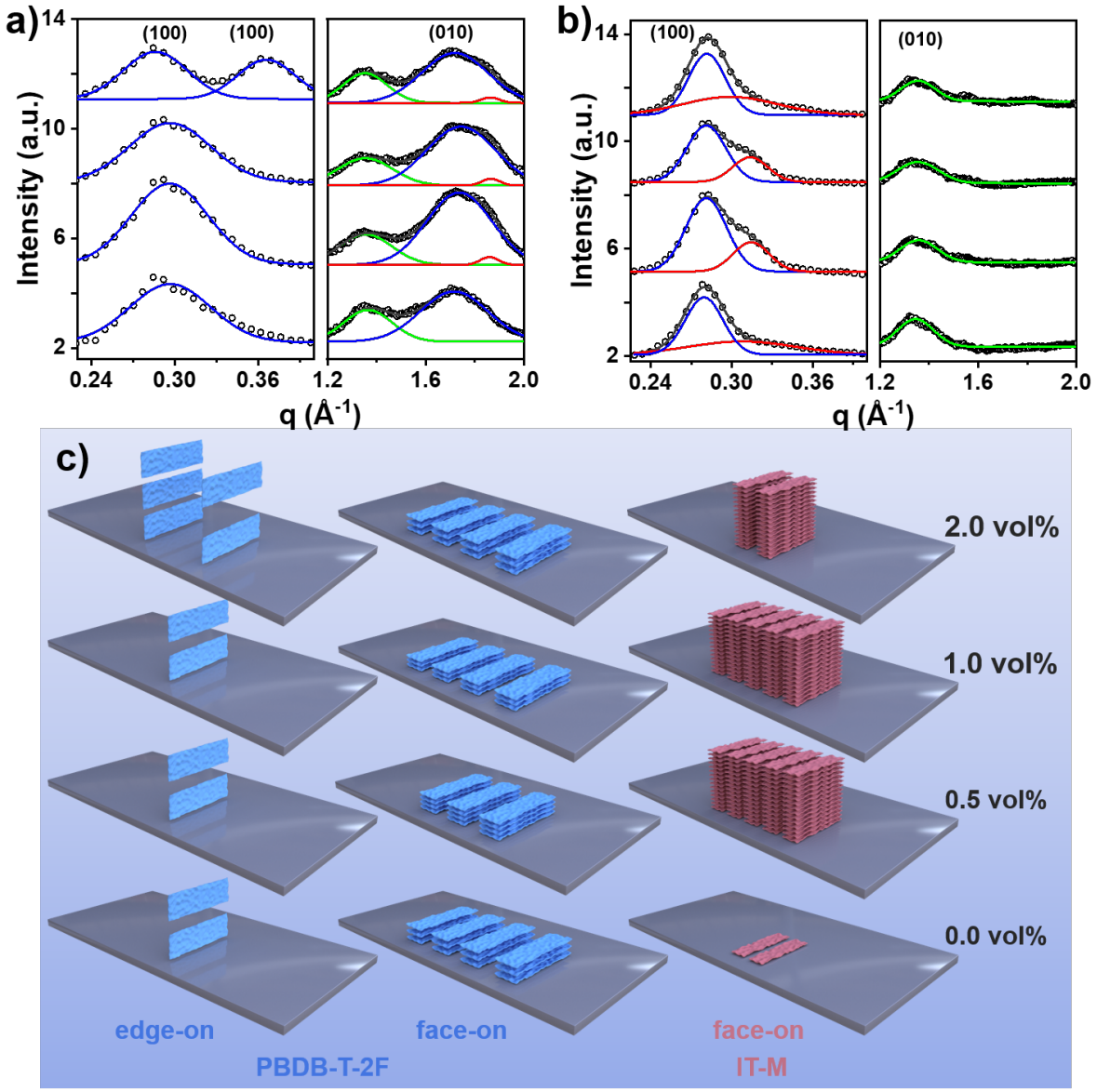

Figure 5.10: Cake cuts of 2D GIWAXS data in a) out-of-plane and b) in-plane direction for PBDB-T-2F: IT-M active layers prepared with the addition of different DIO volumes (from bottom to top: 0.0, 0.5, 1.0, 2.0 vol%). The (100) and (010) peaks are marked. Model fits are shown with solid lines. Blue lines represent oriented PBDB-T-2F crystals, green lines represent isotropous PBDB-T-2F crystals and red lines represent oriented IT-M crystals. All curves shifted along the y-axis for clarity of the presentation. c) Schematic diagram of DIO-induced changes of the crystalline structure in the PBDB-T-2F donor (blue) and IT-M acceptor (red) of PBDB-T-2F: IT-M active layers. Reproduced with permission from the Royal Society of Chemistry, Copyright 2020. [140]

for both PBDB-T-2F and IT-M crystals, indicating a significant increase in the crystallinity of both components at that DIO amount. When 2.0 vol% DIO is added, a second (100) lamellar

Table 5.5: PBDB-T-2F Bragg peaks analysis of the GIWAXS data of blend thin films

DIO (vol%)	IP (100) q (Å^{-1})	FWHM (Å^{-1})	Int.	OOP (100) q (Å^{-1})	FWHM (Å^{-1})	Int.	OOP (010) q (Å^{-1})	FWHM (Å^{-1})	Int.
0.0	0.28 ± 0.01	0.03 ± 0.01	1091	0.30 ± 0.01	0.07 ± 0.01	1165	1.72 ± 0.01	0.32 ± 0.01	158
0.5	0.28 ± 0.01	0.04 ± 0.01	1441	0.30 ± 0.01	0.07 ± 0.01	1496	1.74 ± 0.01	0.31 ± 0.01	213
1.0	0.28 ± 0.01	0.03 ± 0.01	1094	0.30 ± 0.01	0.07 ± 0.01	1104	1.74 ± 0.01	0.33 ± 0.01	166
2.0	0.28 ± 0.01	0.03 ± 0.01	1135	0.29 ± 0.01	0.05 ± 0.01	903	1.72 ± 0.01	0.32 ± 0.01	145
2.0				0.37 ± 0.01	0.05 ± 0.01	757			

Table 5.6: IT-M Bragg peaks analysis of the GIWAXS data of blend thin films

DIO (vol%)	IP (100) q (Å^{-1})	FWHM (Å^{-1})	Int.	OOP (100) q (Å^{-1})	FWHM (Å^{-1})	Int.
0.0	0.31 ± 0.01	0.09 ± 0.01	273	N/A	N/A	N/A
0.5	0.31 ± 0.01	0.03 ± 0.01	614	1.86 ± 0.01	0.09 ± 0.01	25
1.0	0.31 ± 0.01	0.03 ± 0.01	507	1.87 ± 0.01	0.09 ± 0.01	21
2.0	0.30 ± 0.01	0.08 ± 0.01	336	1.86 ± 0.01	0.09 ± 0.01	16

PBDB-T-2F Bragg peak appears in the OOP direction (located at q_z = 0.37 Å^{-1}), which is caused by the change of the crystallization mode of the end-capping group around the polymer. [184] The lamellar as well as the π -π stacking distances (Figure 5.9h) are estimated by calculating

$$d = 2\pi/q \tag{5.1}$$

where q refers to the Bragg peak position. Using the Debye-Scherrer equation the corresponding crystallite sizes are estimated with the assumption of a constant para crystallinity. [185] IT-M chains tend to transform into a pronounced face-on structure when the active layer is processed with DIO.

The lamellar stacking crystal size of IT-M strongly increases from (63 ± 1) Å (0.0 vol%) to (141 ± 1) Å (0.5, 1.0 vol%) and decreases again to (71 ± 1) Å (2.0 vol%). The corresponding lamellar stacking distances remain largely unchanged as (20.3±0.1) Å (0.0, 0.5 and 1.0 vol%) even at 2.0 vol% DIO (20.9 ± 0.1 Å). Moreover, if present, the π -π stacking IT-M crystal size (63 ± 1 Å) and distance (3.4 ± 0.1 Å) do not change. The edge-on crystal structure of PBDBT-2F remains constant with the lamellar stacking distance of (20.9 ± 0.1) Å and crystal size of around (81 ± 1) Å for a DIO amount below 2.0 vol%. At 2.0 vol% in this direction the

Table 5.7: PBDB-T-2F crystals determined with a Gaussian model analysis of the GIWAXS data of blend thin films

DIO (vol%)	IP (100) distance (Å)	Size (Å)	OOP (100) distance (Å)	Size (Å)	OOP (010) distance (Å)	Size (Å)
0.0	22.4 ± 0.1	188 ± 1	20.9 ± 0.1	81 ± 1	3.7 ± 0.1	18 ± 1
0.5	22.4 ± 0.1	141 ± 1	20.9 ± 0.1	81 ± 1	3.6 ± 0.1	18 ± 1
1.0	22.4 ± 0.1	188 ± 1	20.9 ± 0.1	81 ± 1	3.6 ± 0.1	18 ± 1
2.0	22.4 ± 0.1	188 ± 1	21.7 ± 0.1	113 ± 1	3.7 ± 0.1	18 ± 1
2.0			17.0 ± 0.1	113 ± 1		

Table 5.8: IT-M crystals determined with a Gaussian model analysis of the GIWAXS data of blend thin films

DIO (vol%)	IP (100) distance (Å)	Size (Å)	OOP (100) distance (Å)	Size (Å)
0.0	20.3 ± 0.1	63 ± 1	N/A	N/A
0.5	20.3 ± 0.1	141 ± 1	3.4 ± 0.1	63 ± 1
1.0	20.3 ± 0.1	141 ± 1	3.4 ± 0.1	63 ± 1
2.0	20.9 ± 0.1	71 ± 1	3.4 ± 0.1	63 ± 1

crystal size increases to (113 ± 1) Å and two different lamellar stacking distances appear ((21.7 ± 0.1) and (17.0 ± 0.1) Å). The face-on oriented PBDB-T-2F crystals have a size of (188 ± 1) Å in the lamellar stacking direction for all DIO amounts despite of the thin film processed with 0.5 vol% DIO ((141 ± 1) Å). The lamellar stacking distance of face-on PBDB-T-2F crystals remains constant ((22.4 ± 0.1) Å) for all probed DIO amounts. In the π -π stacking direction, the crystal size of face-on PBDB-T-2F crystals remains (18 ± 1) Å and the corresponding π -π stacking stays at (3.6 ± 1) Å (0.5, 1.0 vol%) or (3.7 ± 1) Å (0.0, 2.0 vol%) for all DIO amounts. Notable, in the active layer processed with 0.5 vol% DIO addition, face-on PBDB-T-2F crystals have the smallest lamellar-stacking crystal size, the smallest π -π stacking distance and largest π -π stacking crystal size. In particular, the compact distance and large crystal size in the π -π stacking crystals are beneficial for the charger carrier transport properties of the donor in the active layer. [185] Figure 5.10c summarizes all findings about the changes of the crystalline parts in the active layers upon DIO addition.

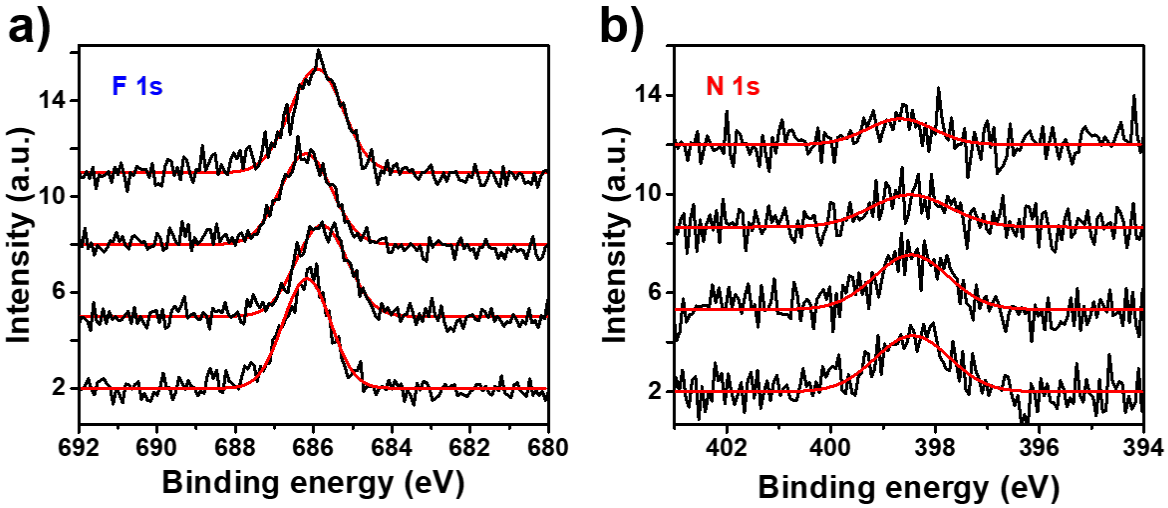

Figure 5.11: XPS spectra (black curves) and the corresponding Gaussian fits (red curves) for c) F 1s and d) N 1s signals. The amount of DIO increases from the bottom to the top, and the curves are vertically stacked for clarity of the presentation. Reproduced with permission from the Royal Society of Chemistry, Copyright 2020. [140]

5.3 Vertical Distribution of the Donor and Acceptor in the Active Layer

5.3.1 Surface Composition

To analyze the surface composition of the active layers, XPS measurements are performed,(Figure 5.11). From the chemical structure, fluorine (F) atoms are only present in the polymer donor PBDB-T-2F and absent in the small molecule donor IT-M. Nitrogen atoms (N) are only present in IT-M and absent in PBDB-T-2F. Thus, the influence of the DIO additive on the thin film surface composition can be estimated from the F/N ratio using the peak areas for the F 1s and N 1s core levels. The XPS core-level spectra are fitted with Gaussian functions and the corresponding parameters are summarized in Table 5.9. While the IT-M molecule contains 4 N atoms, PBDB-T-2F is a polymer with a degree of polymerization n, having 2n F atoms in one PDBD-T-2F polymer. However, n is not known in this work, challenging a quantitative analysis to determine the precise chemical composition at the top surface. We have, nonetheless, normalized the F/N ratio in the XPS to 1.0 for the reference sample without DIO addition, and thus the changes of the determined F/N ratios for different DIO additions can confirm whether the ratio of PBDB-T-2F/IT-M proportion increases or decreases on the surface with respect to the reference. In the PBDB-T-2F: IT-M films, the normalized F/N ratio increases from 1.0 (0.0 and 0.5 vol% DIO) to 1.3 (1.0 vol% DIO) and

Table 5.9: Gaussian fit parameters of the XPS data of the blend thin films

DIO (vol%)	F 1s peak position (eV)	N 1s peak position (eV)	Normalized F/N Ratio*
0.0	686.2 ± 0.1	N/A	1.0
0.5	685.8 ± 0.1	1.86 ± 0.01	1.0 ± 0.1
1.0	686.2 ± 0.1	1.87 ± 0.01	1.3 ± 0.2
2.0	685.9 ± 0.1	1.86 ± 0.01	2.6 ± 0.5

*The F/N ratios are normalized to the value for the sample with 0.0 vol% DIO addition. Individual F/N ratios were determined by using the peak area of the F 1s and N 1s core-level normalized to the specific photoionization cross section at the employed photon energy of 1253.6 eV.

2.6 (2.0 vol% DIO), which shows that with increasing DIO more PBDB-T-2F is located at the surface. A higher donor enrichment at the air surface is not suitable for exciton generation and dissociation. [186] Interestingly, adding 0.5 vol% DIO to the active layer causes a shift of the F 1s core level to lower binding energy (685.8 eV) by 0.4 eV, suggesting a higher electron density around F atoms. This in turn could lead to an increase in the hole collection ability in PBDB-T-2F, and vice versa. [187] However, upon adding DIO to 1.0 vol%, the F 1s signal shifts back upwards to the original binding energy position (686.2 eV), suggesting that the improved hole collection ability decreases again. At 2.0 vol% DIO, the F 1s position shifts again to lower binding energy, which can be tentatively attributed to the end-capping group structure of PBDB-T-2F as found with GIWAXS. Moreover, the shifts of the F 1s signal match the intensity of PBDB-T-2F diffraction peaks in the GIWAXS measurements. In other words, the downward shifts coincide with a higher crystallinity of PBDB-T-2F, while the upward shifts coincide with a lower crystallinity of PBDB-T-2F. Moreover, the shifts of the F 1s signal match the intensity of PBDB-T-2F diffraction peaks in the GIWAXS measurement. In contrast to the F 1s signal, the peak position of the N 1s signal exhibits a shift to higher binding energy only at the largest DIO addition, possibly suggesting an increase in the electron collection ability of the IT-M.

5.3.2 Vertical Distribution

With X-ray reflectivity (XRR) the distribution of the donor and acceptor components is studied along the surface normal of the thin films. It is determined from the scattering length density (SLD) profiles. [188] The XRR data are shown together with the corresponding fits based on the Parrat algorithm in Figure 5.12. For the sample with 0.5 vol% DIO addition, the intensity modulations are most pronounced, indicating the lowest roughness among all samples. [189] As determined from the fits, the roughness within the error bars remains unchanged upon moderate DIO addition (2.0 ± 0.3) nm at 0.0 vol%, (1.9 ± 0.2) nm at 0.5 vol% and (2.1 ± 0.2) at 1.0 vol% but increases to (5.3 ± 0.5) nm at 2.0 vol% DIO. These values

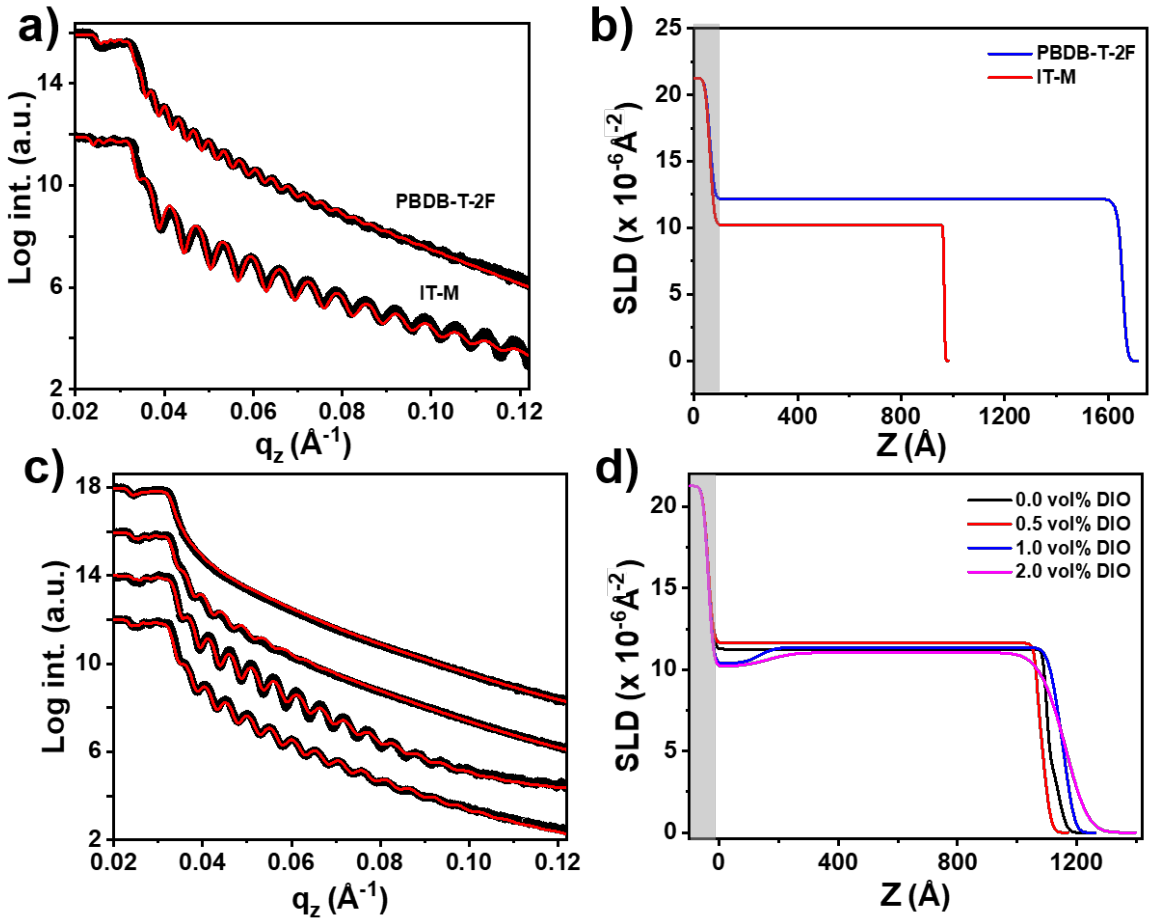

Figure 5.12: XRR data (black symbols) and corresponding fits (red lines) of neat films (a) and active layers with DIO addition(c) (amount increases from bottom to the top). The curves are shifted along the y-axis for clarity of the presentation. The corresponding SLD profiles normal to the surface (z-axis) of neat films (b) and the active layers (d). The position Z = 0 Å indicates the top surface of the silicon oxide (SiO_2) layer (gray). Reproduced with permission from the Royal Society of Chemistry, Copyright 2020. [140]

are in good agreement with the AFM data. The active layer thicknesses are (116 ± 1) nm, (113 ± 1) nm, (120 ± 2) nm, and (137 ± 4) nm, respectively. Figure 4b shows the determined SLD profiles. The SLD values of pure PBDB-T-2F and IT-M are determined with XRR to be (10.20 ± 0.02 ×10^{-6}) $Å^{-2}$ and (12.16 ± 0.02 ×10^{-6}) $Å^{-2}$ (Figure S4), respectively. The SLD differences in the vertical distribution of donor and acceptor material from the bottom to the surface of the blend thin film (Figure 4b), further point to the DIO influences on the drying-mediated molecular self-assembly during the solvent evaporation, too. For the active layers we observe a rather similar average SLD of the blend thin films with a value of (11.26 ± 0.02 ×10^{-6}) $Å^{-2}$ (0.0 vol%), (11.63 ± 0.02×10^{-6})$Å^{-2}$ (0.5 vol%), (11.36 ± 0.02 ×10^{-6}) $Å^{-2}$ (1.0 vol%) and (11.04 ± 0.03×10^{-6}) $Å^{-2}$ (2.0 vol%), respectively. For 1.0 and 2.0 vol% DIO, at

the substrate-active layer interface, an enrichment of IT-M is concluded from the reduced SLD value. Such enrichment can originate from the interaction with the substrate as well as from different solubilities during film preparation. DIO volatilizes much slower than CB, because of the different boiling points between the DIO additive and the CB solvent.

5.4 Conclusion

In summary, the influence of the DIO ratio on the nanoscale morphology, surface enrichment, crystallinity, crystalline orientation, absorbance, exciton dissociation, charge transfer as well as exciton dynamics of PBDB-T-2F: IT-M active layers is studied to provide insights into the related device performance of wide-bandgap non-fullerene OSCs. The best-performing devices are achieved with 0.5 vol% DIO addition due to having the best-suited nanoscale morphology. By adding more DIO, the Jsc and also PCE of the devices decrease. At 0.5 vol% DIO addition, the active layers exhibit the highest absorption over the entire wavelength range, a strongly quenched PL intensity, and the lowest TRPL decay lifetime, which contribute to an enhanced charge carrier separation and transport in combination with more balanced hole and electron mobilities. The improved charge carrier management originates from a compact thin film with improved miscibility, higher crystallinity and an optimized crystal structure of PBDB-T-2F and IT-M, balanced PBDB-T-2F domain distances and sizes on the nanoscale, matching exciton diffusion lengths. At higher amounts of DIO, the decrease in the PBDB-T-2F domain size and inter-domain distance, and the enrichment of PBDB-T-2F at the surface and IT-M at the bottom presumably originate from a lowered miscibility between PBDB-T-2F and IT-M. As a consequence of the less optimized nanoscale film morphology, longer TRPL decay lifetimes and a decreased charge transport cause a reduced device performance. Notably, increasing the DIO amount results in an increased Voc loss, due to the intramolecular charge transfer (ICT) effects of the acceptors.

6 Active Layer Processing via Scaling-Up Fabrication Method

The following chapter is mainly based on the publication "Revealing Donor-Acceptor Interaction on the Printed Active Layer Morphology and the Formation Kinetics for Nonfullerene Organic Solar Cells at Ambient Conditions" *(Xinyu et al., Advanced Energy Materials, 2022, DOI:10.1002/aenm.202103977)* . [104] Reproduced with permission from Wiley, Copyright 2022.

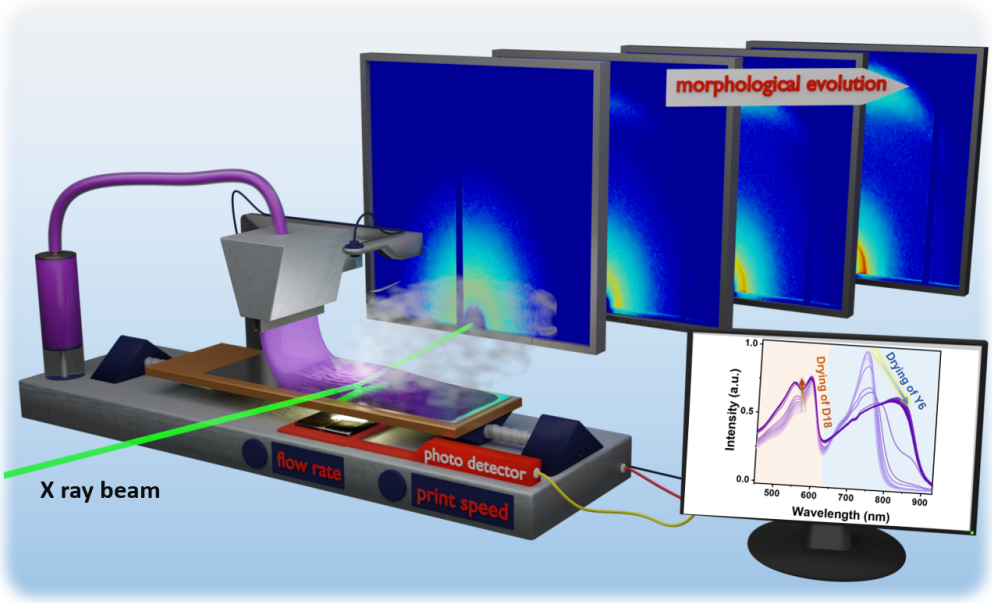

In the previous chapter, a systemical study about the effect of different amounts of solvent additive on the morphology, crystallinity, charge carrier dynamics, as well as the vertical distribution of donor and acceptor of the active layer was demonstrated. An optimized active layer was obtained with 0.5 vol% DIO addition, which has realized high-efficiency OSCs over 10 % PCE. However, these high-performance OSCs are commonly fabricated on a small scale in laboratories by using the spin-coating method under inert conditions, which is not suitable for large-scale production. [190] Therefore, developing a large-area coating technology, which also works at ambient conditions, is crucial for manufacturing energy-efficient, high-throughput, low-cost and low carbon-footprint OSCs. [191] With the merits

of low solution consumption, high film homogeneity and good device performance, the slot-die coating technique is advantageous in sheet-to-sheet and roll-to-roll (R2R) solution printing. Thus, slot-die coating is considered to be a promising tool to print large-scale OSCs. [84],[44],[192] However, high-efficiency OSCs fabricated by slot-die coating are still not as efficient as those produced by spin-coating due to the absence of a deep understanding of the donor/acceptor formation kinetics during the print process. [193],[194] Today, there are reports about using a slot-die coating to print OSCs, which achieve OSCs with efficiencies over 14 % by using auxiliary equipment such as temperature control and/or atmosphere control assistance. [195],[196],[197] However, this additional equipment has the disadvantage of being difficult to handle and expensive concerning commercialization. Based on the above considerations, understanding the relationship between active layer morphology, device efficiency and detailed knowledge about the film formation kinetics is crucial for printed BHJ active layers and to guide future photovoltaic performance enhancement. Unfortunately, knowledge gained from the analysis of spin-coating cannot be easily transferred to printing. Besides the different flow fields, the solvent is kept longer in the polymer film during the film formation procedure for the slot-die-coated films without external assistance. [83],[198],[199] In the literature, it is stated that the host solvent plays a dominant role in the morphology formation of the active layer, which influenced the performance of the final devices. [200],[201],[202] Zhao et al. reported that the effects of halogenated or hydrocarbon solvents on the PDBD-T-2F: BTP-4F active layer-based BHJ OSC are different. A higher degree of crystallinity with a more minor phase separation structure was observed in ortho-xylene processed thin films, yielding the promising champion efficiency of 15.6 %. [201] Moreover, in situ studies helped to understand the morphology evolution of the active layer processed with different solvents during the film formation process. [83] However, only a few studies focused on the individual morphology, optical behavior, and film formation kinetics of the donor and acceptor in printed active layers. Understanding the behavior of the pure donor and acceptor components is essential to comprehend how the donor and acceptor affect the film formation process of the active layer. In addition, the understanding of the relatively novel wide-bandgap polymer PDTBT2T-FTBDT is still minimal, since there are only a few reports on this novel material today. [130],[203] Deep insights into the mechanism of the film formation kinetics of the polymer PDTBT2T-FTBDT and of PDTBT2T-FTBDT blended with small acceptor molecules will be provided to improve the mechanism from highly efficient spin-coated lab-scale devices to a large scale slot-die coating manufacturing. In this chapter, slot-die-coated BHJ OSCs with an active layer formed by the wide-bandgap donor polymer (PDTBT2T-FTBDT) and a non-fullerene acceptor (BTP-4F) in ambient conditions will be analysed. The host solvents chloroform (CF) and chlorobenzene (CB) are selected to tune the morphology of the neat PDTBT2T-FTBDT and BTP-4F films and the

Table 6.1: Optical properties of PDTBT2T-FTBDT (D), BTP-4F (A) and PDTBT2T-FTBDT:BTP-4F (D:A) thin films printed out of CB and CF

Sample	Abs_{max} (nm)	Em_{max} (nm)	Stokes Shift (nm)
D in CB	586	798	212
D in CF	590	825	235
A in CB	859		
A in CF	835		
D: A in CB	590	814	224
D: A in CF	587		

PDTBT2T-FTBDT: BTP-4F blend films. Slot-die coated OSC prepared at ambient conditions with CF as solvent displaying a PCE of 13.2 %, which is the highest efficiency reported for printed OSCs under ambient conditions until it was fabricated. To further understand the underlying mechanisms and the influence of the used solvent, the effect of the specific solvent on the donor and the acceptor performance was studied. The complex relationships between the conformation, charge carrier physics, solvent effects and the morphology of the printed thin films of PDTBT2T-FTBDT, BTP-4F and PDTBT2T-FTBDT: BTP-4F blends are investigated with ultraviolet-visible spectroscopy (UV-vis), photoluminescence (PL), time-resolved photoluminescence (TRPL), atomic force microscopy (AFM), grazing-incidence small-angle X-ray scattering (GISAXS) and grazing-incidence wide-angle X-ray scattering (GIWAXS). In situ UV-vis measurements are performed to further understand the conformational changes of the active layer with different solvents at ambient conditions during the print process. In situ GIWAXS measurements reveal information about the influence of the solvents on the donor and acceptor crystal structure and their crystal orientation formation in the active layer. Thereby, this work gives insights into the relationship between the donor-acceptor morphology evolution and optical device properties being influenced by the solvent. Its understanding sets a perspective for large-scale fabrication of OSC via printing under ambient conditions.

6.1 Optical, Electronic Properties and Device Performance

6.1.1 Absorption and Photoluminescence

The effect of different host solvents on the optical properties is investigated by UV-vis spectroscopy and PL measurements. The corresponding optical parameters are shown in Table 6.1. Normalized UV-vis absorption spectra of printed neat PDTBT2T-FTBDT and BTP-4F thin films fabricated out of CB and CF are shown in Figure 6.1a. Most D-A-based polymers such as PDTBT2T-FTBDT or PDBD-T-2F form J-type aggregates and therefore

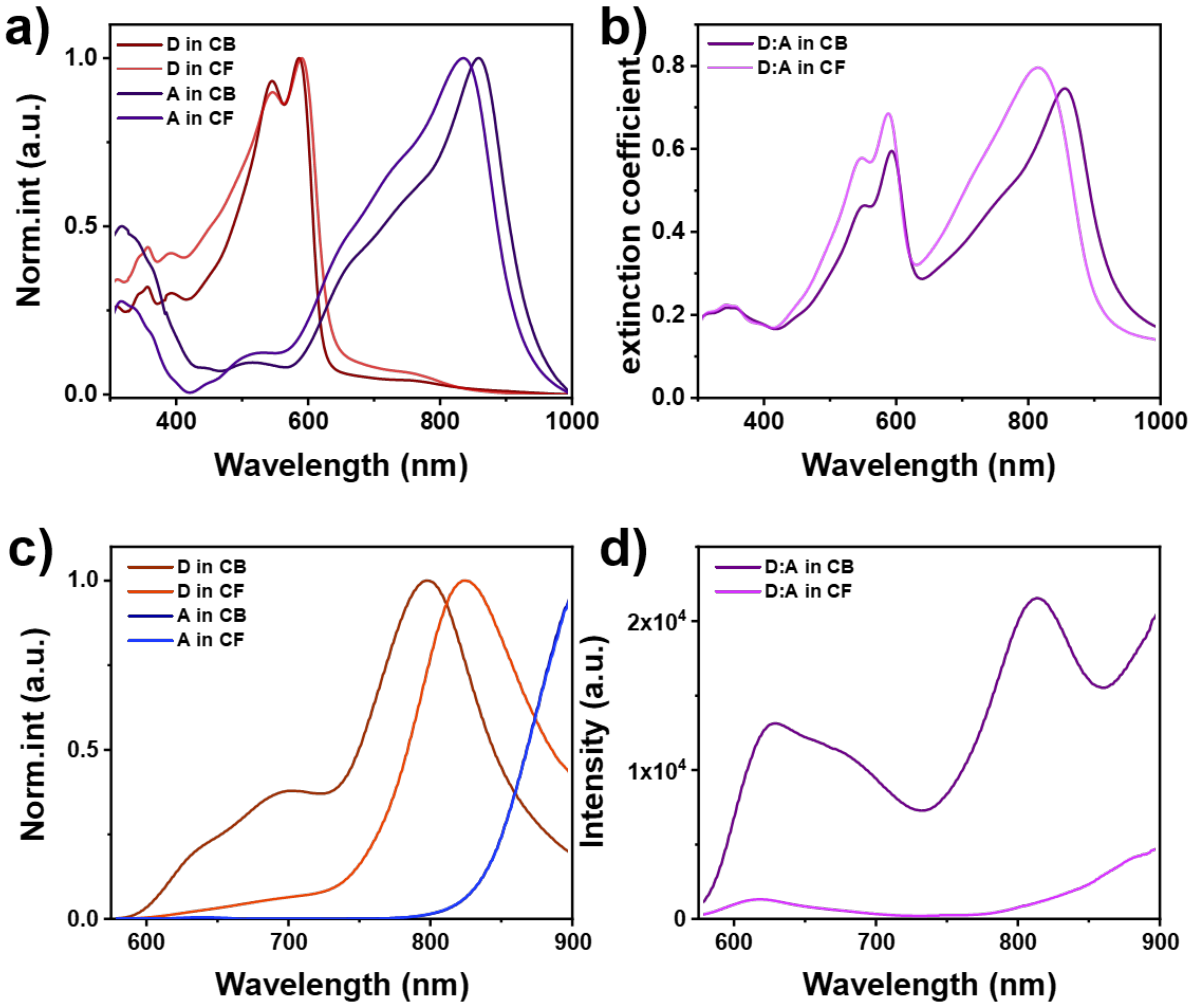

Figure 6.1: a) Normalized absorption spectra of PDTBT2T-FTBDT and BTP-4F thin films processed with different solvents. b) Extinction coefficients (ϵ_{ex}) of PDTBT2T-FTBDT:BTP-4F blend films printed with different solvents calculated from UV-vis spectra. c) Normalized PL spectra of PDTBT2T-FTBDT and BTP-4F thin films processed with different solvents. d) PL data of PDTBT2T-FTBDT:BTP-4F blend films printed with different solvents. Reproduced with permission from Wiley, Copyright 2022. [104]

exhibit an intense 0-0 vibronic (λ_{0-0}) absorption band at a higher wavelength with a less intense vibronic progression (λ_{0-1}) at a lower wavelength. [204] In Figure 6.1a, the maximum absorption peak (λ_{0-0}) of PDTBT2T-FTBDT is located at 586 nm with a shoulder-type absorption peak (λ_{0-1}) at 545 nm, if processed with CB solvent, while the λ_{0-0} peak redshifts to 590 nm and the λ_{0-1} peak redshifts to 546 nm, if processed with CF solvent. The slight redshifts for the PDTBT2T-FTBDT films printed from CF solvent are assumed to be a head-to-tail aggregation preference in comparison with the CB solvent. [205] Unlike the neat PDTBT2T-FTBDT thin film, the CB-processed BTP-4F blend film exhibits an absorption peak

at 859 nm, which blue shifts to 835 nm in case of printing out of CF solvent. This behavior results from a pronounced H aggregate tendency with a side-by-side arrangement in the CF-processed neat BTP-4F film. [206] The extinction coefficients of the blend films are shown in Figure 6.1b. The calculation details are explained in Section 3.1.1. The CF processed PDTBT2T-FTBDT: BTP-4F blend film exhibits a higher extinction coefficient in the whole spectral range, where PDTBT2T-FTBDT shows a λ_{0-0} peak at 587 nm, a λ_{0-1} peak at 546 nm and BTP-4F one at 809 nm. In contrast, CB-processed PDTBT2T-FTBDT: BTP-4F blend films show a lower extinction coefficient. The PDTBT2T-FTBDT λ_{0-0} peak redshifts to 591 nm with a shoulder appearing at 549 nm and the BTP-4F peak redshifts to 858 nm, suggesting preferable J aggregates in mixtures processed with CB. This aggregation behavior is different from the neat PDTBT2T-FTBDT film. The differences demonstrate that the aggregation type in the printed blend film can be tuned by introducing the non-fullerene acceptor BTP-4F. In the PL data seen in Figure 6.1c, the main emission peak of PDTBT2T-FTBDT is located at 798 nm if printed out of CB. It is significantly redshifted to 825 nm when printed out of CF. The λ_{1-0} emission peak of PDTBT2T-FTBDT is located at 700 nm, if processed with CB, and is significantly suppressed when printed with CF. No noticeable peak shifts in the BTP-4F films are determined from the PL spectra. In the blend films (Figure 6.1d), the CB processed film shows two prominent PL emission peaks located at 629 nm and 813 nm attributed to PDTBT2T-FTBDT, which suggests that the exciton transport is inhibited from PDTBT2T-FTBDT to BTP-4F. In contrast, the overall PL emission intensity decreases in the CF-printed PDTBT2T-FTBDT: BTP-4F blend films, which reveals that the charge carrier transfer and exciton dissociation are enhanced between PDTBT2T-FTBDT and BTP-4F. The Stokes shift can be calculated from the difference between the maximum absorption and emission, which provides information about a molecule's reorganization energy between the ground and excited state. [207] In the printed neat donor films using CF, the Stokes shift values are larger than for the CB printed films (212 nm with CB, 235 nm with CF), indicating that the non-radiative transition of CF printed films consumes more energy than for the CB printed films. [208] Moreover, the Stokes shift of the donor in the blend film is higher than that of the neat film printed with CB solvent. Probably, the donor exhibits higher non-radiative energy losses when mixed with BTP-4F.

6.1.2 Charge Carrier Dynamics

To evaluate the charge transfer process of neat PDTBT2T-FTBDT, BTP-4F as well as of PDTBT2T-FTBDT: BTP-4F blend introduced via different solvents during the printing, TRPL measurements of the printed films on glass substrates are performed with an excitation wavelength of 405 nm. The TRPL data of printed neat PDTBT2T-FTBDT and BTP-4F thin films and their blend thin films fabricated out of CB and CF are shown in Figure 6.2a

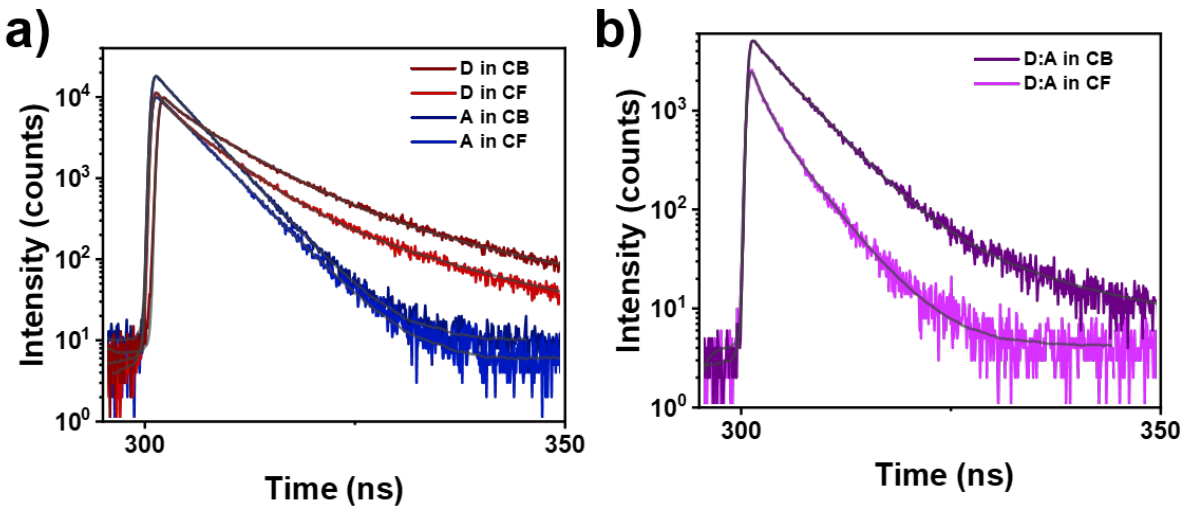

Figure 6.2: TRPL data of a) PDTBT2T-FTBDT and BTP-4F thin films and b) PDTBT2T-FTBDT:BTP-4F blend films printed with different solvents. Reproduced with permission from Wiley, Copyright 2022. [104]

Table 6.2: Charge carrier dynamics of PDTBT2T-FTBDT (D), BTP-4F (A) and PDTBT2T-FTBDT:BTP-4F (D:A) thin films printed out of CB and CF

Sample	A_1	τ_1 (ns)	A_2	τ_2 (ns)	τ_{aver} (ns)	A_1/A_2
D in CB	19.2 ± 0.9	0.21 ± 0.04	2.7 ± 0.2	1.29 ± 0.04	7.52 ± 0.04	7.1
D in CF	28 ± 4	0.14 ± 0.03	2.66 ± 0.4	0.95 ± 0.07	6.29 ± 0.15	10.5
A in CB	20.30 ± 0.08	0.10 ± 0.02	9.7 ± 1.3	0.33 ± 0.02	5.23 ± 0.03	1.9
A in CF	41.9 ± 2.1	0.08 ± 0.02	18.6 ± 1.3	0.29 ± 0.02	8.75 ± 0.07	2.3
D: A in CB	12 ± 1.4	0.15 ± 0.05	1.70 ± 0.67	0.66 ± 0.14	2.92 ± 0.17	7.1
D: A in CF	8.53 ± 0.74	0.08 ± 0.02	0.40 ± 0.17	0.42 ± 0.08	0.85 ± 0.03	21.3

and 6.2b, respectively. They are analyzed with an exponential decay function, where the component of the short lifetime (A_1,τ_1) corresponds to the fast decay processes, and the long lifetime (A_2, τ_2) corresponds to the slow decay processes, which are related to trap-assisted recombination and radiative recombination, respectively. [140] The detailed parameters of TRPL data analysis are summarized in Table 6.2. The ratio of A_1/A_2 is calculated to determine the dominant decay process. The value is larger than one for all thin films, which suggests that fast decay is the main decay process. Notably, for the CF-printed films, the ratio is larger than for the CB-printed thin films, suggesting that the trap-assisted recombination enhanced the use of CF as a solvent for the printing. The average lifetimes of neat PDTBT2T-FTBDT, BTP-4F and PDTBT2T-FTBDT: BTP-4F blend are (7.52 ± 0.04), (5.23 ± 0.03) and (2.93 ± 0.16) ns if printed out of CB, and (6.29 ± 0.15), (8.75 ± 0.07) and (0.85 ± 0.03) ns when processed with CF solvent. For the neat films, the CB-printed PDTBT2T-FTBDT film and the CF-printed BTP-4F film show a longer lifetime, suggesting reduced

recombination in bulk. Interestingly, CF-printed PDTBT2T-FTBDT: BTP-4F blend films show a much shorter lifetime, meaning that the radiative recombination is restrained. Thus, a fast charge transport can be induced from PDTBT2T-FTBDT to BTP-4F when printing from CF, which will increase the short circuit current of the corresponding OSCs.

6.1.3 Device Performance

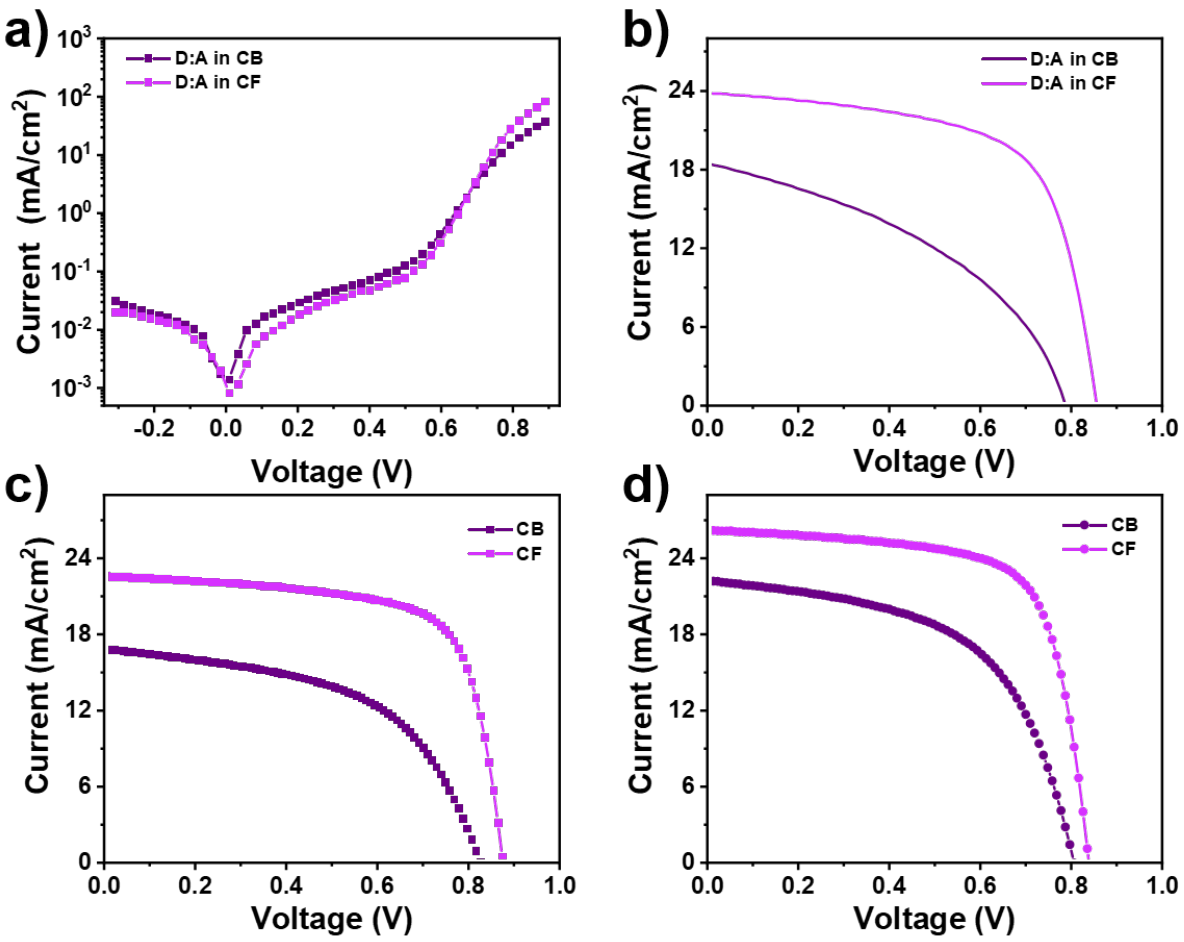

Figure 6.3: a) Dark and b) light J-V curves of PDTBT2T-FTBDT:BTP-4F based OSCs printed under ambient condtions ; light J-V curves of PDTBT2T-FTBDT:BTP-4F based OSCs c) printed in N_2 atmosphere and d) spin-coated in the N_2 glovebox with CF and CB solvent, respectively. Reproduced with permission from Wiley, Copyright 2022. [104]

The photovoltaic performance of the OSCs is systematically studied with an inverted device architecture (functional stack is glass/ITO/ZnO/printed PDTBT2T-FTBDT: BTP-4F/MoO_3/Ag). The J-V curves of the OSCs printed with different solvents under ambient conditions measured in the dark are shown in Figure 6.3a. Compared with CB-printed devices, OSCs printed with CF in ambient conditions show a lower current density in the

Table 6.3: Photovoltaic parameters of PDTBT2T-FTBDT:BTP-4F blend devices with different fabrication procedures under different atmosphere

Sample	Jsc (mA cm^{-2})	Voc (V)	FF (%)	PCE_{avg} (%) *	PCE_{max} (%)
CB_in ambient	18.5 ± 0.45	0.79 ± 0.02	41.39	6.0 ± 0.6	6.6
CB_in N_2	16.8 ± 0.42	0.82 ± 0.02	50.25	6.9 ± 0.6	7.4
CB_spin coat	21.8± 0.38	0.80 ± 0.02	55.49	9.4± 0.5	9.9
CF_in ambient	23.5 ± 0.32	0.85 ± 0.02	64.49	12.8 ± 0.4	13.2
CF_in N_2	22.3 ± 0.30	0.86 ± 0.02	68.21	13.5 ± 0.4	13.9
CF_spin coat	25.9 ± 0.30	0.84 ± 0.02	69.87	15.1 ± 0.3	15.4

* Average values are obtained from 10 devices.

voltage range from -0.2 V to 0.7 V, which suggests a significantly reduced leakage and recombination current. Moreover, a steeper rise of the curve observed in the higher voltage range reveals that the series resistance is higher compared with devices printed with CB under ambient conditions. As shown in Figure 6.3b and Table 6.3, the printed active layer using CB solvent shows a relatively low performance with an average efficiency of 6.0 % and a Voc of 0.79 V, a Jsc of 18.5 mA cm^{-2}, and a FF of 41.39 %. When using CF, the average efficiency increases to 12.8 % with a Voc of 0.85 V, a Jsc of 23.5 mA cm^{-2}, and an FF of 64.49 %. Notably, the active layer printed with CF solvent exhibits a promising champion PCE of 13.2 % with a Jsc of 23.84 mA cm^{-2}, a FF of 64.49 %, and a Voc of 0.85 V. Thus, all characteristic solar cell parameters Jsc, Voc and FF are improved by the choice of the solvent, which all together contribute to the significantly improved PCE. To investigate the influence of the atmosphere, solar cells are fabricated under N_2 atmosphere as well, as shown in Table 6.3 and Figure 6.3c-6.3d. The PCEs of the OSCs are slightly improved for both solvents CB and CF in N_2 atmosphere, which is attributed to the better Voc and FF. Moreover, the printed OSCs are additionally compared with OSCs using an active layer prepared with classical spin-coating in N_2 atmosphere (Figure 2d). The highest PCE of 15.4 % is achieved in the spin-coated OSCs when using CF, whereas using CB also for spin-coated OSCs results in a lower PCE of 9.9 %. Therefore, irrespective of the fabrication method used to deposit the active layer, CB is a poor solvent for the novel PDTBT2T-FTBDT: BTP-4F blend films based on OSCs.

6.2 Film Morphology

6.2.1 Surface Morphology

The surface topography of printed films is investigated by AFM and shown in Figure 6.4. The root-mean-square (RMS) roughness of the neat PDTBT2T-FTBDT film is smaller if

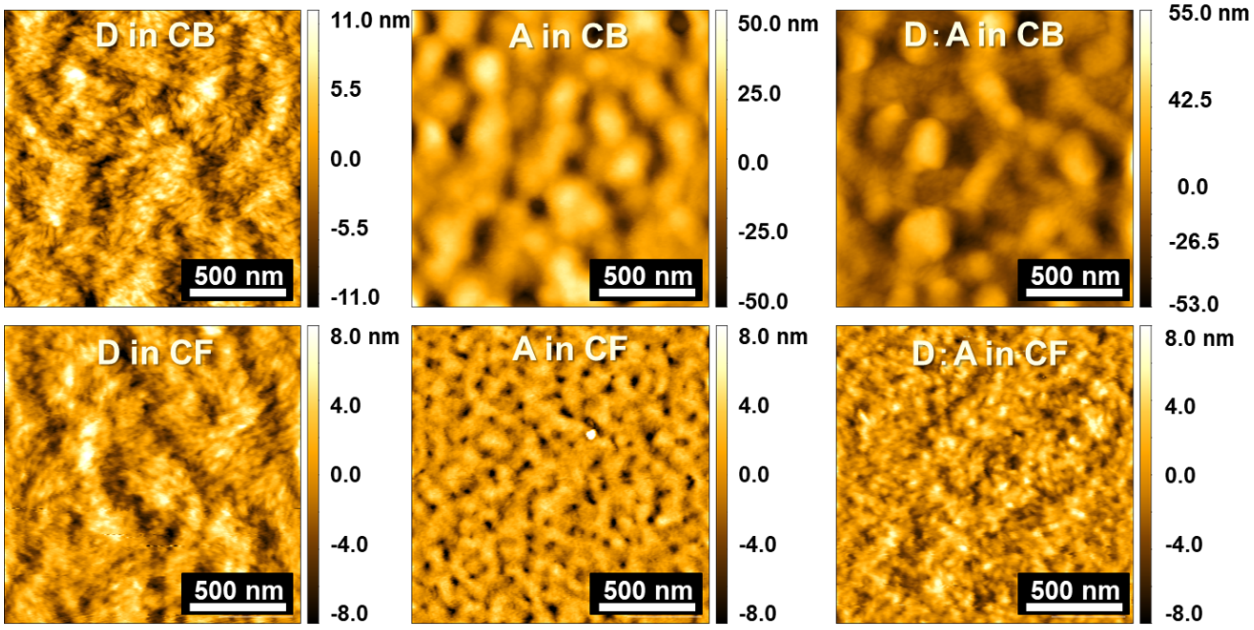

Figure 6.4: AFM surface topography of printed PDTBT2T-FTBDT, BTP-4F, PDTBT2T-FTBDT: BTP-4F blend films using CB (top row) and CF (bottom row), respectively. Reproduced with permission from Wiley, Copyright 2022. [104]

printed out of CF (1.9 nm) than out of CB (2.9 nm). The same behavior is found for the neat BTP-4F film. However, the substantial aggregation of BTP-4F in CB results in a very high roughness of 11.9 nm compared with CF (1.6 nm). Accordingly, also the roughness of the PDTBT2T-FTBDT: BTP-4F blend film is 1.6 nm if printed from CF but 13.2 nm if printed from CB. This significant difference in the surface roughness explains that the surface of the active layer printed out of CF exhibits better contact with the blocking layer and electrode, as well as better miscibility between PDTBT2T-FTBDT and BTP-4F, being beneficial for charge collection in OSCs. Thus, also the smoother film surface contributes to the superior PCE when printed out of CF.

6.2.2 Inner Morphology

Besides the analysis of the surface film morphology, the inner structure of the neat PDTBT2T-FTBDT, BTP-4F and PDTBT2T-FTBDT: BTP-4F blend films printed out of different solvents is investigated with GISAXS. The 2D GISAXS data are displayed in Figure 6.5. Horizontal line cuts of the 2D GISAXS data are performed at the Yoneda region of PDTBT2T-FTBDT and BTP-4F to investigate characteristic lateral structures shown in Figure 6.6. In neat films, the structure can be understood as crystallite domains in an amorphous polymer or small molecules matrix, giving rise to a scattering contrast. In the blend films, it is characteristic

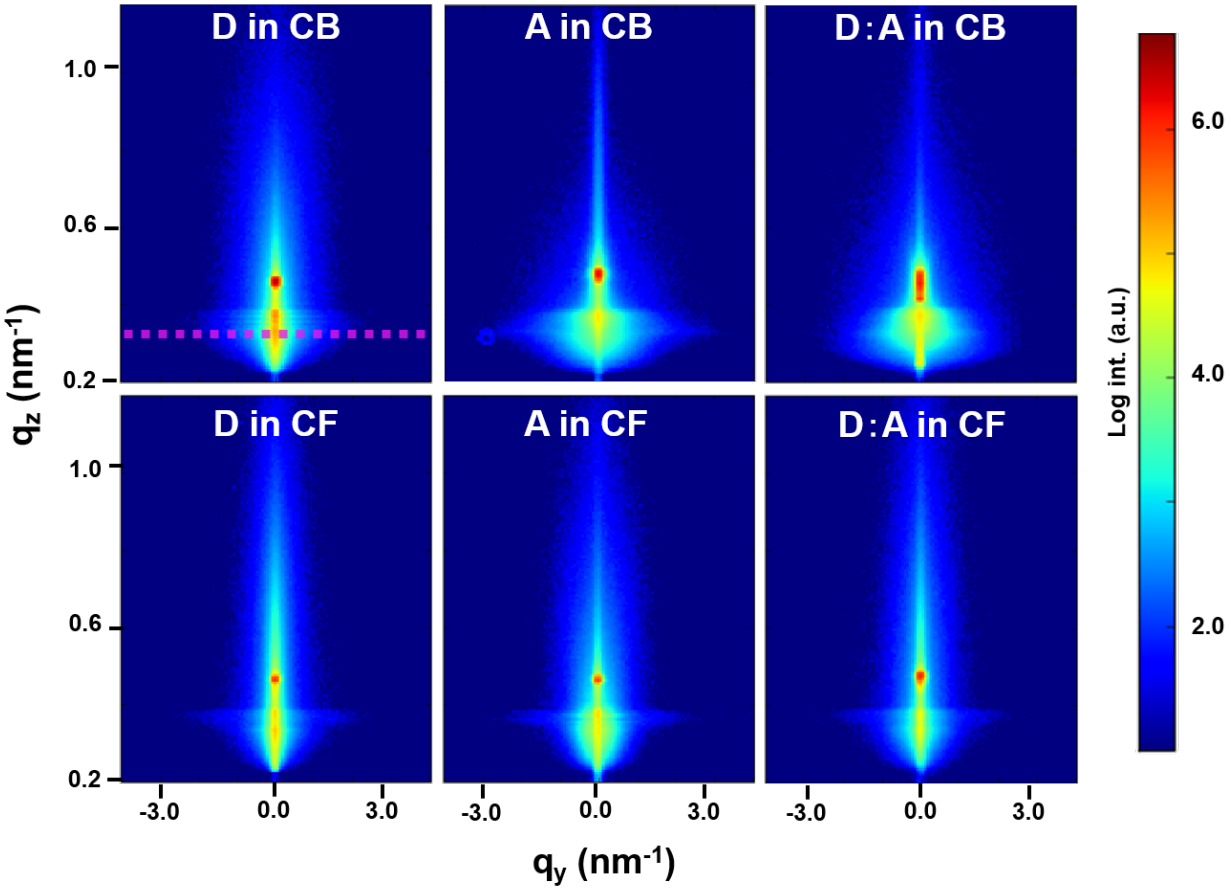

Figure 6.5: 2D GISAXS data of neat PDTBT2T-FTBDT (D), BTP-4F (A) and PDTBT2T-FTBDT: BTP-4F (D: A) blend films printed with CB or CF. Reproduced with permission from Wiley, Copyright 2022. [104]

polymer domains in the small molecule matrix. To model the lateral structures, cylindrical and spherical objects with different radii are used in the framework of the distorted wave Born approximation (DWBA) assuming the effective interface approximation (EIA). [178] The DWBA and EIA-based modeling results are shown in Figure 6.6b. The average large-size domain radii of neat PDTBT2T-FTBDT, BTP-4F and PDTBT2T-FTBDT: BTP-4F blend films are (100 ± 5) nm, (77 ± 6) nm and (90 ± 9) nm when using CB, while they are (108 ± 5) nm, (118 ± 5) nm and (109± 4) nm in case of CF. Typically, such large-scale structures are identified as defects in the films. The middle-size domain radii of neat PDTBT2T-FTBDT, BTP-4F and PDTBT2T-FTBDT: BTP-4F blend films are (40 ± 3) nm, (23 ± 1) nm, (26 ± 1) nm when using CB, and they are (27 ± 4) nm, (42 ± 1) nm, (23 ± 2) nm in case of CB. The average small-size domain radii of neat PDTBT2T-FTBDT, BTP-4F and PDTBT2T-FTBDT: BTP-4F blend films are (13 ± 2) nm, (10 ± 1) nm, (15 ± 1) nm when using CB solvent. They decrease to (10 ± 2) nm, (9 ± 1) nm, and (5 ± 1) nm in the case of CF. As shown in Figure 2b, the average large-size domain radius of the PDTBT2T-FTBDT: BTP-4F blend film printed from

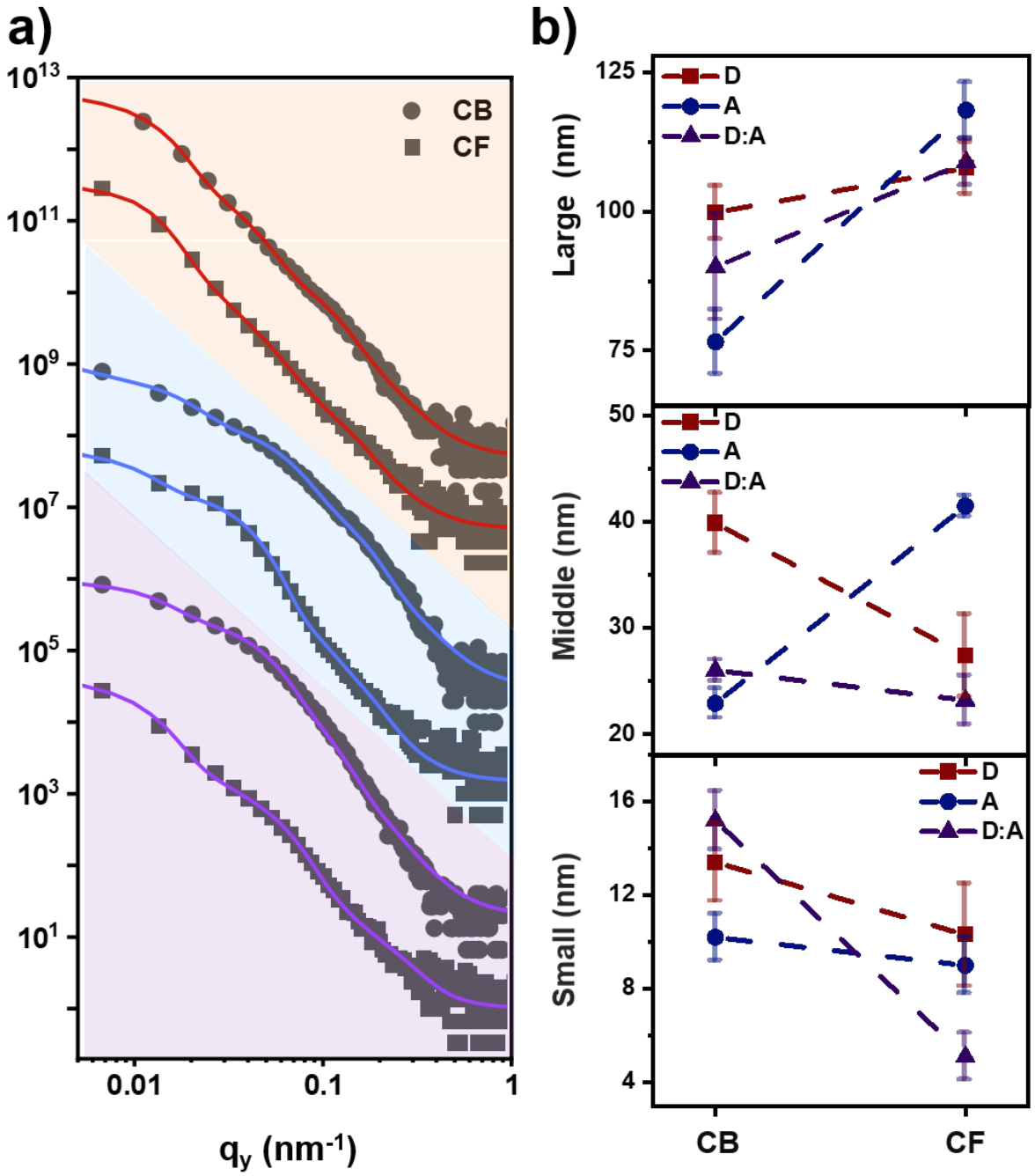

Figure 6.6: a) Horizontal line cuts of the 2D GISAXS data (symbols) with corresponding fits (solid lines) of the PDTBT2T-FTBDT (red line), BTP-4F (blue line), PDTBT2T-FTBDT: BTP-4F blend (purple line) films printed out of CB (circles) and CF (squares), respectively. b) Comparison of the average domain radii for the large, medium and small structures. Reproduced with permission from Wiley, Copyright 2022. [104]

Table 6.4: Bragg peaks analysis of GIWAXS data of PDTBT2T-FTBDT (D), BTP-4F (A) and PDTBT2T-FTBDT: BTP-4F (D: A) thin films printed out of CB and CF

Sample	IP (100) q ($Å^{-1}$)	FWHM ($Å^{-1}$)	Int.	OOP (010) q ($Å^{-1}$)	FWHM ($Å^{-1}$)	Int.
D in CB	0.29 ± 0.01	0.07 ± 0.01	54.4	1.69 ± 0.01	0.34 ± 0.01	180.8
D in CF	0.30 ± 0.01	0.07 ± 0.01	47.1	1.68 ± 0.01	0.32 ± 0.01	175.0
A in CB	0.24 ± 0.01	0.08 ± 0.01	4.8	1.71 ± 0.01	0.53 ± 0.01	20.8
D: A in CB	0.28 ± 0.01	0.07 ± 0.01	14.9	1.65 ± 0.01	0.24 ± 0.01	43.5
D: **A** in CB	0.20 ± 0.01	0.08 ± 0.01	2.6	1.71 ± 0.01	0.64 ± 0.01	16.7
D: A in CF	0.29 ± 0.01	0.08 ± 0.01	26.4	1.66 ± 0.01	0.54 ± 0.01	63.9
D: **A** in CF	0.21 ± 0.01	0.08 ± 0.01	5.5	1.71 ± 0.01	0.24 ± 0.01	107

CB is the smallest among all neat and blend films, suggesting that the blend structure is influenced by both the donor and the acceptor. When using CF instead of CB, the large-size domain radius of the PDTBT2T-FTBDT, BTP-4F and PDTBT2T-FTBDT: BTP-4F blend film increases. Thus, the large size domains in PDTBT2T-FTBDT: BTP-4F blend films follow the same size as in the neat PDTBT2T-FTBDT films. Consequently, the large structures in the BHJ structure of the blend film are influenced more by the PDTBT2T-FTBDT component than by the BTP-4F component. In contrast, Figure 6.5b shows that the middle-size domain radii of the PDTBT2T-FTBDT: BTP-4F blend film decrease when using CF instead of CB, and follow the trend in the neat PDTBT2T-FTBDT film. For the small-size domain of all the films, the radii decrease in CF. According to previous studies, [140] domains on the order of tens of nanometers demonstrate a suitable structure size for splitting excitons into charge carriers. Therefore, the blend film printed out of CF shows a better film morphology in terms of characteristic lateral structures as compared with the one printed with CB. Such improved morphology is beneficial for the device performance and explains why the OSCs printed from CF outperform the ones printed with CB.

6.2.3 Crystalline Structure

To measure the crystalline structure in the thin films printed with different solvents, GIWAXS is performed. Figure 6.7a-6.7b shows the 2D GIWAXS data, line profiles and the corresponding Gaussian fits of the neat PDTBT2T-FTBDT, BTP-4F and PDTBT2T-FTBDT: BTP-4F blend films printed out of CB and CF, respectively. The determined parameters and the calculated stacking distance as well as the crystallite size are listed in Table 6.4 and 6.5. For the wide-bandgap donor polymer PDTBT2T-FTBDT, a (100) Bragg peak is visible at 0.29 $Å^{-1}$, corresponding to a d-spacing of 21.7 Å. The respective (200) Bragg peak at 0.54 $Å^{-1}$ in the in-plane (IP) direction is also observed for both solvents CB and CF. The (010) Bragg peak in out-of-plane (OOP) direction is seen at 1.69 $Å^{-1}$, corresponding to a

Table 6.5: Crystallite parameters determined with Gaussian model analysis of the GIWAXS data of PDTBT2T-FTBDT (D), BTP-4F (A) and PDTBT2T-FTBDT: BTP-4F (D: A) thin films printed out of CB and CF

Sample	IP (100) Distance (Å)	Size (nm)	OOP (010) Distance (Å)	Size (nm)
D in CB	21.7 ± 0.1	8.1 ± 0.1	3.7 ± 0.1	1.7 ± 0.1
D in CF	20.9 ± 0.1	8.1 ± 0.1	3.7 ± 0.1	1.8 ± 0.1
A in CB	26.2 ± 0.1	7.1 ± 0.1	3.7 ± 0.1	1.1 ± 0.1
A in CF	25.1 ± 0.1	5.1 ± 0.1	3.7 ± 0.1	1.6 ± 0.1
D: A in CB	22.4 ± 0.1	8.1 ± 0.1	3.8 ± 0.1	2.4 ± 0.1
D: **A** in CB	31.4 ± 0.1	7.1 ± 0.1	3.7 ± 0.1	0.9 ± 0.1
D: A in CF	21.7 ± 0.1	7.1 ± 0.1	3.8 ± 0.1	1.1 ± 0.1
D: **A** in CF	29.9 ± 0.1	7.1 ± 0.1	3.7 ± 0.1	2.4 ± 0.1

Table 6.6: Calculated area distribution of (100) crystallite orientation from GIWAXS data of PDTBT2T-FTBDT (D), BTP-4F (A) and PDTBT2T-FTBDT: BTP-4F (D: A) thin films printed out of CB and CF

Sample	Edge on Area	Face on Area	Isotropic Area
D in CB	250	9257	1306
D in CF	573	8082	7616
A in CB	49	83	2908
A in CF	24	1472	1328
D: A in CB	90	1549	2089
D: **A** in CB	160	577	3233
D: A in CF	61	4067	1666
D: **A** in CF	48	3494	2434

Table 6.7: Calculated percentage distribution of (100) crystallite orientation from GIWAXS data of PDTBT2T-FTBDT (D), BTP-4F (A) and PDTBT2T-FTBDT: BTP-4F (D: A) thin films printed out of CB and CF

Sample	Edge on (%)	Face on (%)	Isotropic (%)
D in CB	2	86	12
D in CF	4	50	46
A in CB	2	3	95
A in CF	1	52	47
D: A in CB	2	42	56
D: **A** in CB	4	15	81
D: A in CF	2	70	28
D: **A** in CF	1	59	40

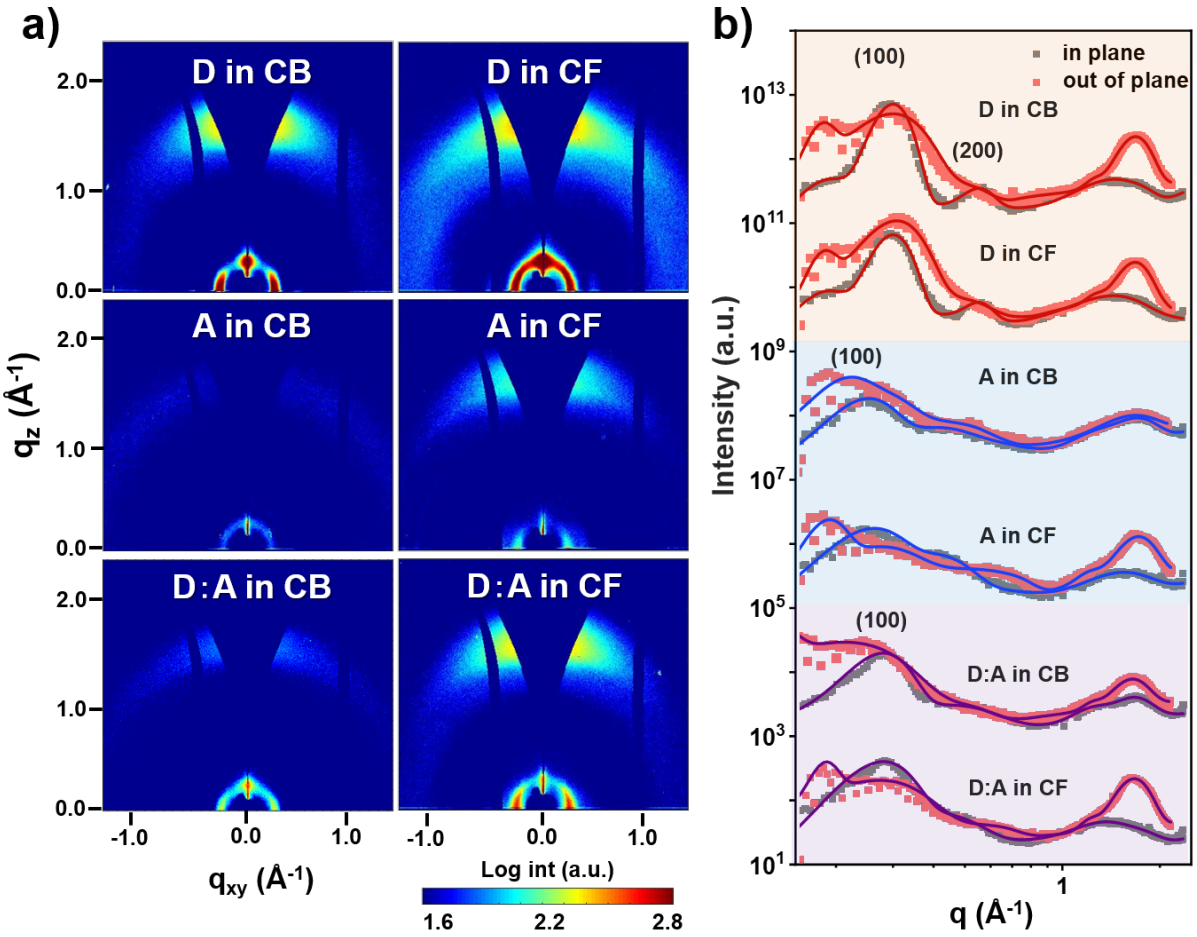

Figure 6.7: a) 2D GIWAXS data for PDTBT2T-FTBDT, BTP-4F and PDTBT2T-FTBDT:BTP-4F films printed out of CB and CF. Scattering profiles obtained from b) cake cuts in (100) peak of pure PDTBT2T-FTBDT (D), BTP-4F (A) and PDTBT2T-FTBDT: BTP-4F (D: A) films printed out of CB and CF, respectively. Reproduced with permission from Wiley, Copyright 2022. [104]

d-spacing of 3.72 Å for CB, while it is located at 1.68 Å^{-1} (d-spacing of 3.74 Å) for CF. For the BTP-4F film printed out of CB, the (010) Bragg peak is located at 1.71 Å^{-1}, corresponding to a d-spacing of 3.67 Å. This Bragg peak is very weak and broadly distributed over the azimuthal angular range, suggesting a low and random distribution of the crystallites with this orientation. In contrast, the BTP-4F film printed out of CF shows a pronounced crystal structure with a face-on orientation. A (100) Bragg peak at 0.25 Å^{-1} (d-spacing of 25.1 Å) and an (11-1) Bragg peak at 0.43 Å^{-1} (d-spacing of 14.6 Å) in the in-plane (IP) direction, as well as a (010) Bragg peak at 1.72 Å^{-1} (d-spacing of 3.65 Å) in the out-of-plane (OOP) direction, emerge. The different crystallization behavior of the neat thin films manifests to a distinct effect in their blended thin films when printed with different solvents. In the case of

printing the blend film with CB, the (100) Bragg peak of PDTBT2T-FTBDT is detected at 0.28 $Å^{-1}$ (d-spacing of 22.4 Å) and the (100) Bragg peak of BTP-4F is located at 0.20 $Å^{-1}$ (d-spacing of 31.4 Å) in the IP direction. The weak (010) Bragg peak of PDTBT2T-FTBDT is at 1.65 $Å^{-1}$ (d-spacing of 3.81 Å) and of BTP-4F at 1.71 $Å^{-1}$ (d-spacing of 3.67 Å) in the OOP direction. Thus, fewer crystallites are present inside the CB printed film, which is attributed to a hindering of the PDTBT2T-FTBDT crystallization by the crystallization of BTP-4F. On the contrary, the CF printed blend film shows a pronounced (100) Bragg peak of PDTBT2T-FTBDT at 0.29 $Å^{-1}$ (d-spacing of 21.7 Å) in the IP direction together with a (010) Bragg peak at 1.66 $Å^{-1}$ (d-spacing of 3.79 Å) in the out-of-plane (OOP) direction. Moreover, BTP-4F exhibits a (100) Bragg peak at 0.21 $Å^{-1}$ (d-spacing of 29.9 Å) concerning the (010) peak of 1.71 $Å^{-1}$ (d-spacing of 3.67 Å). Consequently, when printing out of CF, a better face-on structure of crystallites is formed in the active layer than in the case of CB.

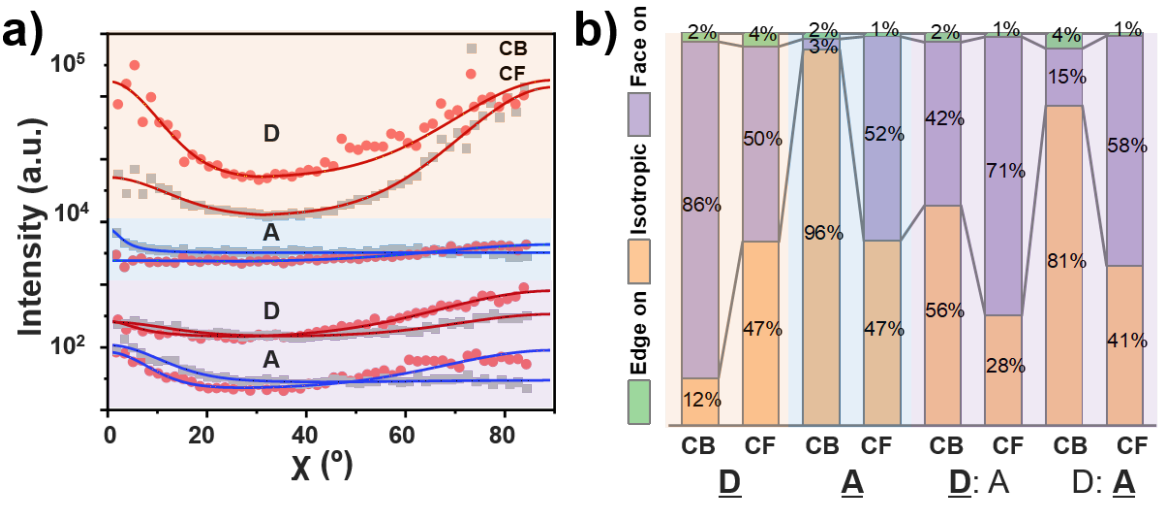

Figure 6.8: a) Scattering profiles obtained from tube cuts in (100) peak of pure PDTBT2T-FTBDT (D), BTP-4F (A) and PDTBT2T-FTBDT: BTP-4F (D: A) films printed out of CB and CF, respectively. Solid lines correspond to the fit of the data. d) Fractions of face-on, edge-on and isotropically oriented crystallites based on the (100) Bragg peak. Reproduced with permission from Wiley, Copyright 2022. [104]

To get an insight into the orientation distribution of the crystalline packing, tube cuts are performed in the 2D GIWAXS data (Figure 6.8a) for the (100) Bragg peaks of PDTBT2T-FTBDT and BTP-4F. The scattering intensity is fitted by three regions, face-on, edge-on and isotropic. The fraction of the face-on, edge-on and isotropically oriented crystallites are shown in Figure 6.8b, calculated by integrating the areas of the corresponding features in the pole figures (corrected $I(\chi) \times \sin(\chi)$ versus χ plots in Figure 6.9-6.10, Table 6.6-6.7). [106],[105] For all films, the edge-on orientation occurs only in a minimal fraction. For the face-on

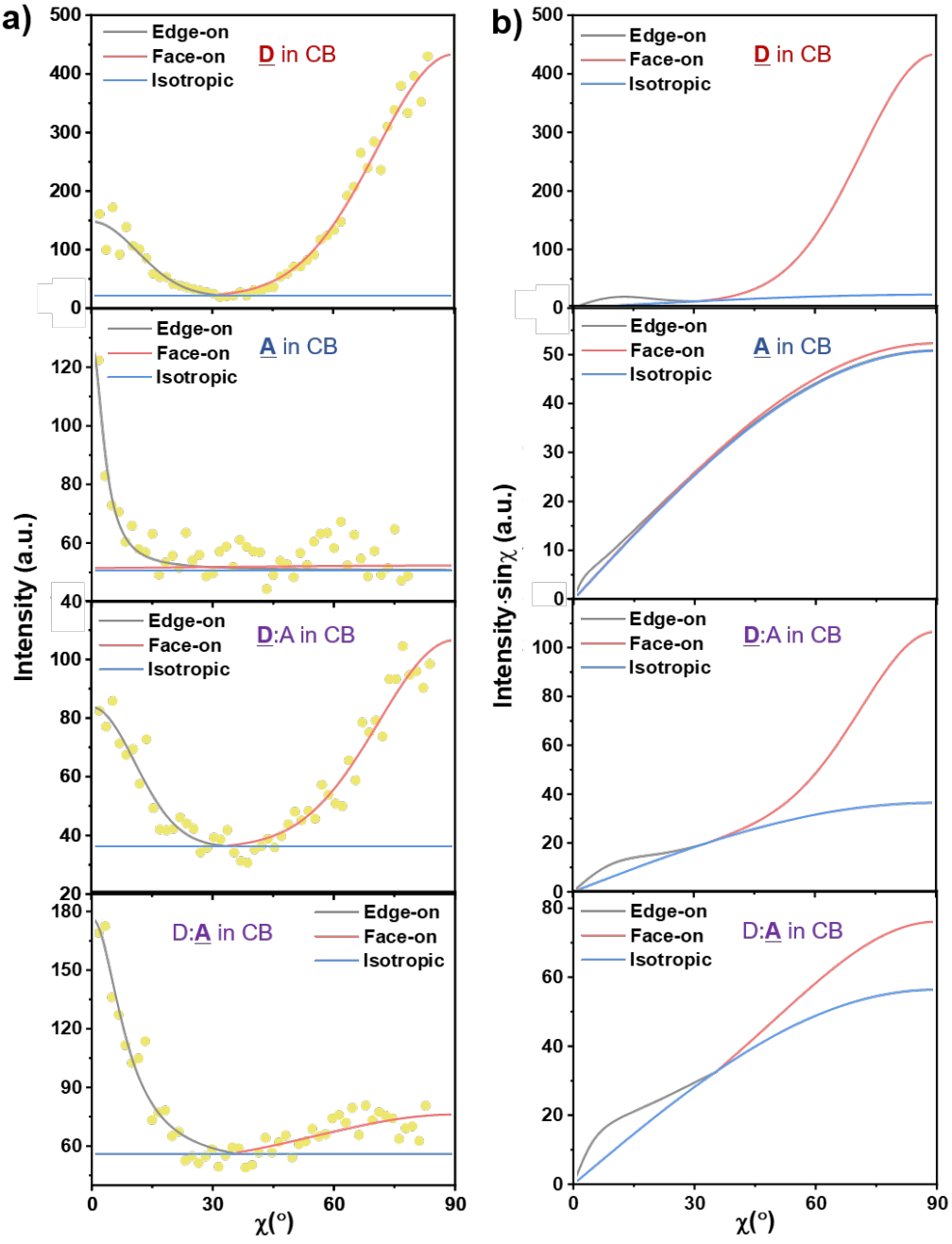

Figure 6.9: a) Fit details of tube cuts of the (100) peak of neat PDTBT2T-FTBDT (D), BTP-4F (A) and PDTBT2T-FTBDT: BTP-4F (D: A) blend films printed out of CB. The data is shown with yellow dots. b) Corresponding calculated crystallite orientation areas after the Lorentz correction. Reproduced with permission from Wiley, Copyright 2022. [104]

orientation, the occurrence depends strongly on the system. Among the thin films printed out of CB, the face-on orientation accounts for 86 % of the total crystallites for the neat PDTBT2T-FTBDT thin film, whereas it is only 3 % in the neat BTP-4F thin film. For the

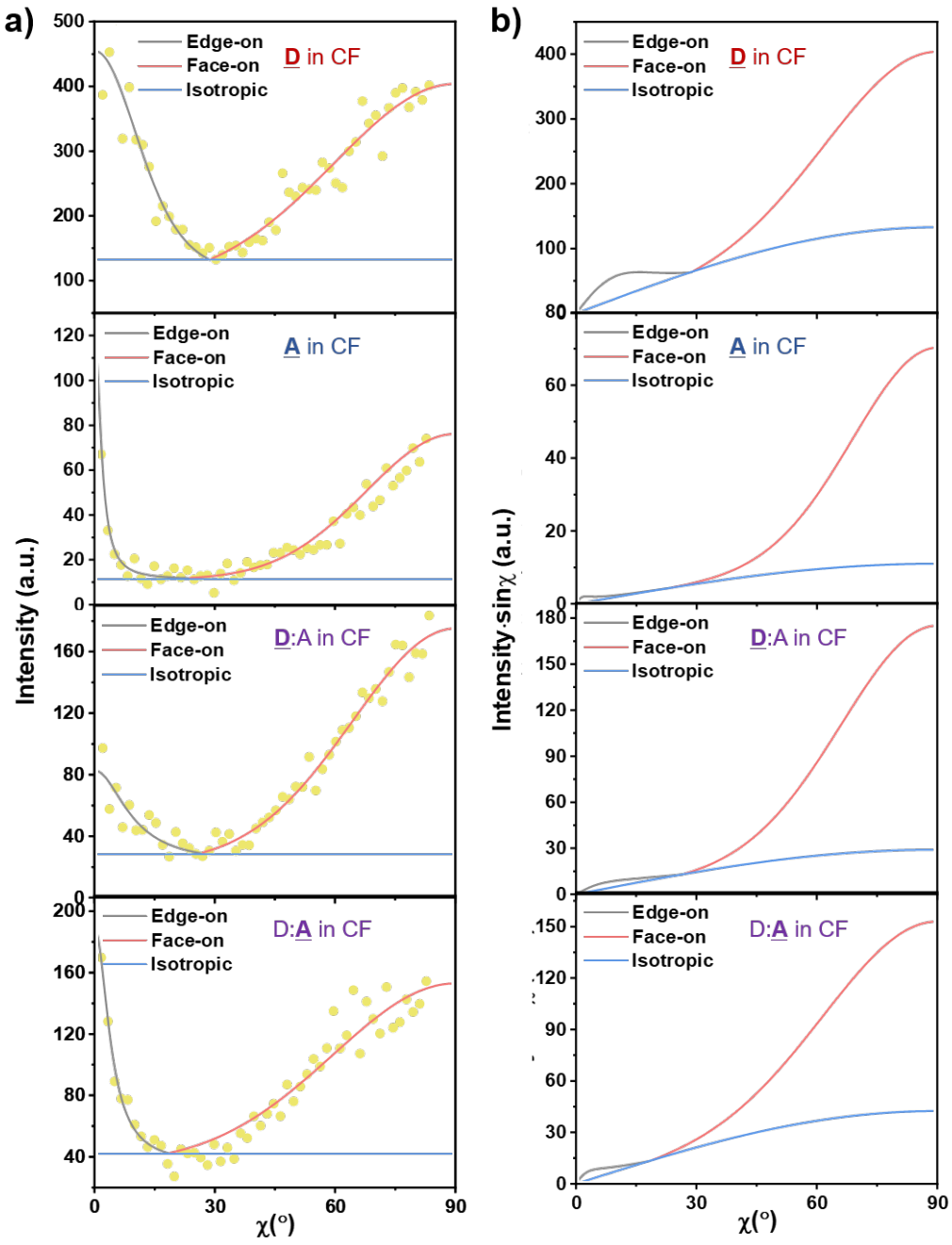

Figure 6.10: a) Fit details of tube cuts of the (100) peak of neat PDTBT2T-FTBDT (D), BTP-4F (A) and PDTBT2T-FTBDT: BTP-4F (D: A) blend films printed out of CF. The data is shown with yellow dots. b) Corresponding calculated crystallite orientation areas after the Lorentz correction. Reproduced with permission from Wiley, Copyright 2022. [104]

PDTBT2T-FTBDT:BTP-4F blend film, the face-on orientation in PDTBT2T-FTBDT decreases to 42 %, and increases to 15 % in BTP-4F. For the thin films printed with CF, the face-on orientation for the neat PDTBT2T-FTBDT is 50 % and 52 % for the neat BTP-4F thin film. In

the blend thin film printed out of CF, the face-on orientation of PDTBT2T-FTBDT increases to 71 %, and the face-on orientation of BTP-4F increases to 58 %. Thus, the CB-printed neat PDTBT2T-FTBDT film exhibits a well-ordered face-on crystal structure with a smaller π -π stacking distance compared to the CF-printed neat PDTBT2T-FTBDT film. However, in the blend film with BTP-4F, the face-on crystallization of PDTBT2T-FTBDT is hindered when using CB. Notably, when the thin films are printed out of CF, the crystal quality in the blend thin film is better than in the neat films, suggesting that the donor and acceptor are facilitating their face-on orientation. Thus, the allover crystallization in the PDTBT2T-FTBDT: BTP-4F blend film is better organized when printing with CF than with CB as the solvent. The superior crystal structure established when printing out CF for both, the donor and acceptor, facilitates the charge carrier transport in the blend thin film. Thus high electron mobility and current density can be obtained. [209]

6.3 Active Layer Formation Kinetics

6.3.1 Aggregation and Conformation Kinetics

To provide a deeper insight into the conformation and aggregation kinetics of the wide-bandgap polymer donor PDTBT2T-FTBDT, the non-fullerene acceptor BTP-4F and the blend of both (PDTBT2T-FTBDT: BTP-4F), in situ UV-vis measurements are performed during the printing out of CB and CF (Figure 6.11), respectively. Since the donor and acceptor have different solubilities in the solvents CF and CB, a different initial aggregation state of the materials can be present in the initial inks. Moreover, due to the different boiling points of the solvent CB (132 ºC) and CF (61.2 ºC) as well as the big difference in the molecular weights between PDTBT2T-FTBDT and BTP-4F, the molecular assembly of donor and acceptor molecules varies with different solvents as established during the drying process. Compared to CF, films printed from CB undergo a slower film formation, resulting in an increased time for the interaction between donor and donor, acceptor and acceptor, and donor and acceptor (Figure 6.11a). To understand the role of solvent effects on the molecule structure, conformation and aggregation development of the donor and acceptor during the film formation process, the temporal evolution of the PDTBT2T-FTBDT absorption peaks λ_{0-0} and λ_{0-1} as well as of the BTP-4F peaks are determined (Figure 6.11b). Due to instrument limitations, we can only observe the film formation kinetics after 4 s. Similar to the earlier work on another active layer blend film studied in situ during printing, here also five stages are distinguished during the thin film formation. In stage I, solvent evaporation is dominant with no obvious changes in the peak position and intensity, suggesting that no molecule aggregation occurs during this period. [210] Notably, stage I is only very prominent

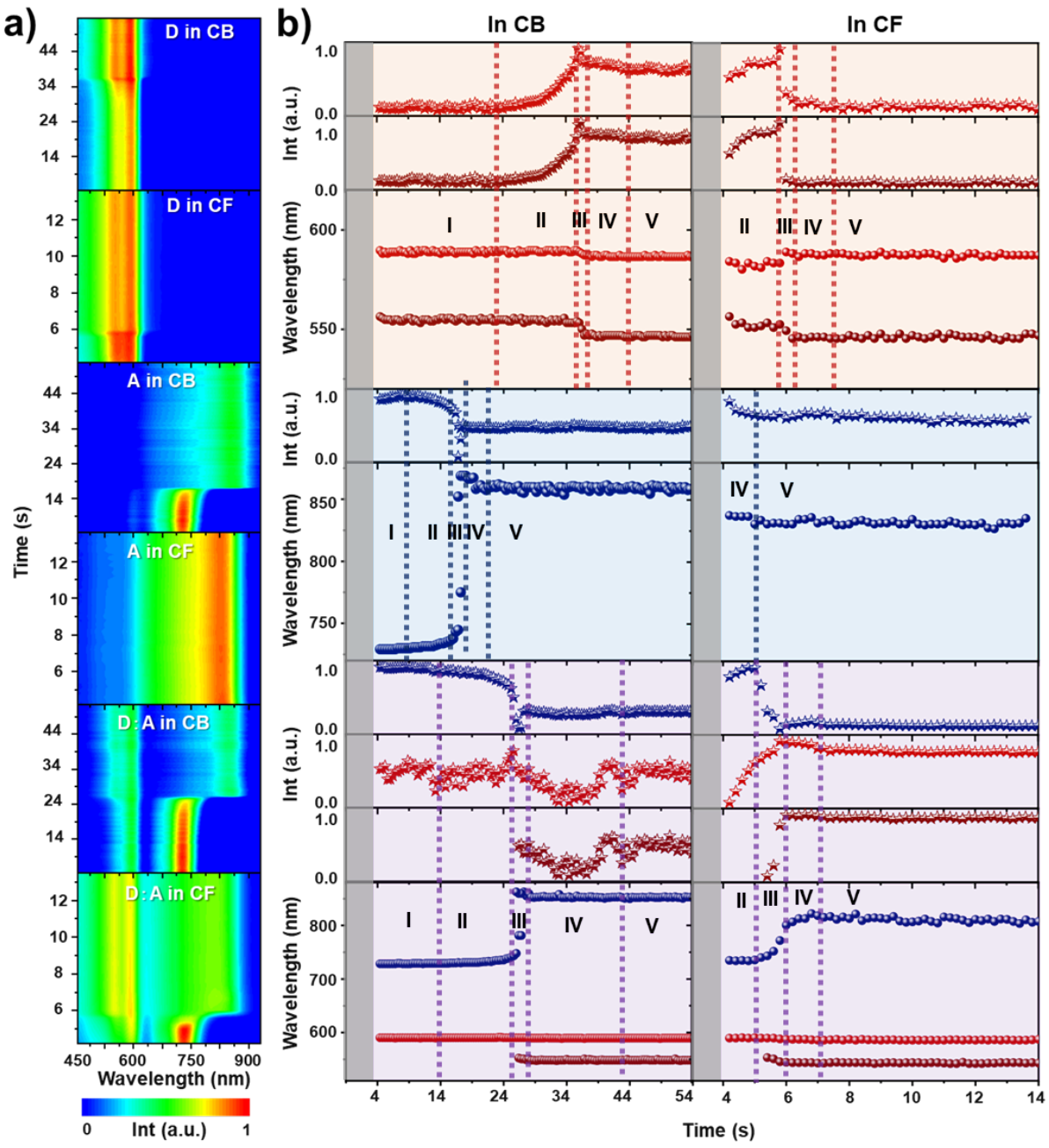

Figure 6.11: a) In situ UV-vis 2D mapping of the film formation kinetics of neat PDTBT2T-FTBDT, BTP-4F and PDTBT2T-FTBDT: BTP-4F blend films printed out of CB and CF, respectively. b) Primary peak position (symbols) and the corresponding normalized peak intensity (stars) of neat PDTBT2T-FTBDT (red bulk), neat BTP-4F (blue bulk) and PDTBT2T-FTBDT: BTP-4F (purple bulk) films printed out of CB and CF during the in situ experiment. Reproduced with permission from Wiley, Copyright 2022. [104]

for the neat PDTBT2T-FTBDT (24 s) as well as the PDTBT2T-FTBDT: BTP-4F blend (within 14 s) films printed out of CB. The initial λ_{0-0} (589 nm) and λ_{0-1} (556 nm) peaks are very distinct in the case of the neat PDTBT2T-FTBDT film, however, only the λ_{0-0} peak (592 nm) of PDTBT2T-FTBDT is observed in the blend film. Interestingly, in the case of the neat BTP-4F film, the spectrum (maximum at 729 nm) shows a red shift and concomitantly gains intensity. This tiny spectral change and the increase in intensity signify a planarization of the disordered chains that leads to an increased conjugation length. For CF, stage I is not resolved. In stage II, upon further solvent evaporation, average solute structures start to interact with each other. The PDTBT2T-FTBDT (in CB and CF) and BTP-4F (blend in CF) peaks are growing in intensity and exhibit a sharp absorption spectrum, which is attributed to an ordered chain conformation. For BTP-4F in CB, a redshift is seen from 732 nm to 743 nm in the neat thin film after 7 s and from 729 nm to 745 nm in the blend thin film after 14 s. This redshift is accompanied by a decrease in intensity, suggesting a disordered chain conformation. [211] In stage III, the majority of the solvent has evaporated and the absorption peak positions begin to shift concerning their initial values due to a rapid aggregate formation. Thus, this stage can be attributed to an order-disorder phase transition. [201] The λ_{0-1} peak of PDTBT2T-FTBDT in the neat film blue shifts to 546 nm after 20 s printing out of CB and to 545 nm after 5 s printing with CF. In contrast, the λ_{0-0} peak of PDTBT2T-FTBDT slightly blue shifts to 586 nm in the case of CB and redshifts to 589 nm in the case of CF, suggesting that the CB solvent is more favorable for an H-aggregate formation of the neat PDTBT2T-FTBDT polymer. Contrary to PDTBT2T-FTBDT, the absorption peak of BTP-4F (shift from 743 nm to 869 nm after 20 s) exhibits a J-aggregated transition behavior in CB. The arising of a new peak at a higher wavelength (852 nm) is associated with a further planarization of the aggregated chain segments during solvent evaporation. In the blend thin film printed out of CB, the PDTBT2T-FTBDT λ_{0-0} peak intensity slightly decreases together with a peak blue shift to 589 nm. The λ_{0-1} peak evolves and blue shifts from 554 nm to 549 nm with a simultaneous intensity decrease. The absorption peak of BTP-4F slightly redshifts till 745 nm with a decreasing intensity to a minimum value. Meanwhile, a new peak attributed to BTP-4F arises at 852 nm and then shifts towards 857 nm with increasing intensity. In the case of the blend printed from CF, the PDTBT2T-FTBDT λ_{0-0} peak slightly blue shifts from 589 nm to 587 nm with an intensity increase reaching a maximum value. The λ_{0-1} peak of PDTBT2T-FTBDT appears then shifts from 553 nm to 544 nm with an intensity increase reaching a maximum. The absorption peak of BTP-4F rises to its highest intensity. Then it shifts strongly from 734 to 800 nm, with a decreasing intensity to its minimum. All these strong changes in the absorption spectrum demonstrate that stage III is very crucial for the film formation behavior and therefore for the quality of the solar cell. In general, it can be deduced, that the neat PDTBT2T-FTBDT exhibits

a well-ordered conformation in CB, and the neat BTP-4F exhibits a better aggregation in CF, respectively. Notably, the PDTBT2T-FTBDT: BTP-4F blends manifest a better-ordered conformation than the corresponding neat thin films in CF (less pronounced in CB solvent), which could be a synergistic effect. In stage IV, the absorption peaks of the PDTBT2T-FTBDT remain constant in their positions but a change in their intensity. The spectrum boarding suggests a planarization of the aggregated phase. The BTP-4F peaks slightly blue shift with an intensity decrease in CB solvent and the neat BTP-4F in CF, suggesting a favorable planarization of the H-aggregated phase. [212] Then, the BTP-4F peak further redshifts to 822 nm accompanied by the intensity slightly increasing in the blend thin film printed out of CF, indicating an enhancement of the ordered structure for the J-aggregates. Interestingly, a decrease followed by an increase in the signal from the donor in CB for the blend thin film is observed, suggesting that the presence of BTP-4F has a stabilizing influence on the conformation of PDTBT2T-FTBDT. In stage V, almost all solvent is almost completely evaporated and no changes in the peak positions and peak intensities can be detected, suggesting no further transition or aggregation process

6.3.2 Crystallinity Formation Kinetics

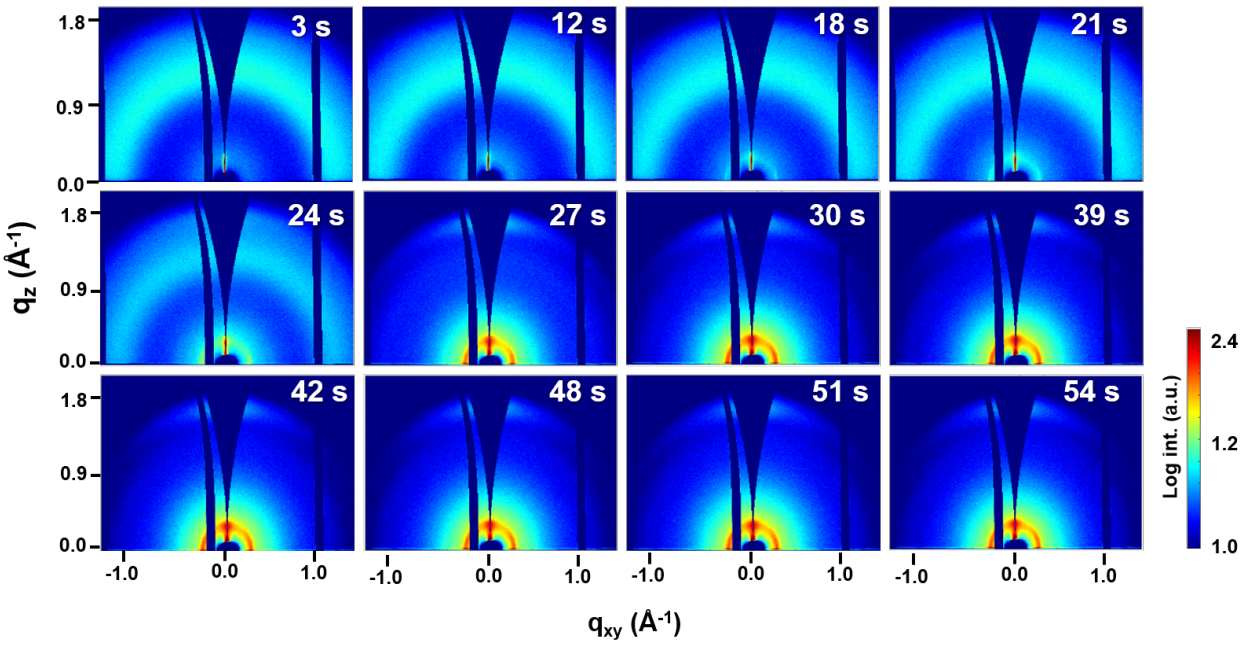

Figure 6.12: Selected in situ 2D GIWAXS data during the film formation of PDTBT2T-FTBDT: BTP-4F blend film printed out of CB solvent at different times. Reproduced with permission from Wiley, Copyright 2022. [104]

To study the real-time evolution of the crystal structure of the PDTBT2T-FTBDT: BTP-4F

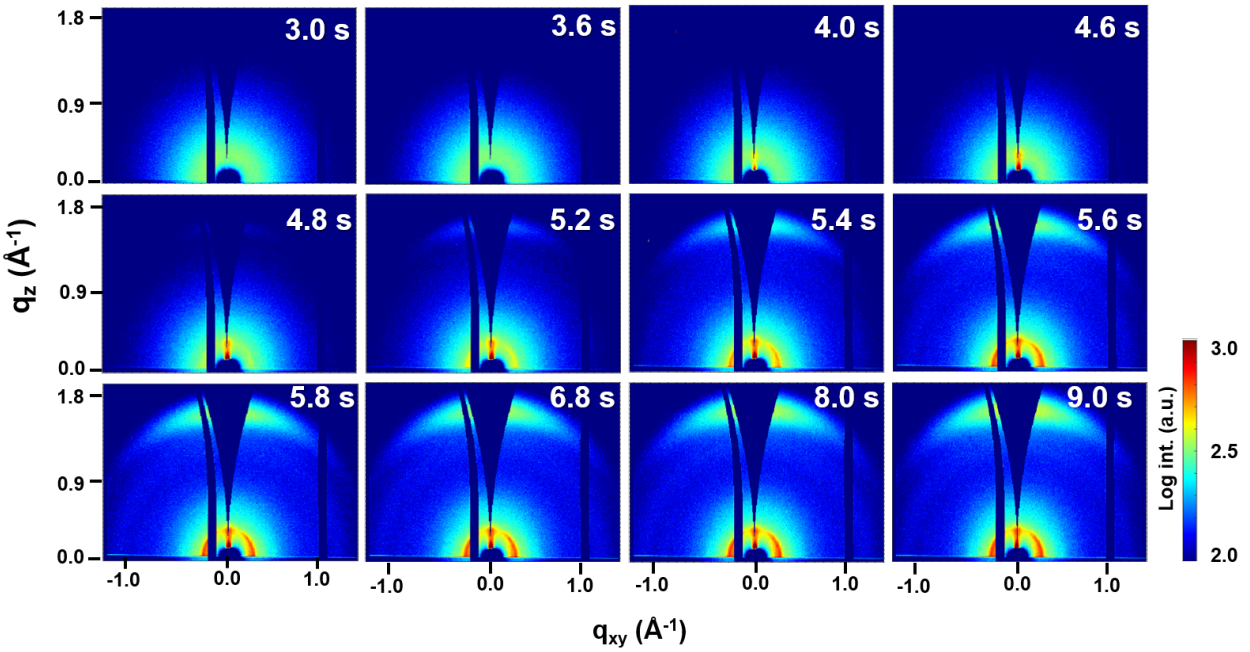

Figure 6.13: Selected in situ 2D GIWAXS data during the film formation of PDTBT2T-FTBDT: BTP-4F blend film printed out of CF solvent at different times. Reproduced with permission from Wiley, Copyright 2022. [104]

blend films printed with both solvents, in situ GIWAXS measurements are carried out. Selected 2D GIWAXS data of the film formation are shown in Figure 6.12 and 6.13. In Figure 6.12, the intense and broad ring located around 1.3 Å^{-1} originates mainly from the scattering of the CB solvent, which is in agreement with previous studies. [213] As the solvent evaporates, the scattering contribution of CB is reduced, whereas the (010) Bragg peak of the crystallites in the blend located in the range of 1.6 to 1.8 Å^{-1} becomes more distinct. As seen in Figure 6.13d, the (010) Bragg peak becomes more pronounced with increased intensity and a slight shift from its initial position can be determined. These changes suggest the formation of a face-on crystallite orientation undergoing slight compaction during the CF evaporation. Background corrected line profiles with the corresponding Gaussian fits of the (010) Bragg peaks in the out-of-plane direction from the 2D GIWAXS data are shown in Figure 6.14c and 6.14d. To give insights into the crystallite formation of the donor and acceptor in different solvents, the development in the (010) Bragg peak extracted from the Gaussian fits provides information about the intensity, the π -π stacking distance (calculated by $2\pi/q$) as well as the crystallite size (estimated by the Debye-Scherrer equation) as shown in Figure 6.15a-6.15b (CB solvent) as well as Figure 6.15c-6.15d (CF solvent). [214] The formation of the (010) OOP crystallites also exhibits five different stages in agreement with the in situ UV-vis data, although the first stage is not resolved in the case of CF. This first stage is the solvent evaporation stage. During stage I, no obvious crystal

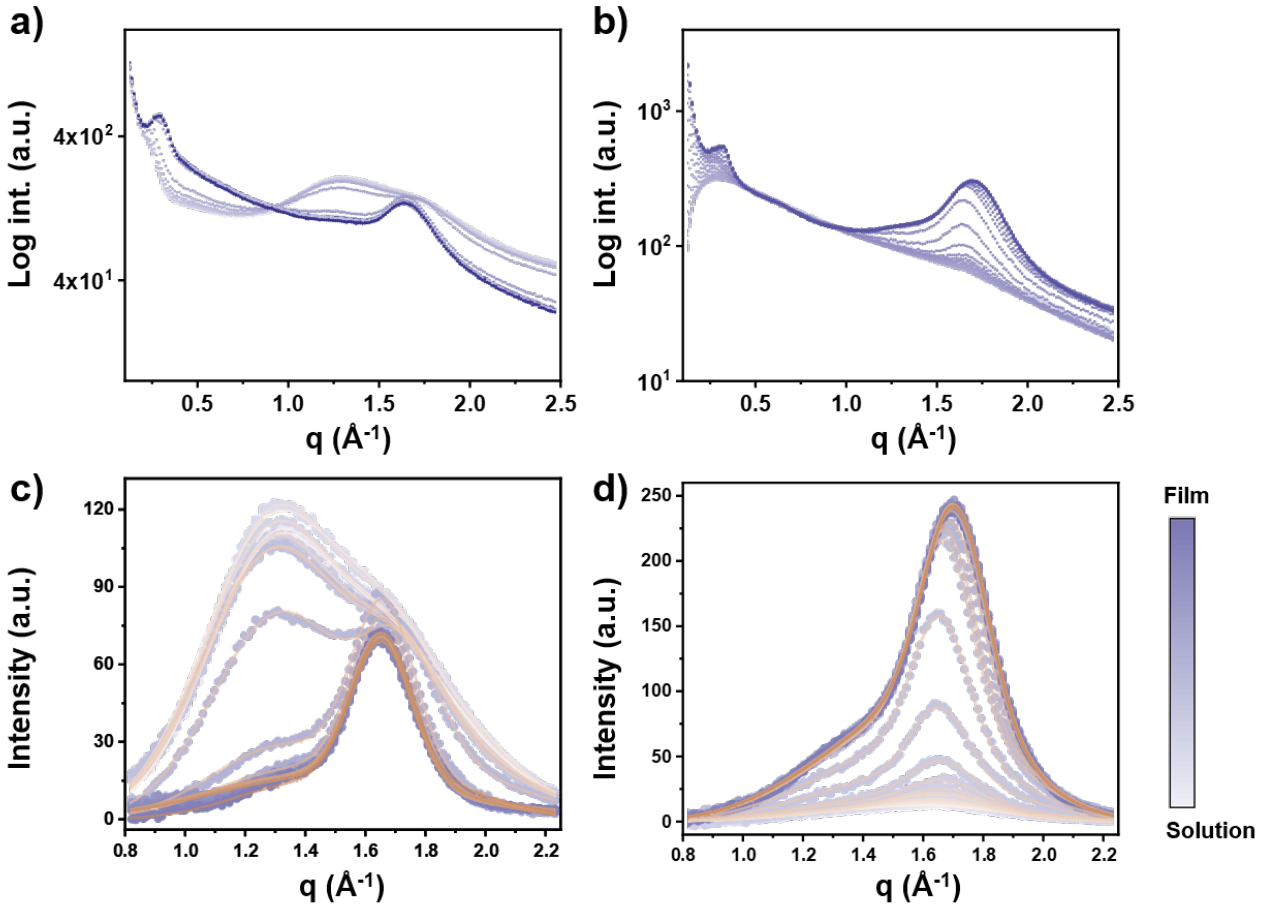

Figure 6.14: Sector integrals (0° - 15°) of the in situ 2D GIWAXS raw data of PDTBT2T-FTBDT: BTP-4F blend film processed out of a) CB and b) CF. The background corrected (010) peak OOP line cuts and their Gaussian fits of the active layer processed out of c) CB and d) CF. The color code indicates the progression from solution to film as indicated. Reproduced with permission from Wiley, Copyright 2022. [104]

growth is observed for CB due to the presence of excess host solvent and the absence of crystallization. However, a certain amount of initial crystals is existing in stage I with donor crystallite sizes of about 2.4 nm and a π -π stacking distance of 3.7 Å, as well as a size of the acceptor crystals of about 1.6 nm and a stacking distance of 3.4 Å. Thus, a pre-aggregation of donor and acceptor happened in CB as well as in CF. At stage II, the crystallite size increases progressively in both solvents, suggesting moderate crystal growth. In addition, the (010) π -π stacking distance of the donor and acceptor decreases with the ongoing evaporation of the solvent, causing more close packing of the crystals. Only for BTP-4F in CF, an increase in the stacking distance is seen in stage II. The intensity of the Bragg peak related to BTP-4F decreases in CB while the increase in CF, shows that in CB the small molecule crystallization is hindered. For PDTBT2T-FTBDT, the intensity increases only moderately, meaning that the

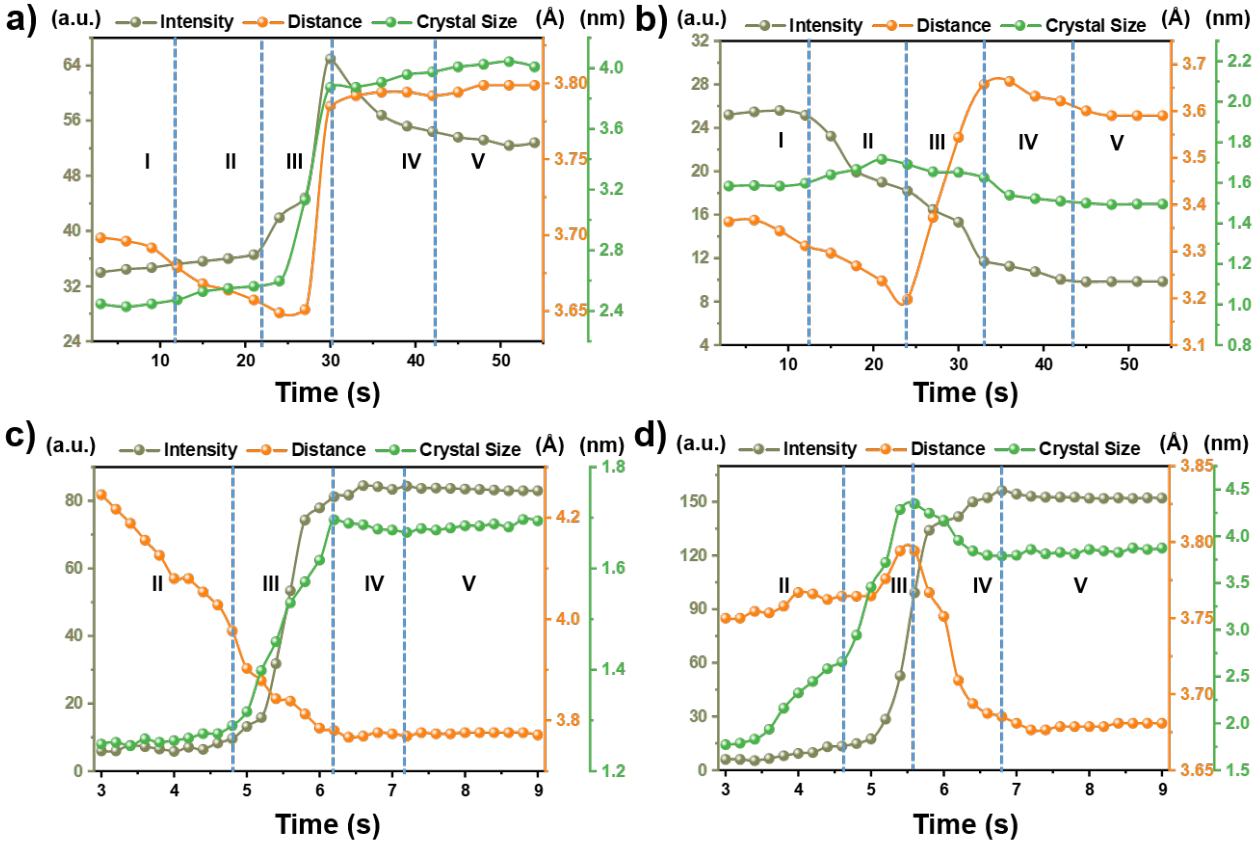

Figure 6.15: Evolution of the out-of-plane (010) Bragg peak of a) PDTBT2T-FTBDT and b) BTP-4F in the blend film printed out of CB. Evolution of the out-of-plane (010) Bragg peak of c) PDTBT2T-FTBDT and d) BTP-4F in case of CF. Reproduced with permission from Wiley, Copyright 2022. [104]

donor polymer is only slowly crystallizing in this stage. In contrast, in stage III where the phase transition happens, for the donor in CB, the Bragg peak intensity, the crystallite size as well as the π -π stacking distance increase massively, indicating a rapid but imperfect crystal growth of the donor. For the acceptor in CB, the intensity and the crystallite size slightly decrease while the stacking distance increases, suggesting a perturbation of the BTP-4F crystallites caused by the PDTBT2T-FTBDT crystallization. For the donor in CF, the Bragg peak intensity and the crystallite size also increase significantly while the π -π stacking distance is further decreasing. Thus, the amount of donor crystallites grow rapidly in conjunction with crystal growth and an improvement of the inner order. For the acceptor in CF, the intensity and the size as well as the stacking distance increase. Thus, small molecule crystallization is hindered by polymer crystallization. In stage IV, for CB the intensity of the Bragg peak of the donor decreases while crystallite size and stacking distance slightly increase, suggesting the stabilization of the crystallites. For the acceptor,

the intensity increases slightly, crystallite size decreases, and the stacking distance remains unchanged. In contrast, in the case of CF the intensity, crystallite size and stacking distance of the donor all slightly decrease, whereas for the acceptor, the intensity increases but size and distance decrease. Finally, all the solvent molecules left the film, the film turns glassy and the film formation stops (stage V) as seen by the constant intensity, distance and size.

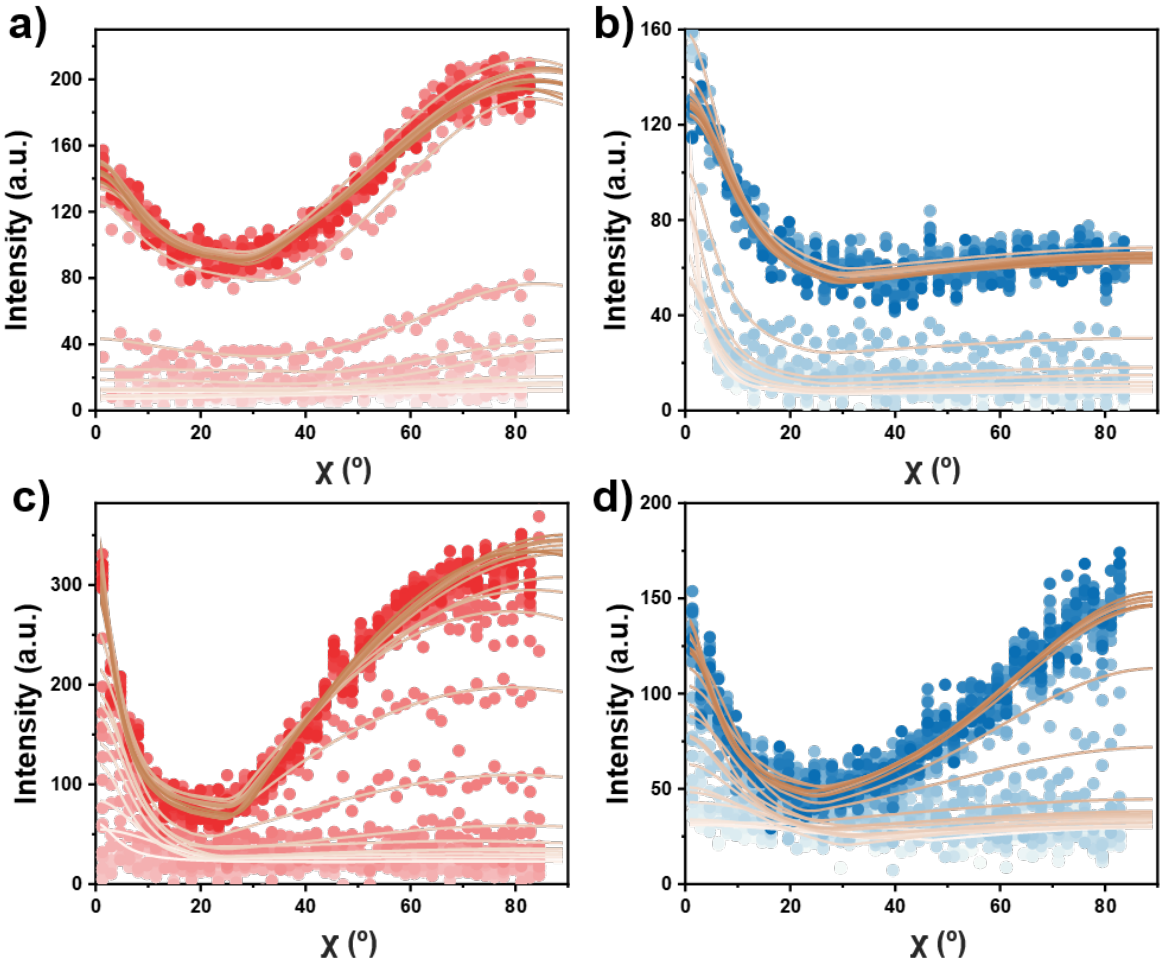

Figure 6.16: Azimuthal tube cuts of the in situ 2D GIWAXS data taken at the (100) peak of a) PDTBT2T-FTBDT and of b) BTP-4F for the blend films printed out of CB, as well as c) PDTBT2T-FTBDT and d) BTP-4F printed out of CF. Reproduced with permission from Wiley, Copyright 2022. [104]

To determine the temporal orientation evolution of the crystallites of the donor and acceptor crystallites in the films printed with different solvents, we perform the (100) peak tube cuts from the in situ 2D GIWAXS data measured during the printing. Figure 6.16a-6.16d shows the corresponding tube cuts data. The change of the face-on, edge-on, as well as isotropic orientation, are determined during the film formation (Figure 6.17a-6.17b). Since the edge-on orientation is not prominent in the films irrespective of the used solvent, it is

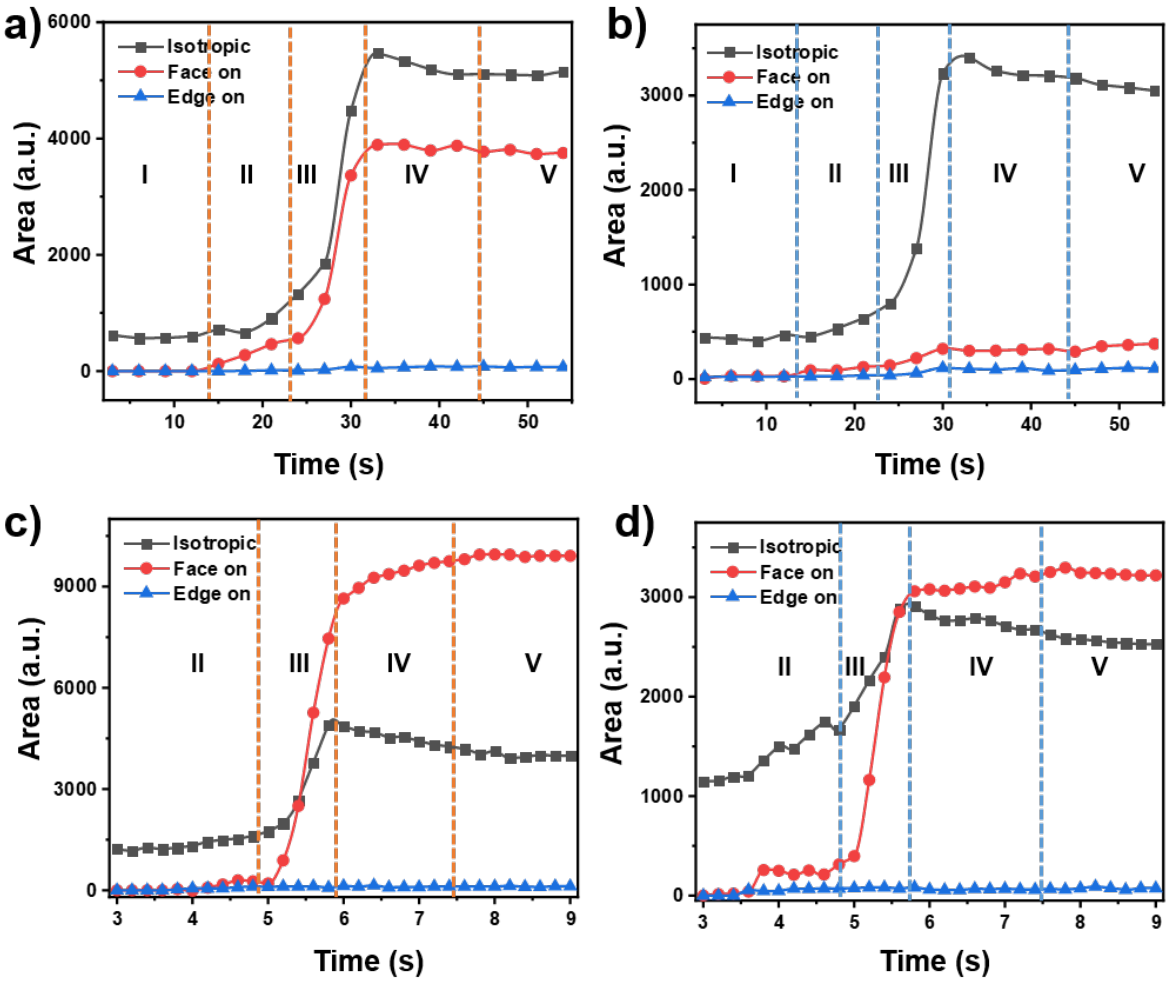

Figure 6.17: Evolution of the (100) crystallite orientation area of a) the donor PDTBT2T-FTBDT and the acceptor b) BTP-4F using CB, as well as the c) PDTBT2T-FTBDT and d) BTP-4F using CF, respectively. Reproduced with permission from Wiley, Copyright 2022. [104]

not further discussed here. During stage I, no obvious changes in crystallite orientation are observed, in agreement with a solvent-rich film. In good agreement with the in situ UV-vis data, the contribution of isotropic crystallites already exists in stage I for CB. In stage II, PDTBT2T-FTBDT, as well as BTP-4F start to aggregate in both solvents, exhibiting a slight increase in the isotropic orientation. In addition, the face-on crystallite orientation appears and grows with time, while it is still less than the isotropic phase. In stage III, the isotropic and the face-on phase grow strongly in all samples due to the rapid crystal growth (around 23 s – 30 s in CB and 5 s – 6 s in CF). For CB, the isotropic PDTBT2T-FTBDT crystallites increase by about 4 times more and the face-on oriented PDTBT2T-FTBDT crystallites by roughly 8 times, with still the isotropic orientation being the majority. Similarly, also the isotropic orientation of BTP-4F dominates (increases about 6 times whereas the face-on

orientation grows by a factor of two). In contrast, in CF, the isotropic orientation is less dominant and surpassed by the face-on oriented crystallites. In stage IV, the isotropic phase decreases slightly in PDTBT2T-FTBDT and BTP-4F for CB and CF, respectively. In addition, the face-on phase is almost constant in CB, while it further increases in CF. Again, stage V means no more change in the distribution of the crystallite orientations.

6.4 Conclusion

Based on the study of the respective neat donor and acceptor films, systematic research of the effect of the donor-acceptor interplay on the absorbance, exciton dissociation, charge transfer, exciton kinetics, nanoscale morphology, and crystallinity of printed PDTBT2T-FTBDT:BTP-4F active layers is performed to provide insights into the related device performance of wide-bandgap non-fullerene acceptor based OSCs. The best-performing devices are achieved with printing out of CF due to the best-suited nanoscale morphology, the presence of well-ordered crystallites, a lower surface roughness and a higher exciton dissociation probability. The relatively poor performance of slot-die coated devices printed from CB is attributed to the imbalanced crystallinity of the PDTBT2T-FTBDT and BTP-4F phases in the BHJ structure inhibiting an efficient exciton diffusion and free charge carrier transport. Moreover, in situ UV-vis and in situ GIWAXS measurements give insights into the film formation kinetics related to the structure conformation, aggregation, and crystallite structure, as well as crystallite orientation. We find that the conformational evolution of the donor and acceptor is different. PDTBT2T-FTBDT preferentially forms H-aggregates and in contrast, BTP-4F prefers J-aggregate formation during solvent evaporation. Interestingly, the aggregate formation of PDTBT2T-FTBDT and BTP-4F causes a synergistic effect when printing out of CF. Therefore, the donor and acceptor in the blend of thin films manifest a pronounced, well-ordered crystallite growth with a majority of the crystallites being face-on-orientated. In contrast, the synergistic effect in the donor and acceptor crystallization is absent when printing out of CB, mainly because BTP-4F experiences an excessive J-aggregation. The unbalanced crystallization of the donor and acceptor gives rise to a more disordered orientation with a reduced donor crystal order. In the late stage of the film formation, isotropic donor and acceptor crystallites order in face-on orientation for CF, whereas for CB this improvement in the film is absent. Thereby, with printing in ambient conditions, OSCs with PCE of 13.2 % are demonstrated when using CF. Thus, this work reveals valuable insights into the solvent effects on the donor-acceptor morphology and the mechanism of film formation kinetics in the field of non-fullerene OSCs, which cause significant differences in the related device performance. Since the OSCs are printed via the slot-die coating technique in an ambient atmosphere, the findings offer great practical

perspectives for bringing OSCs into real-world applications.

7 Formation Kinetics of the Active Layer Printed Out of A Non-Halogen Solvent

The following chapter is mainly based on the work "Film formation kinetics of polymer donor and non-fullerene acceptor active layers during printing out of 1,2,4-trimethylbenzene in ambient conditions" *(Xinyu et al., Solar RRL, 2023, DOI:10.1002/solr.202201077)*. [141] Reproduced with permission from Wiley, Copyright 2023.

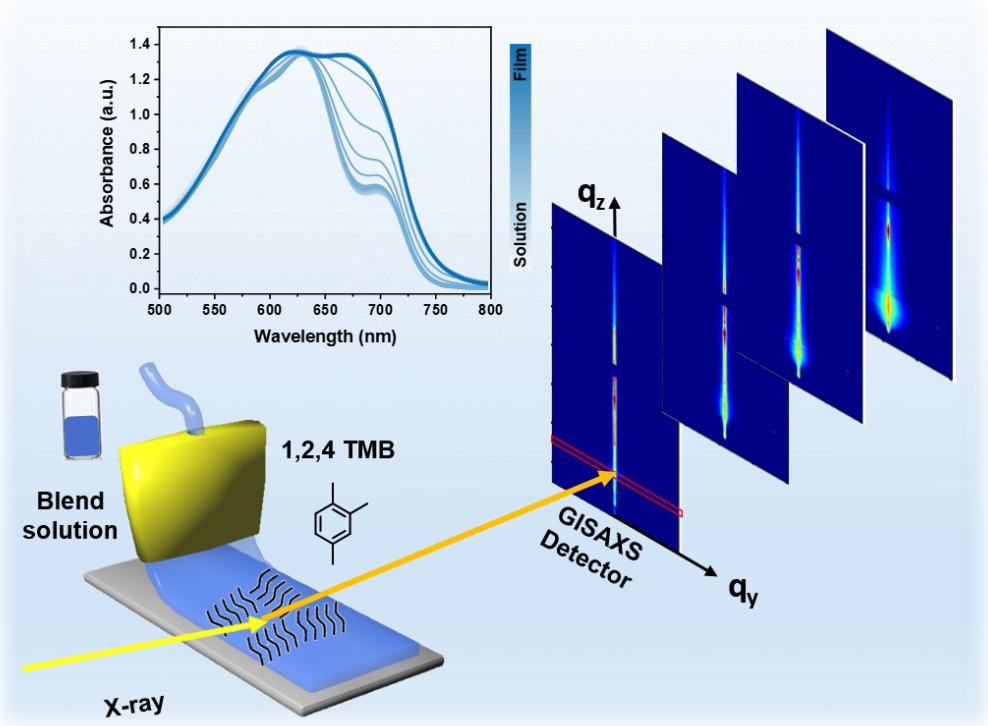

In the last chapter, systematic research of the effect of the donor-acceptor interplay on the absorbance, exciton dissociation, charge transfer, exciton kinetics, nanoscale morphology, and crystallinity of printed PDTBT2T-FTBDT: BTP-4F active layers is discussed. Moreover, the evolution of the active layer formation kinetics induced by the different halogen-based solvents is revealed by a combination of the state-of-art in situ GIWAXS and in situ UV-Vis techniques. The best-performing OSCs realized over 13 % efficiency is achieved by the scaling-up slot-die coating method under ambient, which takes an impact step forward

for commercialization. However, when moving towards an industrial large-scale production of printed OSCs, halogen-based host solvents with high toxicity and carcinogenicity like chloroform (CF) and chlorobenzene (CB), will seriously limit their success. Thus, the utilization of a non-halogen-based host solvent coupled with the slot-die coating method and in-depth analysis of film formation kinetics are of great importance in the field of environment-friendly OSCs. [43],[44]

In the present chapter, the active layer containing the low band gap donor polymer poly[(5,6-difluoro-2,1,3-benzothiadiazol-4,7-diyl)-alt-(3,3‴-di(2-octyldodecyl)-2,2′;5′,2";5",2‴- quarter thiophen-5,5‴-diyl)] (PffBT4T-2OD) and the non-fullerene acceptor (Z)- 5- [5-(15-5-[(Z)-(3-ethyl -4- oxo -2- thioxo -1,3 - thiazolidin -5 -ylidene) methyl]-8- this -7.9 diazabicyclo [4.3.0]nona-1(9),2,4,6-tetraen-2-yl-9,9,18,18-tetrakis (2-ethylhexyl)-5.14 dithiapentacyclo [10.6.0.03, 10.04, 8.013, 17] octadeca -1(12), 2, 4(8), 6, 10, 13(17), 15- heptaen -6- yl) -8-thia-7.9-diazabicyclo [4.3.0] nona-1(9), 2, 4, 6-tetraen- 2 -yl] methylidene -3-ethyl -2-thioxo-1,3-thiazolidin-4-one (EH-IDTBR) is printed out of the environment-friendly halogen-free solvent 1,2,4-trimethylbenzene (TMB) at 60 °C with the slot-die coating method. Due to the advantages of being air-stable and thickness insensitive, active layers based on PffBT4T-2OD: EH-IDTBR are of great interest in the industrial production of OSCs. [215],[216],[217] Furthermore, the high value of the lowest unoccupied molecular orbital (LUMO) energy level of the EH-IDTBR acceptor enables an excellent large open circuit voltage in OSC devices. [218] The evolution of active layer domains and the correlated changes in optical properties are revealed via in situ GISAXS and in situ UV-Vis spectroscopy. Underlying effects of donor and acceptor on the active layer properties are seen in the in situ UV-Vis measurements. Moreover, ex situ grazing-incidence wide-angle X-ray scattering (GIWAXS) measurements reveal information about the crystalline parts of the printed thin films. Thereby, this work gives insights into the morphology formation as well as the interactions between donor and acceptor in non-halogen solvent-processed active layers during printing in ambient conditions.

7.1 Active Layer Formation Kinetics

7.1.1 Morphology Formation Kinetics

In order to give insights into the time evolution of the inner structure of active layers based on the donor: acceptor blend PffBT4T-2OD: EH-IDTBR during slot-die coating, in situ GISAXS measurements are performed. The selected 2D GISAXS data collected during the active layer formation is shown in Figure 7.1. Horizontal line cuts of the 2D GISAXS data are performed at the Yoneda peak position of PffBT4T-2OD and EH-IDTBR to investigate characteristic

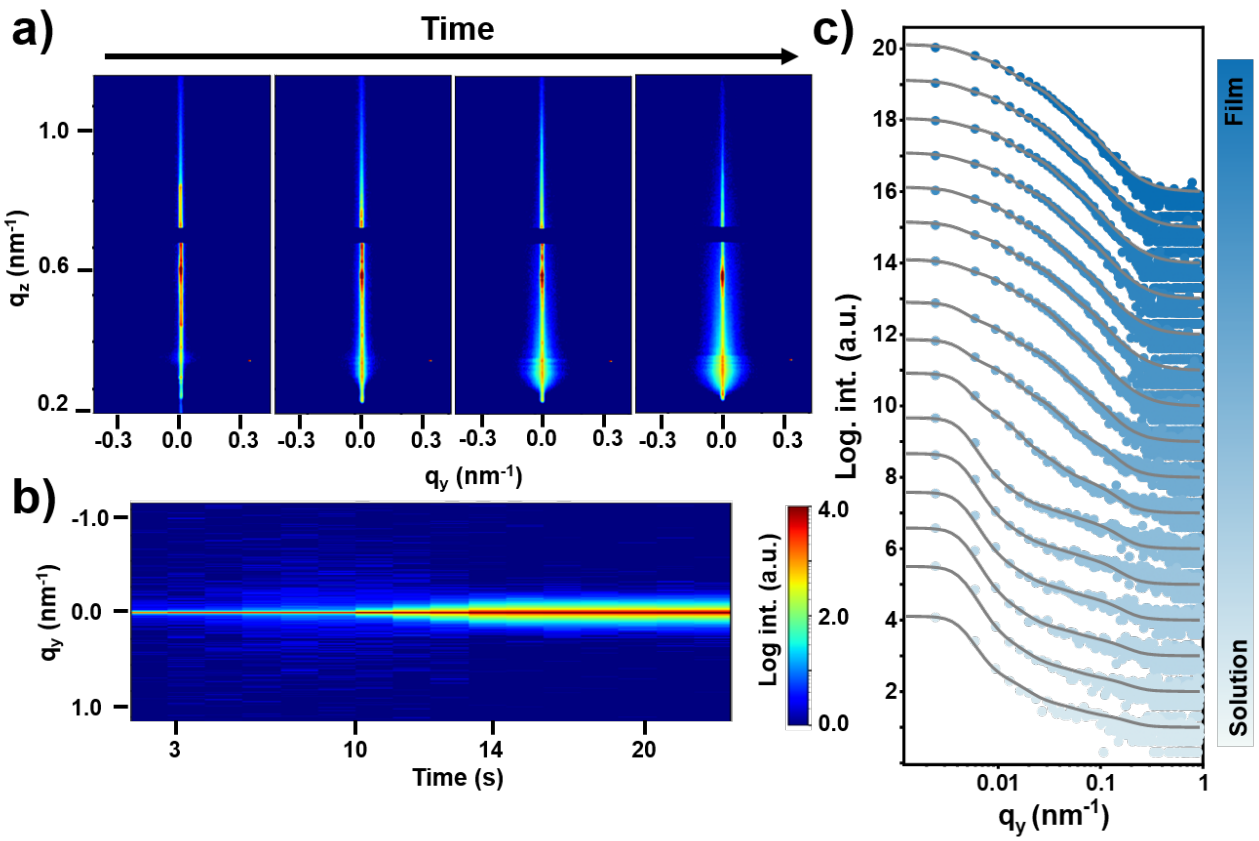

Figure 7.1: a) Selected in situ 2D GISAXS data measured during the film formation of the PffBT4T-2OD: EH-IDTBR blend film printed out of TMB solvent. b) 2D color mapping of the temporal intensity evolution of horizontal line cuts of the 2D GISAXS data at the Yoneda peak position from in situ printing of PffBT4T-2OD: EH-IDTBR active layers out of TMB. c) Selected horizontal line cuts (blue dots) and respective fits (solid lines) for printed PffBT4T-2OD: EH-IDTBR active layers. The data are shifted along the y-axis from bottom to top for clarity and gradually plotted with darker color during the solvent evaporation to underline the transformation from solution to a dry film. Reproduced with permission from Wiley, Copyright 2023. [141]

lateral structures. The 2D color mapping of the horizontal line cuts is shown in Figure 7.1b over the progressive time of thin film drying. Figure 7.1c shows selected horizontal line cuts to demonstrate the kinetics of the inner structure formation. In more detail, the gradual increase in intensity in the high-q_y range reveals a growth of the small-size domains. Thereafter, the intensity further increases and shifts in the low-q_y range, suggesting the growth of large domains. [41] To analyze the lateral structure evolution of the slot-die coated

PffBT4T-2OD: EH-IDTBR active layer in more depth during the film formation process, the data are modelled by assuming three cylindrically shaped object types with different radii (large, middle and small) to fit the horizontal line cut data. [177] To account for polydispersity of the domains a Gaussian size distribution is assumed. The corresponding best fits to the data are shown in Figure 1c. The modelling is done in the framework of the distorted wave Born approximation (DWBA) and of the effective interface approximation (EIA). [219] With the experimental resolution of the in situ GISAXS experiment, domain sizes in the range of one to hundreds of nanometers are covered, which is well-suitable for understanding OSC active layers. From the fit parameters, a domain size distribution is calculated to display

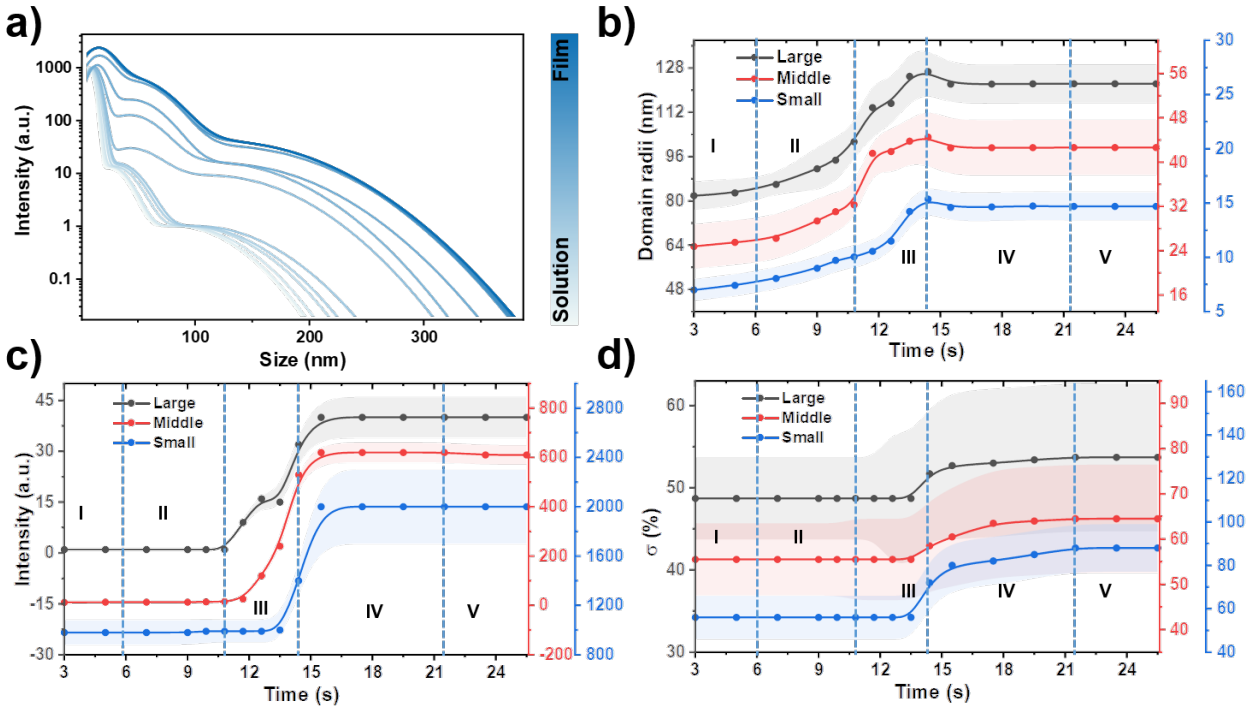

Figure 7.2: a) Temporal domain size evolution during the printing of PffBT4T-2OD: EH-IDTBR active layers out of TMB as determined from the GISAXS fits. The data are not normalized and gradually plotted with darker color during the solvent evaporation to underline the transformation from solution to a dry film. Temporal evolution of fit parameters describing the lateral film structure in terms of average domain b) radii, c) intensity and d) polydispersity (σ) of the active layer. The solid lines act as guides to the eye and the shaded areas denote the error bar regimes. The vertical dashed lines mark the individual regimes I-V. Reproduced with permission from Wiley, Copyright 2023. [141]

the changes in characteristic lateral structures during printing of the active layer (Figure 7.2a). The individual fit parameters related to the small, middle, and large-sized domains such as domain radii, number of domains (intensity) and polydispersity (σ) are shown in

Figure 7.2b-d, respectively. Similar to our previous reports on printing of donor: acceptor active layers, [220],[213] five regimes are also distinguished in the film formation kinetics of the PffBT4T-2OD: EH-IDTBR active layer printed out of TMB as solvent. The initial regime (regime I) refers to the initial ink since the liquid solution is freshly deposited on the substrate and forms a liquid film. Obviously, aggregates have formed in the ink already, which have a constant size, number and polydispersity. The observed domains have average radii of 7 ± 1 nm (small), 24 ± 4 nm (middle) and 81 ± 5 nm (large). Such pre-aggregation in the ink in the slot-die head was found before for other donor: acceptor blend solutions. In the second regime (regime II), a gradual and slow increase in all three domain radii is observed, while no obvious changes in the domain numbers and the domain polydispersities are seen. Thus, parts of the domain solute start to interact as the solvent volatilizes from the printed film. The third regime (regime III) refers to the dramatic phase transition period due to the fast evaporation of the majority host solvent. There is an obvious domain size growth and an abrupt intensity increase reflecting the increase in domain numbers in all three types of domains. Interestingly, in contrast to earlier results, [220],[213] the middle size scale demonstrates significant growth of the domains prior to the small scale. In addition to the original domain growth in the middle-size scale, this trend also might be caused by an additional aggregation of small-size domains. In the fourth regime (regime IV), as most parts of the solvent have evaporated, the solvent plays less of a role in the film formation of the active layer structure. For all three domain types, a decrease in domain radii is seen along with an increase in the corresponding domain numbers. In particular, a pronounced intensity growth of the small domain radii is observed rather than of the large and middle domain sizes. Moreover, there is an increase in the disorder of all three domain structures in regime four (Figure 7.2d). The very limited mobility in the late stages of film formation might cause more small and disordered features to form during this regime. In the last regime (regime V), the solvent is almost entirely evaporated. Thus, all parameters describing the domain structures in the active layer remain constant, thereby demonstrating an absence of mobility in the final PffBT4T-2OD: EH-IDTBR active layer.

7.1.2 Aggregation and Conformation Kinetics

The evolution of the optical properties related to the conformation and aggregation kinetics of the PffBT4T-2OD: EH-IDTBR active layers printed out of TMB solvent as well as their neat thin films are studied in situ during printing with UV-Vis spectroscopy. [221] The detailed UV-vis spectroscopy of the neat PffBT4T-2OD, EH-IDTBR film and the blended film as well as the corresponding 2D color plots over the progressive time of thin film drying are presented in Figure 7.3. The drying behavior of the neat donor (Figure 7.3a, 7.3b), neat acceptor (Figure 7.3c, 7.3d), and their blend films differs significantly (Figure 7.3e, 7.3f).

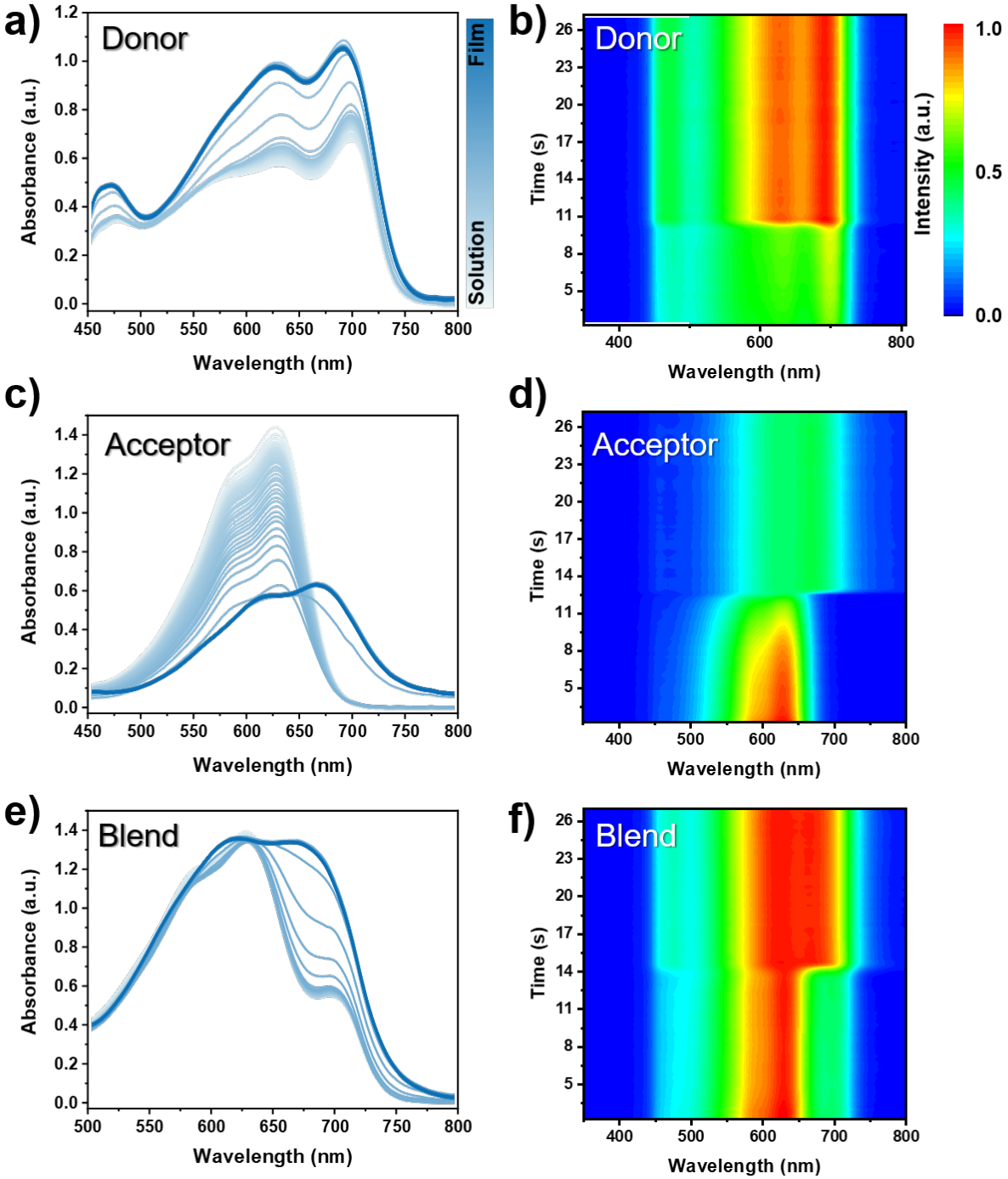

Figure 7.3: In situ UV-vis absorption spectra of a) polymer donor PffBT4T-2OD, c) small molecule acceptor EH-IDTBR, and e) active layer PffBT4T-2OD: EH-IDTBR films print out of TMB solvent, respectively. From solution to dry and from light to dark colors, the line color illustrates the printing process. The corresponding 2D color map during the film formation kinetics of b) neat PffBT4T-2OD, d) neat EHID-TBR and f) PffBT4T-2OD: EH-IDTBR blend films printed out of TMB, respectively. Reproduced with permission from Wiley, Copyright 2023. [141]

During the film formation process, the absorbance of the thin film clearly increases in the case of the neat PffBT4T-2OD thin film while it gradually decreases and redshifts in the case of the neat EH-IDTBR film. No obvious changes despite a redshift are seen for the PffBT4T-2OD: EH-IDTBR blend thin film. Due to an overlap in the absorption ranges of PffBT4T-2OD and EH-IDTBR, their temporal evolution cannot be easily traced in the absorbance data of the blend thin film. To identify the temporal molecular conformation and aggregation kinetics of PffBT4T-2OD and EH-IDTBR in the neat films and in the PffBT4T-2OD: EH-IDTBR blend film, a set of Gaussian functions with equal width that represents various optical transitions is utilized to fit the in situ UV-Vis spectra. [222] Figure 7.4 gives detailed fit information for these films. Six peaks located (Figure 7.4a) at 701.4 nm, 658.5 nm, 622.9 nm, 583.8 nm, 545.8 nm, and 504.0 nm are assigned to the 0-0, 0-1, 0-2, 0-3, 0-4, 0-5, 0-6 electronic transitions in PffBT4T-2OD. Three peaks (Figure 7.4c) at 632.8 nm, 581.1 nm, and 528.3 nm indicate the 0-0, 0-1, and 0-3 transitions in the neat EH-IDTBR. Thus, in total nine peaks with six donor electronic transitions (from 0-0 to 0-6, at 701.9 nm, 658.1 nm, 624 nm, 584 nm, 546 nm and 503 nm) and three acceptor transitions (0-0, 0-1, 0-2, at 632.3 nm, 581.2 nm, and 529 nm) are used for the PffBT4T-2OD: EH-IDTBR blend film (Figure 7.4e). In the final dried thin films (Figure 7.4b, 7.4d, 7.4f), all electronic transitions broadened in both, neat and blend thin films, suggesting an increasing disorder. [223] The peak positions of donor and acceptor shift according to different trends in the neat and blended thin films during the film formation process.

To give insights into the interaction between donor and acceptor during the PffBT4T-2OD: EH-IDTBR blend film formation process, the temporal evolution of 0-0 electronic transitions is compared between neat donor and acceptor films and the blend film (Figure 7.5a- 7.5d). Matching the in situ GISAXS findings, five regimes are also seen in the in situ UV-Vis data. However, in the details, the five different regimes differ from each other, in their temporal duration as well as in their processes. In the neat thin films, the intensity increases for PffBT4T-2OD but decreases for EH-IDTBR films in the initial regime (regime I), suggesting different aggregation behaviors between PffBT4T-2OD and EH-IDTBR. In the blend thin film, an intensity decrease is seen for EH-IDTBR while no changes happen for PffBT4T-2OD. In the second regime (regime II), the peak positions start to shift from their original positions, which is due to the aggregation of domain structures as observed in the GISAXS data analysis. The EH-IDTBR signal redshifts, while the PffBT4T-2OD signal blueshifts, indicating the J-type aggregation of the acceptor and an H-type aggregation of the donor molecules. [224],[225] In the third regime (regime III), the trend of changes continues as in the second regime but with a much higher strength, demonstrating a more intense aggregation of the EH-IDTBR and PffBT4T-2OD molecules. In addition, a rapid increase in the FWHM values is observed, suggesting an increase in the disorder of the molecule packing. In the

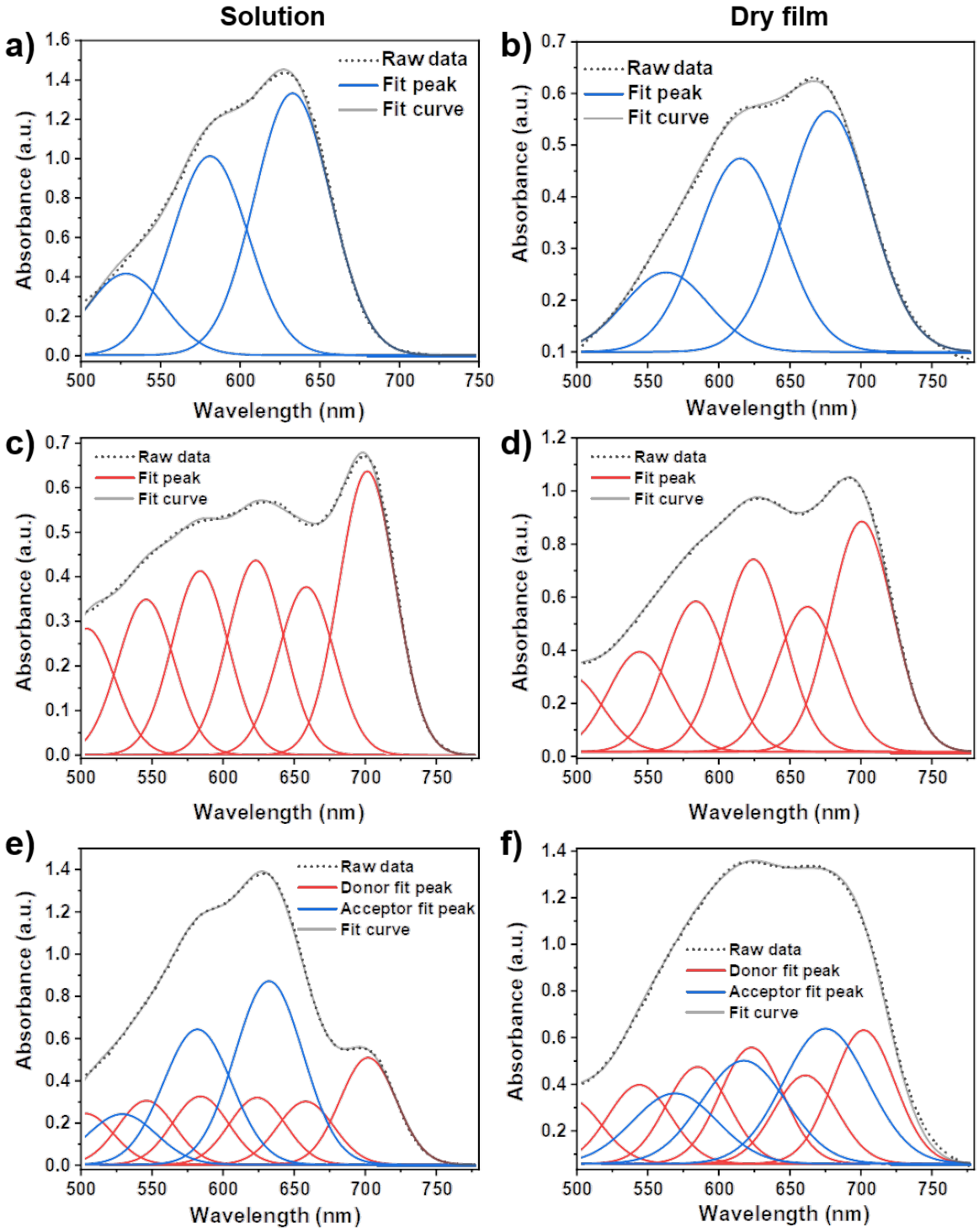

Figure 7.4: The electronic transitions identified from the absorbance spectra of PffBT4T-2OD in the a) solution and b) dry film, respectively. From the EH-IDTBR absorbance spectra in the c) solution and d) dry film, the electronic transitions were identified. The electronic transitions as calculated from the absorbance spectra of PffBT4T-2OD:EH-IDTBR in the e) solution and f) dry film, respectively. The electronic transitions of the neat and blend films (PffBT4T-2OD in red, EH-IDTBR in blue) are determined through modeling with sets of Gaussian functions. Reproduced with permission from Wiley, Copyright 2023. [141]

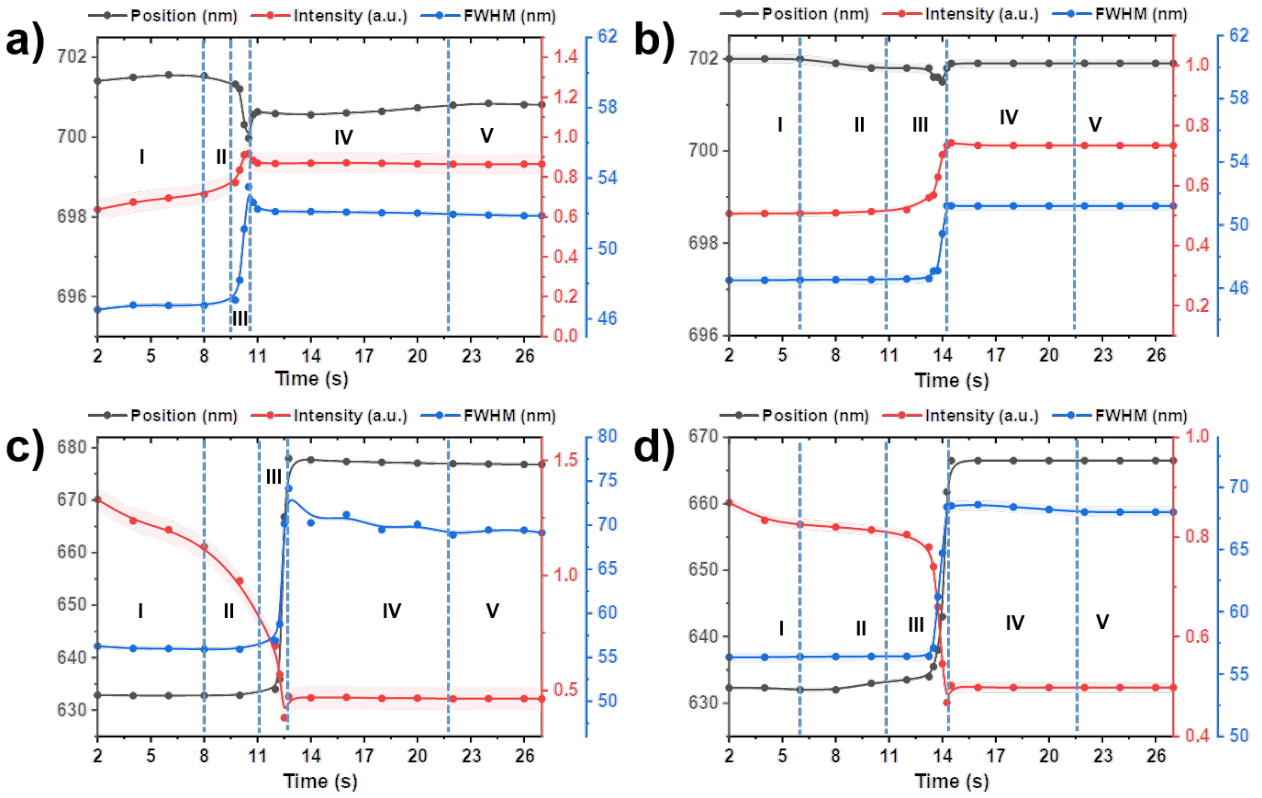

Figure 7.5: Extracted 0-0 transition peak position (grey), peak intensity (red) and the corresponding FWHM (blue) of the polymer donor PffBT4T-2OD in a) neat films and b) PffBT4T-2OD: EH-IDTBR blend films as well as of the small molecular acceptor EH-IDTBR in c) neat films and d) blend films. The solid lines are guides to the eyes. The vertical dashed lines mark the individual regimes I-V. Reproduced with permission from Wiley, Copyright 2023. [141]

fourth regime (regime IV), a small but not negligible fallback of the peak positions, intensities and the FWHM values is observed for the neat thin films. However, this phenomenon is insignificant in the blend thin film, especially in the PffBT4T-2OD signal, revealing the mutual influence on the formation of a donor-acceptor interaction during the drying. In the final regime (regime V), again all parameters are stable, suggesting the thin film is no more changing.

7.2 Crystalline Structure

GIWAXS measurements are utilized to determine the crystallite structure of the final dried thin films. [226],[227] Figure 7.6a - Figure 7.6c demonstrate the 2D GIWAXS data of the neat PffBT4T-2OD film, neat EH-IDTBR film and the PffBT4T-2OD: EH-IDTBR active layer, respectively. The line profiles along the out-of-plane (OOP) and in-plane (IP) directions for

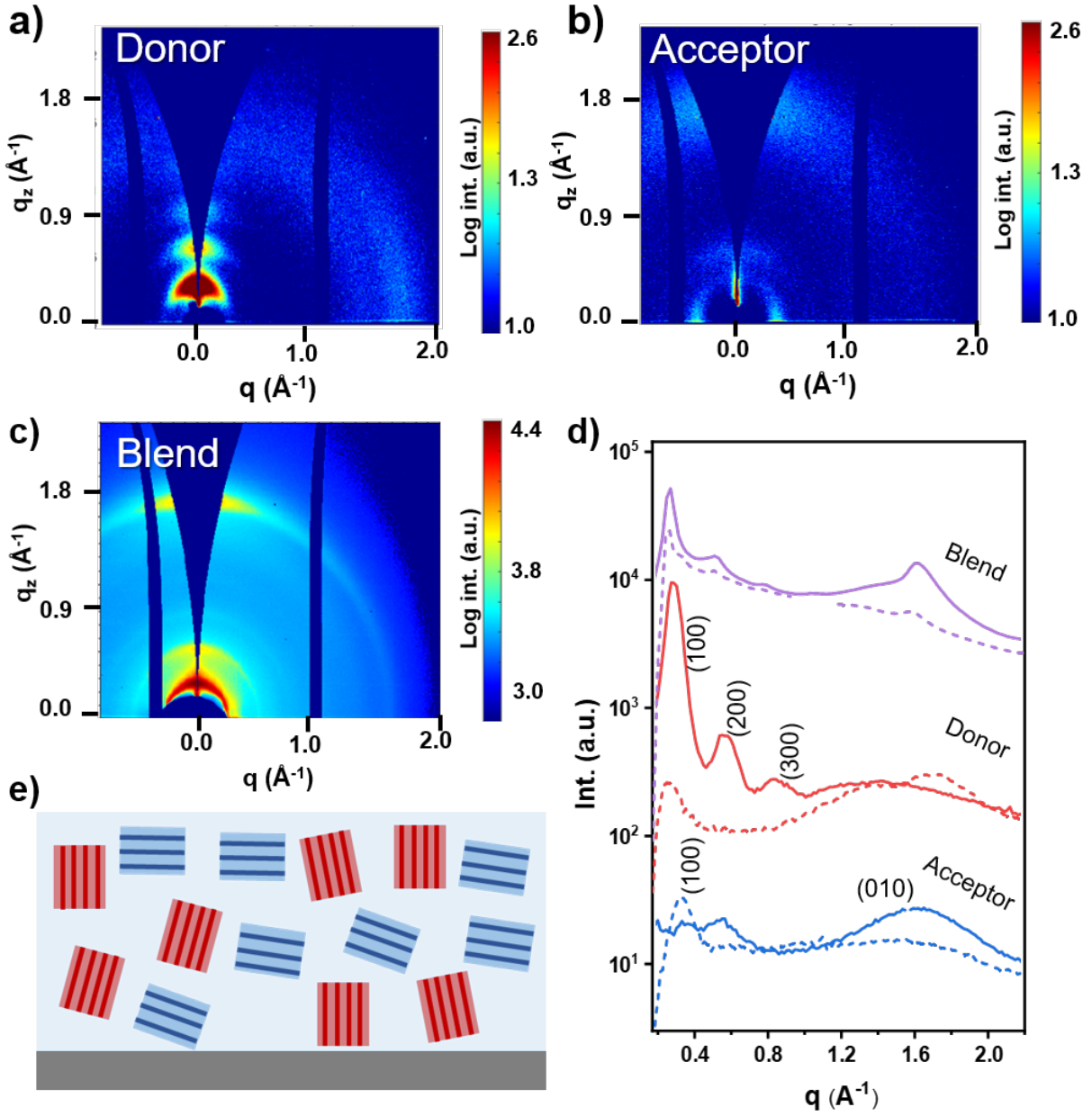

Figure 7.6: a) 2D GIWAXS data of PffBT4T-2OD: EH-IDTBR active layer printed out of TMB solvent. b) Out-of-plane (solid line) and in-plane (dash lines) profiles of the donor (PffBT4T-2OD), acceptor (EH-IDTBR) and blend (PffBT4T-2OD: EH-IDTBR) films, which are shifted along the y-axis for clarity. Characteristic Bragg peaks are indexed. c) Illustration of the crystalline orientation of the donor PffBT4T-2OD crystallites (red) and acceptor EH-IDTBR crystallites (blue) in the blend thin film, which is coated on the glass substrate (grey matrix). Reproduced with permission from Wiley, Copyright 2023. [141]

the thin films are extracted from the 2D GIWAXS data with cake cuts (Figure 7.6d). The stacking distance of the crystallites is estimated by the equation d = $2\pi q^{-1}$, where q refers to the Bragg peak position. The neat donor polymer PffBT4T-2OD exhibits a very pronounced edge-on crystallite orientation along the substrate. The distinct main (100) Bragg peak, the (200) peak, and the (300) peak of PffBT4T-2OD are located at around 0.28 $Å^{-1}$, 0.55 $Å^{-1}$, 0.84 $Å^{-1}$ in the OOP direction, respectively. Moreover, a weak peak (010) peak is located at around 1.69 $Å^{-1}$ in the IP direction, suggesting the excellent long-range ordering of PffBT4T-2OD crystallites in the neat polymer film. In contrast, the neat small molecule acceptor EH-IDTBR shows the opposite behavior. A (100) Bragg peak is located at 0.32 $Å^{-1}$ in the IP direction and a (010) peak is located at 1.63 $Å^{-1}$ along the OOP direction, suggesting a typical face-on crystallite structure in the neat acceptor film. In the PffBT4T-2OD: EH-IDTBR blend thin film, both orientations are observed. Edge-on and face-on crystallites are present in the printed active layer, which are attributed to PffBT4T-2OD and EH-IDTBR, respectively (Figure 7.6e). The dominant edge-on (donor) and face-on (acceptor) orientations remain similar to the neat thin films. However, details of the crystalline structure show changes. Concerning the polymer donor, the (100), (200), and (300) Bragg peaks of PffBT4T-2OD move slightly towards lower values in the OOP direction, which are 0.27 $Å^{-1}$, 0.52 $Å^{-1}$, 0.80 $Å^{-1}$. These changes demonstrate a larger lamellar stacking distance of PffBT4T-2OD in the blend thin film compared with the neat film. Concerning the small molecule acceptor, the (100) Bragg peak of EH-IDTBR moves to a higher q value 0.33 $Å^{-1}$ in the blend thin film, revealing a denser packing of the lamellar distance in the EH-IDTBR crystallites in the blend thin film compared with the neat film. Moreover, the (010) peak of EH-IDTBR decreases in its position to 1.61 $Å^{-1}$ along the OOP direction, which is attributed to the π -π stacking change of EH-IDTBR. Thus, the conclusion is drawn that the presence of PffBT4T-2OD causes the face-on dominant EH-IDTBR crystallites in the blend thin films to exhibit tighter lamellar packing but a looser π -π stacking structure. The edge-on dominated PffBT4T-2OD crystallites are also perturbed by the presence of the small molecule acceptors. Thus, in total, the printed active layer is less perfect in its crystalline structure as compared to the neat films, which offers potential for future optimization of the print process.

7.3 Conclusion

Towards the industrial large-scale production of OSCs, blend films of the non-fullerene small molecule acceptor EH-IDTBR and the polymer donor PffBT4T-2OD are printed out of a non-halogenated solvent using a slot die coater. Utilizing ambient conditions with no need for an inert atmosphere and in combination with low processing temperatures (60 °C), the blend system PffBT4T-2OD: EH-IDTBR is interesting for environmentally friendly upscaling.

To gain a more detailed understanding of the complex film formation process during printing, the temporal evolution of the morphology and of the molecular conformation and aggregation properties is investigated by in situ GISAXS and in situ UV-Vis measurements. A continuous growth process of the domain structures with five regimes is determined during the active layer printing. Notably, in the third regime, the most drastic growth happens for all domain sizes due to the fast evaporation of the solvent. In parallel, an abrupt molecular aggregation occurs in the acceptor as well as in the donor molecules, while the types of aggregates differ as differs the strength of the related 0-0 electronic transitions. Moreover, the abrupt growth of the domains in the middle-size scale prior to the small-size scale can be explained by the additional aggregation of small-size domains. After most of the solvent has evaporated, an increase in disorder across the domain structure is found. In the final dry active layer, the PffBT4T-2OD exhibits an edge-on crystal orientation while the EH-IDTBR has a face-on dominated crystallite structure along the substrate. Furthermore, the EH-IDTBR crystallites in the active layer show a denser lamellar packing but a looser π -π stacking structure, owing to the presence of PffBT4T-2OD. In addition, the PffBT4T-2OD crystallites are perturbed by the presence of EH-IDTBR in the printed active layer. Notably, by a combination of the in situ and ex-situ measurements, this work provides an in-depth study of the active layer formation kinetics while printing out of halogen-free solvent, which is of great importance in the commercialization of OSCs.

8 Active Layer Degradation in Organic Solar Cells

The following chapter is mainly based on the work "Operando study of the influence of the small molecule acceptor on the morphology induced device degradation of organic solar cells with different π -π stacking crystallinity" *(Xinyu et al., under review, 2023)*.

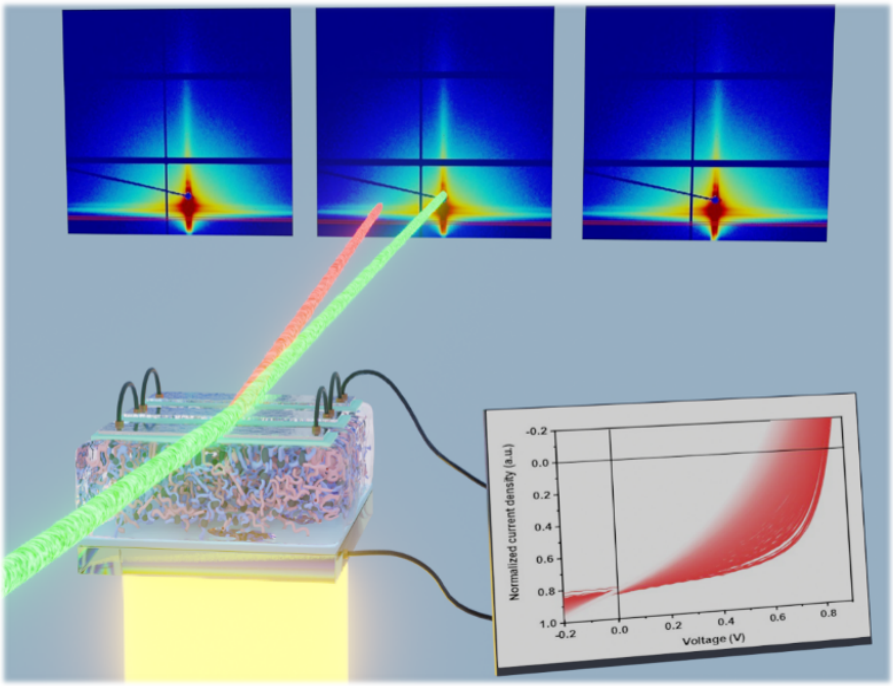

In the previous chapter, the non-fullerene active layer (PffBT4T-2OD: EH-IDTBR) was printed out of the non-halogenated, environmentally friendly solvent 1,2,4-trimethylbenzene (TMB) via slot-die coating method. In situ (GISAXS, UV-Vis) and ex situ (GIWAXS) measurements are used to investigate the temporal evolution of the morphology as well as the molecular conformation and aggregation properties in acquiring a more in-depth understanding of the complex film formation process during printing. It provides an in-depth study of the active layer formation kinetics while printing out of halogen-free solvent, which is of great importance in the commercialization of OSCs. Nonetheless, to meet the requirements of commercialization for the field of OSCs, the poor stability of OSCs remains a significant bottleneck. [81],[228],[229] Multiple issues can cause device degradation,

for example, the operation atmosphere, interfaces, and the actual layer morphology, among others. [178],[230],[231],[232],[233],[234],[235] Generally, these degradation processes can be divided into chemical and physical degradation processes. [77],[45] Chemical degradation is commonly introduced by the presence of oxygen or water. [45],[77] The physical degradation, arising mainly from the morphology deterioration of bulk heterojunction (BHJ) films, is caused both by the device operation itself and the presence of active layer morphologies far from equilibrium. [84],[82] Thus, physical degradation is typically unavoidable and should be considered in the phase of new material development. However, despite initial work involving operando studies, so far, the understanding of the performance loss caused by the active layer morphology, especially in novel non-fullerene acceptor (NFA) molecules is still not well understood.

In addition to the adjustable spectral absorption range, excellent crystallinity with respect to the intermolecular π -π stacking is another advantage of the high-efficiency small molecule NFAs, which is crucial for intermolecular charge transport. [236],[237],[238] However, excessive π -π stacking crystallinity in the acceptor can induce obvious aggregation, thereby causing an unfavorable phase separation between the donor and the acceptor phase, resulting in poor device performance. [239] Multiple efforts focus on optimizing the crystallinity of the NFAs with balanced π -π stacking, thereby achieving a high OSC performance. [240],[241],[242],[43] Nevertheless, little attention has been paid to the understanding of the relationship between the OSC stability and the active layer morphology in conjunction with different degrees of crystallinity. Thus, the identification of degradation mechanisms related to the active layer morphology induced by different degrees of π -π stacking crystallinity will significantly contribute to materials design rules for highly efficient and stable OSCs.

In this chapter, we aim to investigate such a relationship and uncover the degradation mechanisms that can guide material design rules for highly efficient and stable OSCs. Accordingly, we select three different small molecule NFA acceptors, BTP4F, IT4CL, and IT4F, and the reference fullerene acceptor ($PC_{71}BM$), blended with the widely used polymer donor PBDBT-2F (also called PM6), respectively. Full names of the materials are offered in Section 4.1.1. The corresponding OSCs exhibit different degrees of π -π stacking crystallinity of the acceptor molecules. To investigate the underlying correlation between the temporal morphology and the performance of the OSCs dominated by different degrees of π -π stacking crystallinity, we utilize operando grazing-incidence small angle X-ray scattering (GISAXS). [39] This technique allows us to closely examine the underlying active layer morphology during the device operation. [84],[82] As reported previously, Yang et al. found that the residual solvent additive in the active layer is a key cause of solar cell degradation. [230] Thus, to identify the intrinsic degradation caused by the material in a real working device geometry, OSCs are fabricated without any additive. In addition, the operando experiments are

conducted in a vacuum chamber to minimize the effects of oxygen and water present in the air, which could introduce chemical degradation, or even mediate geometrical changes in the donor polymer backbone, which results in severely reduced performance. [84],[243] Moreover, ex-situ measurements are introduced, including atomic force microscopy (AFM), grazing incidence wide angle X-ray scattering (GIWAXS), ultraviolet-visible (UV-Vis) spectroscopy and transient absorption (TA) spectroscopy, to understand the underlying mechanisms of the device degradation based on different crystalline acceptors. This work highlights the complex interplay between charge carrier transport, crystallinity, and the evolution of the device performance and the morphology in OSCs, offering valuable insights into the device stability based on different acceptor molecules dominated by different π -π crystallinity.

8.1 Optical, Electronic Properties and Device Performance

8.1.1 Absorption

The UV-Vis spectra of the pure thin films are provided in Figure 8.1a, with PBDBT-2F displaying two peaks at 576 nm and 617 nm. The primary peaks are located at 721 nm, 748 nm, and 820 nm for IT4F, IT4CL, and BTP4F, respectively. $PC_{71}BM$ exhibits two peaks at 378 nm and 477 nm. The non-fullerene acceptors demonstrate a main absorption towards a higher wavelength range than the PBDBT-2F donor, complementing the polymer absorption and providing a broad light absorption range. Figure 8.1c-d displays the UV-Vis absorption data of the PBDBT-2F blend films with different acceptors before and after device operation. The active layers exhibit a minor reduction in the donor region, while distinct differences are observed in the acceptor region after the operando experiment. Consequently, the main absorption peak of the acceptors in the donor region is analyzed to determine any shift in peak position and change in peak intensity after the operando experiments (Figure 8.1b). The PBDBT-2F:BTP4F sample displays a 5 nm redshift in the peak position and a decrease in the intensity to 0.98 of its initial value, suggesting a J-aggregation tendency. [244],[104] The PBDBT-2F:IT4F and PBDBT-2F:IT4CL samples exhibit no shift in peak position but a decrease in the intensity to 0.93 and 0.94 of their initial values, respectively. The main peak of $PC_{71}BM$ in the PBDBT-2F:$PC_{71}BM$ sample is situated at 357 nm and experiences a 3 nm blue shift with an increased intensity of 1.02 compared to its initial value.
In order to identify the absorption loss in the non-fullerene acceptors of the active layer from neighboring ZnO blocking layer or not, the PBDBT-2F:IT4F active layer coated on the glass substrate and on the ZnO/glass substrate and aged at different times as shown in Figure 8.2. The active layer on the glass indicates very limited absorption loss even after 12h of light degradation. Notably, a more extensive intensity loss on the ZnO/ITO glass substrate

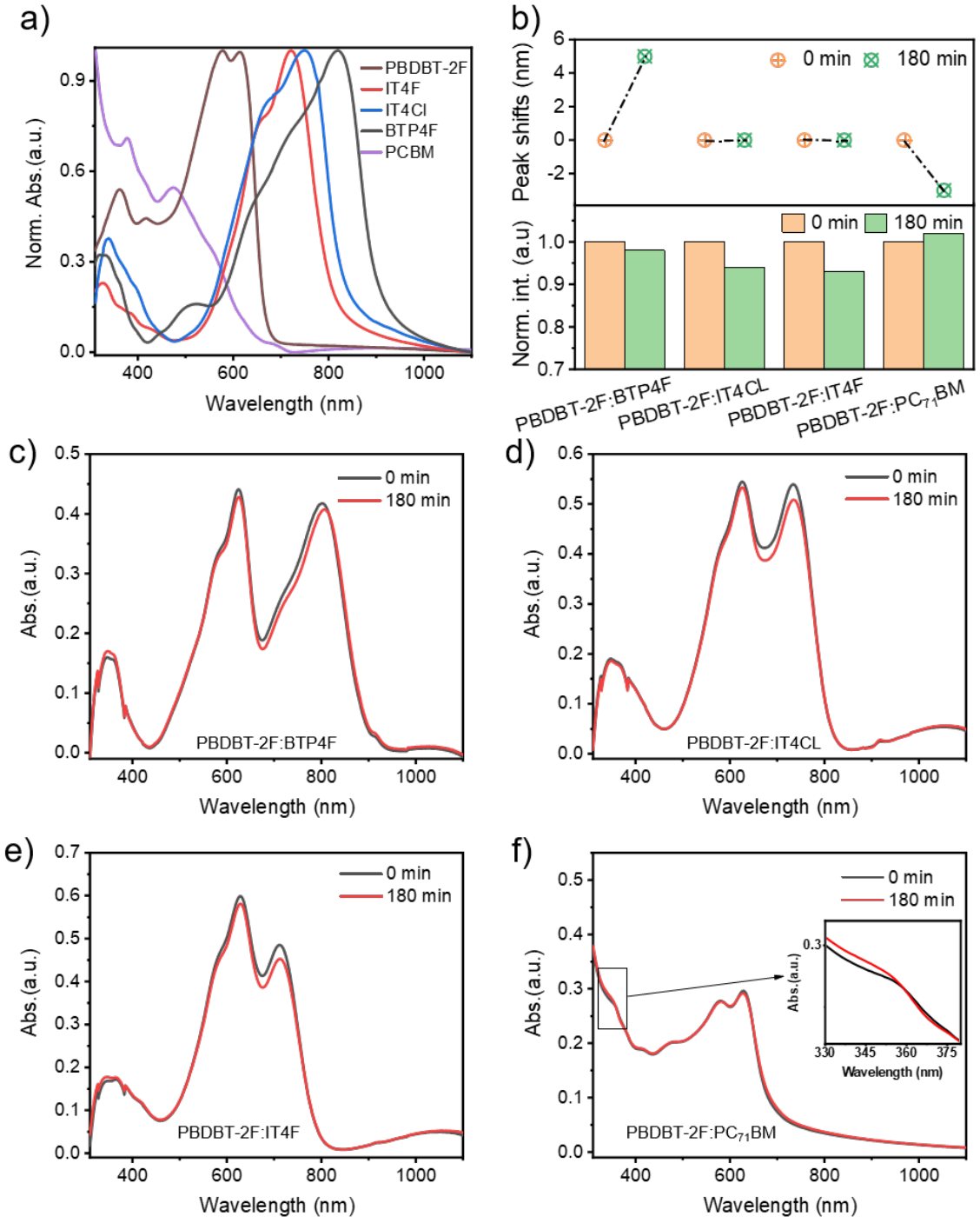

Figure 8.1: a) Normalized UV-Vis spectroscopy of neat thin films. b) Position and normalized intensity changes of the UV-Vis absorption main peak of the acceptor region caused by device operation. UV-vis spectrum of active layer fabricated from c) PBDBT-2F:BTP4F, d) PBDBT-2F:IT4CL, e) PBDBT-2F:IT4F,and f) PBDBT-2F:$PC_{71}BM$ before and after illumination, respectively.

is observed after 12 h of light degradation, which suggests that ZnO is one of the factors accelerating the absorption loss of the non-fullerene acceptors. In addition, the OSCs based

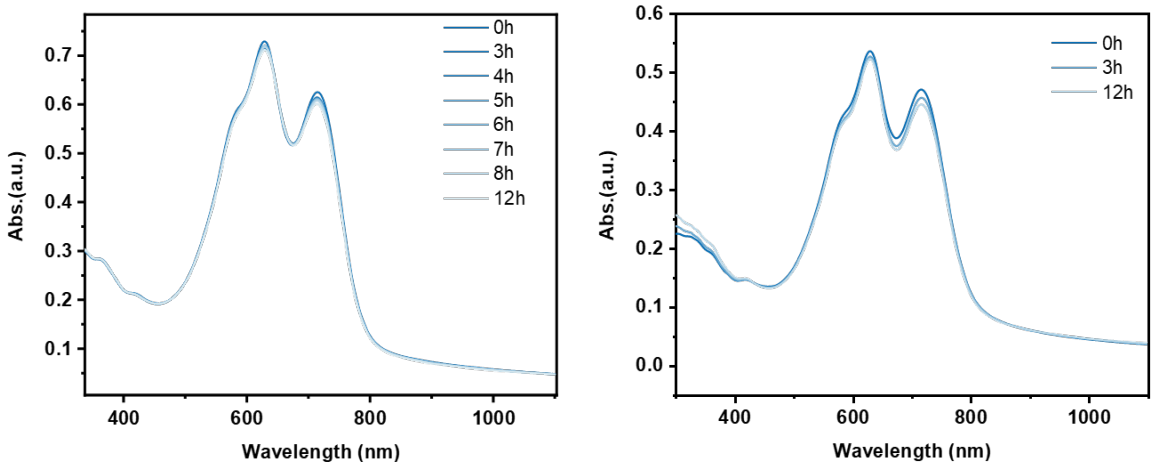

Figure 8.2: UV-Vis spectroscopy of PBDBT-2F:IT4F active layer a) on the glass substrate and b) on the ZnO/ITO glass substrate with different times of light illumination.

on PBDBT-2F:IT4F active layer working continues for 3h under AM 1.5 light illumination, the absorption loss of the acceptor is more severe than the active layer on the ZnO/glass substrate without the voltage sweep under AM 1.5 light illumination for 3h. It suggests that the voltage applied to the device will exacerbate the absorption loss of the non-fullerene acceptor in the active layer.

8.1.2 Transient Absorption

To give insights into the dynamics of the excited states of the active layer before and after light illumination, the fresh and aged blend films are investigated using femtosecond transient absorption spectroscopy (TAS). This technique allows us to have a direct observation of the charge transfer process between the donor polymer and the acceptor. [245],[246] To get the preferable excitation of the NFAs, PBDBT-2F:BTP4F blends are pump at 800 nm, PBDBT-2F:IT4CL and PBDBT-2F:IT4F blends are pump at 730 nm, respectively. And the corresponding TA spectra of PBDBT-2F:BTP4F, PBDBT-2F:IT4CL and PBDBT-2F:IT4CL samples before and after the operando study are shown in Figure 8.3. All NFA blends show a clear acceptor ground state bleach (GSB) at 0.2 ps due to the direct excitation of this component. In addition, the presence of the PBDBT-2F GSB (580-640 nm) at 0.2 ps in all blends suggests that some ultrafast hole transfer occurs. [247] Since the excitation wavelength does not generate excitons on the polymer PBDBT-2F, the ultrafast emergence of the donor GSB likely indicates a dissociation of the NFA excitons generated in close proximity to the donor:acceptor (D:A) interface. [245],[248] As hole transfer progresses, the PBDBT-2F GSB increases, whilst the NFA GSB falls due to overlap with the polaronic PIA

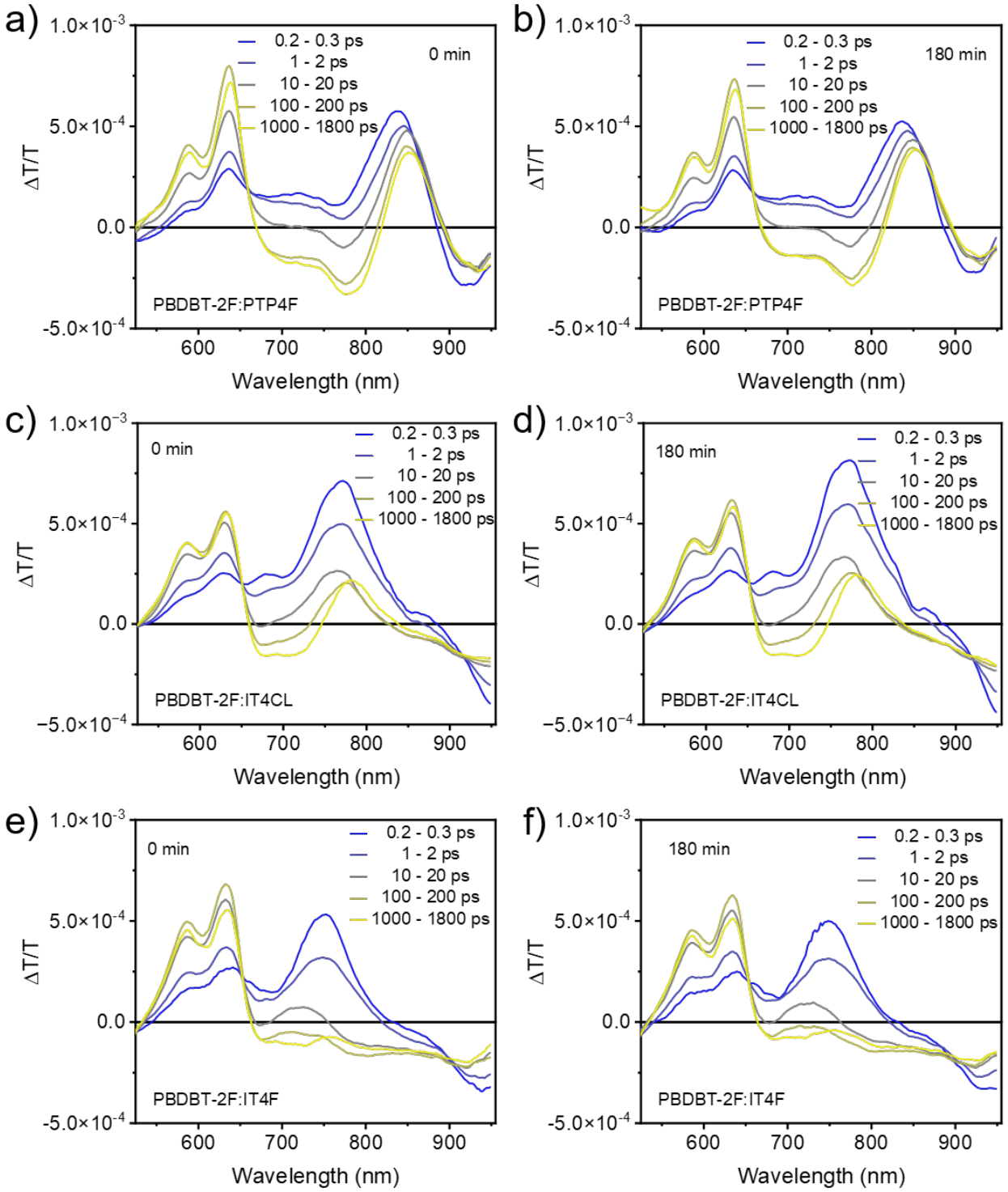

Figure 8.3: TA spectra of a) fresh (0 min) and b) aged (180 min) PBDBT-2F:BTP4F films pumped at 800 nm, c) fresh (0 min) and d) (0 min) aged PBDBT-2F:IT4CL films, e) fresh (0 min) and f) aged (180 min) PBDBT-2F:IT4F films pumped at 730 nm respectively, for preferential NFAs excitation.

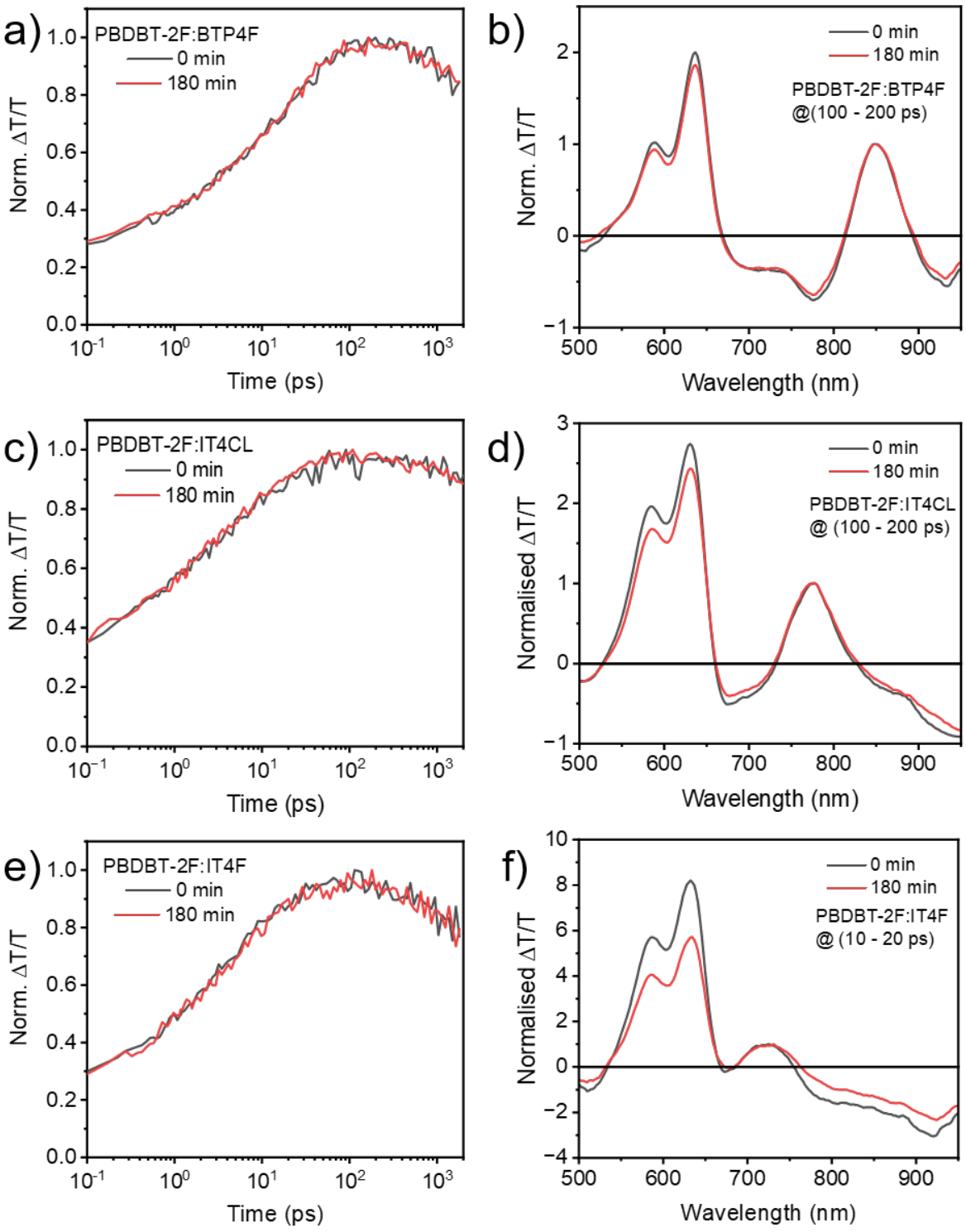

Figure 8.4: Hole transfer kinetics extracted from polymer ground state bleach GSB (580–650 nm) for a) PBDBT-2F:BTP4F, c) PBDBT-2F:IT4CL and e) PBDBT-2F:IT4F blends. Selected normalized spectra to the NFAs GSB of the b) PBDBT-2F:BTP4F, d) PBDBT-2F:IT4CL and f) PBDBT-2F:IT4F after hole transfer is completed.

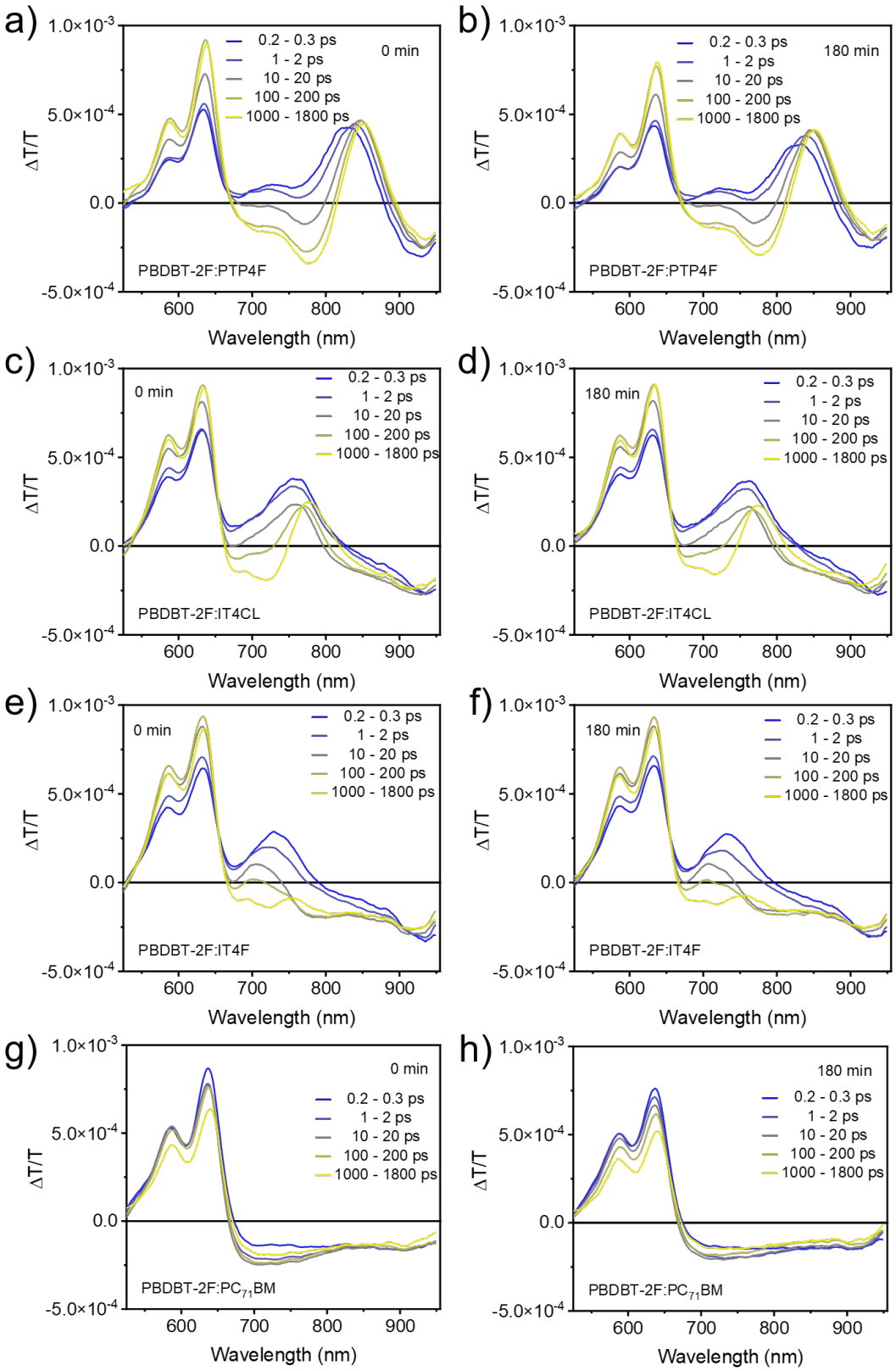

Figure 8.5: TA spectra at different time delays for PBDBT-2F:BTP4F, PBDBT-2F:IT4CL, PBDBT-2F:IT4F and PBDBT-2F:$PC_{71}BM$ before (0 min) and after (180 min) the operando experiments (pump: 580 nm for the preferable excitation of PBDBT-2F).

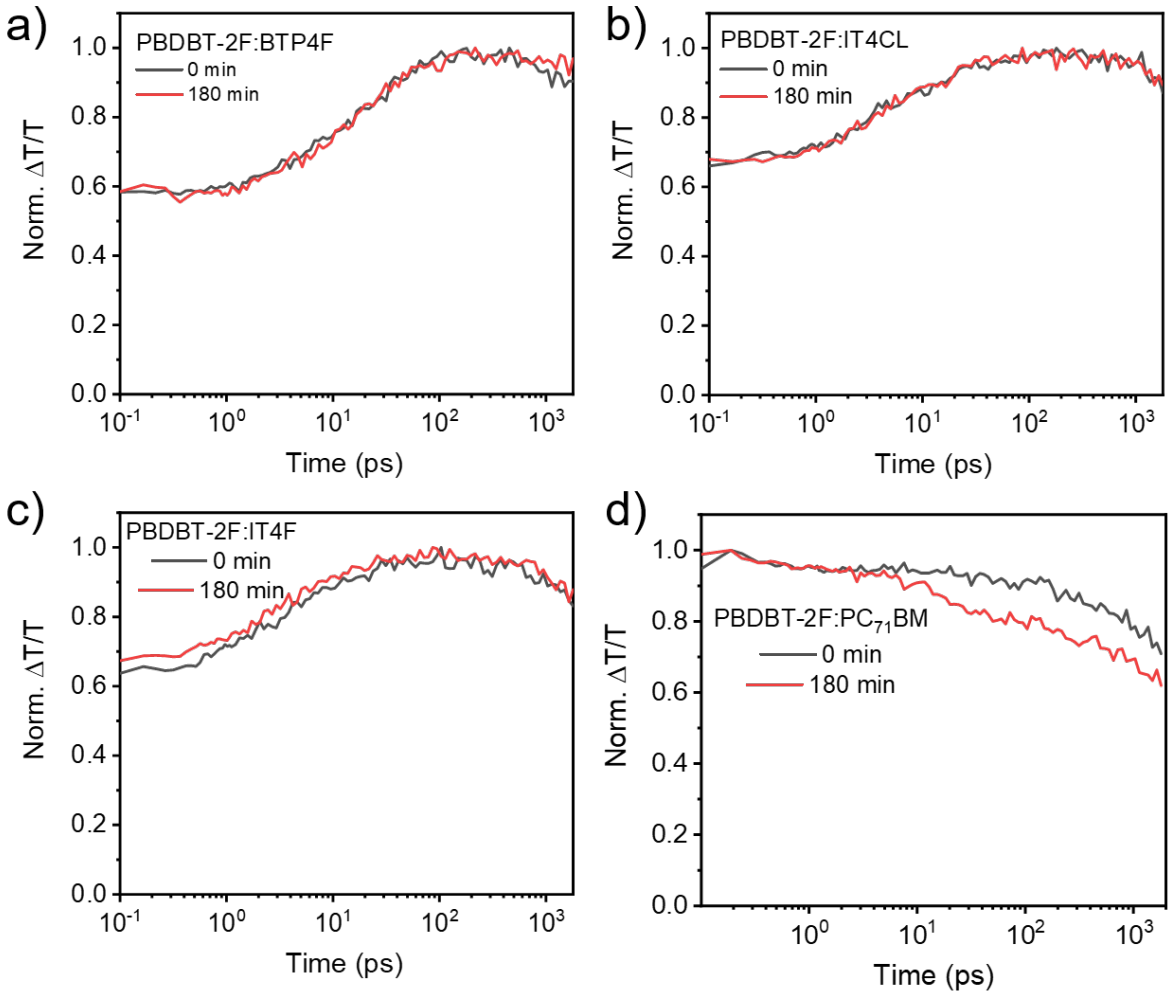

Figure 8.6: Kinetics extracted from polymer ground state bleach (GSB) at 580–640 nm for a) PBDBT-2F:BTP4F, b) PBDBT-2F:IT4CL, c) PBDBT-2F:IT4F and d) PBDBT-2F:$PC_{71}BM$ (pump: 580 nm for the preferable excitation of PBDBT-2F).

on the acceptor. [246],[249] To better understand the hole transfer process of the active layer fabricated between the small molecule and fullerene acceptor individually, the GSB kinetics of the donor (PBDBT-2F, 580-640 nm) are chosen to represent the charge transfer kinetics in Figure 8.4a,c,e. The hole transfer kinetics are comparable in all three NFA samples and show a completion of hole transfer after 100 ps. After the operando experiments, no obvious difference is observed for the intrinsic hole transfer rate for the three small molecules blends, confirming that the interfacial hole transfer process is not noticeably affected by the aging conditions. The normalized spectra to the acceptor peak for various NFA blends are displayed in Figure 8.4b,d,f. to provide insight into the change in hole transfer yield after the operando experiment. For all aged samples, the PBDBT-2F GSB and polaron absorptions (950 nm) are less intense relative to the NFA GSB, which indicates that the hole transfer

yield is reduced. In comparison to PBDBT-2F:BTP4F and PBDBT-2F:IT4CL, the reduction in the polymer GSB and polaron the PBDBT-2F:IT4F sample is much more pronounced, in line with the more severe morphological degradation of this sample.
TA measurements with excitation at 580 nm to primarily excite the polymer PBDBT-2F are also performed, though this wavelength will also excite a fraction of the NFA molecules. [248] As shown in Figure 8.5, the PBDBT-2F GSB initially has a much higher intensity than in the measurements with selective NFA excitation as the excitons are created directly on it. However, the PBDBT-2F GSB also shows the same rise up to 100 ps from the smaller number of excitons generated on the NFA that undergo hole transfer. Figure 8.6 shows the normalized hole transfer kinetics from the polymer GSB between 580 and 650 nm with an excitation of 580 nm. The hole transfer rate appears to be comparable for all NFA combinations in the fresh and aged samples. Notable, for the PBDBT-2F:$PC_{71}BM$ samples, a much faster decay of the excitations on PBDBT-2F, primarily hole polarons as charge transfer occurs on sub-picosecond timescales, is seen after 10 ps in the aged sample (Figure 8.5h). [250] Additionally, the maximum electro-absorption (EA) intensity of PBDBT-2F located at 700 nm at 10 ps decreases in the aged sample (Figure 8.5h), suggesting a fewer charge transfer states are being dissociated into free charge carriers. [246] Thus, the faster decay rate of hole polarons on PBDBT-2F from Figure 8.6d can be ascribed to the increased geminate recombination of charge transfer states in the aged PBDBT-2F:$PC_{71}BM$ blends.
In summary, it can be inferred that the minor reduction in the domain size of the PBDBT-2F: NFAs, accompanied by a slight increase in random distribution, does not significantly impact the D:A interface. Consequently, the hole transfer rate, which is predominantly governed by the interfacial morphology, remains unaltered after the operando experiments. [248] Nevertheless, the domain size decrease coupled with a slightly increased polydispersity result in a reduced hole transfer yield, as a large proportion of excitons decay prior to reaching the D:A interface. This could be due to changes in the shape of the domains, which may impact the transport of excitons to the D:A interface. For the PBDBT-2F:$PC_{71}BM$ blend, which shows a much more severe domain size decay, the morphology surrounding the D:A interface is likely damaged. This results in the increased geminate recombination of charge transfer states before they can separate into free charge carriers.

8.1.3 Device Performance

As previous reports, the solvent additive could play a role in the morphology during the device degradation. [85],[84] To identify the initial degradation mechanism of the material itself, the active layer blends are fabricated without any additive. The corresponding solar cells are fabricated with an inverted device architecture as glass/ITO/ZnO/PBDBT-2F:acceptors /MoO_3 /Ag and the detailed procedure of the device is described in Section

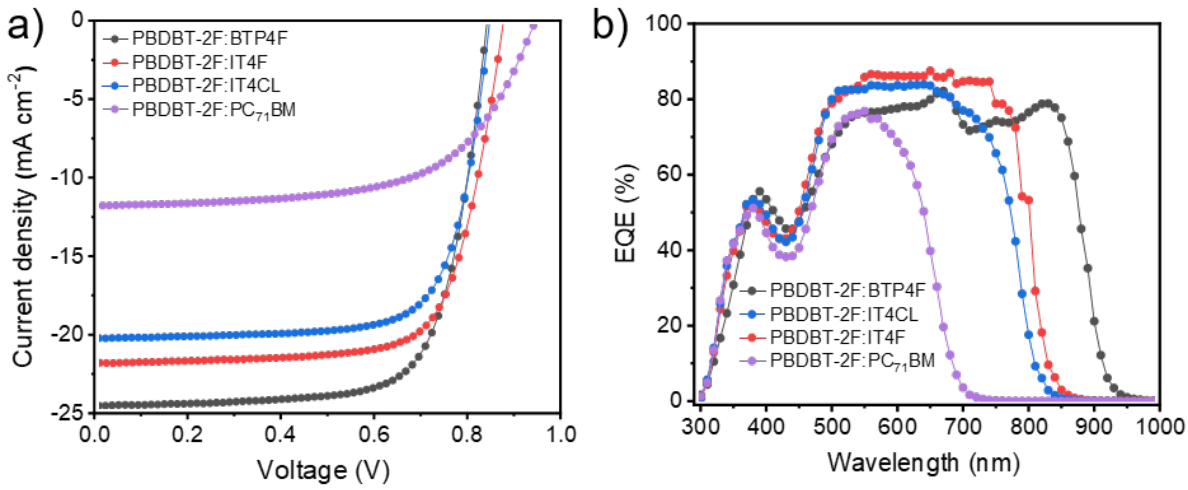

Figure 8.7: a) J-V curves and b) EQE curves of the inverted organic solar cells based on the active layer of PBDBT-2F with different acceptors, respectively.

Table 8.1: Photovoltaic parameters of OSCs fabricated from PBDBT-2F blended with different acceptors, respectively.

Sample	Jsc (mA cm^{-2})	Voc (V)	FF (%)	PCE (%)	PCE$_{max}$ (%)
PBDBT-2F:BTP4F	23.1 ± 1.9	0.83 ± 0.01	70.1 ± 2.0	14.5 ± 0.3	14.9
PBDBT-2F:IT4F	20.1 ± 1.4	0.89 ± 0.01	65.6 ± 1.5	12.9 ± 0.2	13.1
PBDBT-2F:IT4CL	18.9 ± 1.8	0.79 ± 0.01	70.3 ± 1.6	11.5 ± 0.2	11.7
PBDBT-2F:PC$_{71}$BM	11.0 ± 0.8	0.94 ± 0.01	58.9 ± 2.0	6.3 ± 0.4	6.78

4.4.1. Table 8.1 summarizes the photovoltaic parameters. OSCs with NFAs blends show very promising performance and the J-V curves are shown in Figure 8.7a, which are 14.9 %, 13.1 % and 11.7 % with an average Jsc of 23.1 ± 1.9 mA cm^{-2}, 20.1 ± 1.4 mA cm^{-2} and 18.9 ± 1.8 mA cm^{-2}, in the BTP4F, IT4F, and IT4CL, respectively. In comparison, the solar cell with fullerene-based acceptor only reached 6.8 % with an average Jsc of only 11.0 ± 0.8 mA cm^{-2}. The undesired self-aggregation of IT4CL, leading to reduced miscibility with PBDBT-2F, causes a lower PCE than the IT4F samples. From the external quantum efficiency (EQE) results shown in Figure 8.7b, PBDBT-2F:BTP4F-based OSCs exhibit the broadest spectra response range, with an integrated Jsc of 24.0 mA cm^{-2}, PBDBT-2F:IT4F with the highest light responds in the visible range, accumulated an integrated Jsc of 20.9 mA cm^{-2}. The integrated Jsc is 19.7 mA cm^{-2} for the PBDBT-2F:IT4CL is 19.6 mA cm^{-2}. The fullerene-based device shows the lowest spectra response in a narrow range of 300-700 nm, resulting in a poor integrated Jsc of only about 11.6 mA cm^{-2}. Above all, the data obtained from EQE is in good agreement with the trend of J-V results and UV-Vis spectra.

8.2 Film Morphology

8.2.1 Surface Morphology

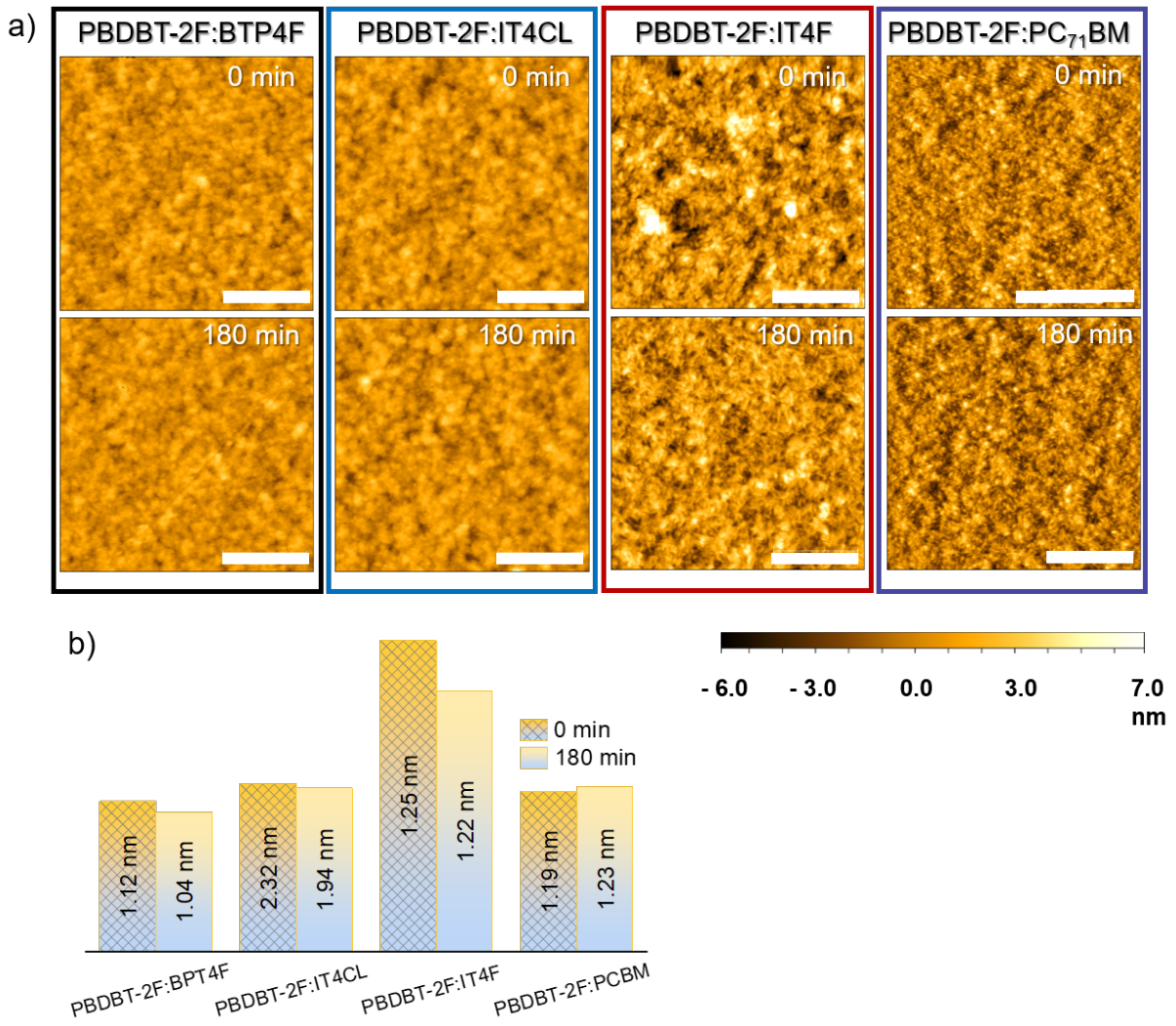

Figure 8.8: a) AFM topography and b)The roughness of the OSC active layer surface before and after operando experiment. (insert scale bar is 1 μm in length)

To investigate the surface morphology changes in the active layer with different acceptors before and after the OSC operando experiments, AFM measurement is carried out and the corresponding height information is shown in Figure 8.8. The initial roughness of the active layer based on PBDBT-2F with different acceptors is very small suggesting very well miscibility between the donor and acceptor. After the OSCs operated under AM 1.5 G light illumination for 180 min, the roughness of the active layer blends with NFAs slightly decrease, indicating the formation of finer structures. In contrast, the active layer with the fullerene acceptor exhibits a slight increase in roughness, which may be attributed to

the significant decomposition of the middle-size structure, affecting the surface geometry. Interestingly, as the roughness of the PBDBT-2F:IT4F sample exceeds 2 nm, it provides sufficient contrast for the AFM measurements to clearly observe the morphological changes due to the device's operation. Due to the operando experiment, the spindle-shaped domains transform into linear and smaller structures on the surface. This observation further supports the crucial role of domain structure stability in determining the performance and stability of OSCs.

8.2.2 Crystalline Structure

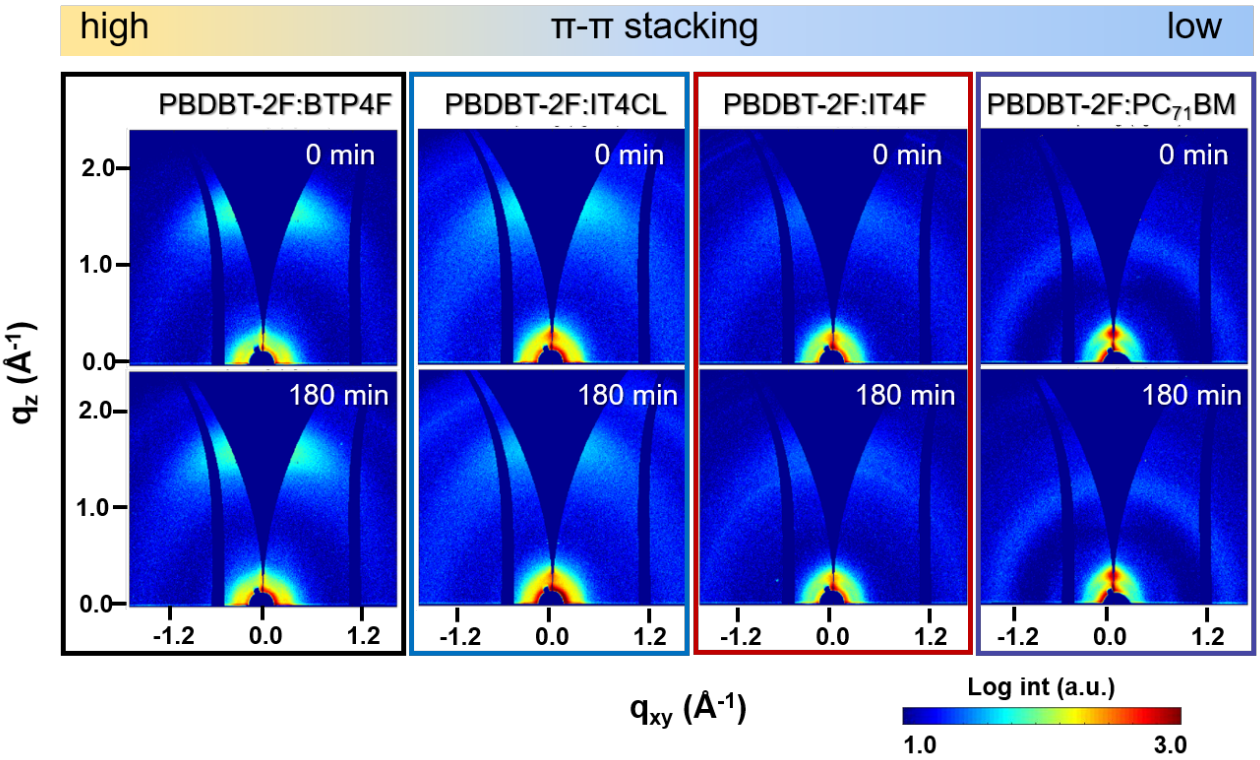

Figure 8.9: 2D GIWAXS data of the active layer based on different acceptors before (0 min) and after (180 min) the operando measurements. The different degrees of π -π stacking in the OOP (out of plane) direction are indicated as high to low.

GIWAXS measurements are used to determine the crystallite structure in the OSCs of PBDBT-2F blended with different acceptors before and after the in operando measurement. Figure 8.9 presents the 2D grazing-incidence wide-angle X-ray scattering (GIWAXS) data of the OSCs (ITO/ZnO/active layer/MoO_3/Ag), where the active layer is fabricated from PBDBT-2F combined with the different acceptors, displaying a decrease in the crystallinity from BTP4F (left) to $PC_{71}BM$ (right). Previous studies showed that the neat PBDBT-2F thin

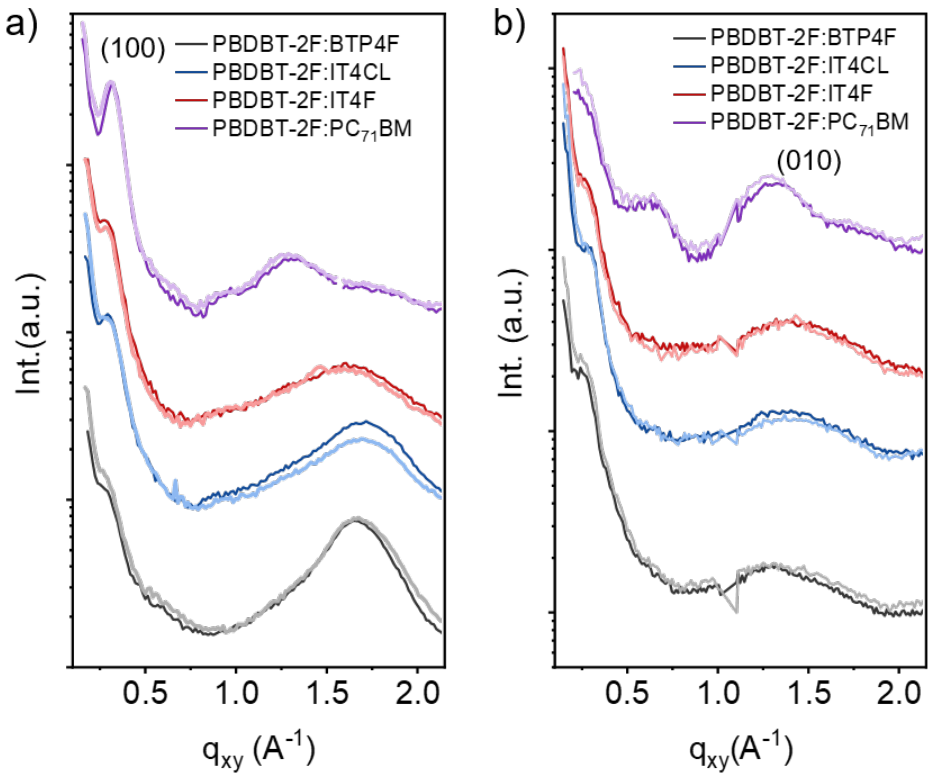

Figure 8.10: a) Out-of-plane (OOP) and b) in-plane (IP) cuts from the 2D GIWAXS data of the active layers based on different accepters before (dark lines) and after (light lines) the operando measurements. The characteristic Bragg peaks are labelled. The curves are shifted along the y-axis for the sake of clarity.

film exhibits a very weak and broad (010) Bragg peak, indicating a poor π -π stacking of the polymer. [132],[140],[134] A prominent ring-like (100) peak at q $\approx$ 0.3 $Å^{-1}$ with a significant intensity distribution in the out-of-plane (OOP) direction suggests a relatively isotropic orientation, while edge-on crystallinity remains discernible in the polymer chains. In the PBDBT-2F:BTP4F blends, a notable face-on crystal orientation is evident, distinguished by the presence of the (100) peak along the in-plane (IP) direction and the (010) peak along the OOP direction. The absence of a discernible (100) peak for the donor polymer in the OOP direction implies a well-intermixed PBDBT-2F and BTP4F phase. In the other three studied blends, the characteristic (100) peak of PBDBT-2F persists, with the peak intensity for the PBDBT-2F:IT4CL sample marginally surpassing that of the PBDBT-2F:IT4F sample Figure (8.10). This finding can be attributed to the replacement of Cl with F atoms in the acceptor molecule, which reduces the steric hindrance effect for the IT4CL packing, thereby promoting its molecular planar self-aggregation and resulting in a much higher π - π

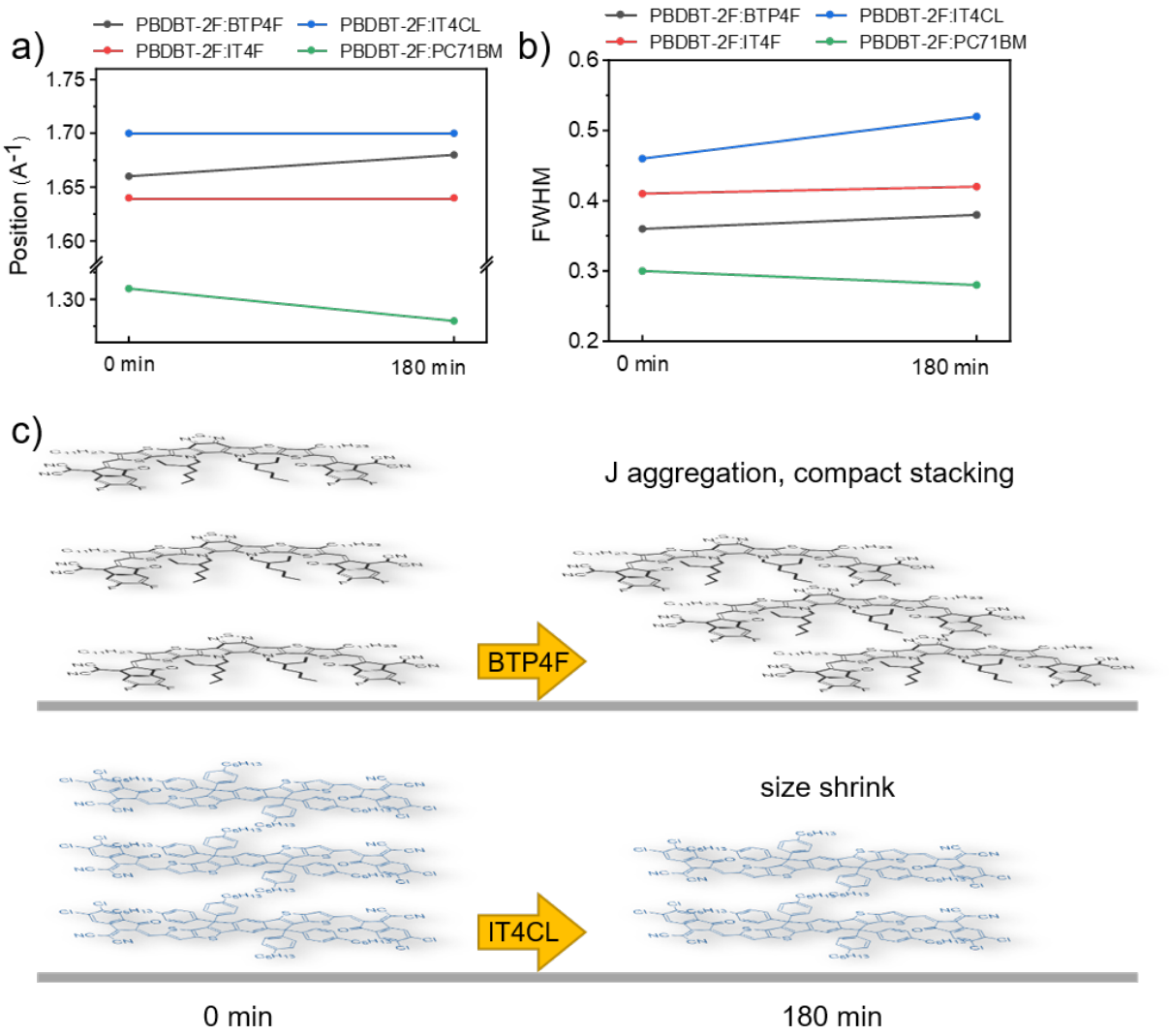

Figure 8.11: The (010) crystal position and b) crystal FWHM of the active layer based on PBDBT-2F with different acceptors along the OOP direction, before (0 min) and after degradation (180 min), respectively. c) Sketch of π -π molecular packing of the BTP4F (upper panel) and IT4CL (lower panel) in the active layer before (0 min) and after degradation (180 min).

stacking crystallinity. [135] It implies a more pronounced donor and acceptor crystalline phase segregation within the PBDBT-2F:IT4CL thin film. As shown in Figure 8.10a, regarding the π -π stacking in the OOP orientation, the PBDBT-2F:BTP4F sample exhibits the highest peak intensity located at 1.66 Å^{-1} with a stacking distance of 3.77 Å. PBDBT-2F:IT4CL shows the second-highest intensity located at 1.70 Å^{-1} with a stacking distance of 3.69 Å, while the PBDBT-2F:IT4F sample has the lowest π -π stacking crystallinity at 1.64 Å^{-1} with a distance of 3.82 Å. Due to the spherical chemical structure of $PC_{71}BM$, there is almost no distinguishable π -π stacking crystallinity in the PBDBT-2F:$PC_{71}BM$ sample. Despite the (100) peak for PBDBT-2F, an isotropic fullerene ring (located at 1.31 Å^{-1}) with a stacking

distance of 4.77 Å is observed. From the above observations, we conclude that OSCs fabricated with PBDBT-2F:BTP4F and PBDBT-2F:IT4CL are dominated by the π -π stacking crystallinity. In addition, the PBDBT-2F:BTP4F blend having a slightly larger π - π stacking distance than the PBDBT-2F:IT4CL blend reveals a better intermixing of the donor-acceptor (010) crystallinity phase.
To have a quantitative analysis of the crystalline change for the PBDBT-2F blended with different acceptors before and after the operando measurement in the OOP direction, the detailed information of the (010) peak is shown in Figure 8.11a-b. In the PBDBT-2F:BTP4F OSC, the (010) peak exhibits a red shift, corresponding to a decreased π -π stacking distance of the crystals. The (010) peak intensity diminishes in the PBDBT-2F:IT4CL blends, indicating a reduction in the π -π stacking crystallites due to the device operation. Due to the relatively poor crystallinity, no significant crystallinity changes are observed for the PBDBT-2F:IT4F blend. The characteristic fullerene ring shifts from 1.31 to 1.29 $Å^{-1}$ in the PBDBT-2F:$PC_{71}BM$ blend, suggesting an increased π -π stacking distance. By combining the GIWAXS and UV-Vis results, it is inferred that BTP4F undergoes a π -π crystalline shrinkage with a J-aggregation tendency, suggesting a de-mixing of the PBDBT-2F and BTP4F. In the case of IT4CL, π -π crystallinity is weakened in the OSC after the operando measurement (Figure 8.11c).

8.3 Active Layer Degradation in Device

In order to observe active layer degradation evolution when the OSC device is in operation, a custom-designed chamber combined with GISAXS measurement which allows the tracking of the photovoltaic characteristics of solar cells and the corresponding active layer morphology simultaneously. To exclude the influence of water, oxygen and temperature, the solar cells are operated in an atmosphere with a constant temperature of 15 °C and a vacuum around 5×10^{-2} Pa. The experiment details including the setup and parameter setting are discussed in Section 3.5.2.

8.3.1 J-V Evolution

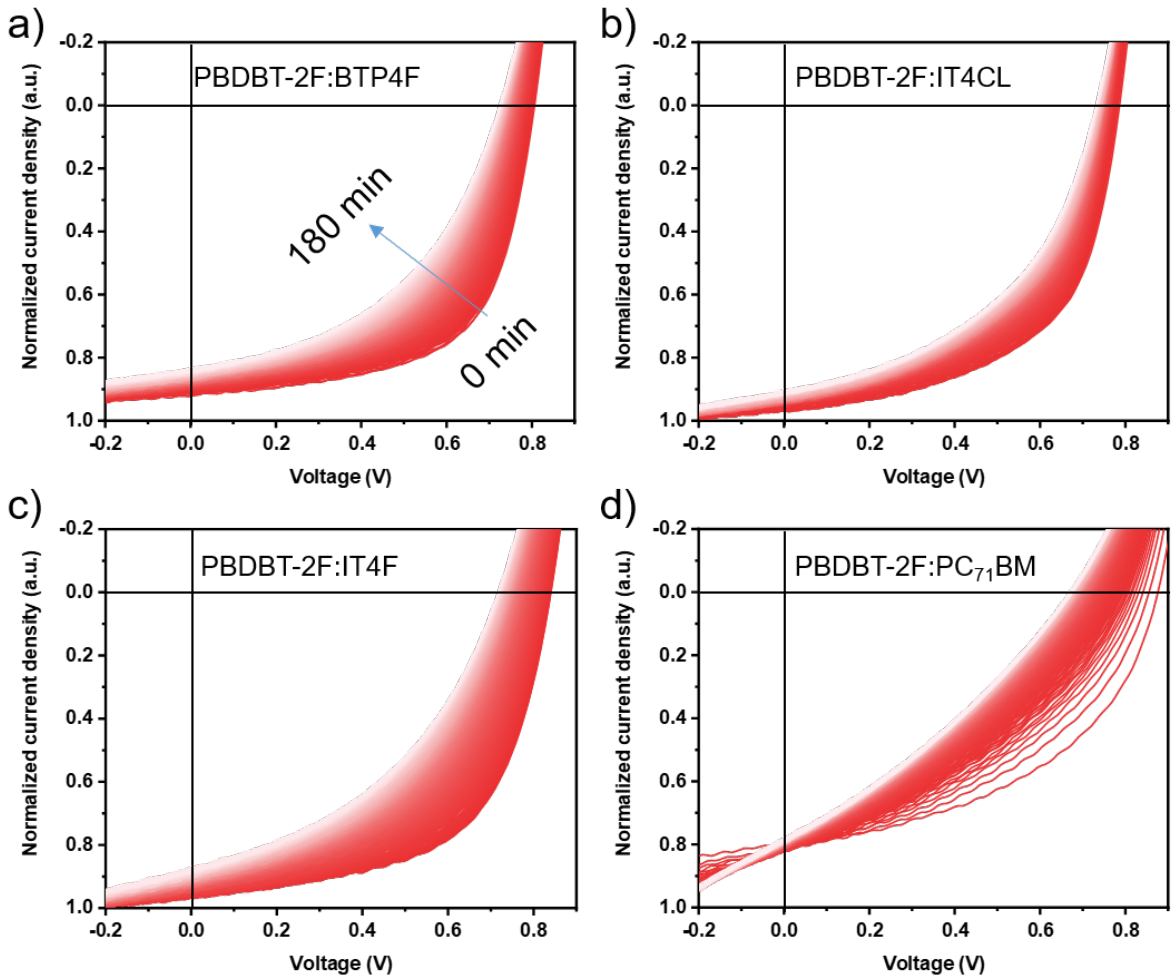

Figure 8.12: Recorded current-voltage curves (with normalized initial short-circuit current density) of the OSC devices based on PBDBT-2F blended with different acceptors under continuous AM 1.5 G light illumination.

Figure 8.12a-d presents the normalized current-voltage (J-V) evolution curves for organic solar cells (OSCs) that incorporate various acceptors in a PBDBT-2F blend during in-operando measurement. These devices demonstrate a unique degradation pathway, underpinning the influence of the acceptor type on device stability. To further assess the impact of different acceptors on the degradation pathway of solar cells, Figure 8.13 illustrates the temporal development of normalized photovoltaic parameters.

For all OSC devices, the short-circuit current (Jsc) remains fairly stable. The drop in power conversion efficiency (PCE) is primarily attributed to losses in open-circuit voltage (Voc) and fill factor (FF). When compared with non-fullerene acceptors, the device containing a PBDBT-2F:$PC_{71}BM$ blend suffers a significant burn-in loss within the initial 5 min, retaining

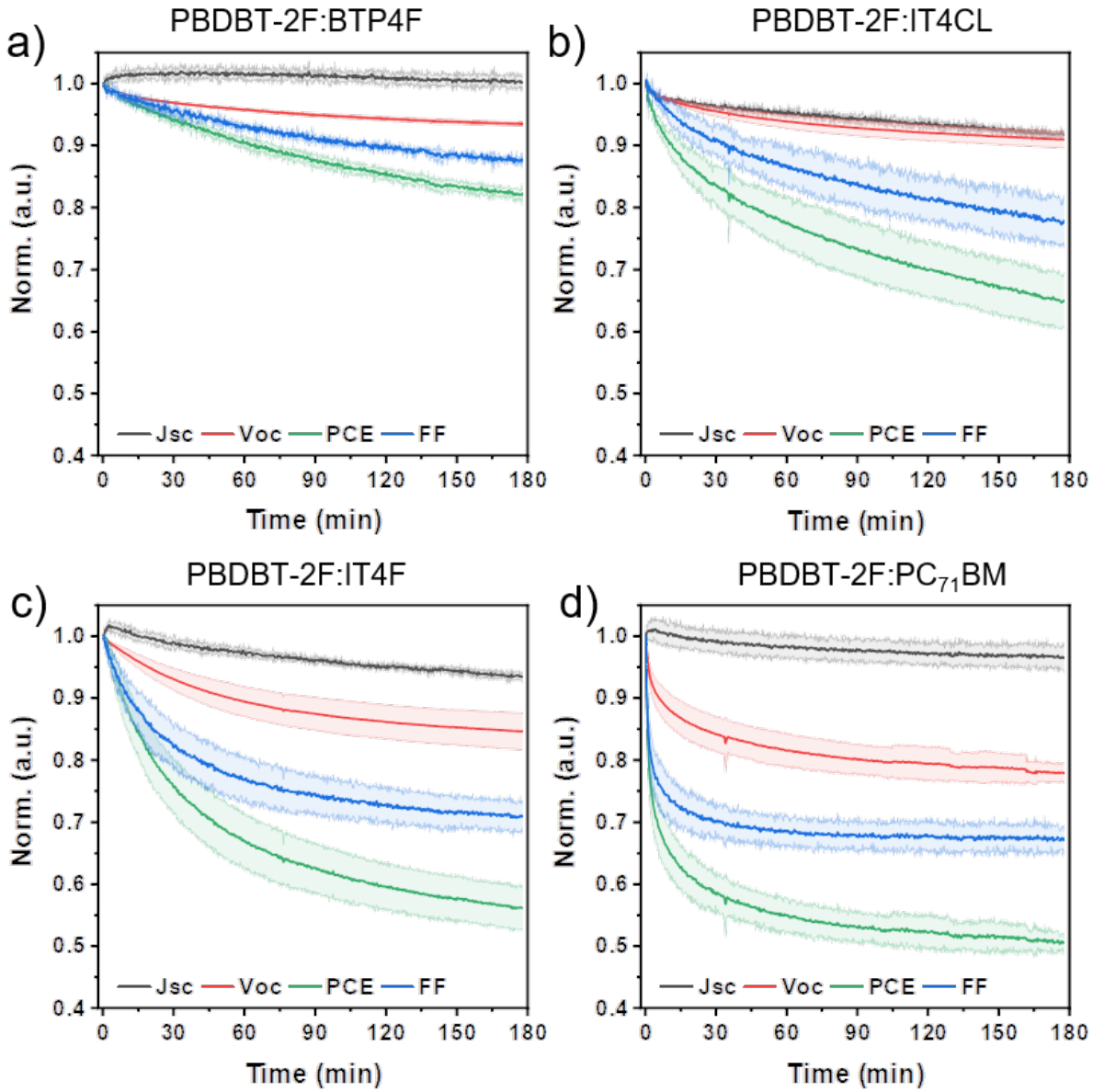

Figure 8.13: Temporal evolution of normalized Jsc, Voc, FF, and PCE the devices fabricated from PBDBT-2F blended with different acceptors.

only about (70 ± 4) % of the initial PCE. The PCE subsequently decays slowly, stabilizing around (50 ± 5) % of the initial value after 60 min.
Interestingly, the device incorporating a chlorine-modified ITIC derivative exhibits superior tolerance to light stress, maintaining about (74 ± 1) % of the initial PCE after 180 min. However, when chlorine is replaced with fluorine, the PCE dwindles to (56 ± 4) % of the initial value after the same duration. In the PBDBT-2F:BTP4F system, the PCE maintains near-constant values of (80 ± 3) % during the first 40 min, but then declines to (65 ± 4) % after 180 min of exposure to illumination.

8.3.2 Inner Morphology Evolution

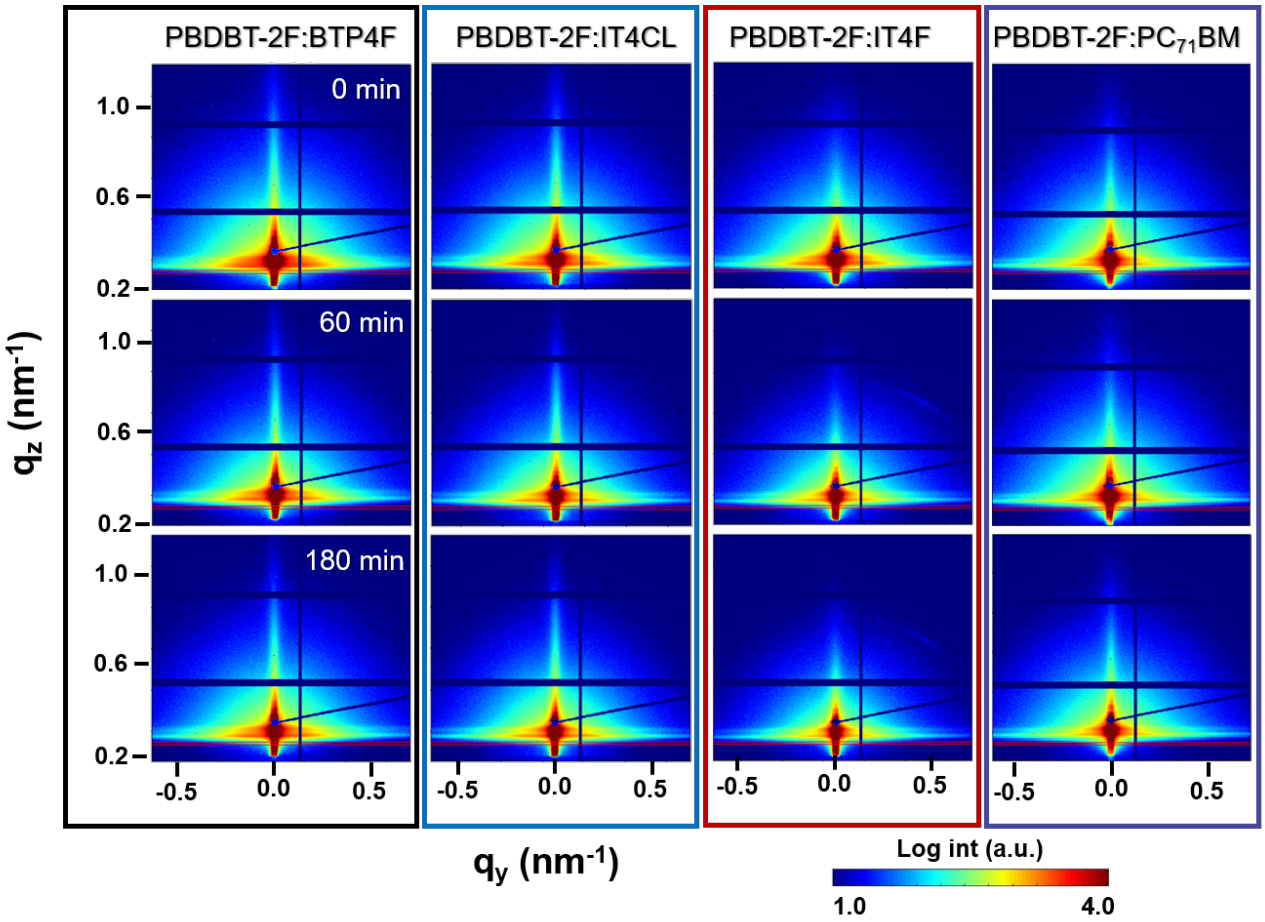

Figure 8.14: Selected in operando 2D GISAXS data of the devices fabricated from PBDBT-2F blended with different acceptors.

Selected 2-dimensional (2D) GISAXS data of each device during the operando process is displayed in Figure 8.14. The detailed morphological evolution of PBDBT-2F is determined from the scattering information by performing horizontal line cuts of the 2D GISAXS data at the Yoneda peak position, as illustrated in Figure 8.15 and Figure 8.16. To investigate the lateral structure evolution of the active layer during the operando process in depth, in the modelling we assume three cylindrical objects with different radii (large, medium, and small) to fit the horizontal line cut data. The fits are performed in the frame of the distorted wave Born approximation (DWBA) and assume the effective interface approximation (EIA). [39],[104] Figure 8.17-8.18 exhibit the fit parameters representing the average domain radii and polydispersity (σ) over time. The initial radii of the large-size structures (structure 1) are (25.3 ± 1.1) nm, (27.7 ± 1.1) nm, (26.6 ± 1.0) nm, and (35.9 ± 1.6) nm, while the medium-sized structures (structure 2) are (6.4 ± 0.5) nm, (8.9 ± 0.5) nm, (6.8 ± 0.5) nm, and (13.5 ± 0.5) nm for the PBDBT-2F:BTP4F, PBDBT-2F:IT4F, PBDBT-2F:IT4CL,

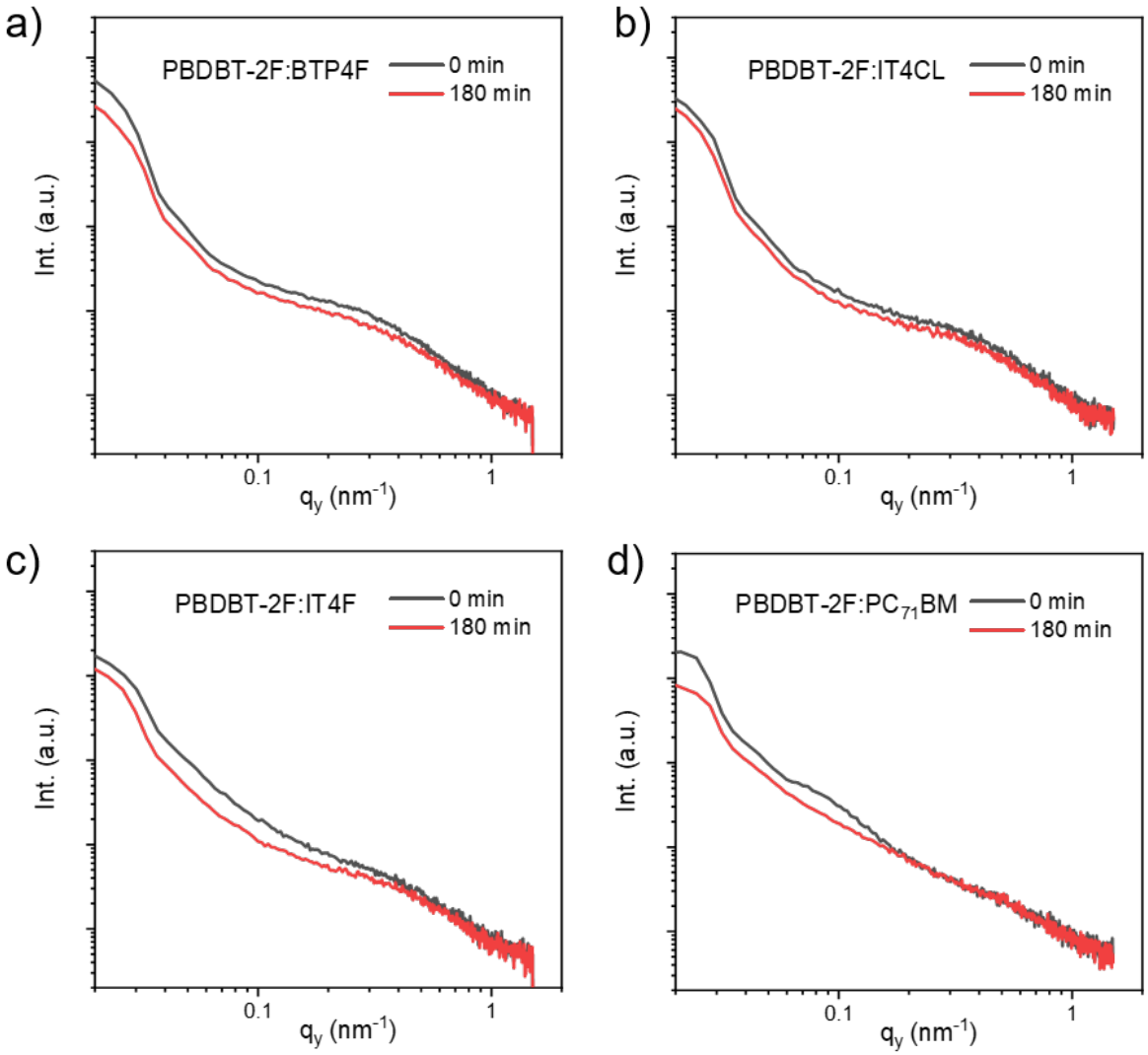

Figure 8.15: Comparison of horizontal line cuts of the 2D GISAXS data taken at the critical angle of the active layer before (0 min) and after (180 min) the operando measurements.

and PBDBT-2F:$PC_{71}BM$-based active layers, respectively. Whilst the fullerene blend exhibits larger domain radii, the active layers of PBDBT-2F blended with NFAs have similar domain radii in the large- and middle-sized structures. The initial radii of the small-size structures (structure 3) indicate very similar values, which are (3.0 ± 0.1) nm, (2.6 ± 0.1) nm, (2.8 ± 0.1) nm, and (2.9 ± 0.1) nm, respectively. As demonstrated in Figure 8.17, the small-size domain structure remains nearly constant during the operando measurements. The large size domain diminishes over time for all devices, with the principal alterations occurring within the initial 40 min, and variations becoming virtually negligible afterwards. The medium domain size remains constant for the PBDBT-2F:BTP4F and PBDBT-2F:IT4CL samples, while

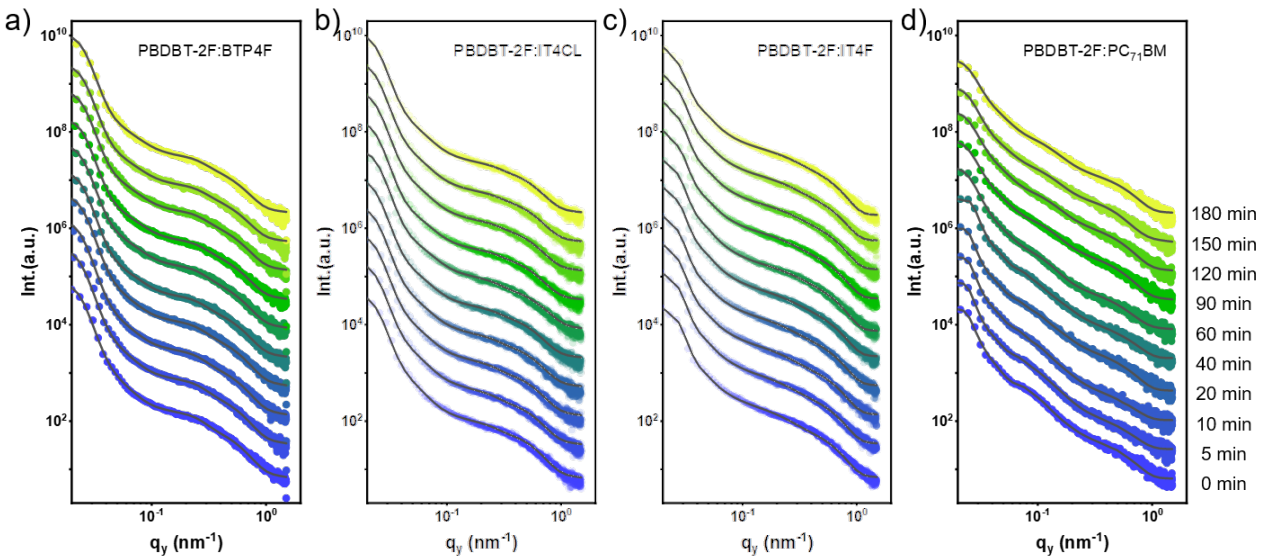

Figure 8.16: Horizontal line cuts of the 2D GISAXS data (dots) and corresponding model fits (black lines) from the operando GISAXS measurements at different times as indicated. The curves are shifted along the y-axis for the sake of clarity.

it notably shrinks for the PBDBT-2F:IT4F and more significantly in the PBDBT-2F:$PC_{71}BM$ devices. The shrinkages of the domains can result in a loss of connectivity between domains, consequently affecting the FF of the devices. Overall, combining these observations with the crystallinity of the active layer, we find that for the active layers with high π -π stacking crystallinity, such as the PBDBT-2F blended with BTP4F and IT4CL, the domains show reduced morphological changes. Notably, although the PBDBT-2F:BTP4F sample shows a higher π -π stacking crystallinity with more intermixing of the donor/accepter phase than the PBDBT-2F:IT4CL sample, the large domain experiences a severe domain shrinkage during the first 30 min, followed by an increased polydispersity (σ) afterward, revealing the growth of a disordered domain size distribution. We deduce that the PBDBT-2F:BTP4F sample undergoes a slightly more severe size decrease with the growth of disordered domains, corresponding to a faster FF decay rate after 80 min for the OSC, which causes an increased PCE loss. Samples containing less π -π stacking crystallinity, such as PBDBT-2F: IT4F, suffer from more serious domains shrinkage, with an obvious decay of the domain size especially for the middle-sized domains during the first 30 min. Moreover, the poyldispersity (σ) of the large structures increases continuously. These changes in the morphology accelerate the FF and Voc loss of the OCSs. In contrast, the fullerene-based PBDBT-2F:$PC_{71}BM$ sample with almost no π -π stacking crystallinity shows the most serious domain size decay. In particular, pronounced radii decrease and an σ increase are observed for the middle struc-

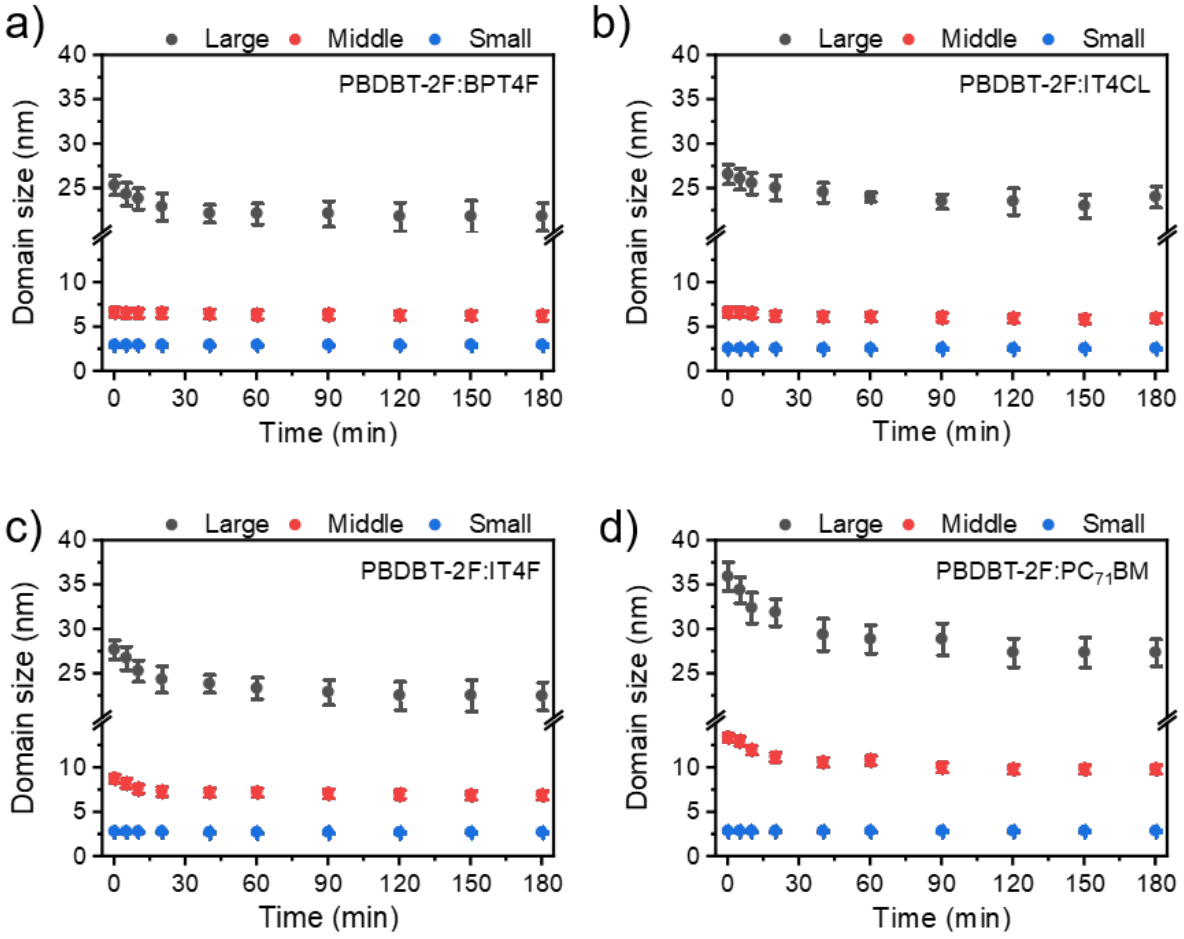

Figure 8.17: Temporal evolution of domain radii of large (black) and middle (red) small structures of the active layer extracted with GISAXS modelling of the operando experiments for the different active layer OSCs as indicated.

ture, corresponding to the decomposition of the medium-sized structure within the first 20 minutes. Accordingly, the PBDBT-2F:$PC_{71}BM$ devices exhibit the largest PCE loss among the investigated systems. Since the OSC performance is also influenced by other factors, the degradation in the active layer domain structures is not as extreme as the loss in the device performance but shows a very similar tendency from the operando experiment, suggesting the strong correlation between the active layer morphology and the OSC performance.

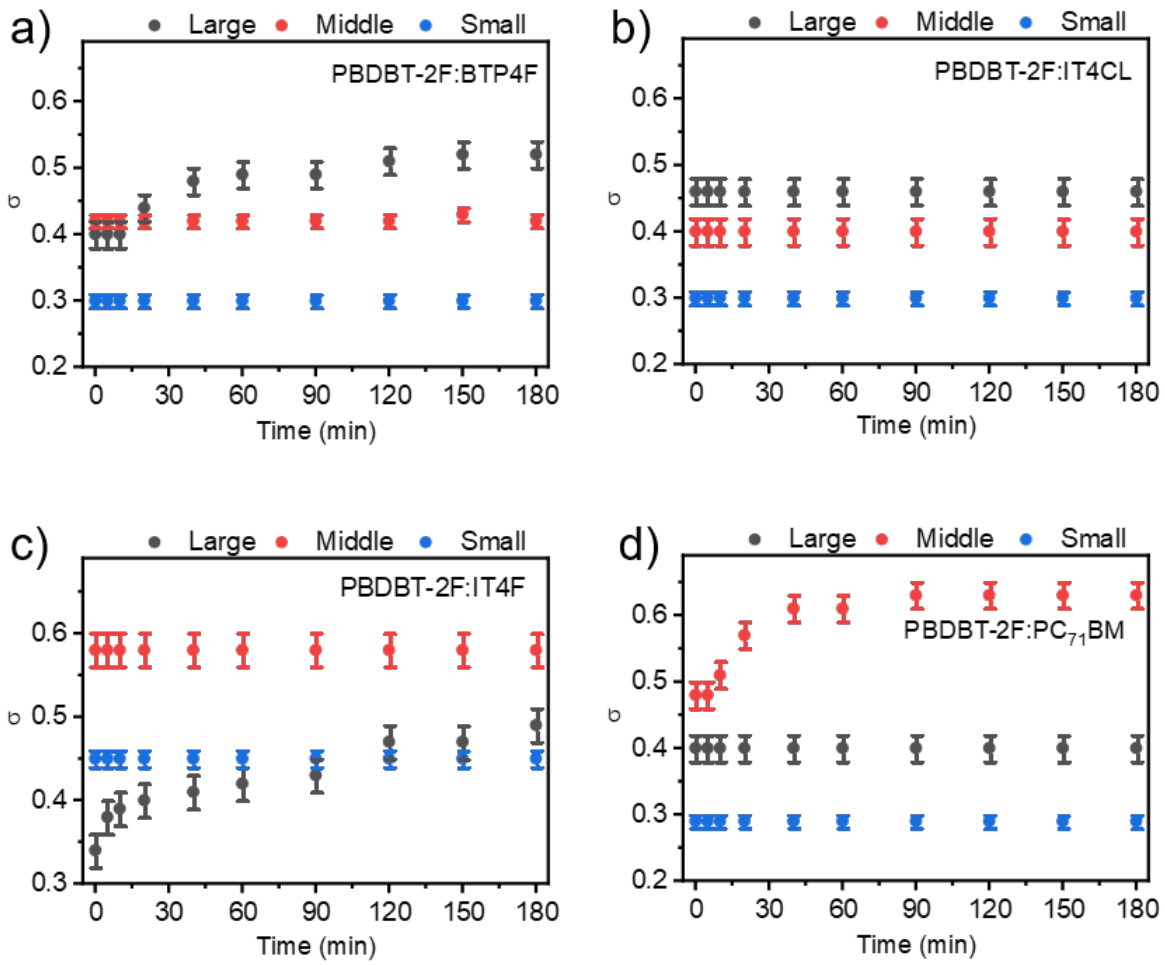

Figure 8.18: Temporal evolution of normalized domain radii polydispersity (σ) of the active layer extracted with GISAXS modelling of the operando experiments for the different active layer OSCs as indicated.

8.4 Conclusion

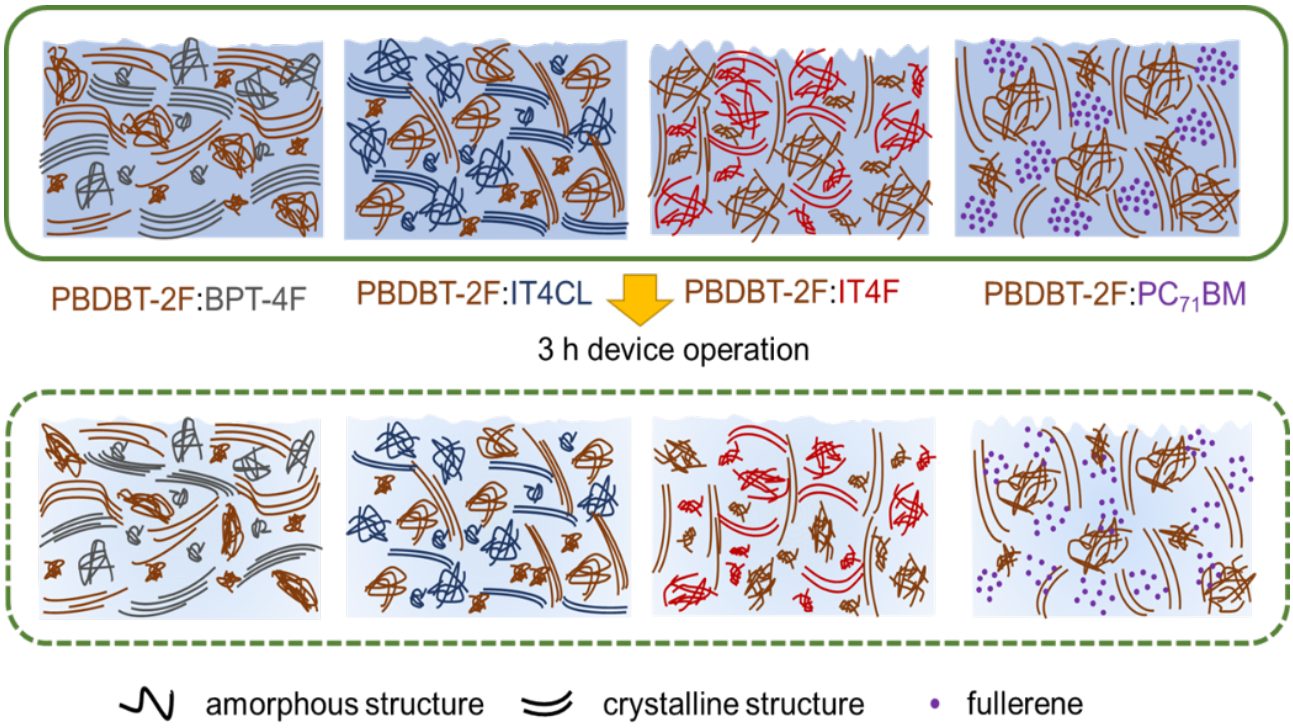

Figure 8.19: Schematic representation of morphology changes in the active layer based on PBDBT-2F with different NFAs having different π -π stacking crystallinity after the operando measurements.

This work demonstrates that OSCs with an active layer exhibiting outstanding π -π stacking crystallinity have a better ability to maintain their morphology during operation. In case of a too high degree of inter-mixing between donor and acceptor, the ability to maintain the active layer morphology is not as good as for blends with a lower inter-mixing despite having higher initial PCE values. In order to visualize the morphological degradation of active layers based on different π -π stacking crystallinities, the domain structures of the PBDBT-2F donor and various acceptors with different levels of π -π crystallinity are schematically illustrated in 8.19. The PBDBT-2F:BTP4F film exhibits the highest π -π stacking crystallinity among all samples, characterized by a well-intermixed face-on orientation crystalline structure of donor and acceptor. In contrast, the PBDBT-2F:IT4CL blends display a strong π -π stacking crystalline framework with a demixing of the donor and acceptor backbones, featuring a strong face-on orientation in the acceptor and a relatively poor edge-on orientation in the donor. Upon device operation of the OSCs, the morphology of the PBDBT-2F:BTP4F thin film tends to phase separate in the donor and acceptor crystalline phases, resulting in a compact molecular packing of BTP4F with J aggregation tendencies. In the PBDBT-2F:IT4CL film, the acceptor only experiences a crystallinity size shrinkage, while the molecular packing

distance remains the same. This phase separation in the PBDBT-2F:BTP4F induces slightly more severe large domain shrinkage and a more disordered distribution compared to the PBDBT-2F:IT4CL blends. The PBDBT-2F:IT4F sample, which has much less π -π stacking crystallinity, suffers from a more severe size shrinkage in both the large and middle-sized domains and exhibits a more disordered distribution in the large domain. The PBDBT-2F:$PC_{71}BM$ blend, on the other hand, exhibits lower crystallinity levels, resulting in more significant morphological degradation in the domain shrinkage under device operation stress. Specifically, $PC_{71}BM$ shows decomposition of the medium-sized structure with looser molecular packing.

In summary, the influence of the choice of the acceptor molecule (BTP4F, IT4CL, IT4F and $PC_{71}BM$) on the device stability of PBDBT-2F donor-based OSCs is investigated via operando GISAXS measurements. For devices, a strong decrease in the domain size structures is observed occurring during the first 40 min, in parallel with an clear decrease in the FF acting as the main factor affecting the OCS stability. Notably, the PBDBT-2F:IT4CL blend based device shows the least J-V loss under operation, which is attributed to the favorable π -π stacking crystallinity undergoing only a minimal shrinkage of the domain structures. In contrast, the serious J-V loss found in the PBDBT-2F:$PC_{71}BM$ blend based device having a poor π -π crystallinity is attributed to a pronounced decomposition of the domain structure. The slight crystallization changes in the NFAs under the device operation stress do not influence the intrinsic interfacial hole transfer rate but reduce the charge generation yield in the active layers, while faster geminate charge carrier recombination occurs in the fullerene blend. These findings provide a thorough analysis of the complicated degradation pathways influencing the stability of OSCs by correlating the device performance and active layer morphological evolution in operando experiments. Accordingly, our observations can have a great importance for material design rules for highly efficient and stable OSCs for real-world applications.

9 Conclusion and Outlook

In the emerging field of next-generation solar cells, non-fullerene acceptor based organic solar cells (OSCs) play an important role in photovoltaics. The main objective of the present work is to reveal the different states of active layer morphology in the field of non-fullerene based organic solar cells. More specifically, the active layer morphology is optimized by the functional solvent additive and its influence on the active layer morphology in the static state is investigated by various characterizations. Moreover, with the aid of the advanced in-situ and operando characterization methods, the mechanism of the active layer formation kinetics via different solvents as well as its degradation process with various non-fullerene acceptors in a real working device is revealed.

To figure out the effects of solvent additives on the BHJ active layer as well as the corresponding donor/acceptor neat thin films, the investigation is based on PBDBT-2F: IT-M system with different volumes of DIO addition. At 0.5 vol% DIO addition, the as-fabricated inverted solar cells show the best performance due to high open-circuit voltage and short-circuit current resulting from an improved charge carrier management due to the optimal inner nanoscale morphology of the active layers in terms of surface enrichment, crystallinity and crystalline orientation. While at higher amounts of DIO, the decrease in the PBDB-T-2F domain size and inter-domain distance, and the enrichment of PBDB-T-2F at the surface and IT-M at the bottom presumably originate from a lowered miscibility between PBDB-T-2F and IT-M. As a consequence of the less optimized nanoscale film morphology, longer TRPL decay lifetimes and a decreased charge transport cause a reduced device performance. Notably, increasing the DIO amount results in an increased Voc loss, which could be due to the intramolecular charge transfer (ICT) effects of the acceptors.

Concerning the slot-die coating fabrication method on a large scale, the choice of solvent is one of the major points for producing suitable active layer morphology in order to have high non-fullerene OSCs performance. Therefore, chlorobenzene (CB) and chloroform (CF) with different boiling points are used as host solvents for printing films of the neat novel fused-ring unit-based donor polymer (PDTBT2T-FTBDT), the small molecule non-fullerene acceptor (BTP-4F) based on a fused ring with a benzothiadiazole core as well as the respective PDTBT2T-FTBDT: BTP-4F blend films by slot-die coating method at room temperature in air. The best-performing devices are achieved with printing out of CF with over 13% efficiency

due to the best-suited nanoscale morphology, the presence of well-ordered crystallites, a lower surface roughness and a higher exciton dissociation probability. The relatively poor performance of only 6% efficiency from CB is attributed to the imbalanced crystallinity of the PDTBT2T-FTBDT and BTP-4F phases in the BHJ structure inhibiting an efficient exciton diffusion and free charge carrier transport. The unbalanced crystallization of the donor and acceptor gives rise to a more disordered orientation with a reduced donor crystal quality. Moreover, five stages are distinguished during the thin film formation by in situ UV-vis and in situ GIWAXS measurements. The stages are the solvent evaporation stage, starting of donor-acceptor interaction and crystalline progressive formation stage, the phase transition stage with the majority of the solvent evaporation, the stabilization stage and the final dried stage as followed. From the in situ GIWAXS measurement, there is an emergence of the face-on orientation of the active layer processed with CF solvent during the phase transition but no strong preferred orientation of the active layer processed with CB during thin film formation kinetics. From the in situ UV-vis result, the donor blueshift (H aggregates) while acceptor redshift (J aggregates) during drying in both solvents, while due to a longer drying time, the acceptor undergoes serious redshift (J aggregates) in the CB solvent. This work gives insights into the relationship between the donor-acceptor morphology evolution and optical device properties being influenced by the solvent. Its understanding sets a perspective for large-scale fabrication of OSC via printing under ambient conditions. For the environment-friendly OSCs, active layer PffBT4T-2OD: EH-IDTBR printed out of non-halogenated solvent 1,2,4-trimethylbenzene. The film formation kinetics of the active layer PffBT4T-2OD: EH-IDTBR is probed in terms of the temporal evolutions in morphology as well as molecular conformation and aggregation as revealed by in situ grazing-incidence small angle X-ray scattering (GISAXS) and UV-Vis spectroscopy during the film printing process. Five regimes of mesoscale domain growth processes are observed in the active layer from the liquid state to the final dry state. The evaporation of solvent induced domain growth is accompanied by molecular stacking in a distinct J-type aggregation of the acceptor and a slight H-type aggregation of the donor molecules. The printed active layers exhibit an edge-on dominated PffBT4T-2OD and a face-on dominated EH-IDTBR crystallite structure. Compared to the neat PffBT4T-2OD and EH-IDTBR films, the crystallite structure deviates slightly from lattice spacing in the active layer.

Towards real-world application, the poor stability of organic solar cells is still one of the major challenges. Since its degradation pathway is still not clear, especially with the springing up of novel small molecule acceptors. Thus, in the last result chapter, PBDB-T-2F (PM6) is selected as the donor, BTP4F, IT4F, IT4CL and $PC_{71}BM$ are selected as the acceptors to fabricated additive free high-efficiency OSCs. With this, the underlying inherent physical degradation of the active layer with different acceptors in a real device during light illumina-

tion is studied. Based on the results obtained in the presented work, for all PBDBT-2F blend devices, a strong decrease in the domain size structures is observed occurring during the first 40 min, in parallel with an obvious decrease in the FF acting as the main factor affecting the OCS stability. Notably, the PBDBT-2F: IT4CL blend-based device shows the least J-V loss under operation, which is attributed to the favorable π-π stacking crystallinity introducing a minimal shrinkage of the domain structures. In contrast, the serious J-V loss found in the PBDBT-2F: $PC_{71}BM$ blend-based device having a poor π-π crystallinity is attributed to a pronounced decomposition of the domain structure.

For future research, it will be interesting to focus on the non-fullerene-based OSCs with environment-friendly solvents. These solvents can significantly minimize the environmental impact of OSC fabrication while maintaining or even enhancing the devices' efficiency and performance. By focusing research efforts on discovering and optimizing such eco-friendly solvents, the OSC technology can become a more attractive and sustainable option for large-scale applications and mass production in renewable energy technologies.

Bibliography

[1] Consumption by fuel type-Exajoules. "bp Statistical Review of World Energy June 2020." In: (2006).

[2] Ansgar Belke, Frauke Dobnik, and Christian Dreger. "Energy consumption and economic growth: New insights into the cointegration relationship." In: *Energy Economics* 33.5 (2011), pp. 782–789.

[3] Marion King Hubbert et al. *Nuclear energy and the fossil fuels*. Vol. 95. Shell Development Company, Exploration and Production Research Division . . ., 1956.

[4] Ruixue Lei, Sha Feng, and Thomas Lauvaux. "Country-scale trends in air pollution and fossil fuel CO2 emissions during 2001–2018: confronting the roles of national policies and economic growth." In: *Environmental Research Letters* 16.1 (2020), p. 014006.

[5] Mark Z Jacobson. "Short-term effects of controlling fossil-fuel soot, biofuel soot and gases, and methane on climate, Arctic ice, and air pollution health." In: *Journal of Geophysical Research: Atmospheres* 115.D14 (2010).

[6] Nathan S Lewis et al. *Basic research needs for solar energy utilization. report of the basic energy sciences workshop on solar energy utilization, april 18-21, 2005*. Tech. rep. DOESC (USDOE Office of Science (SC)), 2005.

[7] Nathan S Lewis and Daniel G Nocera. "Powering the planet: Chemical challenges in solar energy utilization." In: *Proceedings of the National Academy of Sciences* 103.43 (2006), pp. 15729–15735.

[8] Albert Einstein. "Über einen die Erzeugung und Verwandlung des Lichtes betreffenden heuristischen Gesichtspunkt." In: (1905).

[9] Martin A Green. "The path to 25% silicon solar cell efficiency: History of silicon cell evolution." In: *Progress in photovoltaics: research and applications* 17.3 (2009), pp. 183–189.

[10] Andrew W Blakers et al. "22.8% efficient silicon solar cell." In: *Applied Physics Letters* 55.13 (1989), pp. 1363–1365.

[11] Martin A Green, Anita Ho-Baillie, and Henry J Snaith. "The emergence of perovskite solar cells." In: *Nature photonics* 8.7 (2014), pp. 506–514.

[12] Chuantian Zuo et al. “Advances in perovskite solar cells.” In: *Advanced Science* 3.7 (2016), p. 1500324.

[13] Khalil Ebrahim Jasim. “Quantum dots solar cells.” In: *Solar cells-new approaches and reviews* 3 (2015), pp. 303–31.

[14] Prashant V Kamat. “Quantum dot solar cells. The next big thing in photovoltaics.” In: *The journal of physical chemistry letters* 4.6 (2013), pp. 908–918.

[15] Yoshihiro Hamakawa. *Thin-film solar cells: next generation photovoltaics and its applications*. Vol. 13. Springer Science & Business Media, 2003.

[16] Harald Hoppe and Niyazi Serdar Sariciftci. “Organic solar cells: An overview.” In: *Journal of materials research* 19.7 (2004), pp. 1924–1945.

[17] Jan Schmidt et al. “Impurity-related limitations of next-generation industrial silicon solar cells.” In: *2012 IEEE 38th Photovoltaic Specialists Conference (PVSC) PART 2*. IEEE. 2012, pp. 1–5.

[18] Victoria Gonzalez-Pedro et al. “General working principles of CH3NH3PbX3 perovskite solar cells.” In: *Nano letters* 14.2 (2014), pp. 888–893.

[19] Jin Young Kim et al. “High-efficiency perovskite solar cells.” In: *Chemical Reviews* 120.15 (2020), pp. 7867–7918.

[20] Yaowen Li et al. “Flexible and semitransparent organic solar cells.” In: *Advanced Energy Materials* 8.7 (2018), p. 1701791.

[21] Yang Zhao et al. “Inactive (PbI2) 2RbCl stabilizes perovskite films for efficient solar cells.” In: *Science* 377.6605 (2022), pp. 531–534.

[22] Christopher Eames et al. “Ionic transport in hybrid lead iodide perovskite solar cells.” In: *Nature communications* 6.1 (2015), pp. 1–8.

[23] Luis M Pazos-Outón, T Patrick Xiao, and Eli Yablonovitch. “Fundamental efficiency limit of lead iodide perovskite solar cells.” In: *The Journal of Physical Chemistry Letters* 9.7 (2018), pp. 1703–1711.

[24] Yaoguang Rong et al. “Challenges for commercializing perovskite solar cells.” In: *Science* 361.6408 (2018), eaat8235.

[25] Robert Koeppe et al. “Organic solar cells with semitransparent metal back contacts for power window applications.” In: *ChemSusChem: Chemistry & Sustainability Energy & Materials* 2.4 (2009), pp. 309–313.

[26] Gang Yu et al. “Polymer photovoltaic cells: enhanced efficiencies via a network of internal donor-acceptor heterojunctions.” In: *Science* 270.5243 (1995), pp. 1789–1791.

[27] Tracey M Clarke and James R Durrant. "Charge photogeneration in organic solar cells." In: *Chemical reviews* 110.11 (2010), pp. 6736–6767.

[28] L Jan Anton Koster, VD Mihailetchi, and Paul WM Blom. "Ultimate efficiency of polymer/fullerene bulk heterojunction solar cells." In: *Applied Physics Letters* 88.9 (2006), p. 093511.

[29] Chaohong Zhang et al. "Comprehensive investigation and analysis of bulk-heterojunction microstructure of high-performance PCE11: PCBM solar cells." In: *ACS applied materials & interfaces* 11.20 (2019), pp. 18555–18563.

[30] Martin Green et al. "Solar cell efficiency tables (version 57)." In: *Progress in photovoltaics: research and applications* 29.1 (2021), pp. 3–15.

[31] Yanan Wei et al. "Binary organic solar cells breaking 19% via manipulating the vertical component distribution." In: *Advanced Materials* 34.33 (2022), p. 2204718.

[32] Zhong Zheng et al. "Tandem organic solar cell with 20.2% efficiency." In: *Joule* 6.1 (2022), pp. 171–184.

[33] Fuwen Zhao, Chunru Wang, and Xiaowei Zhan. "Morphology control in organic solar cells." In: *Advanced Energy Materials* 8.28 (2018), p. 1703147.

[34] Lijiao Ma et al. "Miscibility Control by Tuning Electrostatic Interactions in Bulk Heterojunction for Efficient Organic Solar Cells." In: *ACS Materials Letters* 3.9 (2021), pp. 1276–1283.

[35] Jie Lv et al. "Additive-induced miscibility regulation and hierarchical morphology enable 17.5% binary organic solar cells." In: *Energy & Environmental Science* 14.5 (2021), pp. 3044–3052.

[36] Sebastian Grott et al. "Solvent Tuning of the Active Layer Morphology of Non-Fullerene Based Organic Solar Cells." In: *Solar RRL* (2022), p. 2101084.

[37] Ruijie Ma et al. "Air-processed efficient organic solar cells from aromatic hydrocarbon solvent without solvent additive or post-treatment: insights into solvent effect on morphology." In: *Energy & Environmental Materials* 5.3 (2022), pp. 977–985.

[38] Jing Liu et al. "Fast charge separation in a non-fullerene organic solar cell with a small driving force." In: *Nature Energy* 1.7 (2016), pp. 1–7.

[39] Peter Müller-Buschbaum. "The active layer morphology of organic solar cells probed with grazing incidence scattering techniques." In: *Advanced materials* 26.46 (2014), pp. 7692–7709.

[40] Simon J Schaper et al. “Revealing the growth of copper on polystyrene-block-poly (ethylene oxide) diblock copolymer thin films with in situ GISAXS.” In: *Nanoscale* 13.23 (2021), pp. 10555–10565.

[41] Matthias Schwartzkopf et al. “From atoms to layers: in situ gold cluster growth kinetics during sputter deposition.” In: *Nanoscale* 5.11 (2013), pp. 5053–5062.

[42] Frederik C Krebs. “Polymer solar cell modules prepared using roll-to-roll methods: knife-over-edge coating, slot-die coating and screen printing.” In: *Solar Energy Materials and Solar Cells* 93.4 (2009), pp. 465–475.

[43] Sandra Hultmark et al. “Suppressing Co-Crystallization of Halogenated Non-Fullerene Acceptors for Thermally Stable Ternary Solar Cells.” In: *Advanced Functional Materials* 30.48 (2020), p. 2005462.

[44] Ling Hong et al. “Recent advances in high-efficiency organic solar cells fabricated by eco-compatible solvents at relatively large-area scale.” In: *APL Materials* 8.12 (2020), p. 120901.

[45] Pei Cheng and Xiaowei Zhan. “Stability of organic solar cells: challenges and strategies.” In: *Chemical Society Reviews* 45.9 (2016), pp. 2544–2582.

[46] Leiping Duan and Ashraf Uddin. “Progress in stability of organic solar cells.” In: *Advanced Science* 7.11 (2020), p. 1903259.

[47] Emily M Speller et al. “From fullerene acceptors to non-fullerene acceptors: prospects and challenges in the stability of organic solar cells.” In: *Journal of Materials Chemistry A* 7.41 (2019), pp. 23361–23377.

[48] AD Jenkins et al. “Glossary of basic terms in polymer science (IUPAC Recommendations 1996).” In: *Pure and applied chemistry* 68.12 (1996), pp. 2287–2311.

[49] Christoph J. Schaffer. “Morphological Degradation in Polymer-Fullerene Solar Cells.” PhD thesis. Technische Universität München, 2016.

[50] Ayyappanpillai Ajayaghosh. “Donor–acceptor type low band gap polymers: polysquaraines and related systems.” In: *Chemical Society Reviews* 32.4 (2003), pp. 181–191.

[51] Xin Guo, Martin Baumgarten, and Klaus Müllen. “Designing π-conjugated polymers for organic electronics.” In: *Progress in Polymer Science* 38.12 (2013), pp. 1832–1908.

[52] Jing Yang et al. “Introducing fluorine and sulfur atoms into quinoxaline-based p-type polymers to gradually improve the performance of fullerene-free organic solar cells.” In: *ACS Macro Letters* 8.6 (2019), pp. 743–748.

[53] Shujiang Yang, Pavel Olishevski, and Miklos Kertesz. “Bandgap calculations for conjugated polymers.” In: *Synthetic Metals* 141.1-2 (2004), pp. 171–177.

[54] Linyi Bian et al. "Recent progress in the design of narrow bandgap conjugated polymers for high-efficiency organic solar cells." In: *Progress in polymer science* 37.9 (2012), pp. 1292–1331.

[55] Cunbin An, Zhong Zheng, and Jianhui Hou. "Recent progress in wide bandgap conjugated polymer donors for high-performance nonfullerene organic photovoltaics." In: *Chemical Communications* 56.35 (2020), pp. 4750–4760.

[56] JW Slotboom. "The pn-product in silicon." In: *Solid-State Electronics* 20.4 (1977), pp. 279–283.

[57] S Francoeur et al. "Band gap of GaAs 1- x Bi x, 0< x< 3.6%." In: *Applied physics letters* 82.22 (2003), pp. 3874–3876.

[58] Holger Spanggaard and Frederik C Krebs. "A brief history of the development of organic and polymeric photovoltaics." In: *Solar Energy Materials and Solar Cells* 83.2-3 (2004), pp. 125–146.

[59] Rongming Xue et al. "Organic solar cell materials toward commercialization." In: *Small* 14.41 (2018), p. 1801793.

[60] Omar A Abdulrazzaq et al. "Organic solar cells: a review of materials, limitations, and possibilities for improvement." In: *Particulate science and technology* 31.5 (2013), pp. 427–442.

[61] Erik Ahlswede et al. "Highly efficient organic solar cells with printable low-cost transparent contacts." In: *Applied Physics Letters* 92.14 (2008), p. 127.

[62] Jean Roncali. "Molecular bulk heterojunctions: an emerging approach to organic solar cells." In: *Accounts of chemical research* 42.11 (2009), pp. 1719–1730.

[63] Fan Yang, Max Shtein, and Stephen R Forrest. "Controlled growth of a molecular bulk heterojunction photovoltaic cell." In: *Nature materials* 4.1 (2005), pp. 37–41.

[64] Yasunari Tamai et al. "Exciton diffusion in conjugated polymers: from fundamental understanding to improvement in photovoltaic conversion efficiency." In: *The journal of physical chemistry letters* 6.17 (2015), pp. 3417–3428.

[65] Lars Onsager. "Initial recombination of ions." In: *Physical Review* 54.8 (1938), p. 554.

[66] Charles L Braun. "Electric field assisted dissociation of charge transfer states as a mechanism of photocarrier production." In: *The Journal of chemical physics* 80.9 (1984), pp. 4157–4161.

[67] Nafees Ahmad et al. "Recent progress in cathode interlayer materials for non-fullerene organic solar cells." In: *EcoMat* 4.1 (2022), e12156.

[68] Youjun He et al. "Indene- C60 bisadduct: a new acceptor for high-performance polymer solar cells." In: *Journal of the American Chemical Society* 132.4 (2010), pp. 1377–1382.

[69] Huiqiong Zhou et al. "Conductive conjugated polyelectrolyte as hole-transporting layer for organic bulk heterojunction solar cells." In: *Advanced Materials* 26.5 (2014), pp. 780–785.

[70] Zhong Zheng et al. "A highly efficient non-fullerene organic solar cell with a fill factor over 0.80 enabled by a fine-tuned hole-transporting layer." In: *Advanced materials* 30.34 (2018), p. 1801801.

[71] Jianqiu Wang et al. "A tandem organic photovoltaic cell with 19.6% efficiency enabled by light distribution control." In: *Advanced Materials* 33.39 (2021), p. 2102787.

[72] Christoph J Brabec et al. "Effect of LiF/metal electrodes on the performance of plastic solar cells." In: *Applied physics letters* 80.7 (2002), pp. 1288–1290.

[73] Hongbin Wu et al. "Efficient electron injection from a bilayer cathode consisting of aluminum and alcohol-/water-soluble conjugated polymers." In: *Advanced Materials* 16.20 (2004), pp. 1826–1830.

[74] Zhi-Guo Zhang et al. "Perylene diimides: a thickness-insensitive cathode interlayer for high performance polymer solar cells." In: *Energy & Environmental Science* 7.6 (2014), pp. 1966–1973.

[75] Guoping Zhang et al. "Efficient All-Polymer Solar Cells Enabled by Interface Engineering." In: *Polymers* 14.18 (2022), p. 3835.

[76] Richard B Fair and Hayden W Wivell. "Zener and avalanche breakdown in As-implanted low-voltage Si np junctions." In: *IEEE Transactions on Electron Devices* 23.5 (1976), pp. 512–518.

[77] Mikkel Jørgensen, Kion Norrman, and Frederik C Krebs. "Stability/degradation of polymer solar cells." In: *Solar energy materials and solar cells* 92.7 (2008), pp. 686–714.

[78] Leiping Duan et al. "Burn-In Degradation Mechanism Identified for Small Molecular Acceptor-Based High-Efficiency Nonfullerene Organic Solar Cells." In: *ACS applied materials & interfaces* 12.24 (2020), pp. 27433–27442.

[79] Emily M Speller et al. "Toward improved environmental stability of polymer: fullerene and polymer: nonfullerene organic solar cells: a common energetic origin of light-and oxygen-induced degradation." In: *ACS energy letters* 4.4 (2019), pp. 846–852.

[80] Yawen Li, Tengfei Li, and Yuze Lin. "Stability: next focus in organic solar cells based on non-fullerene acceptors." In: *Materials Chemistry Frontiers* 5.7 (2021), pp. 2907–2930.

[81] Xiaoyan Du et al. "Unraveling the microstructure-related device stability for polymer solar cells based on nonfullerene small-molecular acceptors." In: *Advanced Materials* 32.16 (2020), p. 1908305.

[82] Christoph J Schaffer et al. "A direct evidence of morphological degradation on a nanometer scale in polymer solar cells." In: *Advanced materials* 25.46 (2013), pp. 6760–6764.

[83] Kerstin S Wienhold et al. "Following in situ the evolution of morphology and optical properties during printing of thin films for application in non-fullerene acceptor based organic solar cells." In: *ACS applied materials & interfaces* 12.36 (2020), pp. 40381–40392.

[84] Christoph J Schaffer et al. "Morphological degradation in low bandgap polymer solar cells–an in operando study." In: *Advanced Energy Materials* 6.19 (2016), p. 1600712.

[85] Dan Yang. "Influence of solvent additives on the morphological degradation in polymer-fullerene solar cells." PhD thesis. Technische Universität München, 2020.

[86] Metin Tolan and M Tolan. *X-ray scattering from soft-matter thin films: materials science and basic research*. Vol. 148. Springer, 1999.

[87] Max Born and Emil Wolf. *Principles of optics: electromagnetic theory of propagation, interference and diffraction of light*. Elsevier, 2013.

[88] Y Yoneda. "Anomalous surface reflection of X rays." In: *Physical review* 131.5 (1963), p. 2010.

[89] BL Henke et al. *A preliminary report on x-ray photoabsorption coefficients and atomic scattering factors for 92 elements in the 10–10,000 eV region*. Tech. rep. Lawrence Berkeley Lab., 1988.

[90] John Lekner. "Reflection theory and the analysis of neutron reflection data." In: *Physica B: Condensed Matter* 173.1-2 (1991), pp. 99–111.

[91] Peter Müller-Buschbaum. "GISAXS and GISANS as metrology technique for understanding the 3D morphology of block copolymer thin films." In: *European Polymer Journal* 81 (2016), pp. 470–493.

[92] Kerstin Sabrina Wienhold. "Printed Organic Solar Cells." PhD thesis. Technische Universität München, 2021.

[93] Rémi Lazzari. "IsGISAXS: a program for grazing-incidence small-angle X-ray scattering analysis of supported islands." In: *Journal of Applied Crystallography* 35.4 (2002), pp. 406–421.

[94] S Dietrich and H Wagner. "Critical magnetic surface scattering of neutrons at grazing angles." In: *Zeitschrift für Physik B Condensed Matter* 59.1 (1985), pp. 35–42.

[95] George H Vineyard. "Grazing-incidence diffraction and the distorted-wave approximation for the study of surfaces." In: *Physical Review B* 26.8 (1982), p. 4146.

[96] S t Dietrich and H Wagner. "Critical surface scattering of X-rays at grazing angles." In: *Zeitschrift für Physik B Condensed Matter* 56.3 (1984), pp. 207–215.

[97] T Salditt et al. "Non-specular X-ray scattering from thin films and multilayers with small-angle scattering equipment." In: *Journal of Physics D: Applied Physics* 28.4A (1995), A236.

[98] SK Sinha et al. "X-ray and neutron scattering from rough surfaces." In: *Physical Review B* 38.4 (1988), p. 2297.

[99] Gilles Renaud, Rémi Lazzari, and Frédéric Leroy. "Probing surface and interface morphology with grazing incidence small angle X-ray scattering." In: *Surface Science Reports* 64.8 (2009), pp. 255–380.

[100] R Hosemann et al. "Novel aspects of the real paracrystal." In: *Acta Crystallographica Section A: Crystal Physics, Diffraction, Theoretical and General Crystallography* 37.1 (1981), pp. 85–91.

[101] Lorenz Bießmann. "Functional Layers for Enhanced Photon Extraction in ITO-free OLEDs." PhD thesis. Technische Universität München, 2019.

[102] PJGWG Scherrer. "Bestimmung der Grösse und der inneren von Kolloidteilchen mittels Röntgenstrahlen Struktur Nachr." In: *Ges Wiss Göttingen* 26 (1918), pp. 98–100.

[103] Johannes Schlipf. "The Morphology of Hybrid Perovskite Thin Films for Photovoltaic Application." PhD thesis. Technische Universität München, 2018.

[104] Xinyu Jiang et al. "Revealing Donor–Acceptor Interaction on the Printed Active Layer Morphology and the Formation Kinetics for Nonfullerene Organic Solar Cells at Ambient Conditions." In: *Advanced Energy Materials* 12.14 (2022), p. 2103977.

[105] Jessy L Baker et al. "Quantification of thin film crystallographic orientation using X-ray diffraction with an area detector." In: *Langmuir* 26.11 (2010), pp. 9146–9151.

[106] Kirt A Page et al. "Confinement-driven increase in ionomer thin-film modulus." In: *Nano letters* 14.5 (2014), pp. 2299–2304.

[107] August Beer. "Bestimmung der absorption des rothen lichts in farbigen flussigkeiten." In: *Ann. Physik* 162 (1852), pp. 78–88.

[108] Masoud Soroush, K Kenneth, et al. *Dye-sensitized solar cells: mathematical modelling, and materials design and optimization*. Academic Press, 2019.

[109] Glenn A Crosby and James N Demas. "Measurement of photoluminescence quantum yields. Review." In: *The Journal of Physical Chemistry* 75.8 (1971), pp. 991–1024.

[110] Aleksander Jabłoński. "Über den mechanismus der photolumineszenz von farbstoffphosphoren." In: *Zeitschrift für Physik* 94.1 (1935), pp. 38–46.

[111] Frank-Julian Kahle et al. "How to interpret absorption and fluorescence spectra of charge transfer states in an organic solar cell." In: *Materials Horizons* 5.5 (2018), pp. 837–848.

[112] Nian Li. "Tailoring titania nanostructures forapplication in solar cells." PhD thesis. Technische Universität München, 2021.

[113] WK Metzger et al. *Time-resolved photoluminescence and photovoltaics*. Tech. rep. National Renewable Energy Lab.(NREL), Golden, CO (United States), 2005.

[114] Alkiviathes Meldrum. "Time-Resolved Photoluminescence Spectroscopy of Semiconductor Nanocrystals and Other Fluorophores." In: *Journal of Visualized Experiments: Jove* 186 (2022).

[115] NIST X-ray Photoelectron Spectroscopy Database. "NIST Standard Reference Database Number 20, National Institute of Standards and Technology, Gaithersburg MD, 20899." In: (2000).

[116] Brunero Cappella and Giovanni Dietler. "Force-distance curves by atomic force microscopy." In: *Surface science reports* 34.1-3 (1999), pp. 1–104.

[117] David Nečas and Petr Klapetek. "Gwyddion: an open-source software for SPM data analysis." In: *Open Physics* 10.1 (2012), pp. 181–188.

[118] Lyman G Parratt. "Surface studies of solids by total reflection of X-rays." In: *Physical review* 95.2 (1954), p. 359.

[119] Andrew Nelson. "Co-refinement of multiple-contrast neutron/X-ray reflectivity data using MOTOFIT." In: *Journal of applied crystallography* 39.2 (2006), pp. 273–276.

[120] Adeline Buffet et al. "P03, the microfocus and nanofocus X-ray scattering (MiNaXS) beamline of the PETRA III storage ring: the microfocus endstation." In: *Journal of synchrotron radiation* 19.4 (2012), pp. 647–653.

[121] Gunthard Benecke et al. "A customizable software for fast reduction and analysis of large X-ray scattering data sets: applications of the new DPDAK package to small-angle X-ray scattering and grazing-incidence small-angle X-ray scattering." In: *Journal of applied crystallography* 47.5 (2014), pp. 1797–1803.

[122] Zhang Jiang. "GIXSGUI: a MATLAB toolbox for grazing-incidence X-ray scattering data visualization and reduction, and indexing of buried three-dimensional periodic nanostructured films." In: *Journal of Applied Crystallography* 48.3 (2015), pp. 917–926.

[123] Subhash Chander et al. "A study on spectral response and external quantum efficiency of mono-crystalline silicon solar cell." In: *International journal of renewable energy research* 5.1 (2015), pp. 41–44.

[124] Axel Herguth et al. "Influence of spectral mismatch, cell reflection properties and IQE on the efficiency measurement." In: *26th European Photovoltaic Solar Energy Conference and Exhibition*. 2011, pp. 1555–1557.

[125] Syed A Moiz et al. "Space charge–limited current model for polymers." In: *Conducting Polymers* 5 (2016), p. 91.

[126] Wenchao Zhao et al. "Molecular optimization enables over 13% efficiency in organic solar cells." In: *Journal of the American Chemical Society* 139.21 (2017), pp. 7148–7151.

[127] Lei Zhu et al. "Single-junction organic solar cells with over 19% efficiency enabled by a refined double-fibril network morphology." In: *Nature Materials* 21.6 (2022), pp. 656–663.

[128] Jules Bertrandie et al. "The Energy Level Conundrum of Organic Semiconductors in Solar Cells." In: *Advanced Materials* (2022), p. 2202575.

[129] Qishi Liu et al. "18% Efficiency organic solar cells." In: *Science Bulletin* 65.4 (2020), pp. 272–275.

[130] Zhixing Cao et al. "Multi-channel exciton dissociation in D18/Y6 complexes for high-efficiency organic photovoltaics." In: *Journal of Materials Chemistry A* 8.39 (2020), pp. 20408–20413.

[131] Yuhang Liu et al. "Aggregation and morphology control enables multiple cases of high-efficiency polymer solar cells." In: *Nature communications* 5.1 (2014), pp. 1–8.

[132] Jun Yuan et al. "Single-junction organic solar cell with over 15% efficiency using fused-ring acceptor with electron-deficient core." In: *Joule* 3.4 (2019), pp. 1140–1151.

[133] Baobing Fan et al. "Achieving over 16% efficiency for single-junction organic solar cells." In: *Science China Chemistry* 62.6 (2019), pp. 746–752.

[134] Yun Zhang et al. "Fluorination vs. chlorination: a case study on high performance organic photovoltaic materials." In: *Science China Chemistry* 61.10 (2018), pp. 1328–1337.

[135] Hao Zhang et al. "Over 14% efficiency in organic solar cells enabled by chlorinated nonfullerene small-molecule acceptors." In: *Advanced materials* 30.28 (2018), p. 1800613.

[136] Sunsun Li et al. "Energy-level modulation of small-molecule electron acceptors to achieve over 12% efficiency in polymer solar cells." In: *Advanced materials* 28.42 (2016), pp. 9423–9429.

[137] Sarah Holliday et al. "High-efficiency and air-stable P3HT-based polymer solar cells with a new non-fullerene acceptor." In: *Nature communications* 7.1 (2016), pp. 1–11.

[138] Fujun Zhang et al. "Influence of PC60BM or PC70BM as electron acceptor on the performance of polymer solar cells." In: *Solar Energy Materials and Solar Cells* 97 (2012), pp. 71–77.

[139] Sih-Hao Liao et al. "Single junction inverted polymer solar cell reaching power conversion efficiency 10.31% by employing dual-doped zinc oxide nano-film as cathode interlayer." In: *Scientific reports* 4.1 (2014), pp. 1–7.

[140] Xinyu Jiang et al. "Internal nanoscale architecture and charge carrier dynamics of wide bandgap non-fullerene bulk heterojunction active layers in organic solar cells." In: *Journal of Materials Chemistry A* 8.44 (2020), pp. 23628–23636.

[141] Xinyu Jiang et al. "Film formation kinetics of polymer donor and non-fullerene acceptor active layers during printing out of 1, 2, 4-trimethylbenzene in ambient conditions." In: *Solar RRL* ().

[142] Dirk W Schubert and Thomas Dunkel. "Spin coating from a molecular point of view: its concentration regimes, influence of molar mass and distribution." In: *Materials Research Innovations* 7.5 (2003), pp. 314–321.

[143] Frederik C Krebs. "Fabrication and processing of polymer solar cells: A review of printing and coating techniques." In: *Solar energy materials and solar cells* 93.4 (2009), pp. 394–412.

[144] Tahir Iqbal Awan, Almas Bashir, and Aqsa Tehseen. *Chemistry of Nanomaterials: Fundamentals and Applications*. Elsevier, 2020.

[145] Richard C Jaeger. "Film Deposition: Introduction to Microelectronic Fabrication." In: *Upper Saddle Rivers: Prentice Hall* 83 (2002).

[146] Bo Zhang et al. "3, 4-Dicyanothiophene—a Versatile Building Block for Efficient Non-fullerene Polymer Solar Cells." In: *Advanced Energy Materials* 10.12 (2020), p. 1904247.

[147] Pei Cheng et al. "Next-generation organic photovoltaics based on non-fullerene acceptors." In: *Nature Photonics* 12.3 (2018), pp. 131–142.

[148] Zhicai He et al. “Single-junction polymer solar cells with high efficiency and photovoltage.” In: *Nature Photonics* 9.3 (2015), pp. 174–179.

[149] Zhenye Li et al. “A generic green solvent concept boosting the power conversion efficiency of all-polymer solar cells to 11%.” In: *Energy & Environmental Science* 12.1 (2019), pp. 157–163.

[150] Alan J Heeger. “25th anniversary article: bulk heterojunction solar cells: understanding the mechanism of operation.” In: *Advanced Materials* 26.1 (2014), pp. 10–28.

[151] Gongchu Liu et al. “15% efficiency tandem organic solar cell based on a novel highly efficient wide-bandgap nonfullerene acceptor with low energy loss.” In: *Advanced Energy Materials* 9.11 (2019), p. 1803657.

[152] Yang Tong et al. “Progress of the key materials for organic solar cells.” In: *Science China Chemistry* 63.6 (2020), pp. 758–765.

[153] Fuguo Zhang et al. “Polymeric, cost-effective, dopant-free hole transport materials for efficient and stable perovskite solar cells.” In: *Journal of the American Chemical Society* 141.50 (2019), pp. 19700–19707.

[154] A Wang, J Zhao, and MA Green. “24% efficient silicon solar cells.” In: *Applied physics letters* 57.6 (1990), pp. 602–604.

[155] Florent Sahli et al. “Fully textured monolithic perovskite/silicon tandem solar cells with 25.2% power conversion efficiency.” In: *Nature materials* 17.9 (2018), pp. 820–826.

[156] Dirk Veldman, Stefan CJ Meskers, and René AJ Janssen. “The energy of charge-transfer states in electron donor–acceptor blends: insight into the energy losses in organic solar cells.” In: *Advanced Functional Materials* 19.12 (2009), pp. 1939–1948.

[157] Haijun Bin et al. “Non-fullerene polymer solar cells based on alkylthio and fluorine substituted 2D-conjugated polymers reach 9.5% efficiency.” In: *Journal of the American Chemical Society* 138.13 (2016), pp. 4657–4664.

[158] Wanbin Li et al. “A wide bandgap conjugated polymer donor based on alkoxyl-fluorophenyl substituted benzodithiophene for high performance non-fullerene polymer solar cells.” In: *Journal of Materials Chemistry A* 7.3 (2019), pp. 1307–1314.

[159] Qunping Fan et al. “High-performance nonfullerene polymer solar cells with open-circuit voltage over 1 V and energy loss as low as 0.54 eV.” In: *Nano Energy* 40 (2017), pp. 20–26.

[160] Qunping Fan et al. “A new polythiophene derivative for high efficiency polymer solar cells with PCE over 9%.” In: *Advanced Energy Materials* 6.14 (2016), p. 1600430.

[161] Mohammed Azzouzi, Thomas Kirchartz, and Jenny Nelson. "Factors controlling open-circuit voltage losses in organic solar cells." In: *Trends in Chemistry* 1.1 (2019), pp. 49–62.

[162] Haijun Bin et al. "11.4% Efficiency non-fullerene polymer solar cells with trialkylsilyl substituted 2D-conjugated polymer as donor." In: *Nature communications* 7.1 (2016), pp. 1–11.

[163] Qunping Fan et al. "Side-chain engineering for efficient non-fullerene polymer solar cells based on a wide-bandgap polymer donor." In: *Journal of Materials Chemistry A* 5.19 (2017), pp. 9204–9209.

[164] Maojie Zhang et al. "A large-bandgap conjugated polymer for versatile photovoltaic applications with high performance." In: *Advanced Materials* 27.31 (2015), pp. 4655–4660.

[165] Yan Wang et al. "High-performance nonfullerene polymer solar cells based on a fluorinated wide bandgap copolymer with a high open-circuit voltage of 1.04 V." In: *Journal of Materials Chemistry A* 5.42 (2017), pp. 22180–22185.

[166] Li Nian et al. "Approaching 16% efficiency in all-small-molecule organic solar cells based on ternary strategy with a highly crystalline acceptor." In: *Joule* 4.10 (2020), pp. 2223–2236.

[167] Runnan Yu, Huifeng Yao, and Jianhui Hou. "Recent progress in ternary organic solar cells based on nonfullerene acceptors." In: *Advanced Energy Materials* 8.28 (2018), p. 1702814.

[168] Lin Zhang et al. "Blade-cast nonfullerene organic solar cells in air with excellent morphology, efficiency, and stability." In: *Advanced Materials* 30.22 (2018), p. 1800343.

[169] Li-Ming Wang et al. "Quantitative Determination of the Vertical Segregation and Molecular Ordering of PBDB-T/ITIC Blend Films with Solvent Additives." In: *ACS applied materials & interfaces* 12.21 (2020), pp. 24165–24173.

[170] Long Ye et al. "High-efficiency nonfullerene organic solar cells: critical factors that affect complex multi-length scale morphology and device performance." In: *Advanced Energy Materials* 7.7 (2017), p. 1602000.

[171] Weijia Wang et al. "Influence of solvent additive 1, 8-octanedithiol on P3HT: PCBM solar cells." In: *Advanced functional materials* 28.20 (2018), p. 1800209.

[172] Kerstin S Wienhold et al. "Effect of solvent additives on the morphology and device performance of printed nonfullerene acceptor based organic solar cells." In: *ACS applied materials & interfaces* 11.45 (2019), pp. 42313–42321.

[173] Yonghai Li et al. "Design of asymmetric benzodithiophene based wide band-gap conjugated polymers toward efficient polymer solar cells promoted by a low boiling point additive." In: *Journal of Materials Chemistry C* 6.11 (2018), pp. 2806–2813.

[174] Zhenghao Hu et al. "Ternary nonfullerene polymer solar cells with a power conversion efficiency of 11.6% by inheriting the advantages of binary cells." In: *ACS Energy Letters* 3.3 (2018), pp. 555–561.

[175] Chenyi Yang et al. "Molecular design of a non-fullerene acceptor enables a P3HT-based organic solar cell with 9.46% efficiency." In: *Energy & Environmental Science* 13.9 (2020), pp. 2864–2869.

[176] Jianhui Hou et al. "Organic solar cells based on non-fullerene acceptors." In: *Nature materials* 17.2 (2018), pp. 119–128.

[177] Shuai Guo et al. "Solvent–morphology–property relationship of PTB7: PC71BM polymer solar cells." In: *ACS applied materials & interfaces* 9.4 (2017), pp. 3740–3748.

[178] Dan Yang et al. "In-operando study of the effects of solvent additives on the stability of organic solar cells based on PTB7-Th: PC71BM." In: *ACS Energy Letters* 4.2 (2019), pp. 464–470.

[179] Mart-Mari Duvenhage et al. "Determination of the optical band gap of Alq3 and its derivatives for the use in two-layer OLEDs." In: *Optical Materials* 42 (2015), pp. 193–198.

[180] Ruihao Xie et al. "Efficient non-fullerene organic solar cells enabled by sequential fluorination of small-molecule electron acceptors." In: *Frontiers in chemistry* 6 (2018), p. 303.

[181] Miao Zhang et al. "Efficient ternary non-fullerene polymer solar cells with PCE of 11.92% and FF of 76.5%." In: *Energy & Environmental Science* 11.4 (2018), pp. 841–849.

[182] Jinyan Li et al. "Broadening the Photoresponse to Near-Infrared Region by Cooperating Fullerene and Nonfullerene Acceptors for High Performance Ternary Polymer Solar Cells." In: *Macromolecular Rapid Communications* 39.4 (2018), p. 1700492.

[183] P Müller-Buschbaum and Manfred Stamm. "Correlated roughness, long-range correlations, and dewetting of thin polymer films." In: *Macromolecules* 31.11 (1998), pp. 3686–3692.

[184] James T Rogers et al. "Structural order in bulk heterojunction films prepared with solvent additives." In: *Advanced materials* 23.20 (2011), pp. 2284–2288.

[185] Nian Li et al. "Nanoscale crystallization of a low band gap polymer in printed titania mesopores." In: *Nanoscale* 12.6 (2020), pp. 4085–4093.

[186] Yuan Pan et al. "Electronic structure and d-band center control engineering over M-doped CoP (M= Ni, Mn, Fe) hollow polyhedron frames for boosting hydrogen production." In: *Nano energy* 56 (2019), pp. 411–419.

[187] Xuemin Hu et al. "2D Fe-containing cobalt phosphide/cobalt oxide lateral heterostructure with enhanced activity for oxygen evolution reaction." In: *Nano Energy* 56 (2019), pp. 109–117.

[188] Lin Song et al. "Composition–Morphology Correlation in PTB7-Th/PC71BM Blend Films for Organic Solar Cells." In: *ACS applied materials & interfaces* 11.3 (2018), pp. 3125–3135.

[189] Wei Cao et al. "Self-assembly of large magnetic nanoparticles in ultrahigh molecular weight linear diblock copolymer films." In: *ACS applied materials & interfaces* 12.6 (2020), pp. 7557–7564.

[190] Sheng Dong et al. "Single-component non-halogen solvent-processed high-performance organic solar cell module with efficiency over 14%." In: *Joule* 4.9 (2020), pp. 2004–2016.

[191] Hongkyu Kang et al. "Bulk-heterojunction organic solar cells: Five core technologies for their commercialization." In: *Advanced Materials* 28.36 (2016), pp. 7821–7861.

[192] Huabing Chen et al. "Precise nanomedicine for intelligent therapy of cancer." In: *Science China Chemistry* 61.12 (2018), pp. 1503–1552.

[193] Y Galagan. "JEJ m. Rubingh, R. Andriessen, CC Fan, PW m. Blom, SC Veenstra, and JM Kroon." In: *Sol. Energy Mater. Sol. Cells* 95 (2011), pp. 1339–1343.

[194] Seyeong Song et al. "Hot slot die coating for additive-free fabrication of high performance roll-to-roll processed polymer solar cells." In: *Energy & Environmental Science* 11.11 (2018), pp. 3248–3255.

[195] Wenchao Zhao et al. "Vacuum-assisted annealing method for high efficiency printable large-area polymer solar cell modules." In: *Journal of Materials Chemistry C* 7.11 (2019), pp. 3206–3211.

[196] Jeongjoo Lee et al. "Slot-die and roll-to-roll processed single junction organic photovoltaic cells with the highest efficiency." In: *Advanced Energy Materials* 9.36 (2019), p. 1901805.

[197] Sheng Dong et al. "Suppressing the excessive aggregation of nonfullerene acceptor in blade-coated active layer by using n-type polymer additive to achieve large-area printed organic solar cells with efficiency over 15%." In: *EcoMat* 1.1 (2019), e12006.

[198] Shafket Rasool et al. "Room temperature processed highly efficient large-area polymer solar cells achieved with molecular engineering of copolymers." In: *Advanced Energy Materials* 9.21 (2019), p. 1900168.

[199] Hyun Wook Ro et al. "Morphology changes upon scaling a high-efficiency, solution-processed solar cell." In: *Energy & Environmental Science* 9.9 (2016), pp. 2835–2846.

[200] Doojin Vak et al. "3D printer based slot-die coater as a lab-to-fab translation tool for solution-processed solar cells." In: *Advanced Energy Materials* 5.4 (2015), p. 1401539.

[201] Heng Zhao et al. "Hot Hydrocarbon-Solvent Slot-Die Coating Enables High-Efficiency Organic Solar Cells with Temperature-Dependent Aggregation Behavior." In: *Advanced materials* 32.39 (2020), p. 2002302.

[202] Dong Zheng et al. "Unexpected solvent effects on the UV/Vis absorption spectra of o-cresol in toluene and benzene: in contrast with non-aromatic solvents." In: *Royal Society open science* 5.3 (2018), p. 171928.

[203] Zhen Wang et al. "Thermodynamic properties and molecular packing explain performance and processing procedures of three D18: NFA organic solar cells." In: *Advanced Materials* 32.49 (2020), p. 2005386.

[204] Alem Araya Meresa and Felix Sunjoo Kim. "Selective Ammonia-Sensing Platforms Based on a Solution-Processed Film of Poly (3-Hexylthiophene) and p-Doping Tris (Pentafluorophenyl) Borane." In: *Polymers* 12.1 (2020), p. 128.

[205] Jianyao Huang et al. "Tuning Frontier Orbital Energetics of Azaisoindigo-Based Polymeric Semiconductors to Enhance the Charge-Transport Properties." In: *Advanced Electronic Materials* 3.11 (2017), p. 1700078.

[206] Nicholas J Hestand and Frank C Spano. "Expanded theory of H-and J-molecular aggregates: the effects of vibronic coupling and intermolecular charge transfer." In: *Chemical reviews* 118.15 (2018), pp. 7069–7163.

[207] Zhi-Peng Yu et al. "Simple non-fused electron acceptors for efficient and stable organic solar cells." In: *Nature communications* 10.1 (2019), pp. 1–9.

[208] Mengmeng Li et al. "Impact of polymorphism on the optoelectronic properties of a low-bandgap semiconducting polymer." In: *Nature communications* 10.1 (2019), pp. 1–11.

[209] Lei Zhu et al. "Efficient organic solar cell with 16.88% efficiency enabled by refined acceptor crystallization and morphology with improved charge transfer and transport properties." In: *Advanced Energy Materials* 10.18 (2020), p. 1904234.

[210] Baojun Lin et al. "Balancing the pre-aggregation and crystallization kinetics enables high efficiency slot-die coated organic solar cells with reduced non-radiative recombination losses." In: *Energy & environmental science* 13.8 (2020), pp. 2467–2479.

[211] Fabian Panzer, Heinz Bässler, and Anna Köhler. "Temperature induced order–disorder transition in solutions of conjugated polymers probed by optical spectroscopy." In: *The journal of physical chemistry letters* 8.1 (2017), pp. 114–125.

[212] Mengmeng Li et al. "Controlling the surface organization of conjugated donor–acceptor polymers by their aggregation in solution." In: *Advanced Materials* 28.42 (2016), pp. 9430–9438.

[213] Dan Yang et al. "In situ studies of solvent additive effects on the morphology development during printing of bulk heterojunction films for organic solar cells." In: *Small Methods* 4.9 (2020), p. 2000418.

[214] Dan Yang et al. "Tailoring Morphology Compatibility and Device Stability by Adding PBDTTPD-COOH as Third Component to Fullerene-Based Polymer Solar Cells." In: *ACS Applied Energy Materials* 3.3 (2020), pp. 2604–2613.

[215] Guichuan Zhang et al. "Overcoming Space-Charge Effect for Efficient Thick-Film Non-Fullerene Organic Solar Cells." In: *Advanced Energy Materials* 8.25 (2018), p. 1801609.

[216] Andrew J Clarke et al. "Non-fullerene acceptor photostability and its impact on organic solar cell lifetime." In: *Cell Reports Physical Science* 2.7 (2021), p. 100498.

[217] Nicola Gasparini et al. "The physics of small molecule acceptors for efficient and stable bulk heterojunction solar cells." In: *Advanced Energy Materials* 8.12 (2018), p. 1703298.

[218] Hyojung Cha et al. "An efficient,"burn in" free organic solar cell employing a nonfullerene electron acceptor." In: *Advanced Materials* 29.33 (2017), p. 1701156.

[219] Anna Lena Oechsle et al. "In Situ Observation of Morphological and Oxidation Level Degradation Processes within Ionic Liquid Post-treated PEDOT: PSS Thin Films upon Operation at High Temperatures." In: *ACS applied materials & interfaces* 14.27 (2022), pp. 30802–30811.

[220] Kerstin S Wienhold et al. "In Situ Printing: Insights into the Morphology Formation and Optical Property Evolution of Slot-Die-Coated Active Layers Containing Low Bandgap Polymer Donor and Nonfullerene Small Molecule Acceptor." In: *Solar RRL* 4.7 (2020), p. 2000086.

[221] Maged Abdelsamie et al. "In situ UV-visible absorption during spin-coating of organic semiconductors: a new probe for organic electronics and photovoltaics." In: *Journal of Materials Chemistry C* 2.17 (2014), pp. 3373–3381.

[222] Sebastian T Hoffmann, Heinz Bässler, and Anna Köhler. "What determines inhomogeneous broadening of electronic transitions in conjugated polymers?" In: *The Journal of Physical Chemistry B* 114.51 (2010), pp. 17037–17048.

[223] Andreas W Götz et al. "Van der Waals effects on structure and optical properties in organic photovoltaics." In: *International Journal of Quantum Chemistry* 119.14 (2019), e25883.

[224] Frank C Spano. "The spectral signatures of Frenkel polarons in H-and J-aggregates." In: *Accounts of chemical research* 43.3 (2010), pp. 429–439.

[225] Frank C Spano and Carlos Silva. "H-and J-aggregate behavior in polymeric semiconductors." In: *Annu. Rev. Phys. Chem* 65.1 (2014), pp. 477–500.

[226] Yu-Wei Su, Yu-Che Lin, and Kung-Hwa Wei. "Evolving molecular architectures of donor–acceptor conjugated polymers for photovoltaic applications: From one-dimensional to branched to two-dimensional structures." In: *Journal of Materials Chemistry A* 5.46 (2017), pp. 24051–24075.

[227] Hansol Lee et al. "Effect of donor–acceptor molecular orientation on charge photogeneration in organic solar cells." In: *NPG Asia Materials* 10.6 (2018), pp. 469–481.

[228] Xiaoyan Du et al. "Efficient polymer solar cells based on non-fullerene acceptors with potential device lifetime approaching 10 years." In: *Joule* 3.1 (2019), pp. 215–226.

[229] Thomas Heumueller et al. "Reducing burn-in voltage loss in polymer solar cells by increasing the polymer crystallinity." In: *Energy & Environmental Science* 7.9 (2014), pp. 2974–2980.

[230] Dan Yang et al. "In Operando GISAXS and GIWAXS Stability Study of Organic Solar Cells Based on PffBT4T-2OD: PC71BM with and without Solvent Additive." In: *Advanced Science* 7.16 (2020), p. 2001117.

[231] Masoud Ghasemi et al. "A molecular interaction–diffusion framework for predicting organic solar cell stability." In: *Nature materials* 20.4 (2021), pp. 525–532.

[232] Jing Guo et al. "Revealing the microstructure-related light-induced degradation for all-polymer solar cells based on regioisomerized end-capping group acceptors." In: *Journal of Materials Chemistry C* 10.4 (2022), pp. 1246–1258.

[233] Yunfei Han et al. "An Efficiency of 16.46% and a T 80 lifetime of over 4000 h for the PM6: Y6 inverted organic solar cells enabled by surface acid treatment of the zinc oxide electron transporting layer." In: *ACS Applied Materials & Interfaces* 13.15 (2021), pp. 17869–17881.

[234] Ling Hong et al. "Simultaneous improvement of efficiency and stability of organic photovoltaic cells by using a cross-linkable fullerene derivative." In: *Small* 17.24 (2021), p. 2101133.

[235] Qing Liao et al. “Highly stable organic solar cells based on an ultraviolet-resistant cathode interfacial layer.” In: *CCS Chemistry* 4.3 (2022), pp. 938–948.

[236] Lijiao Ma et al. “Completely non-fused electron acceptor with 3D-interpenetrated crystalline structure enables efficient and stable organic solar cell.” In: *Nature communications* 12.1 (2021), p. 5093.

[237] Sijing Zhong et al. “Review on Y6-based semiconductor materials and their future development via machine learning.” In: *Crystals* 12.2 (2022), p. 168.

[238] Yunping Huang et al. “Synthesis of regioregular π-conjugated polymers consisting of a lactam moiety via direct heteroarylation polymerization.” In: *Chemical Communications* 53.12 (2017), pp. 1997–2000.

[239] Zhengxing Peng, Long Ye, and Harald Ade. “Understanding, quantifying, and controlling the molecular ordering of semiconducting polymers: from novices to experts and amorphous to perfect crystals.” In: *Materials Horizons* 9.2 (2022), pp. 577–606.

[240] Ruijie Ma et al. “High-efficiency ternary organic solar cells with a good figure-of-merit enabled by two low-cost donor polymers.” In: *ACS Energy Letters* 7.8 (2022), pp. 2547–2556.

[241] Yuzhong Chen et al. “Asymmetric alkoxy and alkyl substitution on nonfullerene acceptors enabling high-performance organic solar cells.” In: *Advanced Energy Materials* 11.3 (2021), p. 2003141.

[242] Dingqin Hu et al. “15.34% efficiency all-small-molecule organic solar cells with an improved fill factor enabled by a fullerene additive.” In: *Energy & Environmental Science* 13.7 (2020), pp. 2134–2141.

[243] Yiwen Wang et al. “The critical role of the donor polymer in the stability of high-performance non-fullerene acceptor organic solar cells.” In: *Joule* 7.4 (2023), pp. 810–829.

[244] Ruijie Ma et al. “In situ and ex situ investigations on ternary strategy and co-solvent effects towards high-efficiency organic solar cells.” In: *Energy & Environmental Science* 15.6 (2022), pp. 2479–2488.

[245] Jeannine Grüne et al. “Triplet Excitons and Associated Efficiency-Limiting Pathways in Organic Solar Cell Blends Based on (Non-) Halogenated PBDB-T and Y-Series.” In: *Advanced Functional Materials* (2023), p. 2212640.

[246] Alexander J Gillett et al. “The role of charge recombination to triplet excitons in organic solar cells.” In: *Nature* 597.7878 (2021), pp. 666–671.

[247] Akchheta Karki et al. “The path to 20% power conversion efficiencies in nonfullerene acceptor organic solar cells.” In: *Advanced Energy Materials* 11.15 (2021), p. 2003441.

[248] Akchheta Karki et al. “The role of bulk and interfacial morphology in charge generation, recombination, and extraction in non-fullerene acceptor organic solar cells.” In: *Energy & Environmental Science* 13.10 (2020), pp. 3679–3692.

[249] Shin-ichiro Natsuda et al. “Cascaded energy landscape as a key driver for slow yet efficient charge separation with small energy offset in organic solar cells.” In: *Energy & Environmental Science* 15.4 (2022), pp. 1545–1555.

[250] Alberto Privitera et al. “Geminate and nongeminate pathways for triplet exciton formation in organic solar cells.” In: *Advanced Energy Materials* 12.16 (2022), p. 2103944.

[251] Yunlong Ma et al. “Efficient organic solar cells from molecular orientation control of m-series acceptors.” In: *Joule* 5.1 (2021), pp. 197–209.

List of Publications

Publications Related to This Dissertation

- X. Jiang, H. Kim, P. S. Deimel, W. Chem, W. Cao, D. Yang, S. Yin, R. Schaffrinna, F. Allegretti, J. V. Bath, M. Schwager, H. Tang, K. Wang, M. Schwartzkopf, S. V. Roth, P. Müller-Buschbaum, "Internal nanoscale architecture and charge carrier dynamics of wide bandgap non-fullerene bulk heterojunction active layers in organic solar cells", **Journal of Materials Chemistry A**, 8 (44), 23628-23636 , 2020.

- X. Jiang, P Chotard, K. Luo, F. Eckmann, S. Tu, M. S. Reus, S. Yin, J. Reitenbach, C. L. Weindl, M. Schwartzkopf, S. V. Roth, P. Müller-Buschbaum, "Revealing Donor-Acceptor Interaction on the Printed Active Layer Morphology and the Formation Kinetics for Nonfullerene Organic Solar Cells at Ambient Conditions" **Advanced Energy Materials**, 12 (14), 2103977, 2022.

- X. Jiang, S. Grott, V. Körstgens, K. S. Wienhold, Z. Li, J. Zhang, C. R. Everett, M. Schwartzkopf, S. V. Roth, P. Müller-Buschbaum, "Film formation kinetics of polymer donor and non-fullerene acceptor active layers during printing out of 1,2,4-trimethylbenzene in ambient conditions" **Solar RRL**, 7, 202201077, 2023.

- X. Jiang, A. J. Gillett, T. Zheng, X. Song, J. E. Heger, K. Sun, L. Spanier, R. Guo, S. Liang, S. Bernstorff, P. Müller-Buschbaum, "Operando study of the influence of the small molecule acceptor on the morphology induced device degradation of organic solar cells with different π -π stacking crystallinity" **under review**, 2023.

Further Publications

- K. S. Wienhold, V. Körstgens, S. Grott, X. Jiang, M. Schwartzkopf, S. V. Roth, P. Müller-Buschbaum, "Effect of Solvent Additives on the Morphology and Device Performance of Printed Nonfullerene Acceptor Based Organic Solar Cells", **ACS Applied Materials & Interfaces**, 11 (45), 42313-42321, 2019.

- N. Li, L. Song, N. Hohn, N. Saxena, W. Cao, X. Jiang, P. Müller-Buschbaum, "Nanoscale crystallization of a low band gap polymer in printed titania mesopores", **Nanoscale**, 12, 4085–4093, 2020.

- K. S. Wienhold, V. Körstgens, S. Grott, X. Jiang, M. Schwartzkopf, S. V. Roth, Müller-Buschbaum, "In Situ Printing: Insights into the Morphology Formation and Optical Property Evolution of Slot-Die Coated Active Layers Containing Low Bandgap Polymer Donor and Nonfullerene Small Molecule Acceptor", **Solar RRL**, 4 (7), 2000086, 2020.

- K. S. Wienhold, X. Jiang, P. Müller-Buschbaum, "Organic Solar Cells probed with Advanced Neutron Scattering Techniques", **Applied Physics Letters**, 116 (12), 120504, 2020.

- D. Yang, B. Cao, V. Körstgens, N. Saxena, N. Li, C. Bilko, S. Grott, W. Chen, X. Jiang, J. E. Heger, S. Bernstorff, P. Müller-Buschbaum, "Tailoring morphology compatibility and device stability by adding PBDTTPD-COOH as third component to fullerene-based polymer solar cells", **ACS Applied Energy Materials**, 3 (3), 2604-2613, 2020.

- D. Yang, S. Grott, X. Jiang, K. S. Wienhold, M. Schwartzkopf, S. V. Roth, P. Müller-Buschbaum, "In situ studies of solvent additive effects on the morphology development during printing of bulk heterojunction films for organic solar cells", **Small Methods**, 4 (9), 2000418, 2020.

- W. Cao, S. Xia, X. Jiang, M. Appold, M. Opel, M. Plank, R. Schaffrinna, L. P. Kreuzer, S. Yin, M. Gallei, M. Schwartzkopf, S. V. Roth, P. Müller-Buschbaum, "Self-assembly of large magnetic nanoparticles in ultrahigh molecular weight linear diblock copolymer films", **ACS Applied Materials & Interfaces**, 12 (6), 7557-7564, 2020.

- R. Guo, A. Buyruk, X. Jiang, W. Chen, L. K. Reb, M. A. Scheel, T. Ameri, P. Müller-Buschbaum, "Tailoring the orientation of perovskite crystals via adding two-dimensional polymorphs for perovskite solar cells" **Journal of Physics: Energy**, 2 (3), 034005, 2020.

- Y. Zou, R. Guo, A. Buyruk, W. Chen, T. Xiao, S. Yin, X. Jiang, L. P. Kreuzer, C. Mu, T.h Ameri, M. Schwartzkopf, S. V. Roth, P. Müller-Buschbaum, "Sodium dodecylbenzene sulfonate interface modification of methylammonium lead iodide for surface passivation of perovskite solar cells", **ACS Applied Materials & Interfaces**, 12 (47), 52643-52651, 2020.

- W. Chen, R. Guo, H. Tang, K. S. Wienhold, N. Li, Z. Jiang, J. Tang, X. Jiang, L. P. Kreuzer, H. Liu, M. Schwartzkopf, X. W. Sun, S. V. Roth, K. Wang, B. Xu, P. Müller-Buschbaum, "Operando structure degradation study of PbS quantum dot solar cells",

Energy & Environmental Science, 14 (6), 3420-3429, 2021.

- X. Song, L. Hou, R. Guo, Q. Wei, L. Yang, X. Jiang, S. Tu, A. Zhang, Z. Kan, W. Tang, G. Xing, P. Müller-Buschbaum, "Synergistic Interplay between Asymmetric Backbone Conformation, Molecular Aggregation, and Charge-Carrier Dynamics in Fused-Ring Electron Acceptor-Based Bulk Heterojunction Solar Cells", **ACS Applied Materials & Interfaces**, 13 (2), 2961-2970, 2021.

- S. Hou, W. Li, S. Watzele, R. M. Kluge, S. Xue, S. Yin, X. Jiang, M. Döblinger, A. Welle, B. Garlyyev, M. Koch, P. Müller-Buschbaum, C. Wöll, A. S. Bandarenka, R. A. Fischer, "Metamorphosis of Heterostructured Surface-Mounted Metal–Organic Frameworks Yielding Record Oxygen Evolution Mass Activities", **Advanced Materials**, 33 (38), 2103218, 2021.

- S. Tu, T. Tian, A. L. Oechsle, S. Yin, X. Jiang, W. Cao, N. Li, M. A. Scheel, L. K. Reb, S. Hou, A. S. Bandarenka, M. Schwartzkopf, S. V. Roth, P. Müller-Buschbaum, "Improvement of the thermoelectric properties of PEDOT: PSS films via DMSO addition and DMSO/salt post-treatment resolved from a fundamental view", **Chemical Engineering Journal**, 429, 132295, 2022.

- S. Yin, Y. Zou, M. A. Reus, X. Jiang, S. Tu, T. Tian, R. Qi, Z. Xu, S. Liang, Y. Cheng, J. E. Heger, M. Schwartzkopf, S. V. Roth, P. Müller-Buschbaum, "Tailored Fabrication of Quasi-Isoporous and Double Layered α-Fe_2O_3 Thin Films and Their Application in Photovoltaic Devices", **Chemical Engineering Journal**, 140135, 2022.

- Y. Wang, J. Xue, H. Zhong, C. R. Everett, X. Jiang, M. A. Reus, A. Chumakov, S. V. Roth, M.A. Adedeji, N.J, K. Zhou, G Lu, Z. Tang, G.T.Mola, P. Müller-Buschbaum, W. Ma, "Control of the Crystallization and Phase Separation Kinetics in Sequential Blade-Coated Organic Solar Cells by Optimizing the Upper Layer Processing Solvent", **Advanced Energy Materials**, 2203496, 2022.

- Y. Li, Y. Li, J. E. Heger, J. Zhou, T. Guan, C. R. Everett, W. Wei, Z. Hong, Y. Wu, X. Jiang, S. Yin, X. Yang, D. Li, C. Jiang, B. Sun, P. Müller-Buschbaum, "Revealing Surface and Interface Evolution of Molybdenum Nitride as Carrier-Selective Contacts for Crystalline Silicon Solar Cells", **ACS Applied Materials & Interfaces**, 15, 13753-13760, 2023.

- R.Ma, X. Jiang, J. Fu, T. Zhu, C. Yan, K. Wu, P. Müller-Buschbaum, G. Li "Revealing the Underlying Solvent Effect on Film Morphology in High-Efficiency Organic Solar Cells by Combined Ex-situ and In-situ Observations", **Energy & Environmental Science**, 15, 13753-13760, 2023.

Scientific Reports

- X. Jiang, W. Cao, S. Xia, N. Li, P. Müller-Buschbaum, "Printing ITO-free electrode for low bandgap polymer solar cells", **Lehrstuhl für Funktionelle Materialien, Annual Report**, 2017.

- X. Jiang, S. Grott, T. Riccitelli, V. Korstgens, K. Wienhold, M. Schwartzkopf, S. V. Roth, P. Müller-Buschbaum, "In-situ investigating morphology formation of printed non-fullerene active layer for solar cells" **Lehrstuhl für Funktionelle Materialien, Annual Report**, 2018.

- X. Jiang, S. Grott, V. Körstgens, K. Wienhold, M. Schwartzkopf, S. V. Roth, P. Müller-Buschbaum, "In-situ tracking the morphology evolution of active layers for non-fullerene organic solar cells", **Lehrstuhl für Funktionelle Materialien, Annual Report**, 2019.

- X. Jiang, H. Kim, S. V. Roth, P. Müller-Buschbaum, "Internal nanoscale architecture of non-fullerene bulk heterojunction active layers in organic solar cells", **Lehrstuhl für Funktionelle Materialien, Annual Report**, 2020.

- X. Jiang, P. Chotard, S. V. Roth, P. Müller-Buschbaum, "Solvent effects on the printed active layer for high performance non-fullerene organic solar cells", **Lehrstuhl für Funktionelle Materialien, Annual Report**, 2021.

- X. Jiang, S. Grott, V. Körstgens, K. Wienhold, M. Schwartzkopf, S. V. Roth, P. Müller-Buschbaum, "Tracking the active layer formation of non-fullerene organic solar cells via in situ methods ", **Lehrstuhl für Funktionelle Materialien, Annual Report**, 2022.

Conference Talks

- X. Jiang, "Fabricating low bandgap polymer bulk heterojunction solar cell with printing technique" **E13 Seminar Talk**, Chair for Functional Materials, Physics-Department, TUMünchen, Germany, 23 May 2018.

- X. Jiang, N. Li, R. Schaffrinna, “UV-VIS spectroscopy”, **E13 Polymer Physics Summer School**, Obertauern, Austria, June 2018.

- X. Jiang, "Investigation polymer-based solar cell with printing technique" **E13 Seminar Talk**, Chair for Functional Materials, Physics-Department, TUMünchen, Germany, 29 May 2019.

- X. Jiang, "Internal Architecture and Charge Carrier Dynamics of Wide Bandgap Non-Fullerene Bulk Heterojunction Layer in Solar Cells" **E13 Seminar Talk**, online, 27 May 2020.
- X. Jiang, S. J. Schaper, S. V. Roth, P. Muller-Buschbaum, "In-situ investigation of sputter deposition electrodes on different layers of non-fullerene organic solar cell" **MRS Spring and Fall Meeting 2020**, online, 27 November -04 December 2020.
- X. Jiang, S. J. Schaper, S. V. Roth, Müller-Buschbaum, "In-situ investigation of sputter deposition electrods on different layers based on non-fullerene organic solar cell", **20th SAXS/WAXS/GISAXS Satellite Meeting of DESY photon science users' meeting 2021**, online, 19 January 2021.
- X. Jiang, "Revealing donor-acceptor interaction on the printed active layer for non-fullerene organic solar cells" **E13 Seminar Talk**, online, 18 May 2021.
- X. Jiang, P. Chotard, K. Luo, F. Eckmann, S. Tu, M. A. Scheel, M. Schwartzkopf, S. V. Roth, Müller-Buschbaum, "Tracking the morphology evolution of active layers for non-fullerene organic solar cells" **16th Coatings Science International 2021**, online, 29 June - 01 July 2021.
- X. Jiang, P. Chotard, K. Luo, F. Eckmann, S. Tu, M. A. Scheel, M. Schwartzkopf, S. V. Roth, Müller-Buschbaum, "In situ study of printing donor:acceptor polymer blends for photovoltaic applications" **EPF European Polymer Congress**, Prague, Czech Republic, 26 June - 1 July 2022.
- X. Jiang, L. Huber, S. Yin, "Scanning Electron Microscopy (SEM)", **E13 Polymer Physics Summer School**, Nassfeld, Austria, July 2022.
- X. Jiang, "Revealing the formation kinetics of the active layer for non-fullerene organic solar cells" **E13 Seminar Talk**, online, 17 May 2022.
- X. Jiang, P. Chotard, K. Luo, F. Eckmann, S. Tu, M. A. Scheel, M. Schwartzkopf, S. V. Roth, Müller-Buschbaum, "Revealing the formation kinetics of the active layer for non-fullerene organic solar cells" **DPG Meeting 2022**, Regensburg, Germany, 04 - 09 September 2022.

Conference Poster Presentations

- X. Jiang, P. Muller-Buschbaum, "Printed low bandgap polymer films" **DPG - Frühjahrstagung**, Berlin, Germany 11 - 16 Mar 2018.

- X. Jiang, W. Cao, P. Muller-Buschbaum, "Printed high-transparent blocking layer for photovoltaics", **8th Colloquium of the Munich School of Engineering**, Garching, Germany, 19 Jul 2018.

- X. Jiang, P. Muller-Buschbaum, "Morphology of printed active layers for organic solar cells as studied with advanced scattering techniques", **4th German SNI Conference**, Garching, Germany, 17 - 19 Sep 2018.

- X. Jiang, W. Cao, W. Chen, P. Muller-Buschbaum, "Printed high-transparent blocking layer for photovoltaics ", **7th SolTech Conference; Solar Technologies go Hybrid**, Würzburg, Germany, 3 - 5 Oct 2018.

- X. Jiang, S. Grott, P. Müller-Buschbaum, "Following the morphology formation of printed non-fullerene active layer for solar cells", **DPG-Frühjahrstagung**, Regensburg, Germany, 31 Mar - 5 Apr 2019.

- X. Jiang, S.Grott, P. Müller-Buschbaum, "Morphology of printed active layers for organic solar cells as studied with advanced scattering techniques", **E13 Summer school**, Granau, Germany, 24 - 27 Jun 2019.

- X. Jiang, S. Schaper, Müller-Buschbaum, "In-situ investigation of sputter deposition electrodes for organic solar cells", **9th Colloquium of the Munich School of Engineering**, Garching, Germany, 1 Aug 2019.

- X. Jiang, S. Grott, W. Chen, Müller-Buschbaum, "Tracking the morphology formation of printed non-fullerene active layers for solar cells by using GISAXS technique", **8th SolTech Conference: Solar Technologies go Hybrid**, Nürnburg, Germany, 30 Sep - 2 Oct 2019.

- X. Jiang, S. Schaper, P. Müller-Buschbaum, "In-situ Investigation of Sputter Deposition Electrodes of Non-Fullerene Organic Solar Cells" **MLZ User Meeting 2019**, Munich, Germany, 10 - 11 Dec 2019

- X. Jiang, S. Schaper, Müller-Buschbaum, "In-situ investigation of sputter deposition electrodes for organic solar cells", **10th Energy Colloquium of the Munich School of Engineering**, online, 30 July 2020.

- X. Jiang, S. Schaper, Müller-Buschbaum, "In-situ sputter deposition of Al electrodes on active layers of non-fullerene organic solar cells", **MLZ User Meeting 2020**, online, 08 - 09 December 2020.

- X. Jiang, S. Tu, S. V. Roth, P. Müller-Buschbaum, "In-situ sputter deposition of electrodes for non-fullerene organic photovoltaics application", **DPG Virtual Spring Meeting 2021**, online, 22 - 24 March 2021.

- X. Jiang, H. Kim, S. V. Roth, P. Müller-Buschbaum, "Internal nanoscale architecture and charge carrier dynamics of wide bandgap non-fullerene bulk heterojunction active layers in organic solar cells", **11th Energy Colloquium of the Munich School of Engineering**, online, 28 July - 29 July 2021.

- X. Jiang, S. Tu, S. V. Roth, P. Müller-Buschbaum, "Following the morphology formation of printed non-fullerene active layer for solar cells", **Virtuelle 84. Jahrestagung der DPG und DPG-Tagung der SKM**, online, 27 September - 01 October 2021.

- X. Jiang, S. J. Schaper, S. V. Roth, P. Müller-Buschbaum, "In-situ observation of electrodes formation on the nonfullerene organic solar cells by GISAXS technique", **MLZ User Meeting 2021**, online, 07 - 08 December 2021.

- X. Jiang, P. Chotard, K. Luo, F. Eckmann, S. Tu, M. A. Scheel, M. Schwartzkopf, S. V. Roth, P. Müller-Buschbaum, "In-situ investigation of the morphology evolution of printed non-fullerene organic solar cells based on different solvent processing", **DESY Photon Science Users' Meeting 2022**, online, 21 - 28 January 2022.

- X. Jiang, P. Chotard, K. Luo, F. Eckmann, S. Tu, M. A. Scheel, M. Schwartzkopf, S. V. Roth, P. Müller-Buschbaum, "Revealing the formation kinetics of the active layer morphology for non-fullerene organic solar cells at ambient conditions", **12th Energy Colloquium "Turning points in the energy transition: Setting the course for the next decades"**, Garching, Germany, 30 July 2022.

Aknowledgements

First and foremost, I would like to thank my supervisor Prof. Dr. Peter Müller-Buschbaum for allowing me to work as a PhD student at the Chair for Functional Materials, with the interesting topic of non-fullerene organic solar cells. Via this topic, I learned the principles and an in-depth understanding of photovoltaics, X-ray scattering and slot-die coating techniques. I appreciate the handy advice and guidance that he provided on my research topic, particularly in the area of X-ray scattering. He has always been supportive of my research during my PhD studies. He also provides me with flexibility in the project I am interested. Despite being constantly busy, he always makes himself accessible to talk to me about the status of my study. He is a highly responsible supervisor, who always finds time to correct my manuscripts meticulously in order to improve the quality. Influenced by his rigorous attitude toward science, I have gradually built my own critical thinking in the research field through numerous discussions with him. I also appreciate all the chances to go to beamtimes and all the great opportunities to go to conferences, which I benefit a lot from during these academic activities. My writing, expression and experimental skills have improved a lot under his supervision these years.

Secondly, I would like to thank the China Scholarship Council (CSC) provided me with the funding to support my living costs during my PhD.

I would like to thank my mentor Prof. Dr. Christine Papadakis for the good working climate at the Chair for Functional Materials and for access to her labs.

It was a great experience for me to operate my experiments in the synchrotron radiation facility. A special thanks to Prof. Dr. Stephan V. Roth who is leading the MiNaXS-beamline at DESY (Hamburg, Germany) for the nice discussion with the in situ sputtering GISAXS data. More importantly, I appreciate his patience, optimistic attitude and encouragement to me during these years. I would like to thank the beamline scientist, Dr. Matthias Schwartzkopf at DESY and Dr. Sigrid Bernstorff at Elettra (Trieste, Italy) for the great support during my beamtime. Successful beamtime is inseparable from the team members behind it. Therefore, I want to acknowledge the beamtime teams: Simon J. Shaper, Sebastion Grott, Julian E. Heger, Manuel A. Reus, Dr. Wei Cao, Dr. Dan Yang, Dr. Wei Chen, Suo Tu, Christopher R. Everett, Marc Gensch, Dr. Kerstin S. Wienhold, Dr. Shanshan Yin, Dr. Volker Körstgens, Kun Sun, Huaying Zhong, Lukas Spanier.

Also, I wish to thank my colleagues for their assistance with my PhD studies in the lab. Without your support and inspiration, it would be an extremely difficult time. I really appreciate the help from Dr. Wei Cao, Dr. Wei Chen, Dr. Senlin Xia, Dr. Lin Song and Dr. Nian Li at the beginning of my PhD study, for the nice discussions and laboratory guidance at E13. Simon J. Schaper's assistance with the GISAXS, GIWAXS, and XRR measurements both in the beamline and downstairs is much appreciated. With the nice discussions with him, I am able to have an in-depth and scientific understanding of the GISAXS measurement from the operation to the data analysis. Thanks a lot for Dr. Lorenz Bießmann, Lennart Reb, Manuel A. Reus, and Christian L. Weindl's help with the great scripts to make my data analysis much easier. Dr. Renjun Guo, Tianle Zheng, Julian E. Heger, Julija Reitenbach, Christopher R. Everett, Dr. Dan Yang, Dr. Jungui Zhou, Dr. Yajuan Li and Zhuijun Xu, are very nice and generous colleagues who are always happy to assist me with my experiment in the lab.

I am really grateful that Julian E. Heger, Julija Reitenbach, Dr. Volker Körstgens, Dr. Ruijie Ma and Kexin Wu for my thesis revision. Thanks to David Paul Kosbahn's great support in modifying the latex formatting for my thesis. All corrections are valuable for the improvement of my thesis.

In addition, many thanks to Dominik Schwaiger and Julian E. Heger for the great help with my teaching activities.

I really enjoyed the collaboration with several external groups, it brings me a new vision of the field of organic solar cells. I would like to express my great thanks to Dr. Alexander J. Gillett for the very nice discussion related to organic solar cells and the strong support of transient absorption measurement from Cavendish Laboratory, University of Cambridge (England). I would like to thank Dr. Xinyu Bai and Dr. Linjie Dai for the PL and TRPL measurements in the Cavendish Laboratory, University of Cambridge. In addition, I would like to thank Dr. Xin Song for the solar cell fabrication and the J-V and EQE measurements from Jiangnan University, China. Thank you, Peter S. Deimel, Dr. Francesco Allegretti and Prof. Dr. Johannes V. Barth for the X-ray photoelectron spectroscopy measurements at E20 group. I want to thank Felix Eckmann, a very nice and smart PhD student for the support of TRPL measurements at the WSI department. Thank Haodong Tang and Prof. Kai Wang for the help with the TRPL measurement from Southern University of Science and Technology (SUSTech), China.

Moreover, I want to thank the master and bachelor students Kexun Luo, Hongwon Kim, Pauline Chotard, Tommaso Riccitelli, Adrian Jurjević, Laura Bauer, Marta Di Girolamo etc... who worked together with me on the organic solar cell topic. I highly appreciate your strong motivation and effort in the experiment.

Also, I would like to thank my internal office mates Dr. Lorenz Bießmann, Dr. Nuri Hohn,

Dr. Nitin Saxena, Dr. Shambhavi Pratap, Dr. Shanshan Yin, Fabian Apfelbeck and external office mate Dr. Volker Körstgens, for the warm and happy atmosphere you brought in our small office. In addition, I would like to thank Julian E. Heger's accompanying me during my last year's PhD time in the office, we worked very late and had a lot of fast food together, it became a very memorable and interesting experience in my life.

It has been a great time for me at the Chair for Functional Materials since here not only have advanced techniques but also friendly colleagues around. We have shared a lot of nice memories together, the everyday lunch at 11:30, every week's seminar talks, every year's summer school, the DPG conference, X-mas party ..... I want to especially thank the colleagues during my PhD study who I do not mention yet in no specific order: Dr. Bo Su, Dr. Kun Wang, Dr. Chia-Hsin Ko, Dr. Jia-Jhen Kang, Jiabin Gui, Andreas Zheng, Lucas P. Kreuzer, Tobias Widmann, Suzhe Liang, Peixi Wang, Yanan Li, Tianxiao Xiao, Tianfu Guan, Suo Tu, Ting Tian, Yuqin Zou, Christina Geiger, Roy Schaffrinna, Anna-Lena Oechsle, Linus Huber, Morgan Le Dü, Bahar Yazdanshenas, Feifei Zheng, Peiran Zhang, Pablo Alvarez Herrera, Guangjiu Pan, Yuxin Liang, Zeirui Li, Jinsheng Zhang, Yingying Yan and Xiongzhuo Jiang from my bottom of my heart.

The help of Marion Waletzki and Carola Kappauf in organizing many lively events and the documentary work for my Visa is deeply appreciated. The technical support for processing useful masks for my experiment with Reinhold Funer and Benjamin Predeschly will always be positively remembered. Many thanks to Dominik Schwaiger for all of his assistance with installing software on my working PC.

I really want to thank my family, my parents, sisters, brother-in-law, my cousins, my niece and naughty nephews. I am really grateful for the great support and understanding about my decision to study for my PhD degree in Germany. Thank you for the relaxed atmosphere you created, which always makes me feel very happy, and I can do my work with peace of mind. Especially, I want to thank my dad, Mr Jiang. To help me get into the habit of getting up early, he wakes me up via WeChat at 8:00 every morning since 2019 uninterrupted. I really appreciated it !

I want to thank my friends who are supporting behind. I want to Dr. Dan Li, who helped me a lot with my writing. In addition, he always enlightens me and gives me a lot of suggestions when I feel helpless. Dr. Hong Yan Dr. Mengjie Zheng and Tong Xiao, my best friends, I really appreciate your accompany when I need you. I want to thank Weiqi Zhang, who helped me a lot to solve the python work issue when I am in trouble. Although they are not in Germany, they are always online when I need them, for which I am really grateful !

In the last, I am thankful for the time that I have spent working on this thesis, as it gave me the chance to grow beyond my limits.